University of Ljubljana
Faculty of Mathematics and Physics
Department of Physics

Rok Žitko

Many-particle effects in resonant tunneling of electrons through nanostructures

Doctoral thesis

ADVISER: Prof. Dr. Janez Bonča
COADVISOR: Prof. Dr. Igor Muševič

Ljubljana, 2007

Univerza v Ljubljani
Fakulteta za matematiko in fiziko
Oddelek za fiziko

Rok Žitko

VEČDELČNI POJAVI PRI RESONANČNEM TUNELIRANJU ELEKTRONOV SKOZI NANOSTRUKTURE

Doktorska disertacija

MENTOR: prof. dr. Janez Bonča
SOMENTOR: prof. dr. Igor Muševič

Ljubljana, 2007

Abstract

Effects of electron-electron interactions on the transport properties of nanostructures are explored, focusing on the conductance through systems of coupled quantum dots and the tunneling spectroscopy of magnetic adsorbates on surfaces; both systems can be modeled using quantum impurity models. The properties of impurity models are described in considerable detail and a new implementation of Wilson's numerical renormalization group is introduced. Double quantum dot systems of various coupling topologies are studied. In parallel double quantum dot, local moments order ferromagnetically and $S = 1$ Kondo effect occurs. In side-coupled double quantum dot, Kondo screening proceeds in two stages. Triple quantum dot is studied using several numerical methods and a low-temperature phase diagram is proposed. A wide regime of non-Fermi liquid behavior is found at finite temperatures in the cross-over region between antiferromagnetic ordering regime and the two-stage Kondo regime. In the second part, construction of a low-temperature scanning tunneling microscope is described. The Kondo effect induced by magnetic adsorbates on surfaces is reviewed and a two-level model is proposed to describe the tunneling spectroscopy experiments performed on single magnetic adatoms.

PACS: 73.63.Kv 72.15.Qm 73.23.Hk 71.10.Hf 68.37.Ef

Keywords: quantum impurity models, Kondo effect, numerical renormalization group, coupled quantum dots, tunneling spectroscopy.

Povzetek

Interakcije med elektroni pomembno vplivajo na transportne lastnosti nanostruktur. Posebno zanimiva sta prevodnost sistemov sklopljenih kvantnih pik in tunelska spektroskopija magnetih nečistoč, adsorbiranih na površinah kovin. Oba sistema lahko opišemo z modeli kvantnih nečistoč, katerih lastnosti so podrobno opisane. Predstavljena je nova izvedba metode numerična renormalizacijska grupa. Proučeni so sistemi dvojne kvantne pike z različnimi topologijami sklopitve. V vzporedni dvojni kvantni piki se lokalna momenta uredita feromagnetno in pride do Kondovega pojava s spinom 1. V stransko sklopljeni dvojni kvantni piki Kondovo senčenje poteka v dveh korakih. Sistem trojne kvantne pike je obravnavan s komplementarnimi numeričnimi metodami in določen je fazni diagram sistema pri nizkih temperaturah. V prehodnem območju med režimoma antiferomagnetnega urejanja in dvostopenjskega senčenja obstaja široko območje, kjer se sistem v nekem temperaturnem intervalu obnaša kot ne-Fermijeva tekočina. V drugem delu doktorskega dela je opisano sestavljanje nizko-temperaturnega vrstičnega tunelskega mikroskopa. Opisan je Kondov pojav na površinah, ki ga povzročijo magnetne nečistoče, in vpeljan nov dvonivojski model, ki opisuje poskuse s tunelsko spektroskopijo na posameznih magnetnih atomih.

PACS: 73.63.Kv 72.15.Qm 73.23.Hk 71.10.Hf 68.37.Ef

Ključne besede: modeli kvantnih nečistoč, Kondov pojav, numerična renormalizacijska grupa, sklopljene kvantne pike, tunelska spektroskopija.

I would like to sincerely thank my advisors, prof. dr. Janez Bonča and prof. dr. Igor Muševič, for guiding, valuable advice, discussions and support, and especially for granting me a considerable extent of autonomy in my work. I also thank prof. dr. Albert Prodan and Erik Zupanič for sharing the joys and sorrows of building an STM. I acknowledge the very fruitful discussions on various topics related to Kondo physics and quantum transport that I have had with Jernej Mravlje, prof. dr. Anton Ramsak and dr. Tomaž Rejec. I also thank Ivan Kvasić for building many electronic gadgets and for troubleshooting, Stefan Fölsch at Paul Drude Institut for design tips and valuable advice on STM hardware, Sven Zöpfel of Createc for assembly instructions, and Peter Panjan for discussions on friction and for hard-coating some of the STM parts. Finally, I thank my parents for support and Tamara for patiently enduring my devotion to science.

Contents

List of abbreviations and acronyms

Abbreviation	Full form
1D	one-dimensional
2CK	two-channel Kondo
2D	two-dimensional
2DEG	two-dimensional electron gas
2IK	two-impurity Kondo
AES	Auger electron spectroscopy
AFM	antiferromagnetic
BA	Bethe Ansatz
CFT	conformal field theory
CPMC	constrained-path Monte Carlo
DFT	density functional theory
DMFT	dynamic mean field theory
DMNRG	density-matrix NRG
DOS	density of states
DQD	double quantum dot
d.o.f.	degree of freedom
e-e	electron-electron
ESCA	electron spectroscopy for chemical analysis
FF	ferromagnetically frozen
FL	Fermi liquid
FI	frozen-impurity
FM	ferromagnetic
FO	free-orbital
FP	fixed point
HF	Hartree-Fock
GS	Gunnarson-Schönhammer (variational method)
LDOS	local density of states
LEED	low-energy electron diffraction
LSDA	local spin density approximation
LHe	liquid helium
LM	local-moment
LN2	liquid nitrogen
LT	low-temperature
MO	molecular orbital
NFL	non-Fermi liquid
NRG	numerical renormalisation group
NS	Neveu-Schwarz
p-h	particle-hole (symmetry)

Abbreviation	Full form
QFT	quantum field theory
QIM	quantum impurity model
QMC	quantum Monte Carlo
QMS	quadrupole mass spectrometer
QPT	quantum phase transition
QD	quantum dot
R	Ramon
RG	renormalization group
RKKY	Ruderman-Kittel-Kasuya-Yosida
RT	room temperature
SC	strong-coupling
SEM	scanning electron microscope
SET	single electron transistor
SIAM	single-impurity Anderson model
STM	scanning tunneling microscope
SWT	Schrieffer-Wolff transformation
TEM	transmission electron microscope
TQD	triple quantum dot
TSK	two-stage Kondo
UHV	ultra-high vacuum
VF	valence fluctuation

List of symbols

Symbol	Description	Conventional unit
ϵ_k	Energy of conduction band electron	eV
$c^\dagger_{k\mu}$	Creation operator for band electron	
k	Crystal momentum, wavenumber	Å^{-1}
μ	Magnetic quantum number, also σ, s_z	
$\boldsymbol{\sigma}$	Pauli matrices	
N_c	Number of conduction band states	
$f^\dagger_{i\mu}$	Hopping Hamiltonian creation operator	
D	Half bandwidth	eV
J	Spin-spin exchange coupling	eV
$\mathbf{S}$	Spin operator	
$\rho(\omega)$	Density of states	1/eV
J, J_K	Kondo exchange interaction	eV
k_B	Boltzmann's constant	$= 86\,\mu$eV/K
β	Inverse temperature, $1/(k_BT)$	1/eV
T_K	Kondo temperature	K
k_F	Fermi wavenumber	Å^{-1}
v_F	Fermi velocity	m/s
v_c, v_s	Velocity of charge/spin modes	m/s
R_W	Wilson's ratio	
i, j	Lattice site indexes	
$t, t_{i,j}$	Tunnel hopping, overlap integral	eV
Q, q	Charge quantum number, $q_i = n_i - 1$	
$\mathbf{I}$	Isospin operator	
ξ_i	Nambu spinor	
P	Parity	
L	Linear size of the system	m
ϵ_d	Energy of impurity orbital	eV
δ	Deviation from p-h symmetric point, $\delta = \epsilon_d + U/2$	eV
$d^\dagger_{i\mu}$	Creation operator for impurity electron	
U	Charge-charge coupling, Coulomb correlation energy	eV
G_0	Conductance quantum, $G_0 = 2e^2/h$	A/V = S
g	Dimensionless conductance, $g = G/G_0$	
$V_{\mathbf{k}}$	Impurity–conduction-band hybridization	eV
Δ, Γ	Tunnel rate, resonance half-width	eV
$G^r_{ij}(t)$	Retarded Green's function	
$A_{ij}(\omega)$	Spectral function	1/eV

Symbol	Description	Conventional unit
χ_{charge}	Impurity charge susceptibility	
$\chi_{\text{spin}}, \chi_{\text{imp}}$	Impurity magnetic susceptibility	
S_{imp}	Impurity entropy	
Z	Partition function	
γ	Linear coefficient in heat capacity, $C = \gamma T$	
g	Gyromagnetic ratio	
μ_B	Bohr magneton	$= e\hbar/2m_e$
Λ	NRG discretization parameter	
N	NRG iteration number	
E	Energy	ev
ϵ	Dimensionless energy, $\epsilon = E/D$	
b	Spectrum broadening parameter	
$\Sigma(\omega)$	Self-energy	eV
$S_{\mathbf{k}\mu,\mathbf{k}'\mu'}$	Scattering matrix	
z, Z	Quasiparticle weight	
n	Electron density	m^{-3}
K	Potential scattering amplitude	eV
δ_{qp}	Scattering phase-shift	rad
τ	Scattering time	s
T_1^*	Local-moment formation temperature	K
J_{RKKY}	Effective spin exchange coupling	eV
T_F^*	Ferromagnetic ordering temperature	K
$T_K^{(1)}$, $T_K^{(2)}$	Upper, lower Kondo temperature	K
A	Asymmetry parameter	
T_Δ	NFL-FL cross-over temperature	K
I	(Tunneling) current	A
V	(Bias) voltage	V
q	Fano form factor	
B	Magnetic field	T

Liberal use of $\hbar = 1$ and $k_B = 1$ system of units is made, especially in longer derivations.

Chapter 1

Introduction

Advances in nanoscience and nanotechnology empower us with new tools for probing systems of increasingly small sizes. Nowadays one can, for example, measure transport properties of semiconductor quantum dots, single molecules, and even individual atoms adsorbed on a surface. The interest in such systems is twofold. On one hand, transport through nanostructures is of fundamental interest since a number of very characteristic quantum effects can be studied. On the other hand, nanostructures represent the ultimate degree of miniaturization of electronic devices and they are likely candidates for the building blocks of the circuitry of tomorrow.

A notable phenomenon that is commonly at play on the nanoscopic scale is quantum tunneling – transmission of electrons through classically-forbidden energy barriers. The use of the electron tunneling as a spectroscopic technique eventually led to the invention of the scanning tunneling microscope (STM) in 1982. Since then, STM has become one of the most versatile tools in nanoscience. In addition to its most common use as a topographic microscope with atomic resolution, STM can be applied to perform lateral manipulations of adsorbed species and to transfer adsorbates from sample to tip and vice-versa. It can also induce dissociation, desorption and conformation changes in molecules and it is even possible to perform chemical synthesis. Finally, STM can be used to perform tunneling spectroscopy of the smallest magnetic objects - single magnetic atoms, clusters and molecules adsorbed on surfaces.

Somewhat larger magnetic nanostructures can be built using quantum dots. Quantum dots are microscopic puddles of electrons which can be considered as artificial atoms, since the confined electrons are quantized and form orbitals much like the electrons in orbit around an atomic nucleus. Particularly interesting are semiconductor quantum dots patterned in high-quality heterostructures grown by molecular beam epitaxy. Lateral quantum dots, for example, are defined in AlGaAs/GaAs heterostructures with a subsurface layer of the high-mobility two-dimensional electron gas by patterning metallic gates on the sample surface.[1] By adjusting the voltages on these gates, it is possible to control the number of the electrons trapped in the quantum dot and change the coupling of the dot with the

electron gas. Quantum dots thus serve as tunable realizations of quantum impurity models – models of point-like impurities with internal degrees of freedom – in which on-site energy and hybridization strength can be easily swept in-situ.

Quantum impurity models attract the interest of the solid state physics community both due to their unexpectedly complex behavior and intrinsic beauty, as well as due to their ubiquitous applicability to a vast array of physical systems such as bulk Kondo systems, heavy-fermion compounds and other strongly correlated systems,[2] dissipative two-level systems,[3] single magnetic impurities and quantum dots.[4–6]

In very small electronic devices the electron-electron interactions are strong and they induce interesting many-particle effects. The most notable is perhaps the Kondo effect which appears to be a relatively generic feature of nanodevices.[7–10] The Kondo effect is a many-particle phenomenon arising from the interaction between a localized spin and free electrons that leads to increased spin-flip scattering rate of the electrons at low temperatures. This gives rise to various anomalies in the thermodynamic and transport properties, in particular to increased conductance through nanostructures. The conductance through a quantum dot in the Kondo regime as a function of temperature, gate and bias voltages is in agreement with theoretical predictions that such dots behave rather universally as single magnetic impurities[11] and can be modelled using single impurity Anderson and Kondo models.[11,12]

Systems of multiple coupled impurities are realizations of generalized Kondo models where more exotic Kondo states may occur. The research in this field has recently intensified due to a multitude of new experimental results; the multi-impurity magnetic nanostructures under study are predominantly of two kinds: clusters of magnetic adsorbates on surfaces of noble metals (such as Ni dimers,[13] Ce trimers,[14] molecular complexes[15]) and systems of multiple quantum dots.[1,16–19] Double quantum dot and dimers of magnetic atoms, for example, are realizations of the two-impurity Kondo model, which exhibits quantum criticality. This model has been applied to study the competition between magnetic ordering and Kondo screening.[20,21] Fermi and non-Fermi liquid behaviors, ferromagnetic and antiferromagnetic correlations, and diverse behavior of heavy fermion systems[22] are all believed to result from the competition between the Kondo effect and magnetic exchange interaction.[16] Recently, several experimental realizations of the two-channel Kondo model using quantum dots have been proposed.[23–27] The two-channel Kondo model exhibits non-Fermi liquid behavior and it has been used in the past to explain the unusual logarithmic temperature dependence of the magnetic susceptibility and linear vanishing of the quasiparticle decay rate in some Ce and U compounds at low temperatures.[28] Research on systems of quantum dots thus also sheds light on the behavior of extended bulk correlated materials.

NRG The method of choice to study the low-temperature properties of quantum impurity models is Wilson's numerical renormalization group (NRG).[29–31] The NRG technique consists of logarithmic discretization of the conduction band, mapping onto a one-dimensional chain with exponentially decreasing hopping constants, and iterative diagonalization of the resulting Hamiltonian. NRG is one of the very few methods which give comprehensive information on the behavior of impurities both at zero and at finite temperatures.

The dissertation is structured as follows. Introductory Part I is largely devoted to the theory of tunneling through nanostructures and related topics. The concepts of quantum impurity models, Kondo effect, effective field theories, spin-charge separation, Fermi liquid and non-Fermi liquid systems are introduced in Chapter 2. Chapter 3 presents the renormalization group approach to the quantum impurity models with a particular emphasis on Wilson's numerical renormalization group, while other numerical methods are briefly presented in Chapter 4. Finally, the transport formalism for calculating the conductance through a nanostructure is given in Chapter 5. Part II presents the main body of the results on the properties of the nanostructures described as single impurity models (Chapter 6), two-impurity models (Chapter 7) or three-impurity models (Chapter 8). Both thermodynamic and transport properties are described; often the knowledge of thermodynamic behavior is essential for proper understanding of the transport properties of a system. Part III is devoted to scanning tunneling microscopy. Chapter 9 describes the construction of a new low-temperature STM and gives some background information on technical aspects of STM operation. The magnetic properties of clusters of magnetic adatoms, with an emphasis on the surface Kondo effect, are described in Chapter 10. Some technical matters are relegated to Appendices.

Part I

Theory of tunneling through nanostructures

Chapter 2

Theory of quantum impurity models

This chapter introduces the concept of quantum impurity models (Section 2.1) and the associated Kondo physics (Sec. 2.2). Section 2.3 is devoted to symmetries which play a central role in these models. The notions of Fermi liquids and non-Fermi liquids are presented in Sec. 2.4. It is shown that quantum impurity problems are one-dimensional field theories (Sec. 2.5) and that spin and charge degrees of freedom separate (Sec. 2.6). I conclude with a short introduction to the boundary conformal field theory which provides a simple account of the essence of the Kondo effect (Sec. 2.7).

2.1 The concept of a quantum impurity model

Quantum impurity models (QIMs) describe interaction between a point-like impurity with internal degrees of freedom and a continuum of states. For example, the impurity may be a substitutional defect such as a magnetic impurity atom carrying local magnetic moment (the quantum degree of freedom is spin), the continuum may consist of itinerant conduction band electrons of the non-magnetic host material, and the interaction may be antiferromagnetic exchange interaction between the local moment and the conduction band electrons:[2,32] a model with such characteristics belongs to the important class of the s-d exchange quantum impurity models. More generally, the impurity degree of freedom may also be orbital moment,[33] orbital pseudo-spin,[34–36] helicity,[37,38] impurity charge (isospin)[39–43] or a discrete coordinate (positional pseudo-spin).[3] The continuum is typically fermionic (conduction band electrons), but may also be bosonic (collective electron excitations in the host,[44] phonon modes[45]), and the interaction can be hybridization or some generalized exchange interaction. The renewed interest in QIMs is largely due to the fact that many nanostructures belong to the class of quantum impurity systems and that they may be easily characterized by transport measurements.[46,47]

The paradigmatic case of a QIM is the Kondo model of a spin-1/2 magnetic impurity interacting with a fermionic band with constant density of states ρ via antiferromagnetic

exchange interaction with a coupling constant J that does not depend on energy nor on the direction in the momentum space.[48] The Kondo Hamiltonian is

$$H = \sum_{k\mu} \epsilon_k c^\dagger_{k\mu} c_{k\mu} + J\mathbf{s}\cdot\mathbf{S}. \tag{2.1}$$

The first term describes the conduction band of non-interacting electrons: $c_{k\mu}$ is the annihilation operator for conduction band electron with momentum k and spin μ. Operator $\mathbf{s}$ is the electron spin-density at the position of the impurity:

$$\mathbf{s} = \sum_{\mu\mu'} f^\dagger_{0\mu} \left(\tfrac{1}{2}\boldsymbol{\sigma}_{\mu\mu'}\right) f_{0\mu'}. \tag{2.2}$$

Here

$$f^\dagger_{0\mu} = \frac{1}{\sqrt{N_c}} \sum_k c^\dagger_{k\mu} \tag{2.3}$$

is the combination of the conduction band operators that create an electron at the position of the impurity, i.e. the Wannier orbital centered at the impurity (N_c is the number of states in the band). $\mathbf{S}$ is the impurity spin operator; its components obey the SU(2) anti-commutation relation $[S_i, S_j] = i\epsilon_{ijk}S_k$. In the conventional Kondo problem $S = 1/2$, but $S > 1/2$ generalizations are also studied. The coupling constant J is assumed to be "small". Considerable attention was devoted to the Kondo problem due to unexpectedly complex behavior of this seemingly simple problem. Even though J is small, the problem cannot be treated by the perturbation theory;[49] it turns out, instead, that the system is strongly renormalized at temperatures below some characteristic Kondo temperature $T_K \sim \exp(-1/\rho J)$, where ρ is the density of states of the conduction band at the Fermi level. This unusual behavior is called the Kondo effect.

The adjective *quantum* in *quantum impurity model* emphasizes that the scattering potential seen by the conduction-band electrons in QIMs is "non-commutative".[28] This means that the scattering T-matrix contains terms where the divergent logarithmic terms are multiplied by a commutator of the interaction matrix elements. This commutator can generally be simplified to a commutator of the operators corresponding to the impurity degrees of freedom: for a *quantum* impurity this commutator is non-zero, while for an impurity with no internal degrees of freedom or for a classical impurity the commutator is zero. In the case of the Kondo problem, the relevant commutator is the spin SU(2) commutator $[S_i, S_j] = i\epsilon_{ijk}S_k$. Since the bracket is non-zero, the model is indeed non-commutative and logarithmic terms appear. These terms indicate the break-down of the perturbation theory and the non-trivial behavior of the system. It should be noticed that in the $S \to \infty$ limit, a spin behaves like a classical angular momentum; in the Kondo model with large impurity spin S, the effective interaction is indeed weakened, the Kondo crossover becomes broader and less pronounced.[50,51]

Other problems that belong to the QIM family are two-level systems like metallic glasses where an atom may tunnel between two positions possessing levels close in energy[52] and the

spin-boson model where a two-level system interacts with harmonic oscillators that mimic the environment responsible for decoherence and dissipation.[45]. Related problems, though not real QIMs, are also the resonant level scattering problem and the X-ray absorption edge singularity problem.[53,54]

2.2 Kondo effect

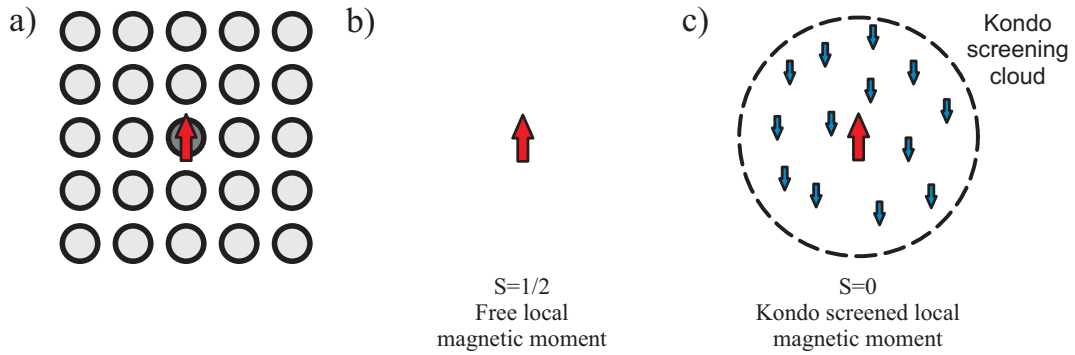

Figure 2.1: Quantum impurity with magnetic moment and the Kondo effect. a) Prototype quantum impurity system: an impurity atom carrying net local magnetic moment embedded in a non-magnetic host material. b) At high temperature the impurity moment is nearly free and the system has magnetic response. c) At low temperature the conduction band electrons screen the local magnetic moment in the Kondo effect. The system is then non-magnetic.

The Kondo effect in magnetic quantum impurity systems (Fig. 2.1) is a subtle many-electron effect in which conduction-band electrons in the vicinity of the impurity screen the local moment to form a collective entangled non-magnetic ground state at low temperatures. Alternatively, in the language of the boundary conformal field theory[55], the Kondo effect consists of the disappearance of the impurity spin degree of freedom from the problem as it is swallowed by the conduction electron spin density (see Sec. 2.7. The Kondo problem was the first known asymptotically free theory:[2,56] the local moment is essentially free at high energies (i.e. for high momentum exchange that probes short-distance behavior, Fig. 2.1b), but the system becomes strongly interacting at low energies (long-distance behavior) and the local moment loses its individuality, Fig. 2.1c . In this sense, Kondo physics is akin to color confinement in quantum chromodynamics: particles with color charge (such as quarks) cannot be isolated since the force between a pair of particles increases with the separation. In the context of magnetic impurities this translates into the absence of magnetic response at low temperatures.

A characteristic feature of the Kondo effect is the emergence of the Abrikosov-Suhl (or Kondo) resonance, a narrow scattering resonance near the Fermi level, at temperatures less than the Kondo temperature. The Abrikosov-Suhl resonance is of many-particle origin and

appears due to correlated behavior of electrons. Since the thermodynamic and transport properties of systems at low temperatures are predominantly determined by electrons with energies close to the Fermi level, this resonance gives significant contributions to the specific heat, magnetic susceptibility and scattering-rate at low temperatures;[57] the Abrikosov-Suhl resonance is thus the origin of the anomalies observed in experiments. This resonance is also directly involved in the enhanced conductance through quantum dots and molecules in the Kondo regime[7,9]. It also appears in the $\mathrm{d}I/\mathrm{d}V$ measurements in scanning tunneling spectroscopy, albeit in more convolved form of a Fano resonance due to the interference between different tunneling channels[4] (see Sec. 10.2 and 10.3).

In the scaling picture (described more thoroughly in the next chapter, Sec. 3.1), the effective model of the Kondo model at lower temperatures again takes the form of the Kondo Hamiltonian, but with a temperature dependent exchange constant $J(T)$. The effect of the high-energy electrons is thus to renormalize the exchange interaction, whose strength grows as the temperature is decreased:

$$J(T) = \frac{J}{1 - \rho J \ln(k_B T/D)}, \tag{2.4}$$

where J is the bare exchange constant which appears in the original Hamiltonian. At the Kondo temperature $k_B T_K = D\exp(-1/\rho J)$, $J(T)$ diverges: this indicates that on this temperature scale the electron scattering becomes strong. The scaling approach thus provides a useful qualitative definition of T_K.

For temperatures below T_K the system is said to be in the *strong-coupling regime* [as indicated by the divergent $J(T)$] where half a unit of the impurity spin is screened by the electrons.[58] As the temperature is increased, the system crosses over to the asymptotically-free *local moment* regime where the free spin behavior is logarithmically approached.[59]

Another interpretation of the Kondo cross-over is possible , according to which the Kondo effect is a way for the system to reduce its energy by "tunneling" through different degenerate impurity states. A "Kondo singlet" bound state is generated in this manner. Its bounding energy is on the scale of the Kondo temperature, which can be demonstrated using a simple variational wave-function.[2,60,61] The "tunneling" point of view makes it clear that the degeneracy of the impurity ground states plays a very important role: the variational calculation shows that degeneracy enters as a factor in the exponential function of the expression for T_K. Increased degeneracy can thus strongly enhance the Kondo temperature. This implies that if the symmetry of the problem is extended by suitably tuning the model parameters (for example using gate voltages of a quantum dot system), the Kondo temperature can increase; in turn, this may lead to enhanced conductance at finite temperatures.[62] It should be emphasized, however, that this may occur only if the symmetry of the entire system is increased; both the impurity and the host system must have matching symmetry.[2] In bulk impurity systems, for example, the orbital degeneracy may increase the Kondo temperature only if there is orbital exchange, i.e. when the effective model is of the Coqblin-Schrieffer kind with the degeneracy factor $N = 2(2l+1)$. If

an impurity with orbital degree of freedom couples to a single orbital channel, there is no such enhancement.[2]

In principle, Kondo effect can occur whenever the impurity ground state is degenerate. In the familiar case of the $S = 1/2$ Kondo model, the two relevant states form a $|S = \frac{1}{2}, S_z = \pm\frac{1}{2}\rangle$ magnetic doublet. In quantum dot systems, the degeneracy between different spin multiplets can be intentionally induced by tuning the magnetic field since the orbital energy strongly depends on the field, whereas the Zeeman energy is small due to the very small gyromagnetic ratio in GaAs. At the degeneracy point, large zero-bias resonances with increased Kondo temperature are observed.[63,64] this is the singlet-triplet Kondo effect that has been a subject of intense studies in recent years.[63–75] We may also obtain more exotic doublet-doublet and doublet-quadruplet Kondo effects.[62]

2.3 Symmetries in quantum impurity models

This work mainly concerns quantum impurity models where one or several impurity sites are coupled to at most two single-mode conduction channels, i.e. to two non-interacting continua of states. Such models are appropriate for most systems where the interacting region is embedded between two conduction leads, as is the case in most experimental situations. We assume that each continuum state carries a spin index $\mu = \uparrow, \downarrow$ and that in the relevant low-energy range the dispersion may be linearized. For convenience we set the chemical potential in the middle of the band, which we also choose as our energy zero. The conduction band Hamiltonian is thus

$$H_{\text{band}} = \sum_{k,\mu,\alpha} \epsilon_k c^\dagger_{k\mu\alpha} c_{k\mu\alpha}, \tag{2.5}$$

where the rescaled wave-number k ranges from -1 to 1, $\epsilon_k = Dk$ where D is the half-bandwidth, and α is the channel index, $\alpha = 1, 2$. The density of states is constant, $\rho = 1/(2D)$. Since $\epsilon_k = \epsilon_{-k}$, the conduction band is particle-hole symmetric. In fact, the Hamiltonian (2.5) has very high degree of symmetry. By decomposing the complex fermionic operators $c^\dagger_{k\mu\alpha}$ into real and complex parts (Majorana fermions,) it can be shown that the symmetry group is SO(8).[21,76] This symmetry group has same very peculiar properties (such as the triality symmetry between its representations) which play a role in the non-Fermi liquid behavior that this class of problems may exhibit.[21,76] The total SO(8) symmetry of the conduction bands is reduced by the impurity-lead coupling to some product of subgroups of SO(8). We thus need to study the possible remaining symmetry of the total model Hamiltonian; we have to find the maximal set of mutually commuting operators that also commute with the Hamiltonian.

In addition to the internal SO(8) symmetry of the particles, the field theoretic version of (2.5) exhibits conformal symmetry:[21,55,77–81] the theory is rotation, translation and scale invariant in the two-dimensional (2D) space-time. In fact, this holds at low temperatures

for all one-dimensional systems of free fermions.[82] This behavior is a direct consequence of the fact that excitations of a Fermi liquid behave in the first approximation as massless particles. The conformal symmetry in 2D is very special because there is an infinite number of generators of the group of local conformal transformations: such high symmetry is extremely constraining and there can in general be only a very small number of free parameters in such conformal field theories (CFTs). In fact, many such theories may be solved exactly.[83] See also Sec. 2.7.

We remark in passing that the symmetry of the Hamiltonian changes under the renormalization flow. In particular, symmetries may be restored at low energies and fixed point Hamiltonians generally have higher symmetry than the underlying microscopic model.[84] For example, while H_{band} is conformally symmetric, the conformal invariance is lost after the impurity is introduced into the system. One of the important insights of the boundary CFT approach is that as the system approaches a fixed point, the conformal symmetry is restored: Lie group symmetry is enhanced to Kac-Moody symmetry.

2.3.1 Spin symmetry $\mathrm{SU}(2)_{\text{spin}}$

The local spin operator for a single orbital is defined as

$$\mathbf{S}_i = \sum_{\mu\mu'} a^\dagger_{i\mu} \left(\tfrac{1}{2}\boldsymbol{\sigma}_{\mu\mu'}\right) a_{i\mu'}, \tag{2.6}$$

where $\boldsymbol{\sigma} = \{\sigma^x, \sigma^y, \sigma^z\}$ are the Pauli matrices. In component form, we find

$$\begin{aligned} S^z_i &= \tfrac{1}{2}\left(a^\dagger_{i\uparrow}a_{i\uparrow} - a^\dagger_{i\downarrow}a_{i\downarrow}\right), \\ S^+_i &= a^\dagger_{i\uparrow}a_{i\downarrow}, \\ S^-_i &= a^\dagger_{i\downarrow}a_{i\uparrow}, \end{aligned} \tag{2.7}$$

where we have defined $S^+_i = S^x + iS^y$ and $S^-_i = S^x - iS^y$. In the absence of magnetic field, the system is isotropic in the spin space and it has $\mathrm{SU}(2)_{\text{spin}}$ symmetry. The generators are the components of

$$\mathbf{S} = \sum_i \mathbf{S}_i \tag{2.8}$$

where index i ranges over all sites of the system (both impurity sites $d^\dagger_i$ and conduction band levels $c^\dagger_k$). Both $\mathbf{S}^2$ and S^z commute with H, therefore the invariant subspaces can be classified according to quantum numbers S and S^z. Furthermore, when the Hamiltonian is rotationally invariant in the spin space, S^z does not play any role in the diagonalization and it can be taken into account using the Wigner-Eckart theorem (see Appendix A).

In the case of an XXZ anisotropy in the spin space (for example due to an anisotropic exchange interaction between the impurities and the conduction band), the SU(2) symmetry

is reduced to $O(2) \sim U(1)_{\text{spin}} \times Z_2$ symmetry. $U(1)_{\text{spin}}$ corresponds to rotations around the z-axis: S^z remains a good quantum number but the Wigner-Eckart theorem no longer applies. Z_2 corresponds to spin inversion, which is still a symmetry operation in this case. Spin inversion can be defined as the mapping

$$a_{i,\mu} \rightarrow (2\mu) a_{i,-\mu}. \tag{2.9}$$

Here $(2\mu) = \pm 1$ for $\mu = \uparrow, \downarrow = \pm 1/2$ is a conventional phase factor. Spin inversion operator $U = \exp(i\pi S_y)$ is an element of the $SU(2)_{\text{spin}}$. In the presence of magnetic field applied along the z-axis, the Z_2 symmetry is lost and the remaining spin symmetry is just $U(1)_{\text{spin}}$.

It should be remarked that for a single site

$$\mathbf{S}_i^2 = \frac{3}{4}(n_{i\uparrow} + n_{i\downarrow} - 2n_{i,\text{pair}}) = \frac{3}{4}(2n_i - n_i^2), \tag{2.10}$$

where $n_{i\mu} = a_{i\mu}^\dagger a_{i\mu}$, $n_i = n_{i\uparrow} + n_{i\downarrow}$ and $n_{i,\text{pair}} = n_{i\uparrow} n_{i\downarrow} = n_i(n_i - 1)/2$. It thus suffices to calculate $\langle n_i \rangle$ and $\langle n_i^2 \rangle$ to determine the local spin. In the case of two and more sites, we need to know the occupancies, squares of occupancies and scalar products of spin. For example, for two sites we have

$$\mathbf{S}^2 = (\mathbf{S}_1 + \mathbf{S}_2)^2 = \frac{3}{4}\left(2n_1 + 2n_2 - n_1^2 - n_2^2\right) + 2\mathbf{S}_1 \cdot \mathbf{S}_2. \tag{2.11}$$

2.3.2 Charge conservation $U(1)_{\text{charge}}$

We define the charge operator $\hat{Q}$ as

$$\hat{Q} = \sum_i (n_i - 1), \tag{2.12}$$

where i again runs over all the sites of the problem. We subtract one so that the charge is defined as the excess charge with respect to a half-filled system. In all physically sensible problems, the total charge Q is a conserved quantity. This conservation is associated with a $U(1)_{\text{charge}}$ symmetry due to global phase (gauge) invariance. Note that the three operators $\hat{Q}$, $\hat{S}^2$ and $\hat{S}_z$ are mutually commuting.

2.3.3 Particle-hole symmetry Z_2

The particle-hole (p-h) transformation maps particle-like excitations above the Fermi energy into hole-like excitations below the Fermi energy. A system is said to be p-h symmetric when it is invariant with respect to the p-h transformation. This is only possible if all spectral functions of the system are symmetric with respect to the Fermi level, $A(\omega) = A(-\omega)$. The p-h transformation is given by the mapping

$$a_{i,-\mu}^\dagger \rightarrow (-1)^i (2\mu) a_{i,-\mu}. \tag{2.13}$$

The reason for the reversed spin on the right hand side of this expression is that an addition of a spin-up particle and removal of a spin-down particle both increase total spin by 1/2; in other words, the spin of a hole excitation in the $\mu = -1/2$ Fermi sea is 1/2. Index i in Eq. (2.13) has a very special meaning. It must be defined so that its parity alternates between sites connected by electron hopping terms. This requirement is equivalent to demanding that the lattice be bipartite in the sense that each site is connected by hopping only to the sites of the opposite sublattice; in other words, the lattice must be a two-colorable graph, Fig. 2.2. On a simply connected lattice (an open chain of any length or a closed ring with even number of sites) i may simply be the site number. A slightly more complicated case is that of parallel quantum dots that are *not inter-coupled by hopping*: all parallel dots must have the same parity of index i. To demonstrate the necessity of the alternating sign in the definition, consider how a typical hopping term transforms:

$$t\left(a_i^\dagger a_{i+1} + a_{i+1}^\dagger a_i\right) \to t\left((-1)^i a_i (-1)^{i+1} a_{i+1}^\dagger + (-1)^{i+1} a_{i+1} (-1)^i a_i^\dagger\right) = t\left(a_i^\dagger a_{i+1} + a_{i+1}^\dagger a_i\right). \tag{2.14}$$

Without sign alternation, the hopping term would flip sign under p-h transformation and the p-h symmetry of the Hamiltonian would be broken. Furthermore, it should be noted that while $(n_i - 1)^2$ terms are p-h invariant, $(n_i - 1)$ maps to $-(n_i - 1)$.

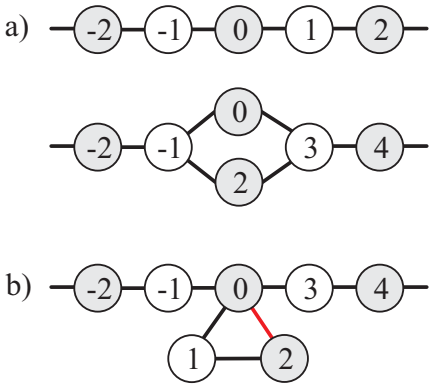

Figure 2.2: Lattice representation of the connectivity between the orbitals. a) Examples of bipartite lattices corresponding to Hamiltonians that may exhibit p-h symmetry. b) If the lattice is not a two-colorable graph, the system cannot be p-h symmetric.

2.3.4 Isospin symmetry $\mathrm{SU}(2)_{\mathrm{iso}}$

Under the p-h transformation, the charge $Q \to -Q$. In fact, the relation between the p-h transformation and the $\mathrm{U}(1)_{\mathrm{charge}}$ symmetry is analogous to the relation between the spin inversion (which maps $S^z \to -S^z$) and the $\mathrm{U}(1)_{\mathrm{spin}}$ symmetry. This suggest that in the presence of the p-h symmetry, the full symmetry in the charge space might be larger than $\mathrm{U}(1)_{\mathrm{charge}}$ if certain conditions are fulfilled. This is in fact the case;[20] such extended $\mathrm{SU}(2)_{\mathrm{iso}}$ symmetry is called the isospin symmetry (sometimes also axial charge symmetry).[20,85–88]

We first define the Nambu spinor[42,89,90] by

$$\eta_{i,\mu} = \begin{pmatrix} a^\dagger_{i,\mu} \\ (-1)^i (2\mu) a_{i,-\mu} \end{pmatrix}, \tag{2.15}$$

where i has the same special meaning as in the previous section on the p-h symmetry. The isospin up component ($\alpha = \frac{1}{2} = \uparrow$) is a particle creation operator, while the isospin down component ($\alpha = -\frac{1}{2} = \downarrow$) is a particle annihilation operator. Often only the spin up Nambu spinor $\xi \equiv \eta_\uparrow$ is needed:

$$\xi^\dagger_i = \begin{pmatrix} a^\dagger_{i,\uparrow} \\ (-1)^i a_{i,\downarrow} \end{pmatrix}. \tag{2.16}$$

The Nambu spinors define local isospin operators[20,91]

$$\mathbf{I}_i = \xi_i \left(\tfrac{1}{2}\boldsymbol{\sigma}\right) \xi^\dagger_i \tag{2.17}$$

where $\boldsymbol{\sigma}$ are the Pauli matrices. We also define $I^+ = I^x + iI^y$ and $I^- = (I^+)^\dagger$. The components are:

$$\begin{aligned} I^z_i &= \tfrac{1}{2}\left(a^\dagger_{i,\uparrow} a_{i,\uparrow} + a^\dagger_{i,\downarrow} a_{i,\downarrow} - 1\right) = \tfrac{1}{2} Q_i \\ I^+_i &= (-1)^i a^\dagger_{i,\uparrow} a^\dagger_{i,\downarrow} \\ I^-_i &= (-1)^i a_{i,\downarrow} a_{i,\uparrow}. \end{aligned} \tag{2.18}$$

The z-component of the isospin is thus charge, while the transverse components are particle pairing operators. The total isospin operator of the system is obtained as a sum of $\mathbf{I}_i$ for all orbitals of the problem (impurities and conduction band):

$$\mathbf{I} = \sum_i \mathbf{I}_i. \tag{2.19}$$

If the Hamiltonian commutes with all three isospin components, we say that the system is invariant in the isospin space. In that case, both $\mathbf{I}^2$ and I^z commute with H and $[\mathbf{I}^2, I^z] = 0$; I and I^z are additional good quantum numbers. Due to isotropy in isospin space, the I^z dependence can again be taken into account using the Wignert-Eckart theorem. Spin and isospin operators commute, $[S^i, I^j] = 0$ for all $i, j \in \{x, y, z\}$. Therefore a problem may have a $\mathrm{SU}(2)_{\mathrm{spin}} \otimes \mathrm{SU}(2)_{\mathrm{iso}}$ symmetry which, when explicitly taken into account, leads to a significant reduction of the numerical task.

The isospin operators have exactly the same SU(2) group properties as the spin operators $\mathbf{S}_i$, for example:

$$\begin{aligned} [I^z_i, a^\dagger_{j,\mu}] &= \delta_{ij} \tfrac{1}{2} a^\dagger_{i,\mu} \\ [I^z_i, a_{j,\mu}] &= \delta_{ij} (-\tfrac{1}{2}) a_{i,\mu} \\ [I^-_i, a^\dagger_{j,\mu}] &= \delta_{ij} (-1)^i (2\mu) a_{i,-\mu} \\ [I^+_i, (-1)^j (2\mu) a_{j,-\mu}] &= \delta_{ij} a^\dagger_{i,\mu}. \end{aligned} \tag{2.20}$$

This implies that a Nambu spinor defined by Eq. (2.15) is, in addition to being a spin doublet tensor operator with respect to $\mathrm{SU}(2)_{\mathrm{spin}}$, also an isospin doublet tensor operator with respect to $\mathrm{SU}(2)_{\mathrm{iso}}$ (see App. A). The following holds for a single orbital i:

$$\begin{aligned} \mathbf{I}_i^2 &= \frac{3}{4}\left(1 - n_{i,\uparrow} - n_{i,\downarrow} + 2n_{\mathrm{i,pair}}\right), \\ &= \frac{3}{4} - \mathbf{S}_i^2. \end{aligned} \tag{2.21}$$

The two states with single occupation thus form an isospin-singlet spin doublet, while zero-occupation and double-occupation states form a spin-singlet isospin doublet. For two sites we have:

$$I_1^x I_2^x + I_1^y I_2^y = -\tfrac{1}{2}\left(a_{1\downarrow}^\dagger a_{1\uparrow}^\dagger a_{2\downarrow} a_{2\uparrow} + a_{2\downarrow}^\dagger a_{2\uparrow}^\dagger a_{1\downarrow} a_{1\uparrow}\right) \tag{2.22}$$

i.e. the transverse part of the isospin exchange interaction $\mathbf{I}_1 \cdot \mathbf{I}_2$ is equal to the two-electron hopping term. Furthermore,

$$I_1^z I_2^z = \frac{1}{4}(n_1 - 1)(n_2 - 1), \tag{2.23}$$

i.e. the longitudinal part of the isospin exchange interaction corresponds to inter-site charge repulsion or, equivalently, to capacitive coupling. We remark that while isospin is related to the p-h transformation, not all particle-hole symmetric models are also isospin invariant. Such is the case of Hamiltonians which contain two-particle hopping terms; they are p-h symmetric, but clearly not isospin invariant.

We remark in passing that the p-h transformation operator $U = \exp(i\pi I^y)$ is an element of $\mathrm{SU}(2)_{\mathrm{iso}}$.

2.3.5 Parity Z_2 and flavor symmetry $\mathrm{SU}(2)_{\mathrm{flavor}}$

In addition to "internal" symmetries in spin and isospin space, impurity problems describing systems of quantum dots may also have real-space symmetries, such as reflection symmetry Z_2 with respect to a mirror plane passing through the middle of the impurity region. The reflection maps the left lead into the right lead and vice versa. Every discrete transformation is associated with a quantum number, in this case the quantum number of parity under left-right reflection transformation. Subspaces with different parities decouple and can be diagonalized separately. We define as even ($P = 1$) those states that are invariant with respect to the reflection, and as odd ($P = -1$) those that change sign.

Parity Z_2 symmetry group is a subgroup of a larger flavor symmetry group $\mathrm{SU}(2)_{\mathrm{flavor}}$ with generators [92]

$$\mathbf{J} = \sum_n \mathbf{J}_n, \tag{2.24}$$

where n runs over one half of the system sites (for example, the left half), and $\mathbf{J}_n$ are "local" flavor operators which mix the states from left ($\alpha = -1/2 = \downarrow$) and right ($\alpha = 1/2 = \uparrow$) conduction channel with the same n (see Fig. 2.3):

$$\mathbf{J}_n = \sum_{\mu} \sum_{\alpha\alpha'} a^{\dagger}_{n\alpha\mu} \left(\tfrac{1}{2}\boldsymbol{\sigma}_{\alpha\alpha'}\right) a_{n\alpha'\mu}. \tag{2.25}$$

Index α therefore plays the role of a channel (flavor) pseudo-spin. Group $\mathrm{SU}(2)_{\mathrm{flavor}}$ commutes with $\mathrm{SU}(2)_{\mathrm{spin}}$, however it does not commute with $\mathrm{SU}(2)_{\mathrm{iso}}$.[21]

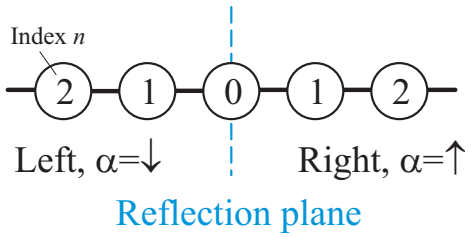

Figure 2.3: Reflection symmetry and the channel pseudo-spin index α.

Affleck et al.[21] have shown that for reflection symmetric problems two types of the particle-hole symmetry can be distinguished. Under the p-h symmetry of the first type

$$\begin{aligned} \psi_{e,E} &\to \psi^{\dagger}_{e,-E}, \\ \psi_{o,E} &\to \psi^{\dagger}_{o,-E}, \end{aligned} \tag{2.26}$$

where e, o denote even or odd combination of electrons from left and right half of the system, $\psi_{e,o} = 1/\sqrt{2}(\psi_L \pm \psi_R)$, while under the p-h symmetry of the second type

$$\begin{aligned} \psi_{e,E} &\to \psi^{\dagger}_{o,-E}, \\ \psi_{o,E} &\to \psi^{\dagger}_{e,-E}. \end{aligned} \tag{2.27}$$

For linear chains of impurities coupled by electron hopping terms, the p-h symmetry is of the first type for odd number of impurities and of the second type for even number of impurities. The symmetry of the first type constrains the possible scattering phases for electrons in even/odd channels and its existence was used in the argument for the existence of the phase transition in the two-impurity Kondo (2IK) problem.[21] It was later shown that this is merely a sufficient, but not a necessary condition for observation of the 2IK non-Fermi-liquid critical behavior.[93]

2.4 Fermi liquid and non-Fermi liquid systems

Quantum impurity models can be classified into two groups: those that behave as Fermi liquids (FL) at low temperatures,[94] and those that do not – non-Fermi liquids (NFL).[95,96]

FL systems are characterized by their behavior near $T = 0$: they have a linear coefficient of heat capacity, a constant zero field magnetic susceptibility and their resistance decreases as T^2.[2] Their excitations are related to the bare excitations of non-interacting Fermi systems; in particular, their finite-size spectra feature equidistant levels at integer or half-integer values.[79] Single-channel Kondo and Anderson models both behave as FL at low temperatures, as do most of the other models studied in this work.

The ground state for a system of a magnetic impurity with spin S interacting antiferromagnetically with N conduction bands must have total spin $S - N/2$. This general theorem has been proved (for a single band) by Mattis.[97] Hence for $S = N/2$ the ground state is a singlet with complete spin compensation, for $S > N/2$ there will be residual spin (underscreening), while for $S < N/2$ the electrons tend to overscreen the impurity. In fact, both for $S > N/2$ and for $S < N/2$ the residual spin is $|S - N/2|$. The important difference lays in that the residual exchange interaction is ferromagnetic and it scales to zero for the case of underscreening, while the residual interaction is antiferromagnetic in the case of overscreening.

Mehta et al. have shown that while for $S \geq N/2$ the system is a FL, the concept of a FL needs to be refined.[98,99] A $S = N/2$ system with complete compensation is a *regular FL* , a $S > N/2$ system with residual spin is a so-called *singular FL*. In a regular FL, the inelastic scattering vanishes quadratically and on the lowest energy scale $\sigma_{\text{total}}(\omega) = \sigma_{\text{elastic}}(\omega)$, where σ is the scattering cross-section. In singular FL, however, the inelastic scattering falls off much more slowly.

NFL systems, on the other hand, have characteristically different properties.[28] For $S < N/2$ the residual interaction is relevant and the FL fixed point is unstable; this leads to non-trivial physics.[99,100] The thermodynamic quantities of NFL systems diverge at low temperatures, the resistivity decreases as $T^{1/2}$ and there is a finite residual entropy which is not a logarithm of an integer number . In this work we will meet two such models: the over-screened two-channel Kondo (2CK) model (with $S = 1/2$ and $N = 2$, see also Section 6.2) , and the two-impurity Kondo model (Sec. 7.4) . Some further examples of NFL systems are the two-channel spin-flavor Kondo model,[92,101] the single-channel Kondo problem with $J = 3/2$ conduction band,[102] the compactified $(\sigma - \tau)$ Kondo model[103–107] and the three-impurity Kondo problem.[37,38]

NFL behavior usually appears for special values of model parameters. It often occurs that two different FL phases are separated by a continuous quantum phase transition (QPT) and that precisely at the transition point the system has a NFL low-temperature fixed point. Near the phase transition, the system may exhibit NFL characteristics at finite temperatures, but as the temperature is decreased it eventually evolves into a FL ground state.

The levels in the finite-size spectra of NFL systems are not equidistant, but can often be expressed as fractions. In the 2CK model, the lowest levels are, for example, 0, 1/8, 1/2, 5/8, 1+1/8, ...[79,108] (see Sec. 8.1). In conformal field theory, excitation energies are determined by the scaling dimensions of operators characterizing the fixed point: one

operator for each eigenvalue. The fact that eigenvalues are not merely integers or half-integers is a direct proof that the system is a NFL, since its excitations cannot be expressed in terms of fermionic operators.[108]

Emery and Kivelson explained the NFL behavior in the 2CK model by the observation that only one of the impurity's Majorana degrees of freedom couples to the conduction electrons[109]. Since one Majorana fermion corresponds, roughly speaking, to one half of a physical Dirac fermion, the deviation from usual FL behavior is not surprising. The idea of obtaining NFL fixed point by "twisting" an odd number of Majorana fermions was further elaborated by J. Maldacena and A. W. W. Ludwig[76] and J. Ye.[92,110–112]

Calculation of thermodynamic properties alone may not suffice to ascertain if the ground state is FL or NFL. Instead, correlation functions or excitation spectra must be determined. Using the NRG, both are easily accessible.

2.5 Effective field theories of the Kondo problem

While models of physical systems that arise in the condensed matter theory naturally take the form of lattice models, effective models may be defined on the continuum. The field theoretic version of the Kondo Hamiltonian (2.1) is a one-dimensional (1D) relativistic quantum field theory (QFT). The theory is one-dimensional since the magnetic impurity is assumed to couple only to a one-dimensional continuum of conduction electron states with s symmetry about the impurity site:[55] this holds more generally and, in fact, all QIMs are essentially one-dimensional. The theory is said to be relativistic since the electron and hole excitations in the vicinity of the Fermi level are dispersionless and therefore behave as ultrarelativistic massless particles.

Due to the presence of an impurity interacting with the 1D continuum, QIMs form a class of quantum models with properties in between 2D models, where critical behavior is possible, and true 1D models where criticality does not occur.[55] In fact, the Kondo effect was described as an "almost broken symmetry",[113] a low-dimensional critical phenomenon involving long-time fluctuations at the magnetic site, but no critical fluctuations in space. In QIMs, low dimensionality of fluctuations prevents the development of a true broken symmetry; as a consequence, the transition to a Kondo correlated state is not a phase transition, but rather a cross-over.

The validity of the effective QFT of the Kondo problem is limited to energies low enough that the linear approximation to the dispersion relation is possible. In real space, the Hamiltonian is expressed in terms of a field $\psi_\mu(x)$ defined on a continuous line parameterized by some fictitious position x:

$$H = iv_F \sum_\mu \int_{-\infty}^{\infty} \mathrm{d}x \psi_\mu^\dagger(x) \frac{d\psi_\mu(x)}{dx} + v_F \lambda \mathbf{J}_S(0) \cdot \mathbf{S}. \tag{2.28}$$

Here v_F is the Fermi velocity, $\lambda = \rho J$ is the dimensionless Kondo antiferromagnetic coupling constant and $\mathbf{J}_S(x)$ is spin density

$$\mathbf{J}_S(x) = \sum_{\mu\mu'} \psi^\dagger_\mu(x) \frac{1}{2} \boldsymbol{\sigma}_{\mu\mu'} \psi_{\mu'}(x), \tag{2.29}$$

QFTs need to be regularized to remove the divergencies that appear due to the infinite number of quantum modes;[82] in effective QFTs of lattice models a natural choice of the high-energy cut-off is provided by the lattice spacing.

2.6 Spin-charge separation

Low-dimensional field theories have unique properties due to topological restrictions in reduced dimensionality; for example, fermions constrained to live on a 1D line can scatter only forwards and backwards. A notable effect in one-dimensional systems is the separation of electron spin and charge which had been intensively studied in Luttinger liquids:[114] fundamental low-energy excitations are not charged spin-1/2 Fermi-liquid quasiparticles, but rather spin-1/2 neutral particles (spinons) and charged spinless particles (holons). Such behavior has been found, for example, in one-dimensional solids such as $SrCuO_2$[115] and ballistic wires in GaAs/AlGaAs heterostructures.[116]

Spin-charge separation also occurs in the Kondo problem. Using bosonization techniques,[106,108,109,117,118] conduction band fermion fields can be described in terms of spin-up and spin-down boson fields. These bosons correspond to the particle-hole excitations in the conduction band and they can be recombined to form separate spin and charge fields which are essentially independent, but subject to a gluing condition [108,118] which is the only remnant of the charge-1, spin-1/2 nature of physical fermion particles. In the single-impurity spin Kondo problem, the impurity spin couples only to the spin field, while the charge field is decoupled.[55,103,119] During the Kondo cross-over, the spectrum of charge excitations remains unchanged, only the spin sector is affected.[55] In this sense, the spin and charge degrees of freedom are separated.

In the absence of interactions, the Fermi velocity v_F is the only characteristic velocity scale of the problem. When interactions in a one-dimensional system lead to the spin-charge separation, two different velocities v_s and v_c appear; these are the velocity of spin and charge excitations.[82] Specific heat coefficient depends both on spin and charge modes and is given by[120]

$$\gamma/\gamma_0 = \tfrac{1}{2}\left(\frac{v_F}{v_c} + \frac{v_F}{v_s}\right), \tag{2.30}$$

while spin susceptibility only depends on the spin mode and is given by

$$\frac{\chi}{\chi_0} = \frac{v_F}{v_s}, \tag{2.31}$$

where γ_0 and χ_0 are specific heat coefficient and spin susceptibility of non-interacting electron gas. Wilson ratio is the ratio of spin susceptibility and the specific heat coefficient: it thus measures the fraction of the specific heat coming from the spin degrees of freedom.[55,56] It is given by

$$R_W = \frac{\chi/\chi_0}{\gamma/\gamma_0} = \frac{2v_c}{v_c + v_s}. \tag{2.32}$$

If there is no spin-charge separation, this ratio is equal to one. Deviations form unity are a sign of spin-charge separation;[120] in the single-channel Kondo problem, for example, we find $R_W = 2$.

2.7 Conformal field theory

The boundary conformal field theory (CFT) for impurity models is a generalization of Nozière's local Fermi liquid approach. It is applicable to both Fermi liquid and non-Fermi liquid Kondo systems and provides a description of the ground state and the leading corrections that determine finite temperature behavior. The technique was developed in a series of papers by I. Affleck and A. W. W. Ludwig.[21,55,56,77–81,121,122] It can be applied to multi-channel and higher-spin Kondo effect,[28,80,81,121] two-impurity Kondo effects ,[21,79] impurity assisted tunneling, and impurities in one-dimensional conductors or 1D antiferromagnets.[56] An important feature of the approach is that the symmetry of the problem and the separation of the spin and charge sectors is directly exhibited.

The essence of the CFT approach to impurity problems is the reformulation of the theory in terms of separate degrees of freedom using non-Abelian bosonization.[56] In the case of a single conduction band, we introduce spin and charge (isospin) "currents" (densities) as

$$\begin{aligned} \mathbf{J}^S(x) &= \sum_{\mu\nu} :\psi^\dagger_\mu(x)\frac{1}{2}\boldsymbol{\sigma}_{\mu\nu}\psi_\nu(x):, \\ \mathbf{J}^C(x) &= \sum_{\alpha\beta} :\xi^\dagger_\alpha(x)\frac{1}{2}\boldsymbol{\sigma}_{\alpha\beta}\xi_\beta(x): \end{aligned} \tag{2.33}$$

where $\xi^\dagger_\alpha(x) = \left\{\psi^\dagger_\uparrow(x), \psi_\downarrow(x)\right\}$ is the real-space Nambu spinor. Normal ordering (double dots) has been introduced to remove divergences due to filled electron levels below the Fermi level. The conduction band Hamiltonian can then be rewritten in the Sugawara form

$$H_{\text{band}} = \frac{\pi v_F}{l}\left[\frac{1}{3}\sum_n :\mathbf{J}^C_n\cdot\mathbf{J}^C_{-n}: + \frac{1}{3}\sum_n :\mathbf{J}^S_n\cdot\mathbf{J}^S_{-n}:\right]. \tag{2.34}$$

Here $\mathbf{J}^S_n$ and $\mathbf{J}^C_n$ are the Fourier modes of the real-space currents $\mathbf{J}^S(x)$ and $\mathbf{J}^C(x)$ in a finite system of length $2l$. They each satisfy $\mathrm{SU}(2)_1$ Kac-Moody commutation relations

$$[J^{S/C,a}_n, J^{S/C,b}_m] = i\epsilon_{abc}J^{S/C,c}_{n+m} + \delta_{ab}\delta_{n+m,0}\frac{1}{2}n, \tag{2.35}$$

where ϵ^{abc} is the antisymmetric tensor.[21] The modes from different sectors commute:

$$\left[J_n^{S,a}, J_m^{C,b}\right] = 0. \tag{2.36}$$

This commutation relation embodies the (trivial) spin-charge separation of the free electrons. The full Kondo Hamiltonian is

$$H = H_{\text{band}} + \frac{\pi v_F}{l}\left(\lambda \sum_n \mathbf{J}_n^S \cdot \mathbf{S}\right). \tag{2.37}$$

I draw attention to the fact that the impurity spin couples only to the spin degrees of freedom of conduction band electrons, while charge degrees of freedom are unaffected. At a special value $\lambda = 1/3$, we can introduce a new current $\vec{\mathcal{J}}^S = \mathbf{J}^S + \mathbf{S}$ which satisfies the same Kac-Moody commutation relations as the old currents. The spin part of the Hamiltonian then becomes (up to a constant term)

$$H^{(S)} = \frac{\pi v_F}{l} \sum_n \frac{1}{3} : \vec{\mathcal{J}}_{-n}^S \cdot \vec{\mathcal{J}}_n^S :, \tag{2.38}$$

from which the spin impurity $\mathbf{S}$ has disappeared (it was "absorbed" by the conduction band). The charge sector remains unaffected by this change. The special value $\lambda = 1/3$ is identified with the strong coupling fixed point of the problem.[55]

Even though the spin Kondo effect occurs in the spin sector, without involving the charge sector, the spin and charge degrees of freedom are not entirely decoupled; they are constrained by the gluing condition. The gluing condition declares which combinations of quantum numbers are allowed taking into account the charge-1 spin-1/2 nature of physical particles – electrons. In the present context the gluing condition depends on the boundary conditions (b. c.) imposed on the field $\psi(x)$.

We first consider the case of anti-periodic b. c., $\psi(l) = -\psi(-l)$. We can obtain half-integer spin only with an odd number of electrons (i.e. for half-integer isospin).[55] Therefore $2I^z$ and $2S^z$ must have the same parity; this is the gluing condition. There are thus two Kac-Moody conformal towers with highest-weight states having $(I, S) = (1/2, 1/2)$ and $(I, S) = (0, 0)$, respectively.

For periodic b.c. $\psi(l) = \psi(-l)$, and keeping in mind that the z-component of the isospin is defined with respect to half filling, we obtain half-integer spin for integer isospin and integer spin for half-integer isospin; $2I^z$ and $2S^z$ must then have different parity. There are two conformal towers, $(I, S) = (1/2, 0)$ and $(I, S) = (0, 1/2)$. Note that changing the b. c. from periodic to anti-periodic (or vice versa) amounts to imposing a phase shift of $\pi/2$ on the wave function.[77]

In the single impurity Kondo model, the finite-size spectrum of the strong coupling fixed point is obtained by a fusion in the spin sector.[55,77] This means that the isospin sector remains intact, while the spin quantum number changes as $S \to 1/2 - S$. As a consequence

$(1/2, 1/2) \rightarrow (1/2, 0)$ and $(0, 0) \rightarrow (0, 1/2)$, i.e. the gluing conditions change from those for the anti-periodic b. c. to those for periodic b. c., and vice versa, which is equivalent to the characteristic $\pi/2$ phase shift for quasiparticle scattering in the Kondo regime.

Chapter 3

Renormalization group

The renormalization group (RG) technique, in particular as applied in the field of condensed matter physics and many-body theory, is an important tool to study the effective behavior of systems at low energies and long wavelengths, i.e. their macroscopic response functions.[29,123–129] RG is more than a computational tool that provides us with effective Hamiltonians; the concepts that emerged from RG (renormalization flow, scaling, running coupling constants, fixed points, criticality, critical exponents, operator content, relevance, irrelevance, marginality, universality, etc.) are the central notions of modern physics. K. G. Wilson's contribution in this domain was acknowledged by the Nobel prize awarded to him in 1982 "for his theory for critical phenomena in connection with phase transitions".

Renormalization is a way of understanding the relation between the different ways a physical system behaves at different energy scales. To study a system at low energies, the irrelevant high-energy short-wavelength degrees of freedom are integrated out to obtain an effective description in terms of modified, "renormalized" coupling constants. Let us consider an example which – while not computationally practicable – illustrates well the perspective from which a system is considered from the renormalization group point of view. We focus on electrons in a piece of metal, neglecting the motion of nuclei (phonons), Fig. 3.1a. As a first step of the renormalization, we can imagine "tracing out" the core electron levels to obtain an effective description of the valence levels. This effective description could, for instance, take the form of a tight-binding model for orbitals near the Fermi level with electron-electron interactions, i.e. a Hubbard-like model, Fig. 3.1b. The next step might consist of "tracing out" the charge-fluctuation degrees of freedom (on the scale of U) to obtain the effective dynamics of spin degrees of freedom (on the scale of t^2/U), i.e. a Heisenberg-like model, Fig. 3.1c. A final RG step might then involve "tracing out" the local moments to obtain a long-wavelength description in terms of collective modes such as the spin density waves on the basis of a Ginzburg-Landau functional approach, Fig 3.1d. We see that a simple Hamiltonian arises from more complicated ones; this is the origin of the universality. Renormalization is thus an essential ingredient of model building in many-body theory.[123]

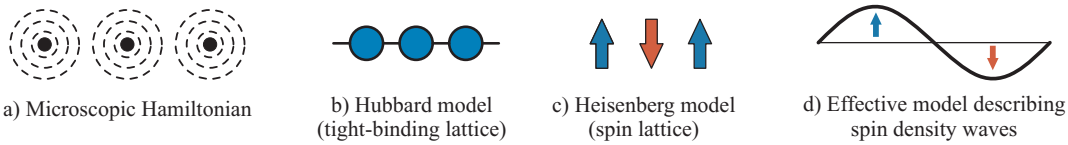

Figure 3.1: Renormalization as a way to proceed from complex microscopic models to simple universal effective models.

In this chapter I present several aspects of the renormalization group theory. Section 3.1 is devoted to the concepts of renormalizability and universality; it also describes the RG approach to the Kondo model in the form of a simple scaling theory. Section 3.2 introduces Wilson's numerical renormalization group (NRG) and contains a brief review of its many applications, while Section 3.3 is an overview of my implementation of this technique for studying general multi-impurity multi-channel quantum impurity models. The following sections are devoted to the main elements of NRG: logarithmic discretization, hopping Hamiltonian (Sec. 3.4), symmetries and basis construction (Sec. 3.5), RG transformations, iterative diagonalization and truncation (Sec. 3.6), finite-size spectra, fixed points, expansions around fixed points, thermodynamic quantities, correlation functions and dynamic properties (Sec. 3.7), and recursion relations (Sec. 3.8). Finally, Section 3.9 introduces the density-matrix NRG technique and its implementation in the basis with well defined charge and total spin quantum numbers.

3.1 Renormalizability, universality and scaling theories

The Kondo Hamiltonian, Eqs. (2.1) and (2.28), defines a *renormalizable* quantum field theory.[130–132] This is equivalent to saying that the field theory is fully determined by a limited number of running coupling (renormalization) constants. The notion of renormalizability is therefore related to the concept of *universality*: the existence of only a limited number of renormalization constants implies that apparently different Hamiltonians can be mapped into each other at low energy scales and will thus exhibit universal properties.

Writing the dimensionless coupling constant in the Kondo model as $\lambda = \rho J$, we find that the Kondo model in the wide-band ($D \to \infty$) limit is a scale-invariant theory, i.e. there appears to be no characteristic length scale. Nevertheless, a length scale given by $\xi = v_F/(k_B T_K)$ is dynamically established due to many-particle corrections. The phenomenon where a dimensionless coupling constant (λ) becomes dimensionful (T_K) is known in particle physics as *dimensional transmutation* and it is closely related to the emergence of the scaling laws.[133–136] In the context of the Kondo problem, the dimensional transmutation means that instead of a range of theories, parameterized by a dimensionless coupling $\lambda = \rho J$, we have a range of theories differing only in the value of a dimensional parameter, the Kondo temperature T_K.[133] This implies that the behavior of all problems in the universality class of the Kondo problem can be described by universal functions; for example, the magnetic

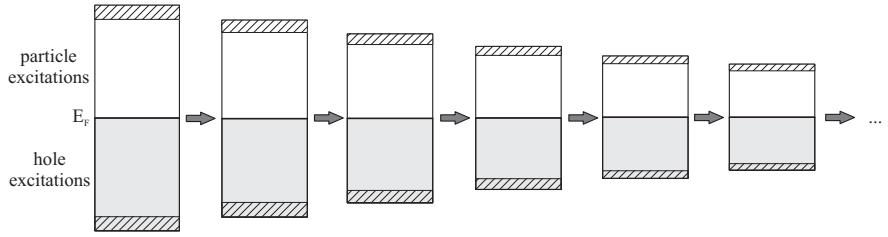

Figure 3.2: Cutoff renormalization: the particle and hole excitations from the hatched regions at the top and bottom of the conduction band are integrated out to obtain an effective Hamiltonian at lower energy scale.

susceptibility χ is a universal function of T/T_K.[29] The Kondo problem therefore has scaling property.

Some of the first applications of the RG ideas to the Kondo problem are due to P. W. Anderson.[137–140] Among other results, he derived the scaling laws of the Kondo model in the perturbative regime using a simple ("poor man's") cutoff renormalization technique.[140] Cutoff renormalization consists of tracing out the degrees of freedom in the two infinitesimal energy intervals near the top (electrons) and bottom (holes) of the conduction band and determining the effect these states have on the coupling constants in the Kondo Hamiltonian, see Fig. 3.2 and Appendix D. It is found that the effective model of the Kondo model is (at least approximately) the same Kondo model with modified coupling constants, i.e. in this so-called scaling regime the Kondo model is self-similar under the *renormalization flow*. In the first-order perturbative renormalization, the following scaling equation is obtained after some simplifications:[2]

$$\frac{d\mathcal{J}}{d\ln\mathcal{D}} = -\rho\mathcal{J}^2, \tag{3.1}$$

with $\mathcal{J}(\mathcal{D} = D) = J$, where D and J are bare bandwidth and bare coupling, $\mathcal{J}$ is the running coupling constant, $\mathcal{D}$ is the running parameter (energy scale), and ρ is the spectral density (density of states) of the conduction band. As the energy scale is reduced, the coupling constant increases. Assuming constant ρ, a solution may be obtained in closed form:

$$\mathcal{J}(\mathcal{D}) = \frac{J}{1 - J\rho\ln(\mathcal{D}/D)}. \tag{3.2}$$

The physics on the energy (or, equivalently, temperature) scale $\mathcal{D}$ depends on the renormalized parameter $\mathcal{J}(\mathcal{D})$ rather than on the bare parameter J: the renormalized parameter takes into account the effects of the high-energy intermediate states. This approach works as long as $\rho\mathcal{J} \ll 1$, so that the use of the perturbation theory makes sense.

The scale of the Kondo temperature is determined by the value of the running parameter $\mathcal{D}$ where the renormalized coupling constant becomes large, for example $\rho\mathcal{J} \sim 1$. We obtain

$$T_K \sim D\exp\left(-\frac{1}{\rho J}\right). \tag{3.3}$$

On this energy scale the perturbative renormalization fails. Higher-order scaling equation can be calculated:[2]

$$\frac{d\mathcal{J}}{d\ln\mathcal{D}} = -\rho\mathcal{J}^2 + \rho^2\mathcal{J}^3 + \mathcal{O}(\mathcal{J}^4). \tag{3.4}$$

It gives a better estimate of the Kondo temperature, however pushing scaling calculations to higher orders does not reveal the behavior of the problem as the temperature tends to zero. The reason is simple: the behavior of the Kondo system is, in fact, qualitatively different for $T \gg T_K$ and for $T \ll T_K$. The self-similarity (scaling) breaks down at the energy scale of T_K. For $T \gg T_K$, the perturbative scaling approach gives adequate results, while for $T \ll T_K$, Nozières' local Fermi liquid theory gives a full account of the behavior.[94] It turns out that the most complex regime is precisely the cross-over at $T \sim T_K$ which links the asymptotically-free high-temperature regime to the strong-coupling low-temperature regime. A non-perturbative approach is required to tackle the Kondo problem on the energy scale of T_K: this is the topic of the following section.

3.2 Numerical renormalization group

The numerical renormalization group (NRG) is a non-perturbative RG approach to the quantum impurity problems.[29–31,129] Being non-perturbative, it does not suffer from logarithmic singularities, as scaling approaches do. NRG builds upon the RG approach to the Kondo problem of Anderson, Yuval and Hamann,[123,137–139] however in NRG the RG transformations are performed numerically. The essential advantage of this approach is that the calculation need not be guided by "physical intuition" and is therefore unbiased; however, by the same token there is no straight-forward description in terms of running coupling constants to provide a simple physical picture.

Schematically, NRG consists of logarithmic discretization of the conduction band(s) and of iterative diagonalisation of a series of Hamiltonians. The method was expounded in K. G. Wilson's seminal paper "The renormalization group: Critical phenomena and the Kondo problem" (Rev. Mod. Phys., 1975)[29] where it was applied to numerically solve the Kondo problem. This work represents a turning point in the field of impurity problems since an essentially exact solution for the temperature dependence of the thermodynamic quantities in the cross-over region between the high-temperature local-moment regime and the low-temperature strong-coupling regime was obtained for the first time.

NRG has since then become the principal tool in the field of the quantum impurity physics. The approach was used to study the potential scattering in the Kondo problem ,[132,141] the s-d problem with spin 1 ,[98,142,143] the two-channel Kondo problem ,[28,80,91,144,145] particle-hole symmetric[30,146] and asymmetric[31] Anderson model, orbitally degenerate Anderson model[147–150] and models where different magnetic configurations are mixed.[151] More complex multi-impurity problems are also tractable: significant effort was devoted to the two-impurity Kondo problem ,[20,152–154] two-impurity Anderson model[155,156] and, more recently, to clusters of three and more Anderson impurities.[157,158] In addition, local phonon modes

can also be taken into account as in the Anderson-Holstein model.[39,40,159–161] New direction are applications of NRG to quantum impurity problems with bosonic continuum bath,[162] non-trivial density of states (pseudo-gap) of the conduction band,[163–168] non-Fermi liquid fixed points ,[105,169–171] magnetic impurities in superconductors[172,173] and quantum phase transitions .[174,175] Recently, NRG has become widely applied to study conductance through single,[176–179] double,[93,180–188] triple[157,158,189] and multiple quantum dots,[51,190] including quantum dots attached to ferromagnetic leads,[191,192] and to study singlet-triplet transitions.[64,73,75,193] A number of exotic Kondo states were found, among them the SU(4) Kondo effect.[194]

NRG is increasingly often used as the impurity solver in the dynamical mean-field theory (DMFT) approach to lattice problems.[129,195,196] DMFT builds on the observation that in the limit of infinite connectivity, lattice models can be mapped to effective impurity models subject to a self-consistency condition that relates the impurity Green's function to the hybridization function. Examples of using NRG as the solver are applications to the Hubbard model,[197] the periodic Anderson model,[198] the Hubbard-Holstein model[199,200] and the two-band Hubbard model.[201]

3.3 Implementation overview

For the purposes of this dissertation a new NRG code (named "NRG Ljubljana"[202]) was designed and implemented from scratch. The main design goals were flexibility in setting up new problems, ease of taking into account various symmetries, and speed. The code was implemented in a layered architecture, see Fig. 3.3. The cornerstone is a Mathematica package `sneg` for performing calculations with second quantization operators. This package is used, on one hand, in deriving the recursion relations for the NRG iteration and, on the other hand, for exactly diagonalizing the initial Hamiltonian and transforming the matrices of all operators of interest in the basis of eigenstates of the Hamiltonian in each invariant subspace. The NRG iteration routines are implemented in C++ for speed. Diagonalisations are performed using `dsyev` and `dsyevr` routines from the `LAPACK` library,[203] while all other matrix and vector operations use the `ublas` library from the project `boost`. Standard Template Library containers are heavily used, which makes the code easy to read (and maintain) and helps avoid memory leaks. Additional information can be found on the "NRG Ljubljana" home page `http://nrgljubljana.ijs.si/`. The package was released freely for general use under the GNU Public license.[204]

3.3.1 Package `sneg`

Package `sneg` is a collection of transformation rules for `Mathematica`, which simplifies calculations using the anti-commuting fermionic second quantization operators. The foundation is a definition of non-commutative multiplication with automatic reordering of opera-

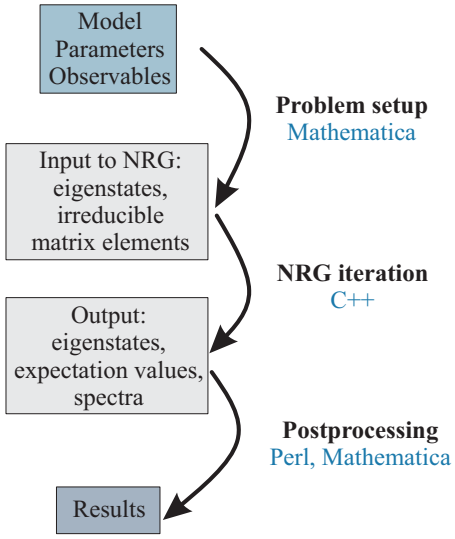

Figure 3.3: The three-step procedure from the problem definition to the results in "NRG Ljubljana" code.

tors in a standard form (normal ordering with creation operators preceding the annihilation operators), which takes into account selected (anti-)commutation rules. Standard form reordering allows simplification of expressions and the choice of normal ordering permits efficient evaluation of matrix elements in a given basis. Some of the additional capabilities of the package that are relevant to the NRG code are:

- Generation of basis states with well-defined number Q and spin S (or other quantum numbers).
- Generation of matrix representations of operators (in particular of the Hamiltonian) in selected basis.
- Collection of functions that generate various operator expressions, such as electron number, electron spin and isospin, one-electron and two-electron hopping, exchange interaction, etc.
- Occupation-number representation of states and evaluation of operator-vector expressions.

Among miscellaneous features of the package are manipulation routines for operator expressions (canonic conjugation, spin inversion), calculation of vacuum expectation values of operator expressions, transformations from product-of-operators to occupation-number representations of states and vice-versa, Dirac's bra-ket notation, simplifications using Wick's theorem, support for sums over dummy indexes (momentum, spin) and simplifications of such expressions, etc. Package `sneg` is useful beyond NRG calculations. It has been applied to perform exact diagonalizations on Hubbard clusters, perturbation theory to higher orders[51] and calculation of commutators of complex operator expressions. It should also be

suitable for educational purposes, since it makes otherwise tedious calculations a routine operation: the nicest feature is perhaps that the use of the package prevents inauspicious sign errors when commuting fermionic operators. Package `sneg` was also released freely for general use under the GNU Public license (`http://nrgljubljana.ijs.si/sneg`).

3.4 Logarithmic discretization

The essential element of the NRG approach is the logarithmic discretization of the conduction band whereby the infinite number of the continuum degrees of freedom is reduced to a finite number; this renders the numerical computation tractable. If we attempted to discretize the band linearly, we would obtain a single interval centered around $k = 0$ that would contain an infinite number of different energy *scales*: this is undesirable, since it is known that in the Kondo problem excitations at each energy scale contribute equally. It is thus preferable to perform a discretization which divides the band into a set of different energy scales; in this manner the energy-scale separation – a known property of QIMs – is achieved explicitly. Viewed from another perspective, the logarithmic mesh gives a good sampling of the states near the Fermi energy which play an essential role in the Kondo problem. Wilson's logarithmic discretization consists of the following steps:[29,30]

1. The conduction band is divided into slices of exponentially decreasing width, for example into intervals $I_m^- = [-\Lambda^{-m}, -\Lambda^{-(m+1)}]D$ for holes and $I_m^+ = [\Lambda^{-(m+1)}, \Lambda^{-m}]D$ for electrons with $m \geq 0$, see Fig. 3.4. $\Lambda > 1$ is called the *logarithmic discretization parameter* (parameter `Lambda` in "NRG Ljubljana"). An upper bound of $\Lambda = 3$ has been established for reliable computation of thermodynamic properties in this discretization scheme.[29,205]

2. Each interval is Fourier-transformed, i.e. we construct a complete set of wave functions $\psi_{ml}^{\pm}$ inside each interval:

$$\psi_{ml}^{+}(\epsilon) = \sqrt{\frac{\omega_m}{2\pi}} \exp(i\omega_m l\epsilon), \quad \text{for } \epsilon \in I_m^+, \tag{3.5}$$

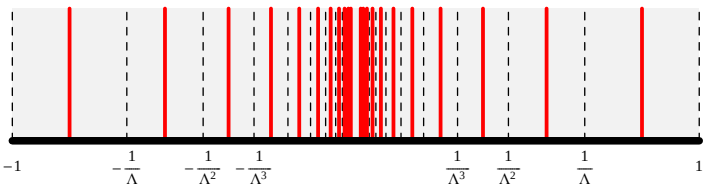

Figure 3.4: Original Wilson's division of the conduction band into bins of geometrically decreasing width. Each thick colored line corresponds to a state which represents the entire interval of conduction band states delimited by a pair of dashed lines.

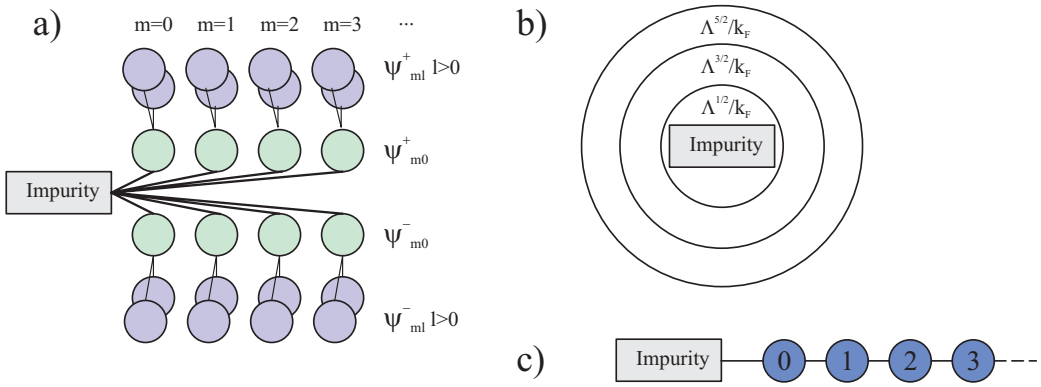

Figure 3.5: Various representations of the logarithmic discretization in quantum impurity problems. **a)** Discretized problem and coupling connectivity of wave-functions $\psi^{\pm}_{ml}$. **b)** Onion-shell representation of Wannier orbitals around the impurity. **c)** Hopping or Wilson chain Hamiltonian.

where ω_m is the fundamental Fourier frequency in the mth interval, $\omega_m = 2\pi\Lambda^m/(1-\Lambda^{-1})$, and $l \geq 0$. Functions ψ^{-}_{ml} are defined similarly for $\epsilon \in I^{-}_{m}$. The first wave function ($l = 0$) in each interval is a constant. Only such "average states" $\psi^{\pm}_{m0}$ couple to the impurity, while other Fourier components are localized away from it, Fig. 3.5a. We therefore retain only $\psi^{\pm}_{m0}$ and drop the remaining states from consideration. This is clearly an approximation, since the states $\psi^{\pm}_{ml}$ couple to $\psi^{\pm}_{m0}$. It was shown that this coupling goes to zero as $\Lambda \to 1$ (i.e. in the continuum limit) and that even for moderately large $\Lambda = 2$ up to $\Lambda = 3$ the approximation is good.[29] Physically, we are neglecting those conduction band states that are localized far away from the impurity in the real space and, at the same time, far away from the Fermi surface in the reciprocal space.[29,206] There is no a priori justification for this approximation; in the words of Wilson: "The only true justification for using the logarithmic division is that a successful calculation results."

3. Unitary transformation to a tridiagonal basis is performed using the Lanczos algorithm. The initial state is the Wannier orbital about the impurity site; this is the orbital to which the impurity is coupled in the standard Kondo problem. Lanczos states correspond to creation operators $f^{\dagger}_{0}$, $f^{\dagger}_{1}$ and have a radial extent of $\Lambda^{1/2}/k_F$, $\Lambda^{3/2}/k_F$, ... about the impurity:[29,91] they form "onion shells" around the impurity, Fig. 3.5b. The conduction band Hamiltonian rewritten in this basis takes the form of a one-dimensional tight-binding model with interacting impurity attached to its end, Fig. 3.5c. This tight-binding Hamiltonian is named the *hopping Hamiltonian* or the *Wilson chain*. The problem is thereby reduced to an effective one dimensional problem. In the $\Lambda \to 1$ limit, a continuum model is recovered. It may be noted that the low-energy levels for small Λ are approximately equidistant (as in the field theory defined on a finite-size system), while for moderate Λ the energies are spaced exponentially starting with the third level, Fig. 3.6.

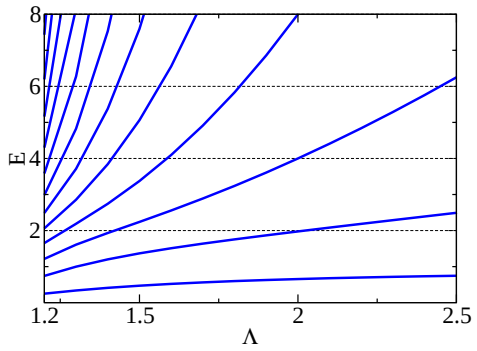

Figure 3.6: Positive one-particle eigenenergies of the Wilson chain Hamiltonian with even number of sites as a function of the discretization parameter Λ.

4. The total Hamiltonian is defined on an infinitely long chain with exponentially decreasing coupling constants:

$$\begin{aligned} H &= H_{\text{imp}} + H_{\text{C}} + H_{\text{chain}} \\ H_{\text{chain}} &= \sum_{n=0}^{\infty} \sum_{\mu\alpha} \xi_n \Lambda^{-n/2} \left(f^{\dagger}_{n,\mu\alpha} f_{n+1,\mu\alpha} + \text{H.c} \right), \end{aligned} \tag{3.6}$$

where H_{imp} is the impurity Hamiltonian, H_{C} is the coupling Hamiltonian, and H_{chain} is the Wilson chain Hamiltonian. In the original Wilson's scheme ξ_n are correction factors

$$\xi_n = \frac{1 - \Lambda^{-(n+1)}}{[(1 - \Lambda^{-(2n+1)})(1 - \Lambda^{-(2n+3)})]^{1/2}}, \tag{3.7}$$

which rapidly tend to 1. The coupling Hamiltonian H_{C} must be rewritten in terms of the Wilson chain operators. In the simplest case of the single-impurity one-channel Kondo problem, it is equal to

$$H_{\text{C}} = J\mathbf{S} \cdot \sum_{\mu,\mu'} f^{\dagger}_{0,\mu} \left(\frac{1}{2} \boldsymbol{\sigma}_{\mu\mu'} \right) f_{0,\mu'}, \tag{3.8}$$

where $\mathbf{S}$ is the impurity spin operator. It was found that to connect the numerical results at finite Λ to the $\Lambda \to 1$ limit, it is necessary to correct the coupling constant Γ (Anderson-model-like coupling) or J (Kondo-model-like coupling) by multiplying it by a correction factor[30,207]

$$A_\Lambda = \frac{1}{2} \frac{1 + \Lambda^{-1}}{1 - \Lambda^{-1}} \ln \Lambda. \tag{3.9}$$

This correction can be enabled in "NRG Ljubljana" by setting the option `Alambda` to `true`. While A_Λ is typically small ($A_2 \approx 1.04$, $A_3 \approx 1.1$, $A_4 \approx 1.16$), it must be recalled that Γ or J enter the exponential function in the expression for the Kondo temperature, therefore A_Λ has a significant effect.

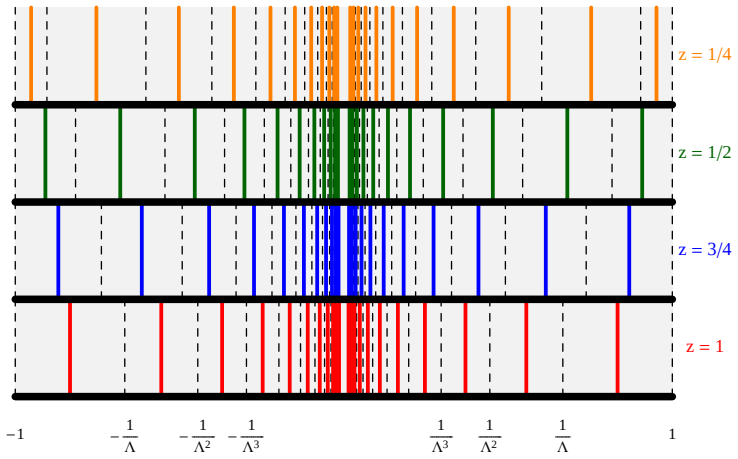

Figure 3.7: Yoshida's discretization scheme and the interleaved method.

One should keep in mind that for $\Lambda \neq 1$, the Hamiltonian obtained from the discretization is only an approximation to the original impurity model and that, strictly speaking, NRG is not an exact method. Nevertheless, by comparing results with known analytical solution (Bethe Ansatz), a remarkable agreement is found. The principal advantage of NRG is its applicability to more complex problems where analytical approaches fail.

Improved discretization schemes are the interleaved method (also known as the "z-trick") [154,205,208] and an approach based on an over-complete basis of states;[209,210] the latter was found to give excellent results and was used in most of the calculations presented in this work. All three approaches are implemented in "NRG Ljubljana": the corresponding configuration options are `disc=wilson`, `disc=yoshida` and `disc=campo`, i.e. they are named after the first authors of the publication where they were introduced. In the interleaved method (`disc=yoshida`), the first positive-frequency interval is $1 > \epsilon > \Lambda^{-z}$, the others are $\Lambda^{1-z-m} > \epsilon > \Lambda^{-z-m}$ $(m = 1, 2, \cdots)$, see Fig. 3.4; for $z = 1$ this reduces to the original discretization. We then average over the sliding (twist) parameter z (`z` in "NRG Ljubljana") in the interval $0 < z \leq 1$ to remove the oscillations in thermodynamic and dynamic quantities which become pronounced for increasing value of parameter Λ.[205] In practice an average over a small number of values of z already gives very satisfactory results. Using the z-trick, the discretization parameter Λ can be increased to large values. In Fig. 3.8 we illustrate the rapid convergence to the $\Lambda \to 1$ limit in the case of both improved methods. In the case of Yoshida discretization, the correction factor A_Λ was used, while no such correction is necessary in the case of Campo discretization.

Varying the sliding parameter z can also be used to assess numerical accuracy of the results by comparing eigenvalue spectra computed for different values of z. This is particularly important if the finite-size spectrum itself is the result of interest: the z-trick namely cannot be used to average the spectra in a meaningful manner. For large Λ, the spectra for

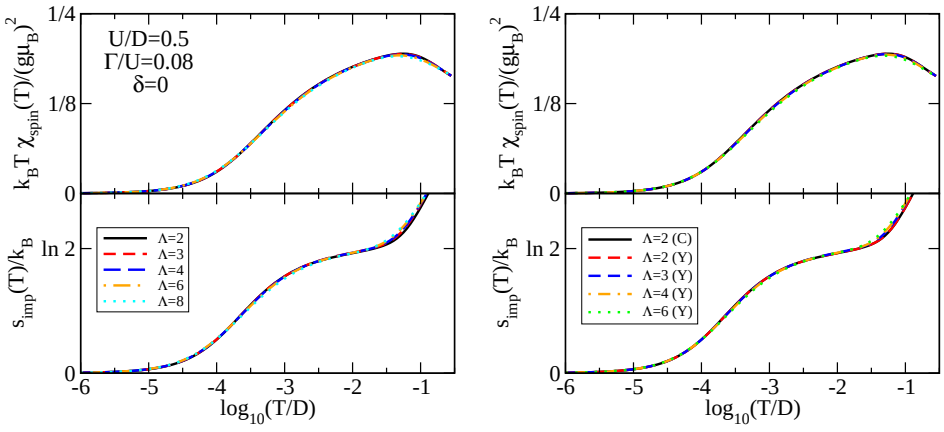

(a) Campo's discretization, effect of increasing Λ

(b) Yoshida's discretization, effect of increasing Λ

Figure 3.8: Comparison of magnetic susceptibility and entropy of the single-impurity Anderson model calculated using two different discretization types for different values of the discretization parameter Λ. The coarse results were post-processed by averaging over z (the z-trick) and even-odd effects were removed by averaging over two consecutive NRG iteration steps.

different z can differ substantially, even though the z-averaged quantities (such as spectral functions) are an excellent approximation to the $\Lambda \to 1$ results.

There is no good a priori recipe for choosing the value of Λ, the number of values of z, and the number of states retained in the NRG iteration; this depends on the number of impurities (i.e. the degeneracy), the values of model parameters and the quantities computed. For each new class of problems, a convergence study should be performed. The majority of computations in this work were performed with $\Lambda = 4$ and for 4 or 8 values of z.

The density of states (DOS) in the conduction band is usually taken to be independent of energy, i.e. $\rho = \text{const}$, which is also known as the flat-band approximation. This choice is particularly convenient as it leads to analytic simplicity and some calculations can be performed in closed form.[211] In addition, RG treatment of the problem has shown that in the case where all the energy scales of the problem are much smaller than the bandwidth, the form of the DOS at large energies is irrelevant in the RG sense.[29] Nevertheless, NRG calculations can be setup for an arbitrary DOS of the conduction electrons.[163,165,208,210,212] "NRG Ljubljana" has built-in support for flat bands (`band=flat`) and for tight-binding bands with cosine dispersion (`band=cosine`) where the hynridisation function is $\Gamma(\epsilon) \propto \sqrt{1-(\epsilon/D)^2}$. There is also a stub for arbitrary DOS to be defined by the user (`band=dmft`), which is required if NRG is used as the impurity solver in DMFT.

3.5 Symmetries and basis construction

The efficiency of NRG calculations can be significantly improved if the symmetries of the problem are taken into consideration. In addition to the performance concerns, the implementation of symmetries is important on a more fundamental ground: if the conservation laws are not built-in, numerical round-off errors tend to induce accidental symmetry breaking which, if relevant, can lead to erroneous results. Continuous symmetries (such as $\mathrm{SU}(2)_{\mathrm{spin}}$, $\mathrm{SU}(2)_{\mathrm{isospin}}$, $\mathrm{U}(1)_{\mathrm{charge}}$) can be taken into account by constructing the basis states using the Lie group representation theory (i.e. Clebsch-Gordan coefficients and the Wigner-Eckart theorem, App. A).[30] Discrete symmetries (such as parity or particle-hole Z_2 symmetries) can be taken into account by projecting basis states to invariant subspaces with well defined Z_2 quantum number using suitable projection operators. By taking explicitly into account the full symmetry of the problem, a formerly intractable problem falls within the reach of modern computers. For example, while not so long ago it was deemed difficult to obtain anything but the NRG eigenvalue flows for the two-channel problems,[28] it is now possible to perform calculations of thermodynamic and even dynamic properties of multi-impurity two-channel problems.[158] In the current implementation of "NRG Ljubljana", the following symmetry types are supported:

- $\mathrm{U}(1)_{\mathrm{charge}} \times \mathrm{U}(1)_{\mathrm{spin}}$, i.e. good quantum numbers are charge Q and spin projection S_z (symmetry type `QSZ` in "NRG Ljubljana") – suitable for general quantum impurity models in the presence of the magnetic field;
- $\mathrm{U}(1)_{\mathrm{charge}} \times \mathrm{U}(1)_{\mathrm{spin}} \times Z_2$, i.e. good quantum numbers are charge Q, spin projection S_z and parity P (symmetry type `QSZLR` in "NRG Ljubljana") – suitable for models with reflection symmetry;
- $\mathrm{U}(1)_{\mathrm{charge}} \times \mathrm{SU}(2)_{\mathrm{spin}}$, i.e. good quantum numbers are charge Q and total spin S (symmetry type `NRG`) – suitable for general QIMs in the absence of the magnetic field;
- $\mathrm{U}(1)_{\mathrm{charge}} \times \mathrm{SU}(2)_{\mathrm{spin}} \times \mathrm{Z}_2$, i.e. good quantum numbers are charge Q, total spin S and parity P (symmetry type `QSLR`);
- $\mathrm{SU}(2)_{\mathrm{iso}} \times \mathrm{SU}(2)_{\mathrm{spin}}$, i.e. good quantum numbers are total isospin I and total spin S (symmetry type `ISO`) – suitable for QIMs at the particle-hole symmetric point;
- $\mathrm{SU}(2)_{\mathrm{iso}} \times \mathrm{SU}(2)_{\mathrm{spin}} \times \mathrm{Z}_2$, i.e. good quantum numbers are total isospin I, total spin S and parity P (symmetry type `ISOLR`).

For each symmetry type, the basis and coefficients for various NRG transformations are derived symbolically using a Mathematica program that uses the `sneg` library. In the following, we will describe the (Q, S) and (I, S) basis; other symmetry types are conceptually similar.

$(\mathbf{q},\mathbf{s})$	States $(\mathbf{k})$
$(-1,0)$	1
$(0,\frac{1}{2})$	$a^\dagger_\uparrow$
$(1,0)$	$a^\dagger_\downarrow a^\dagger_\uparrow$

(a) One channel

$(\mathbf{q},\mathbf{s})$	States $(\mathbf{k})$
$(-2,0)$	1
$(-1,\frac{1}{2})$	$b^\dagger_\uparrow,\ a^\dagger_\uparrow$
$(0,0)$	$b^\dagger_\downarrow b^\dagger_\uparrow,\ \frac{1}{\sqrt{2}}\left(a^\dagger_\downarrow b^\dagger_\uparrow - a^\dagger_\uparrow b^\dagger_\downarrow\right),\ a^\dagger_\downarrow a^\dagger_\uparrow$
$(0,1)$	$b^\dagger_\uparrow a^\dagger_\uparrow$
$(1,\frac{1}{2})$	$a^\dagger_\uparrow b^\dagger_\downarrow b^\dagger_\uparrow,\ b^\dagger_\uparrow a^\dagger_\downarrow a^\dagger_\uparrow$
$(2,0)$	$a^\dagger_\uparrow a^\dagger_\downarrow b^\dagger_\uparrow b^\dagger_\downarrow$

(b) Two channels

Table 3.1: Basis states for additional sites for (Q,S) basis represented by the corresponding electron creation operators that need to be applied on the empty vacuum state. Bold small-case $\mathbf{q}$ and $\mathbf{s}$ are the quantum numbers of charge and spin on the added site(s), while $\mathbf{k}$ indexes different states with the same $(\mathbf{q},\mathbf{s})$.

3.5.1 Construction of (Q,S) basis – symmetry type `NRG`

At the very least, all physically relevant models are charge-conserving. In the absence of the magnetic field, the problems are also rotationally invariant in the spin space; the total spin S and the component S_z are then also conserved. In addition, the component S_z can be eliminated from the problem by the use of the Wigner-Eckart theorem (Appendix A). It follows that we can classify states in subspaces according to quantum numbers Q and S.

We first consider the case of a single conduction channel. For brevity, we denote by $a^\dagger_\mu$ the creation operator for an electron of spin μ on the site of the Wilson chain that is added at the $(N+1)$th NRG iteration, i.e. $a^\dagger_\mu = f^\dagger_{N+1,\mu}$. The Fock space for the new site is composed of four states. Due to rotational invariance, states form spin-multiplets. A single state from each such multiplet needs to be retained, as all other members of the multiplet can be taken into account using the Wigner-Eckart theorem; by convention, in each multiplet with spin S we retain the state with the highest projection $S_z = S$. The four basis states for the additional site are thus represented by the three states given in Table 3.1a. In two-channel channel problems, two sites are added to the Wilson chain in each iteration, one from each conduction band. The creation operators for the second band are denoted by $b^\dagger_\mu = f^\dagger_{N+1,\mu,2}$. The 16 states that form the Fock space of the two newly added sites are represented by the 10 states given in Table 3.1b.

We also need a prescription for generating a basis with well defined Q and S for $(N+1)$-site Wilson chain given the eigenstates of the N-site Wilson chain from the previous iteration. This is easily accomplished using the angular momentum algebra (Clebsch-Gordan coefficients).[29,30] Let $F_i(QS)$ denote the subspace $\tilde{Q}\tilde{S}$ at stage N used to construct states

$|QSS_zri\rangle_{N+1}$ with well defined Q, S, S_z at stage $N+1$; index i numbers the possible ways of adding the angular momenta together ($i = 1, \ldots, 4$ for one-channel case, $i = 1, \ldots, 16$ for two-channel cases), while r numbers the consecutive eigenstates in the subspace $\tilde{Q}\tilde{S}$ at step N. For convenience, we also define $f_i^\mu(S_z) = \tilde{S}_z = S_z - \mu$, the spin projection $\tilde{S}_z$ for μ-term in the expression, and $g_i^\mu(SS_z) = \tilde{S}\tilde{S}_z$. With this short-hand notation established, we are able to write the prescription as

$$|QSS_zri\rangle_{N+1} = \sum_{\mu=-S(i)}^{S(i)} \left\langle g_i^\mu(SS_z); S(i), \mu \middle| SS_z \right\rangle \; |F_i(QS) f_i^\mu(S_z) r\rangle_N \otimes |i, \mu\rangle, \tag{3.10}$$

where $\left\langle S_1 m_1; S_2 m_2 \middle| Sm \right\rangle$ denotes the Clebsch-Gordan coefficient for joining spins S_1 and S_2 into spin S, $|\rangle_{N+1}$ and $|\rangle_N$ denote states for $(N+1)$-site and N-site Wilson chain, $|i, \mu\rangle$ are the states on the added site(s) tabulated in Table 3.1 and $S(i) = \mathtt{s}$, the total spin quantum number of the $|i, \mu\rangle$ state. The rules for forming the new subspaces are given in Table 3.2. In "NRG Ljubljana", these tables can be found in files `coef/1ch-In.cpp` and `coef/2ch-In.cpp` or, generally, in `coef/*-In.cpp`. As an example, $i = 2$ and $i = 3$ in the one-channel case correspond to two different ways of obtaining total spin S by adding a spin-$\frac{1}{2}$ object, either from $\tilde{S} = S - \frac{1}{2}$ or from $\tilde{S} = S + \frac{1}{2}$. It should be noted in passing that a singlet and a triplet never couple into a singlet state (that would be a violation of the triangle inequality). This must be taken into account when constructing state $i = 10$ in the two-channel case; $S = 0$ is then forbidden.

3.5.2 Construction of (I, S) basis – symmetry type `ISO`

When the $\mathrm{U}(1)_{\mathrm{charge}}$ conservation of charge symmetry can be extended to the full $\mathrm{SU}(2)_{\mathrm{iso}}$ isospin symmetry, an additional complication arises due to the phase factor in the definition of the isospin down component of the tensor operator (which corresponds to the annihilation operator). The brackets of creation and annihilation operators must be expressed using the irreducible matrix elements

$$\langle I' I'_z S' S'_z r' | f^\dagger_{i,\mu} | I I_z S S_z r \rangle = \left\langle I I_z; \tfrac{1}{2}\tfrac{1}{2} \middle| I' I'_z \right\rangle \left\langle S S_z; \tfrac{1}{2}\mu \middle| S' S'_z \right\rangle \langle I' S' r' \| f_i \| I S r \rangle \tag{3.11}$$

and

$$\langle I' I'_z S' S'_z r' | f_{i,\mu} | I I_z S S_z r \rangle = (-1)^i (-2\mu) \left\langle I I_z; \tfrac{1}{2}, -\tfrac{1}{2} \middle| I' I'_z \right\rangle \left\langle S S_z; \tfrac{1}{2}, -\mu \middle| S' S'_z \right\rangle \langle I' S' r' \| f_i \| I S r \rangle. \tag{3.12}$$

Here i is the site index which takes even or odd values on the underlying bipartite lattice (see Sec. 2.3 on the isospin symmetry). As the problem is assumed to be spin and isospin isotropic, neither S_z nor I_z play any role in the diagonalization of H_{N+1}. The basis states for the added site of the Wilson chain are given in Table 3.3.

The invariant subspaces are constructed in analogy to the case of (Q, S) basis in the previous subsection. Again $F_i(IS)$ denotes the subspace $\tilde{I}\tilde{S}$ at stage N used to construct

i	$\tilde{Q}$	$\tilde{S}$	$(\mathbf{q},\mathbf{s},\mathbf{k})$
1	$Q+1$	S	$(-1,0,1)$
2	Q	$S-\frac{1}{2}$	$(0,\frac{1}{2},1)$
3	Q	$S+\frac{1}{2}$	$(0,\frac{1}{2},1)$
4	$Q-1$	S	$(1,0,1)$

(a) One channel

i	$\tilde{Q}$	$\tilde{S}$	$(\mathbf{q},\mathbf{s},\mathbf{k})$
1	$Q+2$	S	$(-2,0,1)$
2	$Q+1$	$S-\frac{1}{2}$	$(-1,\frac{1}{2},1)$
3	$Q+1$	$S+\frac{1}{2}$	$(-1,\frac{1}{2},1)$
4	$Q+1$	$S-\frac{1}{2}$	$(-1,\frac{1}{2},2)$
5	$Q+1$	$S+\frac{1}{2}$	$(-1,\frac{1}{2},2)$
6	Q	S	$(0,0,1)$
7	Q	S	$(0,0,2)$
8	Q	S	$(0,0,3)$
9	Q	$S-1$	$(0,1,1)$
10	Q	S	$(0,1,1)$
11	Q	$S+1$	$(0,1,1)$
12	$Q-1$	$S-\frac{1}{2}$	$(1,\frac{1}{2},1)$
13	$Q-1$	$S+\frac{1}{2}$	$(1,\frac{1}{2},1)$
14	$Q-1$	$S-\frac{1}{2}$	$(1,\frac{1}{2},2)$
15	$Q-1$	$S+\frac{1}{2}$	$(1,\frac{1}{2},2)$
16	$Q-2$	S	$(2,0,1)$

(b) Two channels

Table 3.2: Subspaces $F_i(QS) = (\tilde{Q},\tilde{S})$ and basis states for the additional site used to construct ith combination of basis states for the new iteration for (Q,S) basis

$(\mathbf{i},\mathbf{s})$	States $(\mathbf{k})$
$(\frac{1}{2},0)$	$a^\dagger_\downarrow a^\dagger_\uparrow$
$(0,\frac{1}{2})$	$a^\dagger_\uparrow$

(a) One channel

$(\mathbf{i},\mathbf{s})$	States $(\mathbf{k})$
$(1,0)$	$a^\dagger_\downarrow a^\dagger_\uparrow b^\dagger_\downarrow b^\dagger_\uparrow$
$(\frac{1}{2},\frac{1}{2})$	$a^\dagger_\uparrow b^\dagger_\downarrow b^\dagger_\uparrow$, $a^\dagger_\downarrow a^\dagger_\uparrow b^\dagger_\uparrow$
$(0,1)$	$-a^\dagger_\uparrow b^\dagger_\uparrow$
$(0,0)$	$-\frac{1}{\sqrt{2}}\left(a^\dagger_\downarrow a^\dagger_\uparrow + b^\dagger_\downarrow b^\dagger_\uparrow\right)$, $\frac{1}{\sqrt{2}}\left(a^\dagger_\downarrow b^\dagger_\uparrow - a^\dagger_\uparrow b^\dagger_\downarrow\right)$

(b) Two channels

Table 3.3: Basis states for additional site in the isospin-spin (I,S) basis. Bold small-case $\mathbf{i}$ and $\mathbf{s}$ are the quantum numbers of charge and spin on the added site(s), while $\mathbf{k}$ indexes different states with the same $(\mathbf{i},\mathbf{s})$.

i	$\tilde{I}$	$\tilde{S}$	$(\mathbf{i},\mathbf{s},\mathbf{k})$
1	$I-\frac{1}{2}$	S	$(\frac{1}{2},0,1)$
2	$I+\frac{1}{2}$	S	$(\frac{1}{2},0,1)$
3	I	$S-\frac{1}{2}$	$(0,\frac{1}{2},1)$
4	I	$S+\frac{1}{2}$	$(0,\frac{1}{2},1)$

(a) One channel

i	$\tilde{I}$	$\tilde{S}$	$(\mathbf{i},\mathbf{s},\mathbf{k})$
1	$I-1$	S	$(1,0,1)$
2	I	S	$(1,0,1)$
3	$I+1$	S	$(1,0,1)$
4	$I-\frac{1}{2}$	$S-\frac{1}{2}$	$(\frac{1}{2},\frac{1}{2},1)$
5	$I+\frac{1}{2}$	$S-\frac{1}{2}$	$(\frac{1}{2},\frac{1}{2},1)$
6	$I-\frac{1}{2}$	$S+\frac{1}{2}$	$(\frac{1}{2},\frac{1}{2},1)$
7	$I+\frac{1}{2}$	$S+\frac{1}{2}$	$(\frac{1}{2},\frac{1}{2},1)$
8	$I-\frac{1}{2}$	$S-\frac{1}{2}$	$(\frac{1}{2},\frac{1}{2},2)$
9	$I+\frac{1}{2}$	$S-\frac{1}{2}$	$(\frac{1}{2},\frac{1}{2},2)$
10	$I-\frac{1}{2}$	$S+\frac{1}{2}$	$(\frac{1}{2},\frac{1}{2},2)$
11	$I+\frac{1}{2}$	$S+\frac{1}{2}$	$(\frac{1}{2},\frac{1}{2},2)$
12	I	$S-1$	$(0,1,1)$
13	I	S	$(0,1,1)$
14	I	$S+1$	$(0,1,1)$
15	I	S	$(0,0,1)$
16	I	S	$(0,0,2)$

(b) Two channels

Table 3.4: Subspaces $F_i(IS) = (\tilde{I},\tilde{S})$ and basis states for the additional site used to construct ith combination of basis states for the new iteration in the (I,S) basis

states $|II_zSS_zri\rangle_{N+1}$ at stage $N+1$. We also define $f_i^\alpha(I_z) = \tilde{I}_z = I_z - \alpha$, $f_i^\mu(S_z) = \tilde{S}_z = S_z - \mu$, $g_i^\alpha(II_z) = \tilde{I}\tilde{I}_z$ and $g_i^\mu(SS_z) = \tilde{S}\tilde{S}_z$. The new basis is then formed using a double application of the angular momentum addition rules:

$$|II_zSS_zi\rangle_{N+1} = \sum_{\alpha=-I(i)}^{I(i)} \sum_{\mu=-S(i)}^{S(i)} \left\langle g_i^\alpha(II_z);I(i),\alpha\middle|II_z\right\rangle \left\langle g_i^\mu(SS_z);S(i),\mu\middle|SS_z\right\rangle \times |F_i(IS)f_i^\alpha(I_z)f_i^\mu(S_z)r\rangle_N \otimes |i,\mu,\alpha\rangle. \tag{3.13}$$

$I(i)$ and $S(i)$ correspond to $\mathbf{i}$ and $\mathbf{s}$ quantum numbers of states $|i,\mu,\alpha\rangle$. The rules for forming the states are summarized in Table 3.4.

3.6 RG transformation and iterative diagonalisation

In this section we describe how the hopping Hamiltonian is actually solved. We define a series of finite-size Hamiltonians of the form

$$H_N = \Lambda^{N/2}\left[H_{\mathrm{imp}} + H_{\mathrm{C}} + \sum_{n=0}^{N}\sum_{\mu,\alpha}\Lambda^{-n/2}\xi_n\left(f^\dagger_{n,\mu,\alpha}f_{n+1,\mu,\alpha} + \mathrm{H.c}\right)\right], \tag{3.14}$$

so that the full Hamiltonian is given by the limit

$$H = \lim_{N\to\infty}\left(\Lambda^{-N/2}H_N\right). \tag{3.15}$$

The factor $\Lambda^{N/2}$ in the definition of H_N rescales the energy scale so that the smallest dimensionless excitation energy of H_N becomes of order $\mathcal{O}(1)$. In some sense this is reminiscent of the rescaling of the fields in the momentum-space renormalization or rescaling of the free energy per site in the block-spin renormalization. The NRG iteration is then defined by the recursion relation

$$H_{N+1} = R\{H_N\} = \sqrt{\Lambda}H_N + \sum_{\mu,\alpha}\xi_N\left(f^\dagger_{n,\mu,\alpha}f_{n+1,\mu,\alpha} + \mathrm{H.c}\right). \tag{3.16}$$

The energies are rescaled by $\sqrt{\Lambda}$ and one new site (one-channel problems) or two new sites (two-channel problems) from the Wilson chain are attached to the system, see Fig. 3.9. This recursion relation is the fundamental aspect of the NRG.[29,30] Due to even-odd effects, the RG transformation is actually defined by two consecutive NRG iterations:

$$H_{N+2} = R^2\{H_N\}, \tag{3.17}$$

so that the renormalization flow in the NRG is represented by the sequence of Hamiltonians

$$\ldots \to H_{N-2} \to H_N \to H_{N+2} \to \ldots \tag{3.18}$$

A simple way of seeing that R by itself cannot be an RG transformation is that during an iteration step the energy levels are rescaled by $\sqrt{\Lambda}$, therefore R cannot have a fixed point, since two successive energies in the discretized conduction-band Hamiltonian are separated by a factor of Λ.[213] R^2, however, does have fixed points.[29] It is also clear that the fixed point for even and odd N are generally different.[28,29] The number of NRG steps performed is set by parameter `Nmax`.

It should be noted in passing that the word "group" in renormalization group is actually inappropriate; in fact, it is a semi-group. There is namely no inverse transformation. This is related to the fact that information is "lost" (integrated out), either by doing coarse graining (real-space RG) or by truncation (NRG). An inverse NRG iteration is therefore impossible.[126]

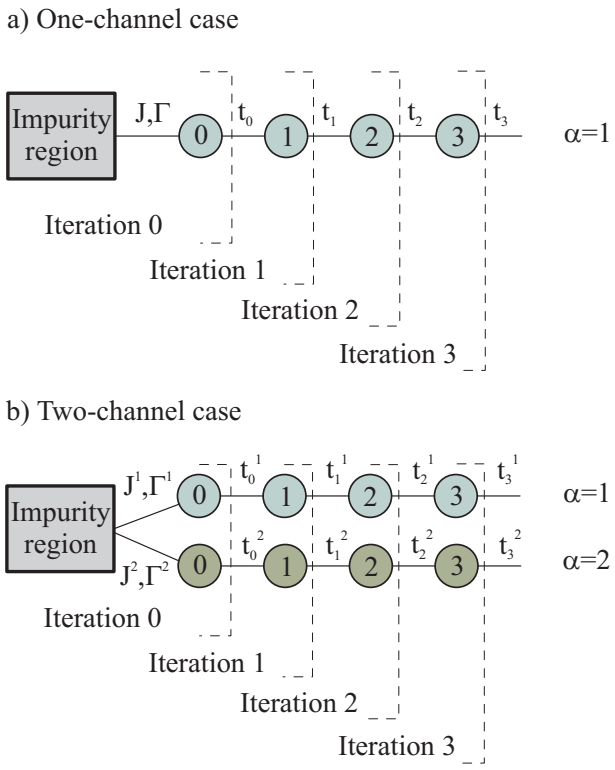

Figure 3.9: Hopping Hamiltonians and the successive iterations of the NRG procedure: one site from each channel is added during each RG step. As far as the NRG iteration is considered, the impurity region is a black box: all that is required are the eigenstates of the sum of the impurity and the coupling Hamiltonians, $H_{\mathrm{imp}} + H_{\mathrm{C}}$, and the irreducible matrix elements of the creation operators for an electron on the first (indexed as 0) site of the hopping Hamiltonian computed in the eigenbasis.

The Hamiltonian H_N describes the physics at the energy (temperature) scale

$$T_N \propto \frac{D}{k_B}\Lambda^{-N/2}/\bar{\beta} \tag{3.19}$$

or, equivalently, at the length scale

$$L_N \propto \bar{\beta}\Lambda^{N/2}/k_F. \tag{3.20}$$

Here $\bar{\beta}$ is a parameter of order $\mathcal{O}(1)$; the corresponding setting in "NRG Ljubljana" is `betabar`. In my calculations I typically used $\bar{\beta} = 0.46$ or $\bar{\beta} = 0.75$. The exact definition of T_N depends on the discretization scheme:

$$\begin{aligned} T_N &= \frac{D}{k_B}\frac{1}{2}(1+\Lambda^{-1})\Lambda^{-(N-1)/2}/\bar{\beta}, \quad \text{for } \texttt{disc=wilson}, \\ T_N &= \frac{D}{k_B}\frac{1}{2}(1+\Lambda^{-1})\Lambda^{-(N-z)/2}/\bar{\beta}, \quad \text{for } \texttt{disc=yoshida}, \\ T_N &= \frac{D}{k_B}\frac{1-\Lambda^{-1}}{\ln\Lambda}\Lambda^{-(N-z)/2}/\bar{\beta}, \quad \text{for } \texttt{disc=campo}. \end{aligned} \tag{3.21}$$

From Eqs. (3.19) and (3.20) it follows that NRG iteration corresponds to $L \to \infty$ and $T \to 0$ at the same time, but in a way that the size of the system is finite at all times. From this it follows that NRG gives *finite-size* spectra. It should be kept in mind that the ground state degeneracy in a finite-size spectrum is obtained by taking the limit $T \to 0$ first, then $L \to \infty$. By taking first $L \to \infty$ and then $T \to 0$, a different ground state degeneracy can be obtained. The two limits do not commute[92,118]! One should be aware of this when comparing with results obtained by means of quantum-field-theoretical methods in the $L \to \infty$ limit.

One might expect that due to the exponential decrease of hopping parameters it might be possible to treat the successive sites in the Wilson chain by perturbation theory. This is not the case:[29] when adding the $(N+1)$st site(s) to a chain of N sites, the coupling of order $\Lambda^{-N/2}$ is a strong perturbation for the lowest eigenstates of the N-site chain which are also on the energy scale of $\Lambda^{-N/2}$. We thus add a new site by performing an exact diagonalisation of a matrix H_{N+1}.

One NRG iteration (3.16) consists of using the states from previous step to construct the Hamiltonian H_{N+1} (`nrg_makematrix` routine), then diagonalizing it numerically (`diagonalize` routine). The full information about the system at step N is contained in the eigenstates of H_N and in the irreducible matrix elements $\langle\|f_N\|\rangle$ (class `IterInfo`); this is clearly a much more detailed description compared to a small set of coupling parameters used in the conventional RG (scaling) approach. The Hamiltonian is written in the direct product basis $|QSri\rangle_{N+1} \sim |QSr\rangle\otimes i$ [here we consider the case of (Q,S) basis, see Sec. 3.5 for other cases], therefore the Hamiltonian matrix takes the form of a block-matrix: diagonal blocks are diagonal matrices, the diagonal elements being the rescaled eigenvalues of the states $|QSr\rangle$

i	i'	coefficient
1	2	1
1	3	1
2	4	$-\frac{\sqrt{2S}}{\sqrt{1+2S}}$
3	4	$\frac{\sqrt{2S+2}}{\sqrt{1+2S}}$

(a) One channel

i	i'	channel	coefficient
1	2	b	1
1	3	b	1
1	4	a	1
1	5	a	1
2	6	b	$-\frac{\sqrt{2S}}{\sqrt{1+2S}}$
2	7	a	$-\frac{\sqrt{S}}{\sqrt{1+2S}}$
2	9	a	1
2	10	a	$\frac{\sqrt{1+S}}{\sqrt{1+2S}}$
3	6	b	$\frac{\sqrt{2(1+S)}}{\sqrt{1+2S}}$
3	7	a	$\frac{\sqrt{1+S}}{\sqrt{1+2S}}$
3	10	a	$\frac{\sqrt{S}}{\sqrt{1+2S}}$
3	11	a	1
4	7	b	$-\frac{\sqrt{S}}{\sqrt{1+2S}}$
4	8	a	$-\frac{\sqrt{2S}}{\sqrt{1+2S}}$
4	9	b	-1
4	10	b	$-\frac{\sqrt{1+S}}{\sqrt{1+2S}}$
5	7	b	$\frac{\sqrt{1+S}}{\sqrt{1+2S}}$
5	8	a	$\frac{\sqrt{2(1+S)}}{\sqrt{1+2S}}$
5	10	b	$-\frac{\sqrt{S}}{\sqrt{1+2S}}$
5	11	b	-1

i	i'	channel	coefficient
6	12	a	1
6	13	a	1
7	12	b	$-\frac{1}{\sqrt{2}}$
7	13	b	$-\frac{1}{\sqrt{2}}$
7	14	a	$-\frac{1}{\sqrt{2}}$
7	15	a	$-\frac{1}{\sqrt{2}}$
8	14	b	1
8	15	b	1
9	12	b	$\frac{\sqrt{-\frac{1}{2}+S}}{\sqrt{S}}$
9	14	a	$-\frac{\sqrt{-\frac{1}{2}+S}}{\sqrt{S}}$
10	12	b	$-\frac{\sqrt{\frac{1+S}{2}}}{\sqrt{S}}$
10	13	b	$\frac{\sqrt{\frac{S}{2}}}{\sqrt{1+S}}$
10	14	a	$\frac{\sqrt{\frac{1+S}{2}}}{\sqrt{S}}$
10	15	a	$-\frac{\sqrt{\frac{S}{2}}}{\sqrt{1+S}}$
11	13	b	$-\frac{\sqrt{\frac{3}{2}+S}}{\sqrt{1+S}}$
11	15	a	$\frac{\sqrt{\frac{3}{2}+S}}{\sqrt{1+S}}$
12	16	a	$-\frac{\sqrt{2S}}{\sqrt{1+2S}}$
13	16	a	$\frac{\sqrt{2(1+S)}}{\sqrt{1+2S}}$
14	16	b	$-\frac{\sqrt{2S}}{\sqrt{1+2S}}$
15	16	b	$\frac{\sqrt{2(1+S)}}{\sqrt{1+2S}}$

(d) Two channels

Table 3.5: Coefficients for off-diagonal blocks in the Hamiltonian matrix in the (Q, S) basis

from the previous iteration; the out-of-diagonal blocks are constructed from the irreducible matrix elements $\langle QSr||f||Q'S'r'\rangle$ weighted by coefficients that can be derived from the corresponding Clebsch-Gordan coefficients (see routine `nrg_makematrix`). These coefficients are given in Table 3.5 for the case of (Q,S) basis (see also Ref. 30). In "NRG Ljubljana", these coefficients can be found in `coef/1ch-offdiag.cpp` and `coef/2ch-offdiag.cpp` or, generally, in `coef/*-offdiag.cpp`.

We then diagonalize the Hamiltonian in each invariant sector separately to obtain the

i	i'	coefficient
2	1	1
4	3	$-\frac{\sqrt{2S'+1}}{\sqrt{S'+1}}$

(a) $Q' = Q - 1$, $S' = S - \frac{1}{2}$

i	i'	coefficient
3	1	1
4	2	$\frac{\sqrt{2S'+1}}{\sqrt{S'}}$

(b) $Q' = Q - 1$, $S' = S + \frac{1}{2}$

Table 3.6: Irreducible matrix elements $\langle QSi\|a^\dagger\|Q'S'i'\rangle$ for creation operator on the additional site in one-channel problems

eigenstates

$$|QS\omega\rangle = \sum_{ri} U_{QS}(\omega, ri)|QSri\rangle, \tag{3.22}$$

where U_{QS} is the unitary matrix which brings each Hamiltonian matrix in its diagonal form. Before proceeding to the next NRG iteration, the irreducible matrix elements of the newly added site(s), $\langle QSi\|f^\dagger_{N+1,\mu\alpha}\|Q'S'i'\rangle$, need to be recomputed from the irreducible matrix elements $\langle QSi\|f^\dagger_{N,\mu\alpha}\|Q'S'i'\rangle$ from the previous iteration. The coefficients are given in tables 3.6 and 3.7 and can be found in files `coef/1ch-spinupa.cpp`, `coef/1ch-spindowna.cpp`, `coef/2ch-spinupa.cpp`, `coef/2ch-spindowna.cpp` `coef/2ch-spinupb.cpp`, `coef/2ch-spindownb.cpp` or, generally, in `coef/1ch-*.cpp`; the corresponding routines in "NRG Ljubljana" are `recalc_f` and `recalc_irreduc`.

Since the total number of states is an exponential function of the iteration number N ($\propto 4^N$ in the one-channel case and $\propto 16^N$ in the two-channel case), Wilson proposed to simply *truncate* the number of states to some manageable size of the order of 1000 after each NRG iteration. The idea is that, since the coupling between consecutive sites of the chain decreases exponentially for increasing chain length, only the lowest-lying eigenstates are renormalized and the separation of scales is thus maintained iteration by iteration.[29,214] This works because the matrix elements of $f^\dagger_N$ are largest for similar eigenstates of H_N, while the matrix elements of $f^\dagger_N$ between the low-lying eigenstates of H_N and the highly excited states that are truncated are small.[29]

In "NRG Ljubljana", truncation is controlled by parameters `keep`, `keepmin` and `keepenergy`. Parameter `keep` represents the maximum number of eigenstates that may be kept at each iteration; it should be increased as much as possible within the limits set by available computational resources. If parameter `keepenergy` is set to a positive value, the energy cut-off truncation scheme is used: only the eigenstates with the (rescaled) energy below the value of the parameter will be retained. The use of the energy cut-off truncation is recommended since a high number of states is kept when the degeneracy is high, and a low number when the degeneracy is low; in this fashion, the computational time is divided optimally between the iterations. Finally, `keepmin` sets the minimum number of states to be kept. It should also be remarked that eigenstates in NRG tend to be clustered. If

i	i'	coefficient
5	1	1
7	2	$\frac{\sqrt{2S'+1}}{2\sqrt{S'}}$
8	4	$\frac{\sqrt{S'+\frac{1}{2}}}{\sqrt{S'}}$
10	2	$-\frac{\sqrt{2S'-1}}{2\sqrt{S'}}$
11	3	-1
13	6	1
14	9	$-\frac{\sqrt{S'+\frac{1}{2}}}{\sqrt{S'}}$
15	7	$-\frac{1}{\sqrt{2}}$
15	10	$-\frac{\sqrt{S'+1}}{\sqrt{2}\sqrt{S'}}$
16	12	$\frac{\sqrt{S'+\frac{1}{2}}}{\sqrt{S'}}$

(a) $Q' = Q-1$, $S' = S+\frac{1}{2}$

i	i'	coefficient
4	1	1
7	3	$-\frac{\sqrt{2S'+1}}{2\sqrt{S'+1}}$
8	5	$-\frac{\sqrt{S'+\frac{1}{2}}}{\sqrt{S'+1}}$
9	2	-1
10	3	$-\frac{\sqrt{2S'+3}}{2\sqrt{S'+1}}$
12	6	1
14	7	$-\frac{1}{\sqrt{2}}$
14	10	$\frac{\sqrt{S'}}{\sqrt{2}\sqrt{S'+1}}$
15	11	$\frac{\sqrt{S'+\frac{1}{2}}}{\sqrt{S'+1}}$
16	13	$-\frac{\sqrt{S'+\frac{1}{2}}}{\sqrt{S'+1}}$

(b) $Q' = Q-1$, $S' = S-\frac{1}{2}$

i	i'	coefficient
3	1	1
6	2	$\frac{\sqrt{S'+\frac{1}{2}}}{\sqrt{S'}}$
7	4	$\frac{\sqrt{2S'+1}}{2\sqrt{S'}}$
10	4	$\frac{\sqrt{2S'-1}}{2\sqrt{S'}}$
11	5	1
12	9	$\frac{\sqrt{S'+\frac{1}{2}}}{\sqrt{S'}}$
13	7	$-\frac{1}{\sqrt{2}}$
13	10	$\frac{\sqrt{S'+1}}{\sqrt{2}\sqrt{S'}}$
15	8	1
16	14	$\frac{\sqrt{S'+\frac{1}{2}}}{\sqrt{S'}}$

(c) $Q' = Q-1$, $S' = S+\frac{1}{2}$

i	i'	coefficient
2	1	1
6	3	$-\frac{\sqrt{S'+\frac{1}{2}}}{\sqrt{S'+1}}$
7	5	$-\frac{\sqrt{2S'+1}}{2\sqrt{S'+1}}$
9	4	1
10	5	$\frac{\sqrt{2S'+3}}{2\sqrt{S'+1}}$
12	7	$-\frac{1}{\sqrt{2}}$
12	10	$-\frac{\sqrt{S'}}{\sqrt{2}\sqrt{S'+1}}$
13	11	$-\frac{\sqrt{S'+\frac{1}{2}}}{\sqrt{S'+1}}$
14	8	1
16	15	$-\frac{\sqrt{S'+\frac{1}{2}}}{\sqrt{S'+1}}$

(d) $Q' = Q-1$, $S' = S-\frac{1}{2}$

Table 3.7: Irreducible matrix elements $\langle QSi\|a^\dagger\|Q'S'i'\rangle$ for creation operator $a^\dagger$ (subtables a and b) and for creation operator $b^\dagger$ (subtables c and d) on the additional site in two-channel problems

the states are truncated in the middle of such a cluster, systematic errors and symmetry breaking may be induced. Parameter `safeguard` enforces retention of additional states, so that the "gap" between the highest retained and the lowest discarded state is at least `safeguard`.

3.7 Computable quantities

While K. G. Wilson originally applied NRG to obtain the spectrum of excitations and the impurity contribution to the magnetic susceptibility,[29] methods to calculate other quantities were soon introduced: one can determine specific heat,[215,216] charge susceptibility,[217] entropy,[209] spin relaxation rates,[218] and various zero-frequency response functions and equal-time correlation functions.[219] NRG is likely the most versatile tool in the field of quantum impurity physics.

3.7.1 Finite-size spectra and fixed points

The most easily obtained result in NRG is the spectrum of excitations above the ground state as a function of the temperature. An important amount of information may be

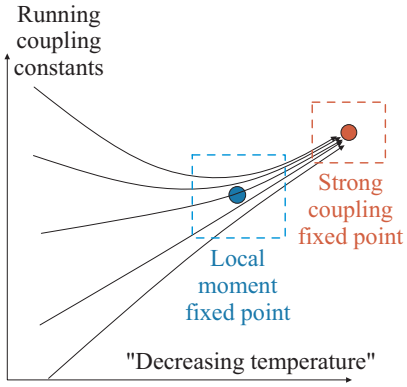

Figure 3.10: Schematic representation of the NRG renormalization flow. The horizontal direction represents the direction of decreasing energy scale (temperature), while the vertical direction represents the multi-dimensional space of the effective Hamiltonians (which can be considered to be parameterized by some large set of coupling constants). When the system is near a fixed point (dashed boxes), its properties can be described by a perturbative expansion around the fixed-point Hamiltonian. The diagram also illustrates the idea of universality: even for widely different microscopic Hamiltonians, the low-temperature behavior of the systems is essentially the same.

extracted from the consideration of such spectra alone. In fact, one of the central questions regarding any strongly correlated system concerns precisely the nature of its low-energy excitations.

It should be noted from the start that the system size in NRG is finite at any iteration step: we say that we obtain *finite-size spectrum*. In contradistinction, the high-energy cutoff scaling methods such as Anderson's poor man's scaling,[140] multiplicative RG[130] and Yuval-Anderson's RG[139] work in the continuum limit ($L \to \infty$, where L is the system size).[108] Some important quantities, such as the ground state entropy, depend on whether the system size is finite or not when the $T \to 0$ limit is taken[92] (see also Sec. 3.6).

If the lowest lying eigenstates for successive ($N \to N + 2$) NRG transformations remain (nearly) unchanged, we say that a *fixed point* has been reached. More accurately, fixed-point Hamiltonian H^* is defined as

$$H^* = R^2\{H^*\}. \tag{3.23}$$

With NRG, one can study the various fixed points of a given QIM, deviations from the universal spectra (determined by the operator content of the fixed point[108]), and the cross-overs between the different fixed points, Fig. 3.10.

If the excitation spectrum of a fixed point is in a one-to-one relation to the excitations of free electron gas, such fixed point is called *Fermi liquid fixed point* (see Section 2.4 on Fermi liquid and non-Fermi liquid systems). The spectra of Fermi liquid fixed points are composed of excitations that change particle number (particle and hole excitations) and

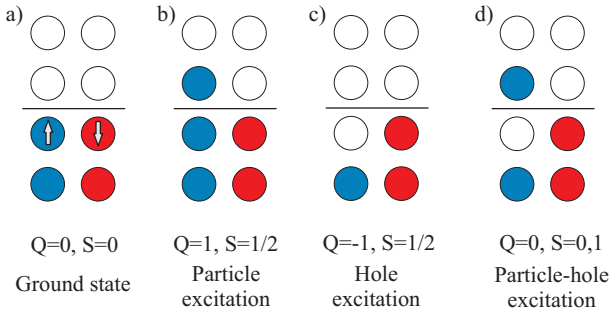

Figure 3.11: Pictorial representation of the ground state and excitations of a Fermi liquid.

excitations where a particle is promoted to a higher level (particle-hole excitations), and combinations thereof, Fig. 3.11. The excitations at non-Fermi-liquid fixed points do not always have comparably simple interpretation.

For Hamiltonian H_N near a fixed point H^*, the NRG recursion relation can be expanded in powers of the deviation from the fixed point and linearized.[29,30] Defining $\delta H_N = H_N - H^*$, we write

$$\delta H_{N+2} = R^2\{H^* + \delta H_N\} - H^* \approx \mathcal{L}^* \delta H_N, \tag{3.24}$$

where $\mathcal{L}^*$ is a linear transformation. Like any linear operator, $\mathcal{L}^*$ can be diagonalized

$$\mathcal{L}^* O_l^* = \lambda_l^* O_l^*, \tag{3.25}$$

and we expand δH_N as

$$\delta H_N = \sum_l C_l {\lambda_l^*}^{N/2} O_l^*. \tag{3.26}$$

For $\lambda_l^* > 1$, the contribution of corresponding eigenoperator O_l^* will grow with N: we say that such operators are *relevant*. For $\lambda_l^* < 1$, the contribution will vanish and we name such operators *irrelevant*. Finally, if $\lambda_l^* = 1$, the operator O_l^* is called *marginal* and its effect must be studied more carefully by considering non-linear corrections to the RG transformation.[220] The operator content of a fixed point determines its stability with respect to perturbations:[30] a fixed point with relevant operators is called *unstable*, while a fixed point with only irrelevant operators is *stable*. Fixed point with marginal operators can be either stable or unstable, or may lead to the emergence of lines of fixed point and to the breakdown of the universality.[220] The knowledge of the leading eigenoperators (i.e. those with the highest eigenvalues λ_l^*) is instrumental in establishing *effective Hamiltonians* given by the fixed point Hamiltonian H^* plus correction terms:[30]

$$H_N^{\text{eff}} = H^* + \omega_1 \Lambda^{(N-1)/2} \delta H_1 + \omega_2 \Lambda^{(N-1)/2} \delta H_2 + \dots \tag{3.27}$$

where ω_1 and ω_2 are some coefficients which can be determined by analyzing the NRG spectrum. For example, finite-temperature corrections to the Fermi-liquid $T = 0$ behavior of the Kondo model are determined by the leading irrelevant operators.[29]

Saving of eigenvalue results in "NRG Ljubljana" is controlled by parameters `trace`, `dumpenergies` and `dumpannotated`.

3.7.2 Static thermodynamic quantities: susceptibilities, entropy, specific heat

Static thermodynamic quantities, such as magnetic susceptibility, heat capacity and entropy, are determined primarily by the energy level splittings of order k_BT. Energies much higher than k_BT above the ground state are exponentially suppressed, while excitations with much lower energy can be considered thermally washed out; this turns out to be a good approximation. Thermodynamic quantities at temperature T_N can thus be calculated from the energy spectrum at the Nth stage of the NRG iteration.[29,30,129] In the following, brakets denote grand-canonical averaging

$$\langle O\rangle = \mathrm{Tr}\left[O\exp(-\beta H)\right]/Z, \tag{3.28}$$

where Z is the partition function $Z = \mathrm{Tr}\left(e^{-\beta H}\right)$ and $\beta = 1/k_BT$. In practice, the traces are computed in the truncated basis of NRG eigenstates at a given iteration step N, i.e. from a finite-size spectrum. In "NRG Ljubljana", the temperature dependence of static thermodynamic quantities is output to file `chi` which must be postprocessed to obtain presentable results.

Magnetic and charge susceptibility

The temperature-dependent impurity contribution to the magnetic susceptibility $\chi_{\mathrm{imp}}(T)$ is defined as

$$\chi_{\mathrm{imp}}(T) = \frac{(g\mu_B)^2}{k_BT}\left(\langle S_z^2\rangle - \langle S_z^2\rangle_0\right) \tag{3.29}$$

where S_z is the total spin and the subscript 0 refers to the situation when no impurities are present (i.e. H is simply the band Hamiltonian H_{band}), g is the electronic gyromagnetic factor, μ_B the Bohr magneton and k_B the Boltzmann's constant. It should be noted that the combination $k_BT\chi_{\mathrm{imp}}/(g\mu_B)^2$ can be considered as an effective moment of the impurities, μ_{eff}. In the presence of the magnetic field applied only to the impurity site, $\langle S_z^2\rangle$ needs to be replaced by $\langle S_z^2\rangle - \langle S_z\rangle^2$ in accordance to the fluctuation-dissipation theorem. It may also be remarked that while K. G. Wilson originally proposed to calculate $\langle S_z^2\rangle_0$ analytically, I find that it is more practical to actually perform a NRG calculation of S_z^2 for a problem without impurities. This has an added benefit in that similar artefacts appear in $\langle S_z^2\rangle$ and $\langle S_z^2\rangle_0$ and they cancel when subtraction is performed.

By analogy, charge susceptibility is defined as

$$\chi_{\mathrm{charge}}(T) = \frac{1}{k_BT}\left(\langle I_z^2\rangle - \langle I_z^2\rangle_0\right), \tag{3.30}$$

where I_z is the total isospin (recall that $I_z = Q/2$). In the absence of the particle-hole symmetry, $\langle I_z^2\rangle$ needs to be replaced by $\langle I_z^2\rangle - \langle I_z\rangle^2$.

Specific heat and entropy

Defining energy as $E = \langle H \rangle = \mathrm{Tr}\left(He^{-\beta H}\right)$, the heat capacity can be calculated from energy fluctuations as

$$C(T) = \frac{\partial E}{\partial T} = k_B \beta^2 \left[\langle H^2 \rangle - \langle H \rangle^2\right], \tag{3.31}$$

and we may define the impurity contribution to the heat capacity (impurity specific heat) as $C_{\mathrm{imp}}(T) = C(T) - C_0(T)$, where C_0 is the heat capacity of the conduction band without impurities. Furthermore, we have $\beta F = -\ln Z$ and $E = F + TS$, therefore

$$\frac{S}{k_B} = \frac{E - F}{k_B T} = \beta E - \beta F = \beta E + \ln Z, \tag{3.32}$$

and we may define the temperature-dependent impurity contribution to the entropy as $S_{\mathrm{imp}}(T) = S(T) - S_0(T)$. From the quantity S_{imp}/k_B we can deduce the effective degrees-of-freedom ν of the impurity as $S_{\mathrm{imp}}/k_B \sim \ln \nu$. In the following the suffix "imp" in χ_{imp}, S_{imp}, etc. will often be dropped if no confusion can arise, but one should keep in mind that impurity contribution to the quantity is always implied. We also set $k_B = 1$.

The convergence with the number of states retained in the NRG iteration depends on the quantity being computed. For example, the energy accuracy required for a specific-heat calculation is considerably higher than that for the susceptibility.[215]

3.7.3 Correlation functions

To characterize the state of a quantum impurity system it is often useful to calculate various correlations functions, i.e. thermodynamic expectation values of operators such as the on-site occupancy $\langle n_i \rangle$, local charge-fluctuations $\langle (\delta n)^2 \rangle = \langle (n_i - \langle n_i \rangle)^2 \rangle = \langle n_i^2 \rangle - \langle n_i \rangle^2$, local-spin $\langle \mathbf{S}_i^2 \rangle$ and spin-spin correlations $\langle \mathbf{S}_i \cdot \mathbf{S}_j \rangle$. In turn, these can be used to compute more complex quantities such as the concurrence which measures the entanglement between two qubits.[221]

In "NRG Ljubljana", the operators of interest are specified by writing the corresponding expression in terms of the second quantization operators. A number of auxiliary routines are available to simplify this process and the most commonly occurring operators are already built in the program (configuration setting `ops`). During the problem setup step, the operators are transformed in their matrix forms and rotated into the eigenbasis of the initial Hamiltonian by performing suitable unitary transformations: all these steps are performed automatically "behind the scenes" by the Mathematica part of the NRG package. This approach turned out to be extremely flexible, since the user can focus on physics rather than hand-code low-level routines and to worry about implementational details.

To be able to make full use of the symmetries of the problem, the operators need to be expressed in the form that makes them singlets with respect to the symmetry group. For

example, n_i^2 is a spin-singlet, and can be directly computed in the (Q,S) basis. It is not, however, an iso-spin singlet, but $(n_i-1)^2=q_i^2$ is. For a computation in the (I,S) basis, one therefore performs a calculation for q_i^2 and adds $2\langle n_i\rangle-1=1$ to the results (recall that $\langle n_i\rangle=1$ due to the p-h symmetry). In the presence of mirror Z_2 symmetry, it must be taken into account that operators may be even or odd with respect to the reflection. In the case of two impurities embedded in a series between two conduction leads, for example, $n_e=n_1+n_2$ is even, while $n_o=n_1-n_2$ is odd. In a calculation where reflection symmetry is explicitly taken into account, the expectation values $\langle n_1\rangle$ and $\langle n_2\rangle$ can be obtained by calculating suitable combinations of $\langle n_e\rangle$ and $\langle n_o\rangle$ after the NRG run.

More generally, "NRG Ljubljana" supports operators that are singlet, doublet or triplet with respect to spin and singlet or doublet with respect to isospin. This is sufficient for all calculations of interest, but support for more general symmetries may in principle be easily added.

3.7.4 Dynamic quantities

A major extension of the NRG was a method to calculate dynamic properties such as the spectral functions.[147,208,222–225] While $T=0$, $\omega=0$ conductance of Fermi-liquid systems may be obtained from finite-size spectra alone, finite-temperature and finite-frequency conductance, as well as the conductance of non-Fermi-liquid systems can only be computed if spectral functions are known .[213,226–230] Using NRG, one can determine local single-particle (spectral function, $\langle\langle d_\mu; d_\mu^\dagger\rangle\rangle_\omega$), magnetic (dynamic spin susceptibility, $\langle\langle S_z; S_z\rangle\rangle_\omega$) and charge excitations (dynamic charge susceptibility, $\langle\langle n; n\rangle\rangle_\omega$). It is also possible to distinguish between elastic and inelastic contributions to the scattering cross-section.[231]

The conventional approach to the NRG spectral function calculations is based on the observation of Sakai et al.[147] that as we proceed from one iteration to the next, the lowest few eigenstates split due to the interaction with the added shell states, while the intermediate lower levels do not show any essential change. The intermediate states thus form a good approximation of the eigenstates of the Hamiltonian in the $N\to\infty$ limit and are thus used to compute the excitation energies and the transition matrices.

The spectral function matrix for multi-impurity problems is defined as (see Appendix B)

$$A_{ij}=-1/(2\pi)\mathrm{Im}(G^r_{ij}+G^r_{ji}), \tag{3.33}$$

where $G^r_{ij}(\omega)=\langle\langle d_{i\mu}; d_{j\mu}^\dagger\rangle\rangle_\omega$ is the (out-of-diagonal for $i\neq j$) retarded Green's function of the impurity. It can be computed using standard NRG techniques from matrix elements of the creation operators using the following spectral decompositions:

$$\begin{aligned}
A_{i,j}(\omega>0)&=\frac{1}{Z}\sum_{m,n_0}\mathrm{Re}\left[\left(\langle m|d_i^\dagger|n_0\rangle\right)^*\langle m|d_j^\dagger|n_0\rangle\right]\times\delta(\omega-E_m),\\
A_{i,j}(\omega<0)&=\frac{1}{Z}\sum_{m_0,n}\mathrm{Re}\left[\left(\langle m_0|d_i^\dagger|n\rangle\right)^*\langle m_0|d_j^\dagger|n\rangle\right]\times\delta(\omega+E_n).
\end{aligned} \tag{3.34}$$

Indices m_0, n_0 with subscript 0 run over (eventually degenerate) ground states and indices m, n without a subscript over all states.

Calculations can be improved by directly calculating the one-particle self-energy $\Sigma(\omega)$;[214] this approach leads to more accurate results and it is especially suitable for applications of NRG as an impurity solver in the DMFT[197] . Further improvements include a better approach to merge partial spectral information from consecutive NRG iterations[232] (in "NRG Ljubljana" the result of the conventional spectrum calculation is output to files `spec_*_pts_*.dat`, while the result obtained with the N/N+2 trick is output to files `spec_*_dens_*.dat`). For problems where the high-energy spectral features depend on the low-energy behavior of the system, the spectral function has to be computed taking into account the reduced density matrix obtained from the density matrix of the low-temperature fixed-point: this is the density-matrix NRG (DMNRG) developed by W. Hofstetter[233] (see Sec. 3.9). This approach is needed, for example, in the case of the Anderson impurity in magnetic field,[233] or for the side-coupled double quantum dot near the points of ground state level crossing (see Sec. 7.3).

Recently, a time-dependent NRG was introduced[234] by generalizing the idea behind the DMNRG: time-dependent NRG makes possible to study the effects of sudden changes of the parameters and the ensuing relaxation to the steady state solution. In this approach, a density matrix in full Fock space is introduced by judiciously using the information from the discarded part of the NRG eigenstates. This idea has led to new approach for calculation of equilibrium spectral functions: the "full density matrix" NRG[235] or "complete Fock space" NRG.[236] This method does not suffer from over-counting of excitations, it fulfills sum rules and correctly reproduces spectral features at energies below the temperature.

An important observation for practical calculations is that as the number of states retained is increased, the calculated spectra do not suddenly change; they rather gradually improve and converge toward the true spectrum.[147] This implies that even rough spectra are qualitatively correct.

3.7.5 Spectrum broadening and smoothing

Since QIMs are represented in NRG by hopping Hamiltonians of a finite size, the computed spectral functions are represented as a sum of delta peaks. To obtain a meaningful continuous function, these peaks need to be broadened. The original approach to obtaining a smooth curve was by Gaussian broadening, followed by separate spline interpolation of results in odd and even steps, and by the averaging of the two curves.[147] A better approach is the logarithmic-exponential broadening:[232] each data point (delta function peak at ω_0) is smoothed into

$$F_b(\omega, \omega_0) = \frac{e^{-b^2/4}}{b\sqrt{\pi}} \exp\left(-\frac{(\ln\omega - \ln\omega_0)^2}{b^2}\right), \tag{3.35}$$

i.e. a Gaussian function on a logarithmic scale, where b is a broadening parameter, typically $b = 0.3$. One should keep in mind an important feature regarding the broadening procedure.

Namely, due to broadening the spectral resolution at energy ω is always limited to

$$\begin{aligned}\delta\omega_+ &= \omega\left(e^{b\sqrt{\ln 2}} - 1\right)\\ \delta\omega_- &= \omega\left(1 - e^{-b\sqrt{\ln 2}}\right)\end{aligned} \tag{3.36}$$

For high-energy part of the spectrum (say $\omega = 1$) this limits the resolution to $[-0.22; 0.28]$ at $b = 0.3$. Peaks sharper than this will thus appear broader than they truly are. Naive application of NRG is therefore not a reliable method to determine the spectral features at high energies.

Furthermore, low energy features are also slightly deformed. The action of the broadening is to replace

$$f(\omega) = \int \mathrm{d}\omega_0 f(\omega_0)\delta(\omega - \omega_0) \quad \rightarrow \quad \tilde{f}(\omega) = \int \mathrm{d}\omega_0 f(\omega_0) F_b(\omega, \omega_0). \tag{3.37}$$

Let us consider its effect on a narrow Lorentzian of width Δ centered at $\omega = 0$:

$$\begin{aligned}\tilde{f}(\omega) &= \int_0^\infty \mathrm{d}\omega_0 \frac{\Delta^2}{\omega_0^2 + \Delta^2} F_b(\omega, \omega_0)\\ &= \int_{-\infty}^{+\infty} \mathrm{d}y_0 \frac{\Delta^2}{\exp(2y_0) + \Delta^2} \frac{e^{-b^2/4}}{b\sqrt{\pi}} \exp\left(-\frac{(y - y_0)^2}{b^2}\right),\end{aligned} \tag{3.38}$$

where we performed substitution $\ln\omega_0 = y_0$ and introduced $y = \ln\omega$. The limit $\omega \to 0$ corresponds to $y \to -\infty$. The integrand is a Gaussian-like function centered at y with a y_0 dependent weight $\propto 1/(\exp(y_0^2) + \Delta^2)$. For small enough ω (to be concrete, $\omega \ll \Delta$), this weight becomes a constant and the integral can be evaluated exactly. We find $\lim_{\omega\to 0} \tilde{f}(\omega) = \exp(-b^2/4)$. For $b = 0.3$, this gives 0.98. In other words, even in the absence of any other approximations, the logarithmic broadening at $b = 0.3$ introduces an error of few percent in the Kondo peak weight. In addition, the Lorentzian is narrowed, see Fig. 3.12. These facts must be taken into account when quantitative details in the results are important. In that case b should be reduced as much as possible. Typically, the value of b is chosen to be 0.3 or less (parameter `loggauss_b`).

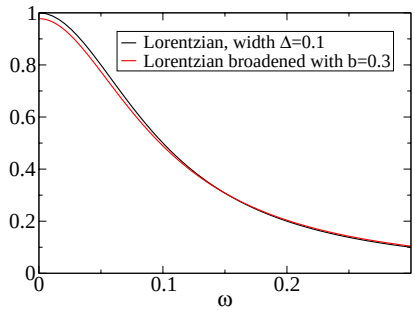

Figure 3.12: Effect of logarithmic broadening on a Lorentzian curve.

3.8 Recursion relations for operators

After each iteration, expectation values of operators of interest are computed and the irreducible matrix elements of these operators recomputed in the new eigenbasis for the next iteration. It is important to note that it is only possible to consider operators that transform as tensor operators with respect to the symmetry group that is taken into account in the NRG implementation. As an illustration, we consider the case of the (Q,S) symmetry and a tensor operator operator $\hat{O}$ of rang M with respect to the spin SU(2) group. The information about the operator $\hat{O}$ at iteration N is entirely contained in a matrix O_N of irreducible matrix elements $\langle QSr\|\hat{O}\|Q'S'r'\rangle$. The non-zero subspaces for singlet operators have $Q = Q'$ and $S = S'$, for doublet (creation) operators we must have $Q = Q' + 1$ and $S = S' \pm 1/2$ and for triplet operators (such as spin) we must have $Q = Q'$ and $S = S'$ or $S = S' \pm 1$. In the basis of eigenvalues $|QS\omega\rangle$ of the $(N+1)$st iteration, we write

$$\langle QS\omega\|\hat{O}\|Q'S'\omega'\rangle_{N+1} = \frac{\langle QSS_z\omega|\hat{O}_\mu|Q'S'S'_z\omega'\rangle_{N+1}}{\left\langle S'S'_z;M\mu|SS_z\right\rangle} \tag{3.39}$$

To make this expression meaningful, we can choose, for example, $S_z = S$, $\mu = M$, $S'_z = S - M$. We then have

$$\langle QS\omega\|\hat{O}\|Q'S'\omega'\rangle_{N+1} = \frac{\sum_{rir'i'} U_{QS}(\omega, ri)U_{Q'S'}(\omega', r'i')\langle QSSri|\hat{O}_M|Q'S', S-M, r'i'\rangle_{N+1}}{\left\langle S', S-M;MM|SS\right\rangle} \tag{3.40}$$

We then take into account the definitions of $|QSS_zri\rangle$ states, (3.10), and write

$$\begin{aligned} \ldots = &\sum_{ri,r'i'}\sum_{\alpha\beta} \frac{c(QS, Q'S', ii', \alpha\beta)}{\left\langle S', S-M;MM|SS\right\rangle} \\ &\times U_{QS}(\omega, ri)U_{Q'S'}(\omega', r'i')\langle F_i(QS)f_i^\alpha(S)r|\hat{O}_M|F_{i'}(Q'S')f_{i'}^\beta(S-M)r'\rangle_{N+1}, \end{aligned} \tag{3.41}$$

where $c(QS, Q'S', ii', \alpha\beta)$ is a scalar product between $(\mathbf{q}, \mathbf{s}, \mathbf{k})$ states on the added sites of the Wilson chain and α, β are the corresponding s_z components of these states. We rewrite

this as

$$\begin{aligned}\ldots = &\sum_{ii',\alpha\beta} \frac{c(QS,Q'S',ii',\alpha\beta)\big\langle g_{i'}^{\beta}(S',S-M);MM|g_i^{\alpha}(SS)\big\rangle}{\big\langle S',S-M;MM|SS\big\rangle} \\ &\times \sum_{rr'} U_{QS}(\omega,ri)U_{Q'S'}(\omega',r'i')\langle F_i(QS)r\|\hat{O}\|F_{i'}(Q'S')r'\rangle_N\end{aligned} \tag{3.42}$$

After taking into account which subspaces $F_i(QS)$ and $F_{i'}(Q'S')$ are connected by operator $\hat{O}$ and performing the sums over α and β, it turns out that for given (QS) and $(Q'S')$ subspaces, only a small number of (ii') combinations contribute. We finally write

$$\langle QS\omega\|\hat{O}\|Q'S'\omega'\rangle_{N+1} = \sum_{ii'} C(QS,Q'S',ii') \sum_{rr'} U_{QS}(\omega,ri)U_{Q'S'}(\omega',r'i')\langle F_i(QS)r\|\hat{O}\|F_{i'}(Q'S')r'\rangle_N. \tag{3.43}$$

The coefficients $C_{QS,Q'S',ii'}$ are computed using a computer algebra system and they are tabulated in the manual (Ref. 237). The corresponding routines in "NRG Ljubljana" are `recalc_singlet`, `recalc_doublet` and `recalc_triplet`; they all call a low-level routine `recalc_general` which performs the actual computation. The coefficient tables can be found in files `*-singlet.cpp` (for singlet operators), `*-doublet*.cpp` (for doublet operators) and `*-triplet*.cpp` (for triplet operators).

3.9 Density-matrix NRG

At iteration N, the information about the behavior of the system at temperatures much lower than T_N is yet unknown; in particular, the true ground state of the system is not yet determined. Since the zero-temperature spectral function is defined by the matrix elements between the ground state and the excited states, there is no guarantee that the high-frequency part of the spectral function calculated by the conventional NRG procedure will be correct. Discrepancies appear, for example, in the presence of the magnetic field: for $H \gg T_K$, the impurity spin is polarized and the true spectral functions are asymmetric. The asymmetry of functions calculated by the conventional NRG approach is strongly underestimated, since at the temperature (energy) scale above H, the magnetic field does not yet significantly affect the finite-size spectrum.[233] Density-matrix NRG technique[188,206,233] remedies the shortcomings of the conventional approach. It was originally implemented by W. Hofstetter for NRG calculations in (Q, S_z) basis for studying the effect of the magnetic field on spin-projected spectral functions. In the absence of a magnetic field, it is advantageous to use the (Q, S) basis. The improvement in numerical efficiency is sufficient to enable consideration of more complex systems, such as the double quantum dot.

Density-matrix NRG technique consists in running the NRG calculations in two runs. The first run is a usual NRG iteration, with the sole exception that the U_{QS} matrices are stored for later use. After the last iteration, the zero-temperature density matrix is estimated

using the truncated basis as

$$\rho = \frac{1}{Z} \sum_{QSS_z\omega} \exp(-\beta E_{QS\omega}) |QSS_z\omega\rangle\langle QSS_z\omega|, \tag{3.44}$$

where ω enumerates different states in each (Q, S) subspace and the grand-canonical statistical sum is

$$Z = \mathrm{Tr}\left[\exp(-\beta H)\right] = \sum_{QSS_z\omega} \exp(-\beta E_{QS\omega}). \tag{3.45}$$

The reduced density-matrices are then computed for higher temperatures. During the second NRG run, the traces are computed with respect to these reduced density-matrices, rather than using the grand-canonical density-matrix $\rho = \exp(-\beta H)/Z$.

We now illustrate how the recursion rules for computing the reduced density matrix are derived in the (Q, S) basis for the single-channel case. Unitary transformation of states from the Nth to $(N+1)$th stage is (see Eq. (3.22))

$$|QSS_z\omega\rangle_{N+1} = \sum_{ri} U_{QS}(\omega|ri)|QSS_zri\rangle_{N+1}, \tag{3.46}$$

where the $|QSS_zri\rangle_{N+1}$ states are defined by Eq. (3.10). They may be expanded as:[30]

$$\begin{aligned}
|QSS_zr1\rangle_{N+1} &= |Q+1, SS_zr\rangle_N, \\
|QSS_zr2\rangle_{N+1} &= u f^\dagger_{(N+1)\uparrow} |Q, S-\frac{1}{2}, S_z-\tfrac{1}{2}, r\rangle_N + v f^\dagger_{(N+1)\downarrow} |Q, S-\tfrac{1}{2}, S_z+\tfrac{1}{2}, r\rangle_N, \\
|QSS_zr3\rangle_{N+1} &= w f^\dagger_{(N+1)\uparrow} |Q, S+\tfrac{1}{2}, S_z-\tfrac{1}{2}, r\rangle_N + y f^\dagger_{(N+1)\downarrow} |Q, S+\tfrac{1}{2}, S_z+\tfrac{1}{2}, r\rangle_N, \\
|QSS_zr4\rangle_{N+1} &= f^\dagger_{(N+1)\uparrow} f^\dagger_{(N+1)\downarrow} |Q-1, SS_zr\rangle_N,
\end{aligned} \tag{3.47}$$

where $f^\dagger_{(N+1)\mu}$ is the creation operator for electrons on the $(N+1)$th site of the hopping Hamiltonian and u, v, w, and y are the Clebsch-Gordan coefficients

$$u = \left(\frac{S+S_z}{2S}\right)^{1/2}, \; v = \left(\frac{S-S_z}{2S}\right)^{1/2}, \; w = -\left(\frac{S-S_z+1}{2S+2}\right)^{1/2}, \; y = \left(\frac{S+S_z+1}{2S+2}\right)^{1/2}. \tag{3.48}$$

Density matrix in the basis of $|QSS_zri\rangle_{N+1}$ states is

$$\rho = \sum_{QSS_z\omega} \exp(-\beta E_{QS\omega}) \sum_{ri,r'i'} U_{QS}(\omega|ri) U_{QS}(\omega|r'i') |QSS_zri\rangle_{N+1} \langle QSS_zr'i'|_{N+1}. \tag{3.49}$$

We now perform a partial trace over the states on the additional $(N+1)$th site to obtain projector operators defined on the chain of length N. Diagonal projectors (those with

$i = i'$) are:

$$\begin{aligned}
\mathrm{Tr}_{N+1}\left(|QSS_zr1\rangle\langle QSS_zr'1|\right) &= |Q+1, SS_zr\rangle_N\langle Q+1, SS_zr'|_N \\
\mathrm{Tr}_{N+1}\left(|QSS_zr4\rangle\langle QSS_zr'4|\right) &= |Q-1, SS_zr\rangle_N\langle Q-1, SS_zr|_N \\
\mathrm{Tr}_{N+1}\left(|QSS_zr2\rangle\langle QSS_zr'2|\right) &= u^2|Q, S-\tfrac{1}{2}, S_z-\tfrac{1}{2}, r\rangle_N\langle Q, S-\tfrac{1}{2}, S_z-\tfrac{1}{2}, r'|_N \\
&\quad + v^2|Q, S-\tfrac{1}{2}, S_z+\tfrac{1}{2}, r\rangle_N\langle Q, S-\tfrac{1}{2}, S_z+\tfrac{1}{2}, r'|_N \\
\mathrm{Tr}_{N+1}\left(|QSS_zr3\rangle\langle QSS_zr3|\right) &= w^2|Q, S+\tfrac{1}{2}, S_z-\tfrac{1}{2}, r\rangle_N\langle Q, S+\tfrac{1}{2}, S_z-\tfrac{1}{2}, r'|_N \\
&\quad + y^2|Q, S+\tfrac{1}{2}, S_z+\tfrac{1}{2}, r\rangle_N\langle Q, S+\tfrac{1}{2}, S_z+\tfrac{1}{2}, r'|_N
\end{aligned} \tag{3.50}$$

The $i = i' = 2$ terms can be simplified after summing over S_z:

$$\begin{aligned}
&\sum_{S_z=-S}^{S} \mathrm{Tr}_{N+1}\left(|QSS_zr2\rangle_{N+1}\langle QSS_zr'2|_{N+1}\right) \\
&= \sum_{S_z=-S+1}^{S} \left(u^2_{SS_z} + v^2_{S,S_z-1}\right)|Q, S-\tfrac{1}{2}, S_z-\tfrac{1}{2}, r\rangle_N\langle Q, S-\tfrac{1}{2}, S_z-\tfrac{1}{2}, r'|_N \\
&= \frac{2S+1}{2S} \sum_{S_z=-(S-\frac{1}{2})}^{+(S-\frac{1}{2})} |Q, S-\tfrac{1}{2}, S_z\rangle_N\langle Q, S-\tfrac{1}{2}, S_z, r'|_N
\end{aligned} \tag{3.51}$$

The spin multiplicity of $(QS)_{N+1}$ space is $2S+1$, while the spin multiplicity of $(Q, S-\frac{1}{2})_N$ is $2S$. The factor $(2S+1)/(2S)$ is therefore merely a normalization factor. In the last line we emphasize that in the N-site space the S_z runs over all permissible values for spin $S-\frac{1}{2}$. An analogous simplification can be performed for $i = i' = 3$. Out-of-diagonal terms which correspond to different charge on the additional site are clearly zero, while other out-of-diagonal terms such as $i = 2$, $i' = 3$ give zero when summed over. Non-zero partial traces of projector operators are therefore:

$$\sum_{S_z} \mathrm{Tr}_{N+1}|QSS_zri\rangle_{N+1}\langle QSS_zr'i'|_{N+1} = \delta_{ii'}c_i(S)\sum_{S_{zi}}|Q_iS_iS_{zi}r\rangle_N\langle Q_iS_iS_{zi}r'|_N \tag{3.52}$$

with $c_1 = c_4 = 1$, $c_2 = \frac{2S+1}{2S}$, $c_3 = \frac{2S+1}{2S+2}$, $Q_1 = Q+1$, $Q_2 = Q_3 = Q$, $Q_4 = Q-1$, $S_1 = S_4 = S$, $S_2 = S-\frac{1}{2}$, $S_3 = S+\frac{1}{2}$ and corresponding S_{zi} ranges over all possible values for a given S_i. The reduced density matrix is diagonal in its (QS) subspace index. In a sense, it has similar symmetry properties as the singlet tensor operators. In general we therefore have

$$\begin{aligned}
\rho^{N+1}_{\mathrm{reduced}} &= \sum_{QSS_z}\sum_{\omega\omega'} C^{QS,N+1}_{\omega\omega'}|QSS_z\omega\rangle_{N+1}\langle QSS_z\omega'|_{N+1} \\
&= \sum_{QSS_z}\sum_{\omega\omega'} C^{QS,N+1}_{\omega\omega'}\sum_{ri,r'i'} U_{QS}(\omega|ri)U_{QS}(\omega'|r'i')|QSS_zri\rangle_N\langle QSS_zr'i'|_N \\
&= \sum_{QS}\sum_{\omega\omega'} C^{QS,N+1}_{\omega\omega'}\sum_{ri,r'} U_{QS}(\omega|ri)U_{QS}(\omega'|r'i)c_i(S)\sum_{S_{zi}}|Q_iS_iS_{zi}r\rangle_N\langle Q_iS_iS_{zi}r'|_N.
\end{aligned} \tag{3.53}$$

This is to be compared with

$$\rho^N_{\text{reduced}} = \sum_{QSS_z} \sum_{rr'} C^{QS,N}_{rr'} |QSS_z r\rangle_N \langle QSS_z r'|_N. \tag{3.54}$$

We finally obtain the recursion relation for calculation of coefficients $C^{QS,N}_{rr'}$ in the reduced density matrix:

$$\begin{aligned} C^{QS,N}_{rr'} = & \sum_{\omega\omega'} C^{Q-1,S,N+1}_{\omega\omega'} U_{Q-1,S}(\omega|r1) U_{Q-1,S}(\omega'|r'1) \\ & + \sum_{\omega\omega'} C^{Q+1,S,N+1}_{\omega\omega'} U_{Q+1,S}(\omega|r4) U_{Q+1,S}(\omega'|r'4) \\ & + \frac{2S+2}{2S+1} \sum_{\omega\omega'} C^{Q,S+\frac{1}{2},N+1}_{\omega\omega'} U_{Q,S+\frac{1}{2}}(\omega|r2) U_{Q,S+\frac{1}{2}}(\omega'|r'2) \\ & + \frac{2S}{2S+1} \sum_{\omega\omega'} C^{Q,S-\frac{1}{2},N+1}_{\omega\omega'} U_{Q,S-\frac{1}{2}}(\omega|r3) U_{Q,S-\frac{1}{2}}(\omega'|r'3) \end{aligned} \tag{3.55}$$

This is the main result of the derivation. Using known U_{QS} matrices, recursion is applied after the first NRG run to calculate density matrices for all chain lengths.

In the DM-NRG scheme the spectral function is evaluated in the second NRG run using the reduced density matrix ρ_{reduced} as

$$A^N_\mu(\omega) = \sum_{ijm} \left(\langle j|d^\dagger_\mu|m\rangle \langle j|d^\dagger_\mu|i\rangle \rho^{\text{reduced}}_{im} + \langle j|d^\dagger_\mu|m\rangle \langle i|d^\dagger_\mu|m\rangle \rho^{\text{reduced}}_{ji} \right) \delta(\omega - (E_j - E_m)). \tag{3.56}$$

Both terms contribute at positive *and* negative frequencies.

Chapter 4

Other methods for impurity models

In this chapter, I briefly describe methods that are used in this work – in addition to NRG – to solve impurity models. Section 4.1 describes the Green's function method for non-interacting models, while sections 4.2 and 4.3 are devoted to the variational methods and Quantum Monte Carlo methods, respectively. I remark at this point that the results of these methods (when used in their respective domains of validity) agree very well with results obtained using NRG; for a direct comparison see, for example, page 154.

I will also make use of the Bethe Ansatz (BA) method, which provides exact solution of the Kondo model.[50,52,59,238,239] Using BA, the thermodynamics of the many-body problem is reduced to a system of infinitely many non-linear integral equations[239,240] which are easily solved numerically. While BA does not clarify the physics behind the Kondo effect, it is extremely useful since it provides exact results that can be compared with NRG calculations to ascertain their reliability.

4.1 Green's function method for noninteracting problems

While the topic of this work are effects of interactions, it is sometimes sufficient to describe physical systems using effective non-interacting models. Since the electron spin then plays no role, it may be dropped from consideration and the model usually takes the form of a tight-binding Hamiltonian for spinless particles. In transport problems, the scatterer is described using

$$H_{\mathrm{imp}} = \sum_{ij} h_{ij} |i\rangle\langle j|, \tag{4.1}$$

where i, j range over the lattice sites of the scattering region. The scatterer couples to the conduction leads via hopping terms of the form

$$H' = -\sum_i t_{L,i} \left(|i\rangle\langle L| + \text{H.c.} \right) - \sum_i t_{R,i} \left(|i\rangle\langle R| + \text{H.c.} \right). \tag{4.2}$$

For simplicity, let us assume that only single site ($i = 1$) is coupled to both the left and right lead (this will, in fact, be the case when this method is applied to study the Fano effect in side-coupled double quantum dot in Sec. 7.3). The retarded self-energy matrix due to the coupling to the leads is

$$\Sigma^r = \Sigma^r_L + \Sigma^r_R, \tag{4.3}$$

$$[\Sigma^r_L]_{11} = t^2 g^r_{LL}, \text{ other components zero,} \tag{4.4}$$

$$[\Sigma^r_R]_{11} = t^2 g^r_{RR}, \text{ other components zero,} \tag{4.5}$$

where g^r_{LL} and g^r_{RR} are retarded Green's function of uncoupled left and right semi-infinite lead, respectively. The effective Hamiltonian $H_{\text{eff}} = H_{\text{imp}} + \Sigma^r$ is then used to obtain the retarded Green's function of the impurity region:

$$G^r = (\epsilon \mathbb{1} - H_{\text{eff}})^{-1}. \tag{4.6}$$

Spectral function is defined as

$$A = \frac{i}{\pi}(G^r - G^a) = -\frac{2}{\pi}\text{Im}\, G^r, \tag{4.7}$$

while the spectral function is simply $\rho = \text{Tr}A$. Finally, we define the transmission function:

$$t_{LR} = \text{Tr}\left(\Gamma_L G^r \Gamma_R G^a\right) \tag{4.8}$$

with $\Gamma_L = i(\Sigma^r_L - \Sigma^a_L)$ and $\Gamma_R = i(\Sigma^r_R - \Sigma^a_R)$, from which follows the conductance:

$$G = G_0 t_{LR}(\epsilon = 0). \tag{4.9}$$

4.2 Gunnarsson-Schönhammer variational method

Variational method is an approximate technique to calculate ground state energy of a quantum system. It can be shown that as the variational Ansatz is improved, the variational *energy* will tend toward the true ground state energy. In general, however, the variational (or "trial") *wavefunction* will not necessarily tend toward the true ground state wavefunction; this implies that there is no guarantee that the calculated correlations approach the actual values (but often they do). Nevertheless, variational methods are valuable in that they allow very complex problems to be solved in a simple analytical manner, often with results in closed form. The earliest application to the Kondo problem is Yosida's wave

function for the s-d model,[60] which was later generalized for the Anderson model.[61] This variational approach correctly reproduces the Kondo energy $\propto \exp(-1/\rho J)$.

The variational method used in this work (the "Gunnarsson-Schönhammer variational method") was originally developed for the Anderson model by K. Schönhammer to study hydrogen atom chemisorption on metal surfaces.[241,242] Solution of this problem requires proper description of electron correlation effects because charge fluctuations on the hydrogen atom are strongly suppressed due to electron-electron repulsion. The method was later extended to N-fold degenerate Anderson model by Gunnarsson and Schönhammer[242–244] to study photoemission and absorption spectra of rare earth and actinide compounds.

Variational calculation consists of finding a trial wavefunction with free parameters, determining the ground state energy as a function of these parameters and performing a minimization. The wavefunction with the lowest energy is then the best approximation to the true wavefunction from the subspace of the trial wavefunctions. A good trial wavefunction must therefore have the characteristics that we expect the true ground state to have. In particular, the exact ground state of the Anderson model is known to be a singlet, so a good starting point for a variational calculation is the restricted Hartree-Fock approximation with identical orbitals for both spins. In the Hartree-Fock solution $|\Psi_{\mathrm{HF}}\rangle$ the charge fluctuations cannot be properly suppressed (since electrons always come in pairs), therefore K. Schönhammer proposed the following Ansatz:[241]

$$|\Phi_0\rangle = (\lambda_0 P_0 + \lambda_{1\uparrow} P_{1\uparrow} + \lambda_{1\downarrow} P_{1\downarrow} + \lambda_2 P_2)\,|\Psi_{\mathrm{HF}}\rangle, \tag{4.10}$$

with variational parameters λ_i and projection operators P_i which project onto the subspaces with i electrons on the impurity atom. In the case of a single orbital we can write the projection operators as:

$$P_0 = (1-n_\uparrow)(1-n_\downarrow) \tag{4.11}$$
$$P_{1,\uparrow} = n_\uparrow(1-n_\downarrow) \tag{4.12}$$
$$P_{1,\downarrow} = n_\downarrow(1-n_\uparrow) \tag{4.13}$$
$$P_2 = n_\uparrow n_\downarrow. \tag{4.14}$$

The motivation for Ansatz (4.10) is obvious: if $\lambda_{1\mu}$ are large compared to λ_0 and λ_2, the charge fluctuations in the Kondo regime are suppressed.

Improved results can be obtained if, instead of $|\Psi_{\mathrm{HF}}\rangle$, one uses a generalized Hartree-Fock state $|\tilde{\Psi}_{\mathrm{HF}}\rangle$, constructed from non-interacting eigenstates ϕ_k of an effective single-particle Hamiltonian H_{eff}:[242]

$$H_{\mathrm{eff}} = \sum_{k,\mu} \epsilon_k n_{k\mu} + \sum_\mu (\epsilon_d + U n_0) n_{d\mu} + \tilde{V} \sum_\mu (c^\dagger_{1\mu} d_\mu + \mathrm{h.c.}). \tag{4.15}$$

If $n_0 = n_{HF}$ and $\tilde{V} = V$, then $|\tilde{\Psi}_{\mathrm{HF}}\rangle$ goes over to the restricted Hartree-Fock ground state $|\Psi_{\mathrm{HF}}\rangle$. In general, n_0 and $\tilde{V}$ are additional free variational parameters.

The variation of the λ_i leads to a 4×4 eigenvalue problem of the form $\det(H - \epsilon S) = 0$. Here S is the 4×4 over-lap matrix, since the projected states $|\Psi_\alpha\rangle = P_\alpha|\Psi_{\rm HF}\rangle$ do not form an orthonormal basis: $S_{\beta\alpha} = \langle\Psi_\beta|\Psi_\alpha\rangle$. The lowest eigenvalue gives the ground-state energy as a function of n_0 and $\tilde{V}$. A minimization with respect to n_0 and $\tilde{V}$ is then performed in order to obtain the variational ground-state energy.

Schönhammer's variational Ansatz for the single-impurity Anderson model becomes exact in three limiting cases: (a) noninteracting case, $U = 0$, (b) uncoupled case, $\Gamma = 0$, and (c) zero band-width case, $D = 0$. The Ansatz is also known to give a very good interpolation for all values of parameters.[241] In fact, the test results for a single Anderson site match very well the exact Bethe Ansatz results .[245,246] It can be shown that this variational method always gives ground-state energy which is lower or equal to the corresponding Hartree-Fock ground-state energy.[245] Like all variational methods, this technique is, however, limited to zero temperature calculations.

The procedure can be generalized to interacting systems with M sites.[157,221,245,247,248] In the auxiliary noninteracting Hamiltonian, the arbitrary parameters are matrix elements describing the hopping between the leads and the central region and all the matrix elements of the central region C. The variational Hilbert space is spanned by a set of $\alpha = 1, \ldots, 4^M$ basis functions

$$|\Psi_\alpha\rangle = P_\alpha|\tilde{\Psi}_{\rm HF}\rangle = \prod_{i\in C} P^i_{\alpha_i}|\tilde{\Psi}_{\rm HF}\rangle, \tag{4.16}$$

where P^i_n are projection operators on unoccupied, singly occupied and doubly occupied site $i = 1, \ldots, M$. Variation of corresponding parameters λ^i_n again leads to a diagonalisation of the original Hamiltonian in the reduced basis:

$$H_{\beta\alpha}d_\alpha = ES_{\beta\alpha}d_\alpha, \tag{4.17}$$

with $H_{\beta\alpha} = \langle\psi_\beta|H|\psi_\alpha\rangle$ and $S_{\beta\alpha} = \langle\psi_\beta|\psi_\alpha\rangle$, where $|\psi_\alpha\rangle = P_\alpha|\tilde{\Psi}_{\rm HF}\rangle$. To obtain the variational ground state we minimize the lowest eigenstate of this eigenvalue problem with respect to the variable parameters of the auxiliary Hamiltonian.

Finally, the variational technique can also be extended to cases where phonon degrees of freedom are present in the interacting region.[41,249] In this case, $|\tilde{\Psi}_{\rm HF}\rangle$ is the ground state of the effective electron-phonon system which is solved numerically exactly, while Kondo interaction are treated variationally, as previously described.

To calculate expectation value of a local operator (for example the total occupancy $N = \sum n_i$), we write the variational wavefunction as

$$\Psi = \sum_\alpha d_\alpha\psi_\alpha, \tag{4.18}$$

where d_α are the variational coefficients of the ground state. We know that, by construction, ψ_α is associated with some definite occupancy N_α. We thus have $N|\psi_\beta\rangle = N_\beta|\psi_\beta\rangle$. We

write

$$N = \sum_{\alpha,\beta} d^*_\alpha \langle \psi_\alpha | N | \psi_\beta \rangle d_\beta \tag{4.19}$$

$$= \sum_{\alpha,\beta} d^*_\alpha d_\beta \langle \psi_\alpha | \psi_\beta \rangle N_\beta \tag{4.20}$$

$$= \sum_{\alpha,\beta} d^*_\alpha d_\beta S_{\alpha\beta} N_\beta. \tag{4.21}$$

In this manner we can obtain the expectation values of all operators that can be expressed in terms of occupancies n_i; such operators are, for example, charge fluctuation n_i^2 and local spin $\mathbf{S}_i^2 = 3/4(2n_i - n_i^2)$. Expectation values of more general operators, such as $\langle \psi_\alpha | c_1^\dagger c_2 | \psi_\beta \rangle$, need to be evaluated using Wick's theorem.

4.3 Quantum Monte Carlo method

Quantum Monte Carlo (QMC) methods are in many cases the only reliable numerical tool for exploring the properties of quantum systems with very strong correlations between the particles. Lattice fermion problems can be tackled with the auxiliary field (determinantal) QMC method where the fermion degrees of freedom are integrated out of the problem at the expense of introducing classical scalar auxiliary fields.

4.3.1 Projection to the ground state

The ground state of a quantum system can be projected out of an (almost) arbitrary trial wavefunction Ψ_T by applying an exponential operator $e^{-\Theta H}$ and taking the $\Theta \to \infty$ limit.[250] For simplicity we disregard the normalization and we write

$$|\Psi_0\rangle = \lim_{\Theta\to\infty} e^{-\Theta H} |\Psi_T\rangle, \tag{4.22}$$

where Ψ_0 is the ground state. A necessary condition for the method to work is that the trial wavefunction has some overlap with the ground state, $\langle \Psi_0 | \Psi_T \rangle \neq 0$. In practice this requirement is easy to satisfy.

All measurable physical quantities can be obtained from the partition function

$$Z = \mathrm{Tr}\left[e^{-\Theta H}\right] = \sum_{|\psi\rangle} \langle \psi | e^{-\Theta H} | \psi \rangle. \tag{4.23}$$

At zero temperature, Θ goes to infinity and the ground state is projected out of any state ψ. The expression above then reduces to

$$Z = \langle \Psi_T | e^{-\Theta H} | \Psi_T \rangle, \tag{4.24}$$

where Ψ_T is again an arbitrary trial wavefunction. The expectation value Z of the evolution operator $e^{-\Theta H}$ is therefore the quantity of central interest.

4.3.2 Trotter decomposition

We consider the evolution operator for a Hamiltonian which can be decomposed into hopping and interaction part, $H = H_t + H_I$:

$$e^{-\Theta H} = e^{-\Theta(H_t+H_I)}. \tag{4.25}$$

An exponential of a sum of *commuting* operators [1] can be exactly decomposed in the form of a product of exponentials using the Glauber formula[251]

$$e^{A+B} = e^A e^B e^{-[A,B]/2}, \quad \text{if } [A,B] = \text{const.} \tag{4.26}$$

Kinetic and electron-electron repulsion terms do not commute, so this simple expression does not apply to interacting cases. Nevertheless, the two terms can still be approximately separated. We divide the imaginary time Θ into small time steps (time slices):

$$e^{-\Theta H} = \left(e^{-\Delta\tau H}\right)^m. \tag{4.27}$$

Here m is the number of the time slices and $\Delta\tau$ is the length of a time step, so that $\Theta = m\Delta\tau$. If $\Delta\tau$ is small, we can perform the approximate Trotter decomposition:[252]

$$e^{-\Delta\tau H} = e^{-\Delta\tau(H_t+H_I)} = e^{-\Delta\tau H_t} e^{-\Delta\tau H_I} + \dots. \tag{4.28}$$

The dots denote a remainder of the order of $\Delta\tau$. Putting (4.27) and (4.28) together, we obtain the final expression

$$e^{-\Theta H} = \left(e^{-\Delta\tau H_t} e^{-\Delta\tau H_I}\right)^m + \mathcal{O}(\Delta\tau). \tag{4.29}$$

By decreasing the step size $\Delta\tau$, the systematic error can be made arbitrarily small, but then the number of time steps needs to be increased. In reality, a compromise is made between the number of steps and the numerical stability of the method.

4.3.3 Hubbard-Stratonovich transformation

Electron-electron interaction terms are quartic in operators:

$$H_I = U\left(n_\uparrow - \tfrac{1}{2}\right)\left(n_\downarrow - \tfrac{1}{2}\right) = U\left(d_\uparrow^\dagger d_\uparrow - \tfrac{1}{2}\right)\left(d_\downarrow^\dagger d_\downarrow - \tfrac{1}{2}\right). \tag{4.30}$$

It is possible to transform quartic form $x^2 = y^4$ into quadratic ones $x = y^2$ using Gaussian identity in the reverse:

$$e^{\frac{1}{2}x^2} = \frac{1}{\sqrt{2\pi}} \int \mathrm{d}\phi \; e^{-\frac{1}{2}\phi^2 + \phi x} \tag{4.31}$$

[1] Commuting in the broader sense that the commutator is a number and not an operator.

The exponential of a quartic form x^2 is then found to be an integral over an auxiliary variable ϕ of the exponential of a quadratic form $x = y^2$, weighted by the Gaussian factor $e^{-\frac{1}{2}\phi^2}$. If x is an operator quantity, this is called a Hubbard-Stratonovich transformation,[253] and ϕ is called the auxiliary field conjugated to the operator x.

In the case of the Anderson Hamiltonian one can form a square of quadratic forms by writing

$$\left(n_\uparrow - \frac{1}{2}\right)\left(n_\downarrow - \frac{1}{2}\right) = -\frac{1}{2}\left(n_\uparrow - n_\downarrow\right)^2 + \frac{1}{4}, \tag{4.32}$$

and we obtain

$$e^{-\Delta\tau U\left(n_\uparrow-\frac{1}{2}\right)\left(n_\downarrow-\frac{1}{2}\right)} = \frac{e^{-\Delta\tau U/4}}{\sqrt{2\pi}}\int \mathrm{d}\phi\; e^{-\frac{1}{2}\phi^2} e^{\sqrt{\Delta\tau U/2}\phi\left(n_\uparrow-n_\downarrow\right)}. \tag{4.33}$$

There is also a discrete version of the Hubbard-Stratonovich transformation due to Hirsch[254] where instead of the continuous integral one has a sum over two terms:

$$e^{-\Delta\tau U\left(n_\uparrow-\frac{1}{2}\right)\left(n_\downarrow-\frac{1}{2}\right)} = \frac{e^{-\Delta\tau U/4}}{2}\sum_{s=\pm 1} e^{\alpha s\left(n_\uparrow-n_\downarrow\right)}. \tag{4.34}$$

Here α is a numerical constant defined by $\cosh(\alpha) = e^{\Delta\tau U/2}$. The Hubbard-Stratonovich transformation can be considered as a replacement of the two-particle part H_I of the Hamiltonian by an effective single-particle Hamiltonian $\mathscr{H}_I(s)$, which depends on the stochastic spin variable s.

We rewrite the projector $e^{-\Theta H}$ as

$$\begin{aligned} e^{-\Theta H} = \prod_{n=1}^{m}\left[e^{-\Delta\tau H_I} e^{-\Delta\tau H_t}\right] &= \prod_{n=1}^{m}\left[\sum_{s_n} e^{-\Delta\tau \mathscr{H}_I(s_n)} e^{-\Delta\tau H_t}\right] \\ &= \sum_{s_1,\ldots,s_m}\left[\prod_{n=1}^{m}\left(e^{-\Delta\tau\mathscr{H}_I(s_n)} e^{-\Delta\tau H_t}\right)\right]. \end{aligned} \tag{4.35}$$

We introduce the evolution operator $U_{\mathbf{S}}(\Theta)$ for the effective single-particle Hamiltonian $H' = H_t + \mathscr{H}_I(\mathbf{S})$ in a given configuration $\mathbf{S}$ ($\mathbf{S}$ denotes the set of field variables s_n for all time slices):

$$U_{\mathbf{S}}(\Theta) = \prod_{n=1}^{m}\left(e^{-\Delta\tau\mathscr{H}_I(s_n)} e^{-\Delta\tau H_t}\right). \tag{4.36}$$

Operator $U_{\mathbf{S}}(\Theta)$ makes the independent particles evolve for an imaginary time Θ in a varying magnetic field $\mathbf{S}$. Using the evolution operators, the projector can be rewritten as

$$e^{-\Theta H} = \sum_{\mathbf{S}} U_{\mathbf{S}}(\Theta). \tag{4.37}$$

We have split the interacting problem into a large number of non-interacting ones (one for each realization of $\mathbf{S}$) and we will have to sum over all possible configurations of the auxiliary fields to recover the physics of e-e interactions.

4.3.4 Integration over fermion degrees of freedom

The exponentials of single-particle operators that appear in the expression (4.36) can be integrated exactly (recall that these are basically Gaussian "integrals"). Trial wavefunctions are usually Slater determinants represented by matrices of coefficients P. It can be shown that an exponential of a single-particle operator simply transforms a Slater determinant into another Slater determinant, therefore

$$\langle \Psi_T | U_{\mathbf{S}}(\Theta) | \Psi_T \rangle = \det[P^\dagger B_{\mathbf{S}} P], \tag{4.38}$$

where $B_{\mathbf{S}}$ is the matrix representation of the evolution operator $U_{\mathbf{S}}$. The fermion degrees of freedom then no longer appear in the problem, but now we have to sum over all possible configuration of the auxiliary field:

$$\langle \Psi_T | e^{-\Theta H} | \Psi_T \rangle = \sum_{\mathbf{S}} \det[P^\dagger B_{\mathbf{S}} P]. \tag{4.39}$$

This problem can, in principle, be simulated with classical Metropolis algorithm.[255] Unfortunately, simulations of fermion systems are unavoidably[256] plagued by the so-called minus sign problem[257–259] caused by the anti-commuting nature of the fermion fields. Here the minus sign problem shows up in Eq. (4.39), since the determinant is not necessarily positive definite.

4.3.5 Constrained Path Quantum Monte Carlo

In the Constrained Path Quantum Monte Carlo method,[157, 260–264] the ground state wave function $|\Psi_0\rangle$ is projected from a known trial function $|\Psi_T\rangle$ using a branching random walk that generates an over-complete space of Slater determinants $|\phi\rangle$:

$$|\Psi_0\rangle = \sum_{\phi} c_\phi |\phi\rangle, \tag{4.40}$$

where $c_\phi > 0$. To completely specify $|\Psi_0\rangle$, only determinants satisfying $\langle \Psi_T | \phi \rangle > 0$ are needed, because $|\Psi_0\rangle$ resides in either of two degenerate halves of the Slater determinant space separated by a nodal plane. In this manner, the minus-sign problem is alleviated. Extensive testing has demonstrated a significant insensitivity of the results to reasonable choices of $|\Psi_T\rangle$.[260,261,265] In the context of quantum dots, this method has been applied to the single-impurity Anderson model[246] and to the chain of three Anderson impurities[157] (Section 8.1).

Chapter 5

Quantum transport theory

Mesoscopic effects occur when the coherence length of electrons exceeds the size of the device through which the electric current flows; electrons then travel coherently through the system and behave in a wave-like manner so that quantum mechanical interference effects can occur. As the electrons scatter only off the boundaries (walls) of the device, rather than on the defects or phonons, we say that the transport is ballistic. The conductance through nanoscopic constrictions is often found to be quantized in units of the *conductance quantum*

$$G_0 = \frac{2e^2}{h} = \frac{e^2}{\pi\hbar} \approx [12.9\,\mathrm{k}\Omega]^{-1}. \tag{5.1}$$

This is the conductance of a single-mode conduction channel taking into account both spin orientations.[266,267] In lateral quantum dots, for example, the tunnel barriers from the two-dimensional electron gas to the quantum dot are obtained by successively pinching off the propagating channels using the gate electrodes. When the last channel is nearly pinched off, the Coulomb blockade regime develops. In this regime, only one channel in each lead is coupled to the dot.[69,70] Similar situation naturally occurs in the scanning tunneling microscopy when the tip is controllably brought into atomic contact with the surface or an adsorbate;[268,269] the number of channels is then related to the chemical valence of the contact atoms.

It is interesting to note in passing that thermal conductance also becomes quantized when the thermal wavelength $\lambda_{\mathrm{th}} = 2\pi\hbar c/(k_B T)$ exceeds the size of the device; in ballistic one-dimensional channel the thermal conductance approaches $\pi^2 k_B^2 T/3h$ per phonon mode.[270,271]

We focus on systems where a very small (essentially zero dimensional) scatterer is embedded between two metallic contacts, i.e. on systems that can be described by quantum impurity models. The two types of systems mentioned above are particularly relevant: quantum dots and adsorbed atoms (or molecules) on surfaces of metals, Fig. 5.1, a1 and b1. Both systems can be modeled using discrete lattice models as an impurity in contact with two semi-infinite tight-binding chains. The main difference is that typically a quantum dot is

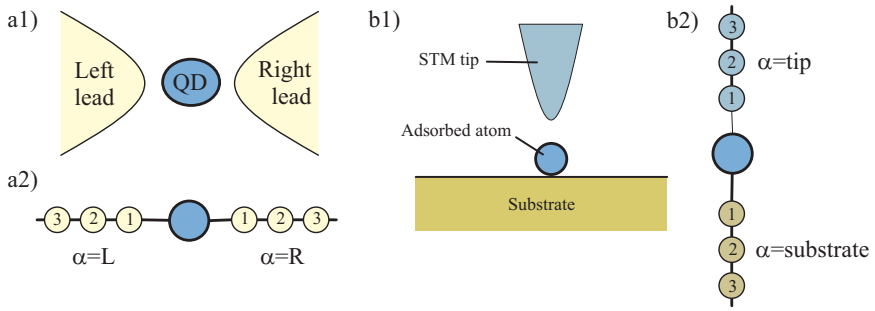

Figure 5.1: **a1**) Typical conductance measurement setup for probing transport properties of quantum dots. **b1**) STM measurement of the tunneling current through an adsorbed impurity atom. **a2**, **b2**) Tight-binding model representations of both systems.

coupled to the conduction leads with comparable strengths, while adatom electron levels are strongly hybridized with the substrate conduction bands and only weakly to the STM tip unless the STM tip is brought from the tunneling regime to the atomic contact regime with individual adatoms.[269]

It was observed that the temperature, source-drain bias, and magnetic field dependences of the conductance through a magnetic impurity are qualitatively (but not necessarily quantitatively) similar to each other.[75] Finite-temperature and finite-bias conductance can therefore be inferred from the magnetic field dependence of the $T = 0$ zero-bias (i.e. linear) conductances which is easily calculated using several different approaches.

In this chapter I describe calculation of conductance by extracting quasiparticle scattering phase shifts from Fermi liquid fixed point NRG eigenvalue spectra (Sec. 5.1), by subtracting total energies for periodic and anti-periodic boundary conditions of an auxiliary ring into which the interacting region is embedded (Sec. 5.2) or using impurity spectral functions in conjunction with Meir-Wingreen formula (Sec. 5.3). All three methods are used later on in this dissertation.

5.1 Conductance from phase shifts

The low-temperature fixed point of the majority of quantum impurity models that are relevant to describe transport through nanostructures is Fermi liquid; in fact, observing non-Fermi liquid behavior is exceedingly difficult and is a subject of significant experimental efforts.[272] Fermi liquid systems are particularly simple, since they are essentially non-interacting free fermion systems with twisted boundary conditions which determine scattering phase shifts. At zero temperature, the transport properties of a scatterer can be related to the phase shifts of electrons at the Fermi surface; the conductance is then computed using the Landauer-Büttiker formula. The advantage of this approach is that the quasiparticle scattering phase shifts can be extracted directly from the Fermi-liquid fixed

point NRG eigenvalue spectra .[54,69,75,79,98,189,190,194,273,274] For a single-channel problem, the conductance is fully determined by two phase shifts, $\delta_{\rm qp}^{\uparrow}$ and $\delta_{\rm qp}^{\downarrow}$, which are equal in the absence of the magnetic field. Two-channel problems can be characterized by four phase shifts, $\delta_{\rm qp}^{{\rm even},\uparrow}$, $\delta_{\rm qp}^{{\rm even},\downarrow}$, $\delta_{\rm qp}^{{\rm odd},\uparrow}$ and $\delta_{\rm qp}^{{\rm odd},\downarrow}$. These phase shifts encode all information about the physics at zero temperature.[94] This approach is also useful at finite temperatures as long as the system is near the Fermi liquid fixed point, i.e. for $T \ll T_K$ in the case of Kondo systems.

In the Landauer formulation, the conductance of a mesoscopic system is determined by the scattering properties of the impurity region.[69,266,275–277] The scattering of electrons near the Fermi level is described by the scattering matrix S. Its elements are the amplitudes of scattering $S_{\alpha\alpha'}^{\mu}$ of electrons with spin μ from lead $\alpha \in \{L, R\}$ to lead α':

$$S^{\mu} = \begin{pmatrix} S_{LL}^{\mu} & S_{RL}^{\mu} \\ S_{LR}^{\mu} & S_{RR}^{\mu} \end{pmatrix} = \begin{pmatrix} r_{L}^{\mu} & t_{R}^{\mu} \\ t_{L}^{\mu} & r_{R}^{\mu} \end{pmatrix}, \tag{5.2}$$

where we have introduced alternative notation in terms of the reflection and transmission matrices r and t. The scattering matrix can be diagonalized by rotation in the $R-L$ space to the new basis of channels a and b[69]

$$US^{\mu}U^{\dagger} = \begin{pmatrix} e^{2i\delta_{\rm qp}^{a\mu}} & 0 \\ 0 & e^{2i\delta_{\rm qp}^{b\mu}} \end{pmatrix}. \tag{5.3}$$

The unitary transformation is $U = \exp(i\theta\tau^{y})\exp(i\phi\tau^{z})$, where τ^{i} are the Pauli matrices in the $R-L$ space. Angle θ mixes left and right conduction channel:

$$\exp(i\theta\tau^{y}) = \begin{pmatrix} \cos\theta & \sin\theta \\ -\sin\theta & \cos\theta \end{pmatrix}, \tag{5.4}$$

while ϕ changes the phase (it is zero for problems where wavefunction can be made real). Note also that the phase shifts are defined only modulo π, so that $\delta_{\rm qp}$ and $\delta_{\rm qp}+\pi$ are equivalent. According to Landauer formula , the zero-temperature conductance is determined by the transmission probability $t_{R}^{\mu} = S_{RL}^{\mu}$:[266,276]

$$G(T=0) = G_0 \tfrac{1}{2} \sum_{\mu} |S_{RL}^{\mu}|^2. \tag{5.5}$$

In terms of the scattering phase shifts this equals[69]

$$G = G_0 \sin^2(2\theta) \tfrac{1}{2} \sum_{\mu} \sin^2(\delta_{\rm qp}^{a\mu} - \delta_{\rm qp}^{b\mu}). \tag{5.6}$$

The expression does not depend on ϕ, while θ sets the maximal conductance: the unitary limit can be achieved only when $\theta = \pm\pi/2$, which corresponds to a symmetric (or antisymmetric) problem with respect to reflection symmetry.

In the case of particle-hole symmetry, we have $S^{\mu}S^{-\mu} = 1$ for the scattering matrix, so that $\delta_{\rm qp}^{\gamma\uparrow} + \delta_{\rm qp}^{\gamma\downarrow} = 0$, where $\gamma \in \{a, b\}$.[11] Even in the presence of the magnetic field we may then write, for example,

$$G = G_0 \sin^2(2\theta) \sin^2(\delta_{\rm qp}^{a\uparrow} - \delta_{\rm qp}^{b\uparrow}), \tag{5.7}$$

or an equivalent expression in terms of $\delta_{\rm qp}^{\gamma\downarrow}$.

In the case of reflection symmetry (parity), a and b are even and odd channels. It should be stressed that here the names 'even' and 'odd' refer to the combinations of states in the conduction leads. Since in this case we also have $\theta = \pm\pi/2$, we finally obtain

$$G = G_0 \tfrac{1}{2} \sum_{\mu} \sin^2(\delta_{\rm qp}^{{\rm even},\mu} - \delta_{\rm qp}^{{\rm odd},\mu}). \tag{5.8}$$

This is the expression for conductance that will be used in this work.

The required phase shifts are calculated from excitation energies. The approximate form of the single-particle levels in a Fermi liquid for odd NRG iteration N are given by[54]

$$\begin{aligned} \eta_{l+1}^{+} &\approx \Lambda^{l-\delta_{\rm qp}/\pi}, \quad \text{electrons}, \\ \eta_{l+1}^{-} &\approx \Lambda^{l+\delta_{\rm qp}/\pi}, \quad \text{holes}. \end{aligned} \tag{5.9}$$

An attractive potential (positive phase shift) decreases electron excitation energies and increases hole excitation energies; the opposite holds for repulsive potential.[28,79] These expressions hold to high accuracy for all l, except for the lowest $l = 0$ level. Exact $\eta_{l+1}^{\pm}$ can be calculated numerically by diagonalizing the logarithmically discretized band Hamiltonian in the single-particle basis; due to exponentially differing energy scales, such calculations are best performed using arbitrary-precision arithmetics using computer algebra software such as Mathematica. Results from such a calculation are presented in Fig. 5.2a, while in Fig. 5.2b we show the full Fermi liquid excitation spectrum as a function of $\delta_{\rm qp}$.

It may be noted that for $|\delta_{\rm qp}| \ll \pi/2$, the lowest electron and hole excitation energies are linear in $\delta_{\rm qp}$:[79]

$$\eta_1^{\pm}(\delta_{\rm qp}) \approx 2\eta_1(0) \left(\frac{1}{2} \mp \frac{\delta_{\rm qp}}{\pi} \right). \tag{5.10}$$

This result is equivalent to continuum free-electron theory prediction for twisted boundary condition with $\delta_{\rm qp}$ phase shift. This is another manifestation of that fact that even for fairly large Λ, the lowest excitation levels calculated by NRG can be compared to field-theoretical predictions.

To determine $\delta_{\rm qp}^{\gamma\mu}$, we need to extract the single-particle energies from the full many-particle spectrum. The best approach is to make use of the known quantum numbers of the NRG eigenvalues. Let us consider a general two-channel problem with reflection symmetry in the presence of magnetic field, i.e. the (Q, S_z, P) basis is used. Let Q', S_z' and P' denote the quantum numbers of the ground state. Then the single-electron excitations necessarily

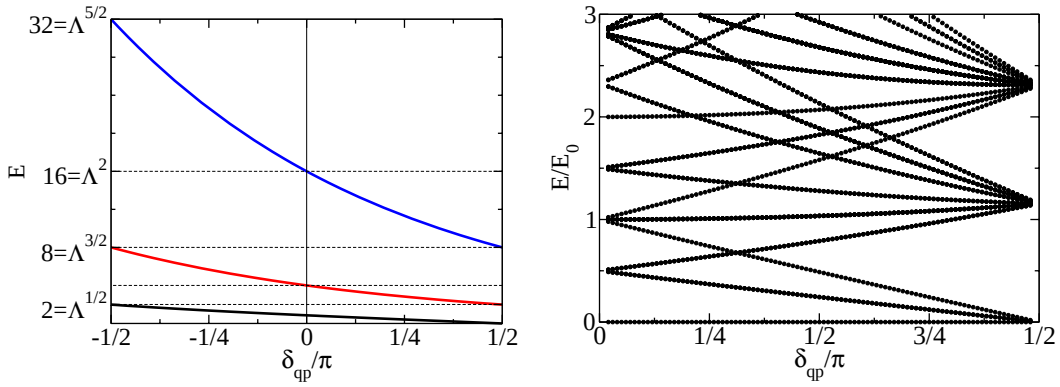

(a) Single-electron levels

(b) Many-particle levels

Figure 5.2: **(a)** Single-electron energy levels and **(b)** the energy spectrum of the Fermi-liquid many-particle excitations built from non-interacting particles and holes as a function of the scattering phase shift $\delta_{\rm qp}$ in the case of a single channel and in the absence of the magnetic field, i.e. $\delta_{\rm qp}^{\uparrow} = \delta_{\rm qp}^{\downarrow}$. Discretization parameter is $\Lambda = 4$.

carry quantum numbers $Q'+1$, $S'_z \pm 1/2$ and $\pm P$. More specifically:

$$\begin{aligned} E(Q'+1, S'_z+1/2, P') &\longrightarrow \eta_1^{+\uparrow,\text{even}}, \\ E(Q'+1, S'_z-1/2, P') &\longrightarrow \eta_l^{+\downarrow,\text{even}}, \\ E(Q'+1, S'_z+1/2, -P') &\longrightarrow \eta_l^{+\uparrow,\text{odd}}, \\ E(Q'+1, S'_z-1/2, -P') &\longrightarrow \eta_1^{+\downarrow,\text{odd}}. \end{aligned} \tag{5.11}$$

The phase shifts are then extracted from known $\eta_1^{+\mu\gamma}(\delta_{\rm qp}^{\mu\gamma})$ dependence or from the hopping Hamiltonian Green's function.[189,190] As a check, $\eta_1^{-\mu\gamma}$ could be calculated from $E(Q'-1, S'_z \pm 1/2, \pm P')$, or even the low-lying part of the many-particle eigenvalue spectrum could be reconstructed to verify that the system is fully renormalized to the Fermi liquid fixed point.

This approach can be generalized to other symmetry types, taking $Q'+1, S'+1/2, \pm P'$ to obtain $\delta_{\rm qp}^{\text{even}\uparrow} = \delta_{\rm qp}^{\text{even}\downarrow}$ and $\delta_{\rm qp}^{\text{odd}\uparrow} = \delta_{\rm qp}^{\text{odd}\downarrow}$ in the case of $\mathrm{U}(1)_{\rm charge} \times \mathrm{SU}(2)_{\rm spin} \times \mathrm{Z}_2$ symmetry, or taking $I'+1/2, S'+1/2, \pm P'$ in the case of $\mathrm{SU}(2)_{\rm iso} \times \mathrm{SU}(2)_{\rm spin} \times \mathrm{Z}_2$, and so forth.

When the parity quantum number P is not tracked, it is not always possible to unambiguously assign the $\gamma \in \{\text{even}, \text{odd}\}$ label to the extracted phase shifts. Nevertheless, Eq. (5.8) is symmetric with respect to the interchange of the labels γ, therefore the conductance can still be determined.[75]

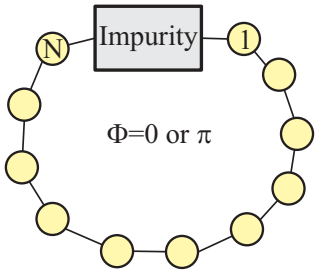

Figure 5.3: Auxiliary ring system with embedded impurity region. The ring is pierced by a flux $\Phi = 0$ of $\Phi = \pi$, which is equivalent to having periodic or anti-periodic boundary conditions along the ring.

5.2 Sine formula

When the ground state of the quantum impurity model is Fermi liquid, the $T = 0$ conductance is given by the "sine formula":[245,247,278]

$$G = G_0 \sin^2 \left[\frac{\pi}{2} N\rho(\epsilon_F)(E_0 - E_\pi) \right]. \tag{5.12}$$

Here $E_{0,\pi}$ are the ground state energies of a large N-site auxiliary ring into which the interacting system is embedded, with periodic and anti-periodic boundary conditions, respectively (Fig. 5.3). The condition of validity is[245]

$$N \gg \frac{1}{\rho(\epsilon)} \left| \frac{\partial t(\epsilon)}{\partial \epsilon} \right|, \tag{5.13}$$

where $\rho(\epsilon)$ is the density of states in the leads and $t(\epsilon)$ is the energy dependent transmission function. The method becomes exact in the thermodynamic $N \to \infty$ limit, while in finite rings the errors scales approximately as N^{-1}.[245]

The sine formula can be proved rigorously for a non-interacting system by relating the conductance to persistent currents in the auxiliary ring.[245] The reason this approach also works for interacting systems with Fermi liquid zero-temperature fixed point is, basically, that the fixed-point effective Hamiltonian is non-interacting, therefore the same proof goes through unchanged for the quasiparticle Hamiltonian. The method does not seem to be suitable for singular Fermi liquid systems , such as the problem of two parallel quantum dots (Section 7.2), when the ground state energies are calculated using the variational method (Section 4.2).[279] Since at $T = 0$ this problem is equivalent to a Fermi liquid system and an entirely decoupled spin-1/2 degree of freedom, in principle the presence of the residual spin should not affect the energy difference in any way and the conductance formula should apply. It seems likely that the problem is either the use of the variational method for a problem with degenerate ground state or the very slow (logarithmic) approach to the $T = 0$ fixed point;[98] in either case, the problem seems to be computational in nature and not a weakness of the formalism per se. Finally, it should be remarked that

charge transfer between the conduction bands destabilizes known non-Fermi liquid fixed points, [93,158] therefore all systems with finite conductance from left to right conduction lead are necessarily Fermi liquids. This implies that the sine formula holds for any two-lead system in which conductance calculations makes any sense at all, i.e. it is fairly general. Unfortunately, in a system with very small energy scales or very slow approach to the FL fixed point, calculations of energy are impracticable since an exceedingly large auxiliary ring system is required. The calculation of the quasiparticle phase shifts using NRG is the method of choice in such cases.

5.3 Meir-Wingreen formula

Meir and Wingreen considered the problem of transport through an interacting region embedded between two conduction leads in full generality.[280] The system is described by the generic Hamiltonian:

$$H = \sum_{k,\alpha\in L,R} c^\dagger_{k\alpha} c_{k\alpha} + H_{\rm int}(\{d^\dagger_n\},\{d_n\}) + \sum_{n,k,\alpha\in L,R} \left(V_{k\alpha,n} c^\dagger_{k\alpha} d_n + \text{h.c.} \right). \tag{5.14}$$

Operator $c^\dagger_{k\alpha}$ creates an electron with momentum k in *channel* α in either the left (L) or the right lead (R), while operators $d^\dagger_n$ form a complete orthonormal set of creation operators in the interacting region. Here α and n are multi-indexes which include all quantum numbers that are necessary to uniquely specify the state (in addition to momentum k for lead electrons). In other words, α may include spin and orbital quantum numbers, as well as a lateral mode quantum number indicating the quantization level of the state in the lateral confinement potential of the lead or of the contact area. Index n typically includes site index and spin. Using Keldysh formalism,[281] the expression for current is derived to be[280]

$$I = \frac{ie}{2h} \int d\epsilon \left(\text{Tr}\left\{ \left[f_L(\epsilon)\mathbf{\Gamma}^L - f_R(\epsilon)\mathbf{\Gamma}^R \right] (\mathbf{G}^r - \mathbf{G}^a) \right\} + \text{Tr}\left\{ \left(\mathbf{\Gamma}^L - \mathbf{\Gamma}^R \right) \mathbf{G}^< \right\} \right), \tag{5.15}$$

with

$$\Gamma^L_{n,m} = 2\pi \sum_{\alpha\in L} \rho_\alpha(\epsilon) V^{\alpha,n}(\epsilon) \left[V^{\alpha,m}(\epsilon) \right]^* . \tag{5.16}$$

$\mathbf{G}^r$, $\mathbf{G}^a$ and $\mathbf{G}^<$ are retarded, advanced and lesser Green's function matrices, respectively (see Ref. 281 and Appendix B), $\rho_\alpha(\epsilon)$ is the density of states in channel α and $V_{\alpha,n}(\epsilon)$ equals $V_{k\alpha,n}$ for $\epsilon = \epsilon_{k\alpha}$. Fermi-Dirac distribution functions are given by $f_L(\epsilon) = [1 + \exp((\epsilon - \mu_L)/k_BT)]^{-1}$ and an analogous expression for f_R; the source-drain bias voltage V is defined as $\mu_L - \mu_R = eV$. In equilibrium $f_L(\epsilon) = f_R(\epsilon) = f_{\rm eq}(\epsilon)$ and, furthermore, $\mathbf{G}^< = -f_{\rm eq}(\mathbf{G}^r - \mathbf{G}^a)$, therefore the current vanishes.

Usually the tunnel coupling is spin-conserving and the hopping elements $V^{\alpha,m}$ are diagonal in spin indexes. Then n and m indexes of $\mathbf{\Gamma}$ matrices must be of the same spin and the

coupling matrices $\mathbf{\Gamma}$ have block-diagonal structure with respect to spin:

$$\mathbf{\Gamma} = \begin{bmatrix} \mathbf{\Gamma}_{\uparrow\uparrow} & 0 \\ 0 & \mathbf{\Gamma}_{\downarrow\downarrow} \end{bmatrix} \tag{5.17}$$

with $\mathbf{\Gamma}_{\uparrow\downarrow} = \mathbf{\Gamma}_{\downarrow\uparrow} \equiv 0$. In Meir-Wingreen formulas the $\mathbf{\Gamma}$ matrix always left-multiplies a Green function matrix and a trace is performed. We find

$$\mathrm{Tr}\left\{ \begin{bmatrix} \mathbf{\Gamma}_{\uparrow\uparrow} & 0 \\ 0 & \mathbf{\Gamma}_{\downarrow\downarrow} \end{bmatrix} \begin{bmatrix} \mathbf{G}_{\uparrow\uparrow} & \mathbf{G}_{\uparrow\downarrow} \\ \mathbf{G}_{\downarrow\uparrow} & \mathbf{G}_{\downarrow\downarrow} \end{bmatrix} \right\} = \mathrm{Tr} \begin{bmatrix} \mathbf{\Gamma}_{\uparrow\uparrow}\mathbf{G}_{\uparrow\uparrow} & \mathbf{\Gamma}_{\uparrow\uparrow}\mathbf{G}_{\uparrow\downarrow} \\ \mathbf{\Gamma}_{\downarrow\downarrow}\mathbf{G}_{\downarrow\uparrow} & \mathbf{\Gamma}_{\downarrow\downarrow}\mathbf{G}_{\downarrow\downarrow} \end{bmatrix} = \mathrm{Tr}\left(\mathbf{\Gamma}_{\uparrow\uparrow}\mathbf{G}_{\uparrow\uparrow}\right) + \mathrm{Tr}\left(\mathbf{\Gamma}_{\downarrow\downarrow}\mathbf{G}_{\downarrow\downarrow}\right). \tag{5.18}$$

The important conclusion one can draw from this calculation is that in the case of spin-conserving tunneling, we only need consider the Green's functions that are diagonal in their spin index. If the problem is, in addition, spin-isotropic, it suffices to consider a single spin projection and then multiply the final result by 2.

For the purposes of this work, I consider the specialization to single-mode channels with spin degree of freedom (no orbital degeneracy) and spin-conserving tunnel coupling described by the general Hamiltonian

$$H = \sum_{k,\alpha=\{L,R\},\mu} \epsilon_{k\mu} c^\dagger_{k\alpha\mu} c_{k\alpha\mu} + H_{\mathrm{int}}(\{d^\dagger_{n\mu}\},\{d_{n\mu}\}) + \sum_{n,k,\alpha=\{L,R\},\mu} \left(V^{\alpha\mu}_{k,n} c^\dagger_{k\alpha\mu} d_{n\mu} + \mathrm{h.c.} \right). \tag{5.19}$$

Now the channel index α takes only two values, L and R, and n indexes sites in the interacting region; spin μ has been factored out and it now appears explicitly in the expressions. The Meir-Wingreen formula for current is rewritten as

$$I = \frac{ie}{2h} \int d\epsilon \sum_\mu \left(\mathrm{Tr}\left\{ \left[f_L(\epsilon)\mathbf{\Gamma}^{L\mu} - f_R(\epsilon)\mathbf{\Gamma}^{R\mu} \right] \left(\mathbf{G}^{r\mu} - \mathbf{G}^{a\mu} \right) \right\} + \mathrm{Tr}\left\{ \left(\mathbf{\Gamma}^{L\mu} - \mathbf{\Gamma}^{R\mu} \right) \mathbf{G}^{<\mu} \right\} \right), \tag{5.20}$$

with

$$\Gamma^{L\mu}_{n,m} = 2\pi\rho_L(\epsilon) V^{L\mu,n}(\epsilon) \left[V^{L\mu,m}(\epsilon) \right]^*. \tag{5.21}$$

It should be appreciated that Meir-Wingreen approach applies under very general conditions (for example, the system need not be in a Fermi-liquid ground state).

5.3.1 Proportionate coupling

We now consider the case of proportionate coupling where the couplings to the leads differ only by a constant factor, so that $\mathbf{\Gamma}^L(\epsilon) = \lambda \mathbf{\Gamma}^R(\epsilon)$ for all energies. The lesser Green's function $\mathbf{G}^<$ then cancels from a symmetrized expression for current which takes a simpler form:

$$I = -\frac{2e}{h} \int \mathrm{d}\epsilon \left[f_L(\epsilon) - f_R(\epsilon) \right] \sum_\mu \mathrm{Im}\,\mathrm{Tr}\left[\mathbf{\Gamma}^\mu \mathbf{G}^{r\mu} \right], \tag{5.22}$$

where

$$\mathbf{\Gamma}^{\mu} \equiv \mathbf{\Gamma}^{L\mu}\mathbf{\Gamma}^{R\mu}/(\mathbf{\Gamma}^{L\mu} + \mathbf{\Gamma}^{R\mu}) = \mathbf{\Gamma}^{L\mu}\frac{\lambda}{1+\lambda}. \tag{5.23}$$

Note that in the symmetric case $\mathbf{\Gamma}^L = \mathbf{\Gamma}^R$, i.e. $\lambda = 1$, we have $\mathbf{\Gamma} = \mathbf{\Gamma}^L/2$.

The zero-bias differential conductance $G(T) = (dI/dV)_{V=0}$ is given by

$$G(T) = -G_0 \int \mathrm{d}\epsilon \frac{1}{2T(1+\cosh(\epsilon/k_BT))} \sum_{\mu} \mathrm{Im}\,\mathrm{Tr}\left[\mathbf{\Gamma}^{\mu}\mathbf{G}^{r\mu}(\epsilon)\right]. \tag{5.24}$$

Taking the zero-temperature limit and noting that

$$\lim_{T\to 0} \frac{1}{2T(1+\cosh(\epsilon/k_BT))} = \delta(\epsilon), \tag{5.25}$$

we obtain (for real $\mathbf{\Gamma}$)

$$G(T=0) = -G_0 \sum_{\mu} \mathrm{Tr}\left[\mathbf{\Gamma}^{\mu}\mathrm{Im}\,\mathbf{G}^{r\mu}(\epsilon=0)\right]. \tag{5.26}$$

Application: single-impurity Anderson model

If a single dot is coupled to the leads, the matrix $\mathbf{\Gamma}^{\mu}$ reduces to a scalar quantity Γ_{μ} and the current is determined by the spectral function $A_{\mu} = -\frac{1}{\pi}\mathrm{Im}\,\mathbf{G}^{r\mu}$ of the dot at $\epsilon = 0$:

$$G = G_0\pi\left[\Gamma_{\uparrow}A_{\uparrow}(\epsilon=0) + \Gamma_{\downarrow}A_{\downarrow}(\epsilon=0)\right]. \tag{5.27}$$

For spin-isotropic problems (i.e. in the absence of the magnetic field), $\Gamma_{\uparrow} = \Gamma_{\downarrow} \equiv \Gamma$ and $A_{\uparrow} = A_{\downarrow}$. Defining the spectral function as $A = A_{\uparrow} + A_{\downarrow}$, we obtain

$$G = G_0\pi\Gamma A(\epsilon=0). \tag{5.28}$$

For a Fermi-liquid system $A(\epsilon=0) = \sin^2\delta_{\mathrm{qp}}/(\pi\Gamma)$, and we recover the expected result $G = G_0\sin^2\delta_{\mathrm{qp}}$.

In Fig. 5.4 I compare conductance calculated from the spectral function to that obtained using the phase shift method from Section 5.1. While the results agree qualitatively, there are nevertheless noticeable quantitative discrepancies due to systematic errors in NRG calculations of spectral functions; in particular, the conductance does not reach unitary limit as it should. Phase shift method is therefore more accurate if $T = 0$ results are sought. On the other hand, spectral functions provide additional information about the behavior of the system at finite frequencies from which one can also infer behavior at finite temperatures.

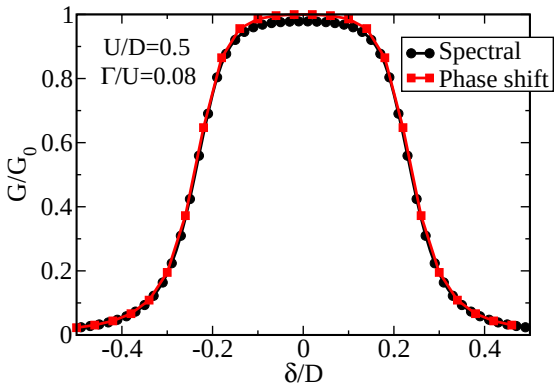

Figure 5.4: Conductance through a quantum dot described by the single impurity Anderson model as a function of the gate voltage δ. NRG discretization parameter is $\Lambda = 4$ and averaging over 8 values of the sliding parameter z was used for the spectral function method. The extracted phase shifts overlap for different values of z.

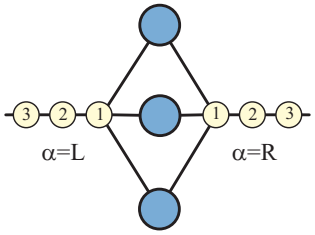

Figure 5.5: Three parallel quantum dots.

Application: parallel quantum dots

If several quantum dots (say $N = 3$) are coupled in parallel between two conduction leads, Fig. 5.5, and there is no magnetic field, the components of the hybridization matrix are

$$\Gamma_{n,m} = \pi\rho(\epsilon)V_n(\epsilon)V_m^*(\epsilon), \tag{5.29}$$

where V_n is the hopping amplitude from the impurity orbital $n = 1, \ldots, N$ to the conduction band. In a simplified model we assume a constant density of states ρ_0 and an energy-independent hybridization strength $\Gamma = \pi\rho_0|V|^2$ which is the same for both orbitals. All components of the hybridization matrix are then the same: $\Gamma_{n,m} = \Gamma$. Equation (5.26) simplifies to

$$G = -G_0\pi\Gamma\sum_{nm}\mathrm{Im}\left(-\frac{1}{\pi}G^r_{nm}\right). \tag{5.30}$$

The quantity in the parenthesis is related to the spectral matrix for all orbitals, $A_{nm} = -1/(2\pi)\mathrm{Im}(G^r_{nm}+G^r_{mn})$. We are particularly interested in the symmetrized and normalized spectral density function $g(\epsilon)$ defined by

$$g(\epsilon) = \pi\Gamma\sum_{nm}A_{nm}(\epsilon) \tag{5.31}$$

where $n, m = 1, \ldots, N$. This quantity appears in the final expression for the $T = 0$ conductance:

$$G = G_0 g(\epsilon = 0). \tag{5.32}$$

In a simple approximation, the temperature dependence of the conductance through the quantum dots can be deduced from the energy dependence of the function $g(\epsilon)$.

5.3.2 Strongly asymmetric coupling

In the case where an atom is chemisorbed on a surface and it is being probed by the STM tip in the tunneling regime, the hybridization of the atom is much stronger to the substrate than to the tip. Let index $\alpha = L$ stand for the substrate, and $\alpha = R$ for the tip. Assuming that the voltage drop occurs between the adatom and the STM tip (i.e. in the tunneling junction), and that the current is not too high, the atom must be in thermodynamic equilibrium with the substrate and we may assume $\mathbf{G}^< = -f_L(\mathbf{G}^r - \mathbf{G}^a)$. The expression for current then simplifies to

$$\begin{aligned} I &= \frac{ie}{2h} \sum_\mu \int \mathrm{d}\epsilon \, (f_L(\epsilon) - f_R(\epsilon)) \, \mathrm{Tr}[\mathbf{\Gamma}^{R\mu}(\mathbf{G}^{r\mu} - \mathbf{G}^{a\mu})], \\ &= \frac{e}{h} \sum_\mu \int \mathrm{d}\epsilon \, (f_L(\epsilon) - f_R(\epsilon)) \, \mathrm{Tr}[\mathbf{\Gamma}^{R\mu} \mathrm{Im}\, \mathbf{G}^{r\mu}]. \end{aligned} \tag{5.33}$$

Like in the case of proportionate coupling, only the spectral function is needed. It can be computed for an effective equilibrium problem in which the STM tip is absent. The current may then be computed even at finite bias voltage, since we assumed that the tip does not probe the atom intrusively. Of course, the physical content of Eq. (5.33) is fully equivalent to the Tersoff-Hamman approach which relates the tunneling current to the local density of states.[282] This is the approach I will use in later chapters to study the scanning tunneling spectroscopy of magnetic impurities on surfaces of noble metals.

Part II

Systems of coupled quantum dots

Chapter 6

Properties of single impurity models

Familiarity with the properties of simple single-impurity models is a necessary background for understanding more complex models discussed in the following chapters. I thus present the results of NRG calculations for the Kondo model (Sec. 6.1), the two-channel Kondo model (Sec. 6.2), and the Anderson model (Sec. 6.3). In fact, these results alone demonstrate most of the unusual behavior of QIMs; multi-impurity models differ mostly in that Kondo screening may compete in a non-trivial way with other effects, in particular with magnetic ordering.

6.1 Single-channel Kondo model

The single-channel $S = 1/2$ Kondo model was already introduced in Sec. 2.2 on the Kondo effect. Its Hamiltonian is

$$H = \sum_{k\mu} \epsilon_k c^\dagger_{k\mu} c_{k\mu} + J\mathbf{s}\cdot\mathbf{S}. \tag{6.1}$$

Henceforth we assume a constant density of states $\rho = 1/(2D)$ in the conduction band (unless explicitly stated otherwise), where D is the half-bandwidth. The thermodynamic properties for a range of values of the Kondo exchange constant J are shown in Fig. 6.1.

In Fig. 6.1a we observe the Kondo screening of the impurity spin degree of freedom from the local moment value of 1/4 to the strong coupling value of 0. At the same time, the dissolution of the impurity degree of freedom into the conduction band can be observed as the decrease of entropy from $\ln 2$ to 0, Fig. 6.1b. Note also that the decrease of the entropy occurs in a much narrower temperature range than the reduction of the susceptibility. Finally, the Kondo effect is associated with a peak in the impurity contribution to the heat capacity, Fig. 6.1c; this peak is yet another manifestation of the disappearance (freezing-out) of a degree of freedom in the system. (Since the specific heat is simply the temperature derivative of the entropy, it contains the same physical information.) The specific heat

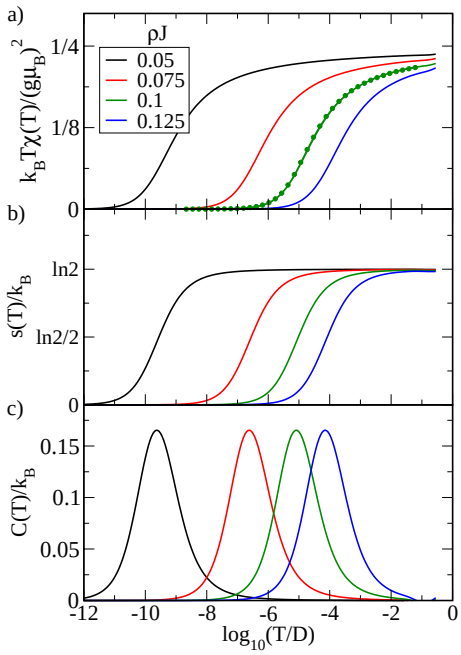

Figure 6.1: Impurity contribution to a) magnetic susceptibility, b) entropy and c) heat capacity. Parameters used are $\Lambda = 4$, $\bar{\beta} = 0.46$, energy cutoff $15\omega_N$, 8 values of slide parameter z. Symbols on the curve for $\rho J = 0.1$ correspond to the exact Bethe Ansatz results for $S = 1/2$ Kondo model magnetic susceptibility.

peak occurs somewhat below T_K.[215] The Kondo temperature itself can be accurately extracted by fitting the NRG results for the magnetic susceptibility with the universal Kondo magnetic susceptibility curves obtained using the exact Bethe Ansatz approach; for $\rho J = 0.1$ we thus determine $T_K/D = 1.07 \times 10^{-5}$, which agrees well with the estimate $T_K = D_{\text{eff}}\sqrt{\rho J}\exp(-1/\rho J) \approx 1.14 \times 10^{-5}$, where I took $D_{\text{eff}} = 0.85D$.[215]

These plots reproduce known results for the strong-coupling regime at $T \ll T_K$.[29,215] The specific heat is linear in temperature,

$$C_{\text{imp}}(T) = \frac{\pi^2 k_B}{6}\frac{w}{T_K}T, \tag{6.2}$$

and the magnetic susceptibility is constant,

$$\chi_{\text{imp}}(T) = (g\mu_B)^2\frac{w}{4k_B T_K}. \tag{6.3}$$

Here $w \approx 0.4128$ is the universal number for the Kondo model which is known as the Wilson number. Even for calculations with relatively large $\Lambda = 4$ that were used to produce Fig. 6.1, I obtain $w \sim 0.421$ from specific heat and $w \sim 0.429$ from magnetic susceptibility calculation, i.e. an error for 2% and 4%, respectively. Incidentally, this also

implies that the Wilson ratio

$$R_W = \frac{\chi/\chi_0}{\gamma/\gamma_0} = \frac{4\pi^2 k_B^2}{3(g\mu_B)^2}\frac{\chi}{\gamma} = 2 \tag{6.4}$$

to a good precision [here γ is the linear coefficient of the heat capacity, $\gamma = C/T$, while χ_0 and γ_0 are magnetic susceptibility and heat capacity coefficient of the conduction electrons in the absence of the impurity, see also Sec. 2.6].

Potential scattering in the Kondo model can be described using perturbation Hamiltonian

$$H' = \sum_{kk'\mu\mu'} K c^\dagger_{k\mu} c_{k'\mu'}. \tag{6.5}$$

This term only affects the charge sector, but not the spin sector, therefore the Kondo effect persists. In fact, the potential scattering operator is exactly marginal, therefore the strong-coupling fixed point is extended into a line of fixed points parameterized by the scattering phase shift δ_{qp} (for $K = 0$, $\delta_{\mathrm{qp}} = \pi/2$) and the universality is lost.

In general, T_K for the Kondo model is defined by

$$k_B T_K = D_{\mathrm{eff}} e^{-\Phi(\rho J)}, \tag{6.6}$$

where Φ is some universal function of ρJ and D_{eff} is an effective bandwidth.[29] The first terms in the expansion of Φ are

$$\Phi(y) = \frac{1}{y} - \frac{1}{2}\ln|y| + \mathcal{O}(y). \tag{6.7}$$

The first two terms are usually retained, which gives

$$k_B T_K = D_{\mathrm{eff}} \sqrt{\rho J} e^{-\frac{1}{\rho J}}. \tag{6.8}$$

The effective bandwidth is $\tilde{D} \sim 0.85D$.[215]

The Kondo resonance can be observed in the spectral function of the first site of the Wilson chain, i.e. of the Wannier orbital to which the impurity orbital couples via the exchange interaction, Fig. 6.2. It should be noticed that the presence of the impurity affects the conduction band spectral density even at energies above the scale of the Kondo temperature.

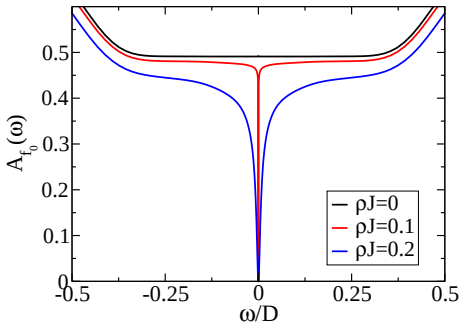

Figure 6.2: Spectral function of the first site of the Wilson chain for the Kondo model. The increase of the spectral function at high frequencies is due to the band-edge effects.

6.2 Two-channel Kondo model

The two-channel Kondo (2CK) model was introduced by Nozières and Blandin in their paper on the Kondo effect in real metals (Ref. 100) where they considered various extensions of the original $S = 1/2$ single-channel Kondo model. The 2CK model consists of a magnetic impurity with spin $S = 1/2$ coupled to two equivalent channels. It was the first QIM with a non-trivial NFL fixed point and it was studied by a variety of methods: NRG,[79,91,144] bosonization and refermionization,[108,109] Bethe-Ansatz[52,239,283,284] and CFT.[55,77,285] The 2CK model describes the quadrupolar Kondo effect in some cerium and uranium heavy-fermion materials.[286] Since a single QD embedded between two non-interacting leads couples only to the symmetric combination of the electrons from both leads,[46] such a system is governed by the single-channel Kondo model. To observe 2CK behavior, more elaborate setups with several QDs need to be used.[23,24,26,158] A related two-level system model was proposed to explain zero-bias anomalies seen in tunnel junctions and point contacts where two-level tunneling systems couple to the conduction electrons.[287–291]

An experimental realization of the 2CK model has been proposed in the form of a modified single electron transistor (SET) with a large side-coupled quantum dot playing the role of an additional "lead".[23] By finely tuning the gate voltages, an equal coupling of the leads to the $S = 1/2$ local moment on the SET can be achieved.[25,26] The two-channel Kondo effect in this system has been recently observed.[272]

The 2CK Hamiltonian is[100]

$$H = \sum_{k\alpha\mu} \epsilon_k c^\dagger_{k\alpha\mu} c_{k\alpha\mu} + \sum_\alpha J_\alpha \mathbf{s}_\alpha \cdot \mathbf{S}, \tag{6.9}$$

where $\alpha = 1, 2$ is the channel index and $\mathbf{s}_\alpha$ is the electron spin-density at the impurity site of channel α:

$$\mathbf{s}_\alpha = \sum_{\mu\nu} f^\dagger_{0\alpha\mu} \left(\tfrac{1}{2}\boldsymbol{\sigma}_{\mu\nu}\right) f_{0\alpha\nu}. \tag{6.10}$$

2CK system is said to be channel symmetric if $J_1 = J_2 \equiv J$. For channel asymmetric models

we define the average exchange constant $J_{\rm avg} = \frac{1}{2}(J_1+J_2)$ and parameter $\Delta = \rho(J_1-J_2)$; the asymmetry may be quantified by the asymmetry parameter $A = \Delta/(\rho J_{\rm avg})^2$ (see below).

The two channels are strongly coupled through the impurity spin operator; the spins of conduction electrons at the impurity site tend to be glued together to form a total spin $S = 1$.[100] For infinite coupling J, the impurity spin would therefore be over-screened. What happens instead is that the model scales into a strong-coupling fixed point with a finite value of the coupling constant, where the screening is perfect.[91, 100, 108] A fixed point with finite coupling leads to critical behavior and to power-law dependences in thermodynamic properties as H and T tend to zero (the critical point is $H = T = 0$). The ground state is not a singlet and the entropy at zero temperature is finite $S(T = 0) = \ln 2/2$,[77, 283, 284, 292] see Fig. 6.3.

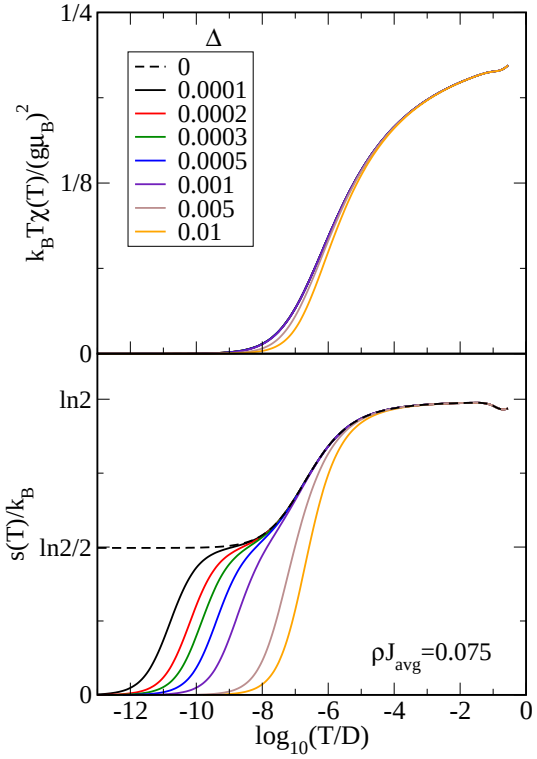

Figure 6.3: Impurity contribution to magnetic susceptibility and entropy in the two-channel Kondo model for different values of the parameter $\Delta = \rho(J_1 - J_2)$. NRG parameters are $\Lambda = 4$, $\bar{\beta} = 0.75$, cutoff $8\omega_N$ or at most 2000 states. $\mathrm{SU}(2)_{\rm spin} \times \mathrm{SU}(2)_{\rm iso}$ NRG code was used.

Perturbative scaling estimate of the Kondo temperature is[28]

$$T_K \sim D_{\rm eff}\rho J \exp\left(-\frac{1}{\rho J}\right). \tag{6.11}$$

Using NRG, it can be verified that this expression gives a correct description for small ρJ, Fig. 6.4. For large ρJ, the Kondo temperatures decreases exponentially with $1/\rho J$;

moreover, small J and large J regimes are related by a duality transformation up to higher-order logarithmic corrections.[293] The self-duality point occurs for $J^*/D \approx 0.7$, where the Kondo temperature is of the order of the bandwidth, $T_K^* \sim 0.5D$.[293]

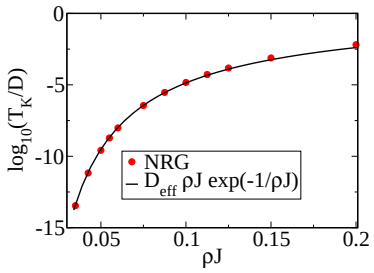

Figure 6.4: Dependence of T_K on the Kondo exchange constant J. I find $D_{\text{eff}} \approx 3D$.

Resistance (scattering rate) due to a 2CK impurity goes as $R(T)/R(0) \approx 1 - AT^{1/2}$,[28] which is to be compared with the familiar T^2 law for Fermi liquid systems. Such temperature dependence has been observed in point contact experiments.[28]

The NFL strong-coupling fixed point has $O(3) \times O(5)$ symmetry and its finite-size spectrum is $0, 1/8, 1/2, 5/8, 1, 1 + 1/8$.[79,111] Such non-integer succession of energies can be observed in the NRG eigenvalue spectra, Fig. 6.5. two-channel Kondo model

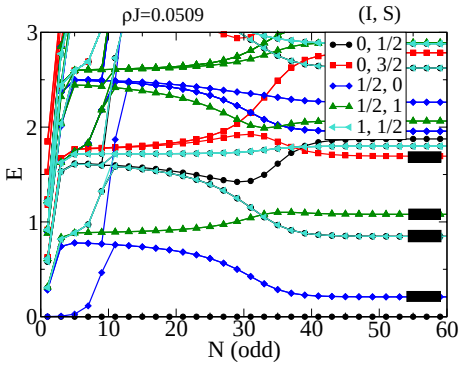

Figure 6.5: NRG eigenvalue flow of the 2CK model ($\Lambda = 4, z = 1/6$). The black strips correspond to the 2CK NFL fixed point spectrum $1/8, 1/2, 5/8, 1$ as predicted by the conformal field theory (after rescaling by 1.71781).

The model needs not be particle-hole symmetric to have a NFL fixed point. The potential scattering only affects the charge sector which remains noninteracting, while the Kondo physics occurs in the spin sector without affecting the charge sector.[81] The potential scattering is an exactly marginal operator, just like in the single-channel Kondo model; we thus obtain a line of stable NFL fixed points.[81] Interestingly, the zero-temperature scattering matrix is universal even in the presence of p-h symmetry breaking;[81] this implies that the zero-temperature resistivity is independent of the phase shift if the channel symmetry is maintained.

The NFL fixed point is unstable with respect to channel symmetry breaking. If $\Delta = \rho(J_0 - J_1)$ is not strictly zero, another cross-over occurs at some low temperature T_Δ[26]

$$T_\Delta \propto T_K \times \frac{\Delta^2}{(\rho J_{\rm avg})^4}, \tag{6.12}$$

and the system ends up in the stable Fermi-liquid fixed point of the conventional single-channel Kondo model. The criterion for observability of the NFL regime is clearly $T_\Delta \ll T_K$, or $A = \Delta/(\rho J_{\rm avg})^2 \ll 1$.

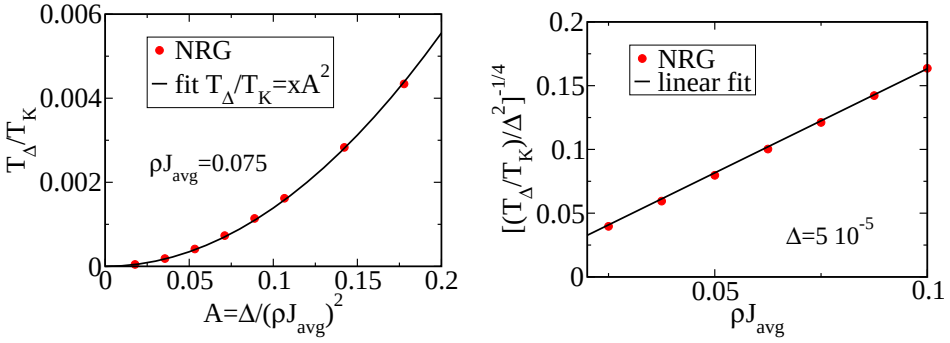

Figure 6.6: Dependence of T_Δ/T_K on the asymmetry parameter Δ (left plot) and the average exchange constant $\rho J_{\rm avg}$ (right plot). The expected dependence is $T_\Delta/T_K = xA^2$ with $A = \Delta/(\rho J_{\rm avg})^2$. I find consistently $x \approx 0.14$.

When magnetic field is applied, the system crosses over to a FL ground state. The NFL fixed point is, however, stable with respect to the exchange anisotropy.[79,91,108] The broken spin SU(2) symmetry of the original model is restored in the vicinity of the NFL fixed point.[108]

6.3 Anderson model

The single-impurity Anderson model (SIAM) was introduced by P. W. Anderson as a model of the formation of local moments in solids.[294] It consists of a single impurity orbital with electron-electrion (e-e) repulsion U, hybridized with a band of conduction electrons. The Hamiltonian is $H = H_{\rm band} + H_{\rm imp} + H_{\rm c}$, with

$$\begin{aligned} H_{\rm band} &= \sum_{k\mu} \epsilon_k c^\dagger_{k\mu} c_{k\mu}, \\ H_{\rm imp} &= \epsilon_d n + U n_\uparrow n_\downarrow, \\ H_{\rm c} &= \sum_{k\mu} V_k (c^\dagger_{k\mu} d_\mu + {\rm H.c.}), \end{aligned} \tag{6.13}$$

are the band Hamiltonian, the impurity Hamiltonian and the coupling Hamiltonian, respectively. The number operator n_μ is defined as $n_\mu = d_\mu^\dagger d_\mu$ and $n = n_\uparrow + n_\downarrow$, ϵ_d is the on-site energy and U is the on-site Coulomb electron-electron (e-e) repulsion. $H_{\rm imp}$ can be rewritten as

$$H_{\rm imp} = \delta(n-1) + \frac{U}{2}(n-1)^2. \tag{6.14}$$

The advantage of this form is that the isotropy in spin space and (for $\delta = 0$) in isospin space becomes manifest. I remark that for spin-1/2 operators (which are, essentially, Pauli matrices) $(I^z)^2 = 1/3\mathbf{I}^2$. Therefore e-e repulsion term $U/2(n-1)^2$, which is not manifestly isospin invariant, is indeed isospin symmetric since $U/2(n-1)^2 = 2U(I^z)^2 = 2/3U\mathbf{I}^2$. The relation between the parameter δ and the more conventional on-site energy ϵ_d is $\delta = \epsilon_d + U/2$. For $\delta = 0$ the model is particle-hole symmetric under the transformation $c_{k\mu}^\dagger \to c_{k,-\mu}$, $d_\mu^\dagger \to -d_{-\mu}$. Parameter δ thus represents the measure for the departure from the particle-hole symmetric point. Equivalently, gate voltage δ is the isospin-space analog of the magnetic field in spin space.

To cast the model into a form that is more convenient for a NRG study, we make two approximations. We assume a constant density of states, $\rho = 1/(2D)$. Second, we approximate the dot-band coupling with a constant hybridization strength, $\Gamma = \pi\rho|V_{k_F}|^2$. Neither of these approximations affects the results in a significant way.

The strong interaction regime in SIAM is defined by $U/(\Gamma\pi) \gg 1$.[295] At this value of the U/Γ ratio the Hartree-Fock theory fails and gives an unphysical magnetic ground state with broken symmetry, $\langle n_{d,\mu}\rangle \neq \langle n_{d,-\mu}\rangle$.[2,296] Sometimes it is said that SIAM becomes non-perturbative in U for $U > \Gamma\pi$. In fact, the perturbation theory is valid for all values of U as evidenced by the Bethe Ansatz solution:[2] the impurity susceptibility has the form of a power series in argument U/Γ which is absolutely convergent for all U.[297] This is, however, of limited use, since an infinite number of diagrams would need to be summed. It should be noted, however, that the Kondo problem is clearly not perturbative in Γ.

For every U and Γ, SIAM will end up in the strong-coupling (SC) fixed-point (FP) below some temperature. If $U \gg \Gamma$, the cross-over temperature is the Kondo temperature $T_K(\Gamma, U)$; for $\Gamma \gg U$, the threshold temperature is of the order Γ, assuming $\Gamma < D$.[30] If we are at $T = 0$, we can't tell from the fixed point properties alone whether we are in the Kondo regime or not. At $T = 0$, there is no difference between the Kondo screened system and the strongly hybridized (effectively non-interacting) impurity system as far as the adiabatic measurements are concerned (magnetic susceptibility, specific heat, linear conductance), as long as $U \neq 0$. Only high-energy probes (photoemission) can detect the difference. To talk about Kondo effect, there really must be a local moment regime at intermediate temperatures.

The fixed points are identified by considering special values (namely 0 and ∞) for the parameters δ, U and Γ and comparing the resulting Hamiltonian H_N in the limit $N \to \infty$ with the free-electron Hamiltonian.[31] Depending on the values of parameters δ, U, Γ and T, the system can be in a number of different regimes which are associated with different

fixed points of the model:[31]

1. *FO*: *free-orbital regime*: the high-temperature regime where spin and charge fluctuations occur and states $|0\rangle, |\uparrow\rangle, |\downarrow\rangle, |2\rangle$ are equally probable. The entropy is clearly $S_{\rm imp} = \ln 4$, while the effective moment $\mu_{\rm eff} = k_B T\chi/(g\mu_B)^2$ is 1/8.

2. *VF*: *valence-fluctuation regime*, characteristic of the asymmetric Anderson model: the regime where fluctuations between two values of charge occur. The low-energy impurity states are, $|0\rangle$, $|\uparrow\rangle$ and $|\downarrow\rangle$ for $\delta > 0$, or $|\uparrow\rangle$, $|\downarrow\rangle$ and $|2\rangle$ for $\delta < 0$. The entropy is $S_{\rm imp} = \ln 3$, the effective moment is $\mu_{\rm eff} = 1/6$.

3. *LM*: *local-moment regime*, where the system behaves like a Kondo model, eventually with potential scattering if $\delta \neq 0$. The impurity states are $|\uparrow\rangle$ and $|\downarrow\rangle$; the magnetic susceptibility is Curie-Weiss like. The entropy is $S_{\rm imp} = \ln 2$, and $\mu_{\rm eff} = 1/4$.

4. *SC*: *strong-coupling regime*, this is the regime below the Kondo temperature where the impurity magnetic moment is screened. The impurity spin and the conduction band electrons form a singlet state; there are only residual interactions between renormalized conduction-electron degrees of freedom. The magnetic susceptibility is constant and the specific heat is linear: the system is a Fermi liquid.

5. *FI*: *frozen-impurity regime*, this is essentially the same regime as *SC*. The two are related by potential scattering, i.e. there is a line of fixed points joining *FI* and *SC* fixed points.

The various regimes are schematically outlined in the "phase diagram", Fig. 6.7, for constant U and Γ such that $U/\Gamma\pi \gg 1$. We consider only $\delta \geq 0$, since due to the symmetry of the Anderson model with respect to simultaneous particle-hole and $\delta \to -\delta$ transformation, the phase diagram is symmetric about the $\delta = 0$ axis. For $\delta/U < 1$, cross-over from *FO* to *VF* occurs at $T_1^* = U/\alpha$, where α denotes a numeric value of order 1 (typically $\alpha \sim 5$).[31] On this scale the excitations to the doubly occupied $n = 2$ states freeze out. In the *VF* regime, the hybridization-induced virtual transitions from the $n = 1$ to the $n = 0$ subspace are still important; they renormalize the impurity on-site energy ϵ_d which becomes temperature dependent:[31,211]

$$E_d(T) \approx \epsilon_d + \frac{\Gamma}{\pi} \ln \frac{U}{T}. \tag{6.15}$$

If $E_d(T) < 0$ and $|E_d(T)| \gg \Gamma$ as T decreases, the system is unstable with respect to *LM* regime.[31] The cross-over occurs at T_2^* given by

$$T_2^* \sim -E_d(T_2^*) \equiv -E_d^*. \tag{6.16}$$

or $E_d^* \approx \epsilon_d + \frac{\Gamma}{\pi} \ln(-U/E_d^*)$. The condition for the existence of the *LM* regime is

$$-\epsilon_d \gg \frac{\Gamma}{\pi \ln(U/\gamma)}, \tag{6.17}$$

where γ is some constant. In the LM regime, the impurity behaves like a Kondo impurity and undergoes Kondo screening at the Kondo temperature T_K that will be defined below in the section on the Schrieffer-Wolff transformation. For increasing δ/U, the effective exchange coupling ρJ becomes of order unity and T_K rises to become of order T_2^*.

If $E_d(T)$ goes positive, the system crosses over from VF to FI regime at a temperature[31]

$$T_3^* \sim E_d(T_3)^* = E_d^{**}. \tag{6.18}$$

When $|E_d(T)| \lesssim \Gamma$, there is a regime with non-universal properties where LM, VF and FI regions of the phase diagram meet.

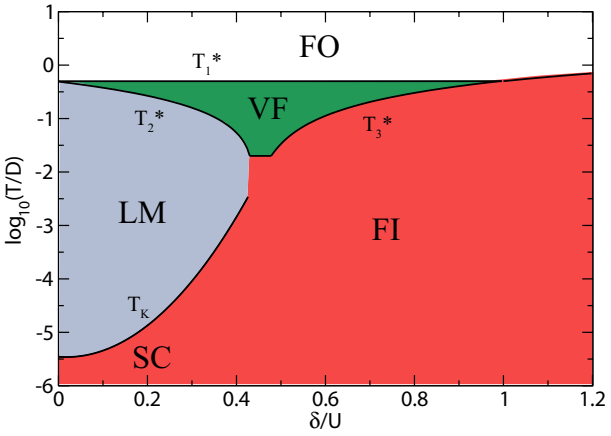

Figure 6.7: "Phase diagram" for the single-impurity Anderson model. All transitions are smooth cross-overs, hence the boundaries and cross-over temperatures are "fuzzy". Only $\delta > 0$ half-plane is shown due to symmetry.

The behavior of thermodynamic quantities in the symmetric case ($\delta = 0$) is shown in Fig. 6.8. For $T \ll T_1^*$, the behavior is identical to that of the Kondo model as described in Sec. 6.1. The only new feature is the presence of the FO regime at high temperatures. At $T \sim T_1^*$, the impurity charge degree of freedom is frozen, which is reflected in the decrease of χ_{charge}, in the reduction of the entropy for $\ln 4 - \ln 2 = \ln 2$, and in the peak in the specific heat. Since on a single site charge and spin degrees of freedom are interlocked (at one time, a single site can behave either as a spin or as an isospin), the freezing out of the charge degree of freedom directly leads to an increase of the magnetic susceptibility to $\sim 1/4$.

6.3.1 Schrieffer-Wolff transformation

The Schrieffer-Wolff transformation (SWT) relates the Anderson model to the Kondo model and SIAM parameters U, δ and Γ to Kondo parameters J and K[28,33,207,298–300] It may be generalized to more complex models with additional degrees of freedom on the impurity

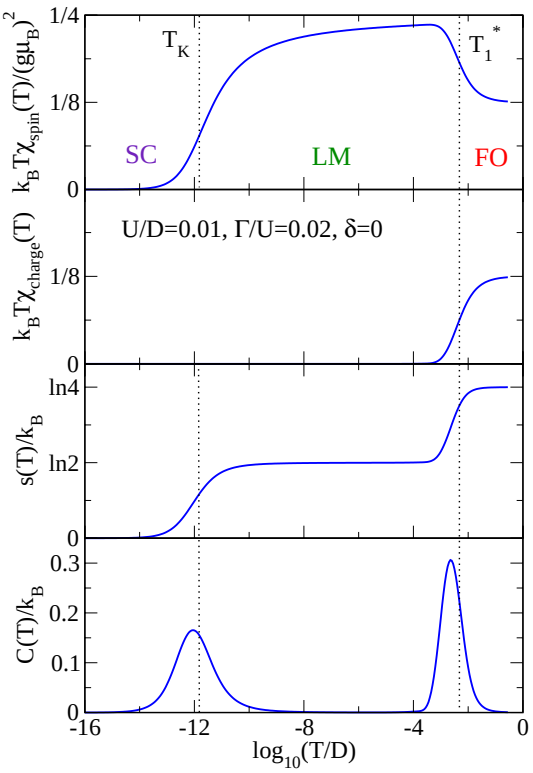

Figure 6.8: Impurity contribution to the magnetic susceptibility, charge susceptibility, entropy and specific heat in the single-impurity Anderson model at the particle-hole symmetric point $\delta = 0$. Parameters used are $\Lambda = 4$, $\bar{\beta} = 0.46$, energy cutoff $25\omega_N$, 6 values of slide parameter z.

and to multi-impurity models.[51] A transformation similar to SWT is related to the physics of the superexchange interaction;[301] it relates the Hubbard model to the Heisenberg model with exchange interaction $J = 4t^2/U$.

SWT is a canonical transformation which eliminates hopping terms V_k in H_c to first order.[28] We require that

$$\bar{H} \equiv e^{\mathcal{S}} H e^{-\mathcal{S}} \tag{6.19}$$

have no terms which are first order in V_k. We expand $\bar{H}$ in terms of nested commutators:

$$\bar{H} = H + [\mathcal{S}, H] + \frac{1}{2}[\mathcal{S}, [\mathcal{S}, H]] + \ldots \tag{6.20}$$

and write $H = H_0 + H_c$, where $H_0 = H_{\text{band}} + H_{\text{imp}}$. We choose $\mathcal{S}$ to be first order in V_k and that

$$[\mathcal{S}, H_0] + H_c = 0. \tag{6.21}$$

The resulting effective Hamiltonian will then be given by[298]

$$H_{\text{eff}} = H_0 + \frac{1}{2}[\mathcal{S}, H_c]. \tag{6.22}$$

The general result is that the strength of the effective antiferromagnetic exchange interaction is proportional to the hybridization $|V_k|^2$ divided by the change in energy during the charge fluctuations, which is of order U. For SIAM, the generator $\mathcal{S}$ is

$$\mathcal{S} = \sum_{k\mu} \sum_{\alpha=\pm} \frac{V_k}{\epsilon_k - \epsilon_\alpha} n^\alpha_{-\mu} c^\dagger_{k\mu} d_\mu - \text{H.c.} \tag{6.23}$$

with $\epsilon_\pm = \delta \pm U/2$ and the projection operators $n^\alpha_{-\mu}$ are defined by

$$\begin{aligned} n^+_{-\mu} &= n_{-\mu}, \\ n^-_{-\mu} &= 1 - n_{-\mu}. \end{aligned} \tag{6.24}$$

Here $\alpha = +$ corresponds to virtual transitions through doubly occupied states, and $\alpha = -$ through unoccupied states. SWT then maps SIAM into the Kondo Hamiltonian with potential scattering term:[30,298]

$$H_{\text{Kondo}} = H_{\text{band}} + J \sum_{k,k'} \sum_{\mu,\mu'} \mathbf{S} \cdot \left(c^\dagger_{k\mu} \frac{\boldsymbol{\sigma}_{\mu\mu'}}{2} c_{k',\mu'} \right) + K \sum_{k,k'} \sum_{\mu} c^\dagger_{k\mu} c_{k'\mu}. \tag{6.25}$$

where J is spin-dependant scattering amplitude

$$\rho J = \frac{2\Gamma}{\pi} \left(\frac{1}{-\epsilon_d} + \frac{1}{U + \epsilon_d} \right) = \frac{2\Gamma}{\pi} \left(\frac{1}{\frac{U}{2} - \delta} + \frac{1}{\frac{U}{2} + \delta} \right) = \frac{8\Gamma}{\pi U} \frac{1}{1 - 4(\delta/U)^2}, \tag{6.26}$$

and K is the potential scattering amplitude

$$\rho K = \frac{\Gamma}{2\pi} \left(\frac{1}{-\epsilon_d} - \frac{1}{U + \epsilon_d} \right) = \frac{\Gamma}{2\pi} \left(\frac{1}{\frac{U}{2} - \delta} - \frac{1}{\frac{U}{2} + \delta} \right) = \frac{\delta}{2U} \rho J. \tag{6.27}$$

Here $\Gamma = \pi \rho V^2$. These expressions hold for $\delta \ll U$ and for a flat density of states $\rho = 1/(2D)$. In the VF regime ($\delta \to U/2$), the impurity-orbital energy is renormalized to $E^*_d \approx \epsilon_d + (\Gamma/\pi) \ln(-U/E^*_d)$.[31,207,211] Then we have

$$\begin{aligned} \rho J &\approx \frac{2\Gamma}{\pi} \left(\frac{1}{-E^*_d} + \frac{1}{U + E^*_d} \right), \\ \rho K &\approx \frac{\Gamma}{2\pi} \left(\frac{1}{-E^*_d} - \frac{1}{U + E^*_d} \right). \end{aligned} \tag{6.28}$$

Whereas in the Kondo model only spin fluctuations are possible, in SIAM with $U \ll D$ and $|\delta| \ll D$ real charge fluctuations occur on the impurity at high temperatures. They freeze out on the temperature scale U; at lower energy scales only virtual charge fluctuations are possible and the Anderson impurity behaves as a spin (Kondo) impurity. If SIAM is to be mapped to the Kondo model, the effective bandwidth in the Kondo problem must therefore be associated with the energy scale U.[2,207] In general, the effective particle and

hole effective bandwidths D_1 and D_2 may be different. Haldane argued that the effective bandwidth $D_{\rm eff}$ is given by the geometric mean, since half the processes generating $\ln T$ behavior are particle-like and half are hole-like:[207]

$$D_{\rm eff} = \sqrt{D_1 D_2} \tag{6.29}$$

with $\ln D_i = \ln(W_i/4) + 1/4$ and $W_1 = \gamma|U/2 + \delta|$, $W_2 = \gamma|U/2 - \delta|$, where $\gamma = (2/\pi)\exp C \approx 1.13387$ and C is Euler's constant. We obtain

$$D_{\rm eff} = \frac{\gamma e^{1/4}}{8} U \sqrt{1 - 4(\delta/U)^2}, \tag{6.30}$$

which gives in the particle-hole symmetric point ($\delta = 0$)

$$D_{\rm eff} = 0.182U. \tag{6.31}$$

This compares well with the NRG calculations for $U/D \ll 0.1$. For $U \gg D$, $D_{\rm eff}$ is given by the scale of the bandwidth D (recall that the effective bandwidth for the $S = 1/2$ Kondo impurity is $D_{\rm eff} \sim 0.85D$, Ref. 215). In the intermediate $U \sim D$ case, $D_{\rm eff}/D$ is some smooth function f of the argument $\xi = U/D$ with asymptotic behavior $f(\xi) \to 0.182\xi$ for $\xi \to 0$ and $f(\xi) \to$ const for $\xi \to \infty$.

In this work, I will often approximate the Kondo temperature using the following expression :

$$T_K = 0.182U\sqrt{\rho J_{\rm K}} \exp\left(-\frac{1}{\rho J_{\rm K}}\right), \tag{6.32}$$

with $\rho J_K = 8\Gamma/\pi U$. This expression is valid for $U \ll D$ and $\delta = 0$, i.e. for the symmetric model in the wide-band limit.

6.3.2 Correlation functions

Additional insight in the behavior of SIAM can be obtained by computing correlation functions, for example as a function of hybridization Γ for fixed U, Fig. 6.9. The first panel presents charge fluctuations $\langle q^2\rangle = \langle n^2\rangle - \langle n\rangle^2$ on the impurity site. Charge fluctuations decrease linearly in Γ for $\Gamma \gg U$, exponentially on the scale $\Gamma \sim U$, while the low-temperature asymptotic behavior is linear in Γ/U and is given by a universal function $\langle q^2\rangle = (4/\pi)(\Gamma/U)$.[302]

The second panel presents charge fluctuations $\langle q_f^2\rangle$ on the first site of the Wilson chain. As this site is part of the non-interacting conduction band, $\langle q_f^2\rangle \approx 1/2$ for all Γ/U. The deviation from 1/2 is proportional to U/Γ and drops to zero exponentially on a scale set by Γ. The increase of the deviation with the interaction strength U indicates that e-e repulsion on the impurity site induces correlated electron behavior also in the conduction band, as expected. The third panel present the charge-charge correlation function $\langle qq_f\rangle =$

$\langle (n-1)(n_f-1)\rangle$. A positive value of this correlation function indicates that occupancy tends to be the same on both sites, i.e. both impurities tend to be either both empty or both occupied; conversely, a negative value indicates that the impurity is doubly occupied when the first site on the chain is empty and vice versa. For large value of Γ, $\langle qq_f\rangle$ is strongly negative. This is not unexpected: for large Γ, only short-distance behavior is important. Taking into consideration only the impurity site and the first site on the Wilson chain, and considering both sites half-filled on the average, the only charge fluctuation mechanism is the transfer of one electron from one site to the other (if this is allowed by the Pauli principle), resulting in one of the sites being empty and the other doubly occupied: such fluctuations lead to negative charge-charge correlations, as explained above. On the scale of $\Gamma \sim U$, the charge-charge correlations become positive since for small Γ large-distance behavior becomes important – there is a small energy gain if the impurity and the first site on the chain are both empty or both occupied at the same time. Finally, for $\Gamma \ll U$ the charge-charge correlations drop to zero. The fourth panel presents spin-spin correlation function between the impurity site and the first site of the Wilson chain, $\langle \mathbf{S}\cdot\mathbf{S}_f\rangle$. It is negative for all Γ/U, as expected from the sign of the effective Kondo exchange interaction as obtained using the Schrieffer-Wolff transformation. It should be noted that for small Γ/U ratio, the spin-spin correlation function tends to zero in spite of the fact that the Kondo effect must occur at some low temperature T_K. This seems to be in contradiction with the common description of the strong coupling fixed point as consisting of the first site of the Wilson chain strongly bound into a spin-singlet state with the impurity site, while the rest of the chain is decoupled. In reality, the Kondo screening cloud is an extended object of size $\propto 1/T_K$ and for that reason the short-range spin-spin correlation $\langle \mathbf{S}\cdot\mathbf{S}_f\rangle$ may be small. There is, however, a sum-rule

$$\int_0^\infty \langle \mathbf{S}\cdot\mathbf{s}(\mathbf{r})\rangle \mathrm{d}\mathbf{r} = -\frac{3}{4}, \tag{6.33}$$

where $(\mathbf{r})$ is the spin-density at point $\mathbf{r}$.[303]

6.3.3 Effect of magnetic field

The effect of the magnetic field applied to the quantum dot depends on the direction of the field. If the field is applied in the plane of the 2DEG, there will be Zeeman splitting of the spin states in the dot, while the orbital energies will be only slightly affected.[69] Conversely, for a perpendicular field the orbital energies will be strongly shifted and Zeeman splitting can be in the first approximation neglected. Therefore in-plane field can be modeled as a "Zeeman field",

$$H' = g\mu_B B S_z \tag{6.34}$$

while perpendicular field can be absorbed in the definition of the on-site energies. In my calculations, the gyromagnetic ratio g and the Bohr magneton μ_B will be absorbed in the field B, so that the perturbation term is $H' = BS_z$ and the field is measured in units of energy.

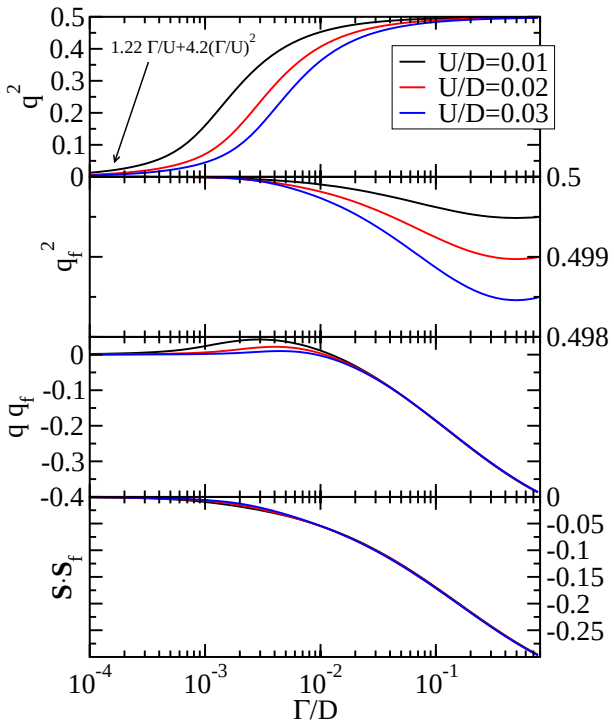

Figure 6.9: Charge fluctuations, charge-charge and spin-spin correlation functions in SIAM. Quantities without a subscript refer to the impurity, while quantities with a subscript f refers to the zero-th site of the Wilson chain, i.e. the localized conduction-band Wannier orbital that the impurity hybridizes with.

The effect of the Zeeman field on impurity spin and charge fluctuations is demonstrated in Fig. 6.10. For $B \ll T_K$, the magnetic field has no effect, while for $B \gg T_K$ the impurity spin is completely polarized. The transition occurs on the scale $B \sim T_K$, but the approach to asymptotic values is slow (logarithmic). There is also some effect on the charge fluctuations $\langle \Delta n^2 \rangle$ for moderate B, but it only becomes appreciable when B becomes comparable to U (such fields are mostly of academic interest; the highest laboratory continuous magnetic fields are of the order of 45 T (National High Magnetic Field Laboratory, Tallahassee), which corresponds to $\sim 5\,\mathrm{meV}$ for $g = 2$).

6.3.4 Spectral functions and conductivity

Systems of coupled quantum dots and magnetic impurities on surfaces are mainly characterized by measuring their transport properties. Conductance can be determined by calculating the spectral functions or the quasiparticle scattering phase shifts (see Chapter 5). Since in quantum dots the impurity level δ (or ϵ_d) can be conveniently controlled using gate voltages, we study the conductance as a function of δ. If the coupling to the left and right electrode of a single impurity is symmetric, it can be shown that the dot couples

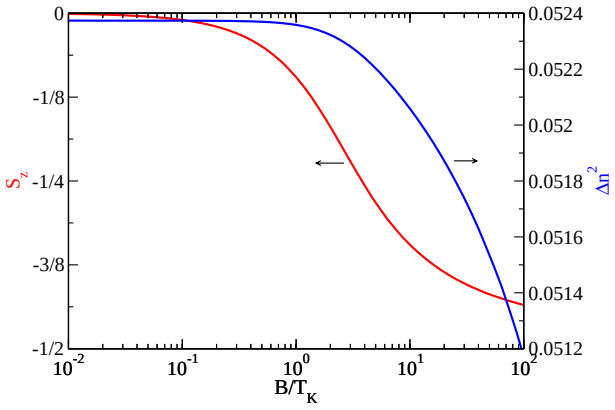

Figure 6.10: (Color online) Operator expectation values for an Anderson impurity in a magnetic field. $U/D = 1$, $\Gamma/U = 0.05$, $T_K = 2.14 \times 10^{-5} D$.

only to the symmetric combination of conduction electron wave-functions from left and right lead, while the antisymmetric combinations of wave-functions are totally decoupled and are irrelevant for our purpose.[46] We use Meir-Wingreen's formula for conductance in the case of proportionate coupling; at zero temperature, the conductance is

$$G = G_0 \pi \Gamma A(0), \tag{6.35}$$

where $G_0 = 2e^2/h$, $A(\omega)$ is the spectral function (local density of states) of electrons on the impurity site and $\Gamma = \pi \rho V^2$.

In Fig. 6.11 I plot the spectral function $A(\omega)$ and the corresponding conductance of the Anderson model for a range of values of the "gate voltage" δ. The conductance is high for a range of δ where the system is in the Kondo regime. This wide conductance peak is sometimes called the Kondo plateau; it is delimited approximately by $|\delta/U| < 0.5$.

The $\omega = 0$ spectral function is related to the quasiparticle phase-shift through

$$A(\omega = 0) = \frac{\sin^2 \delta_{\rm qp}}{\Gamma \pi}. \tag{6.36}$$

According to Friedel sum rule, we have $\delta_{\rm qp} = \frac{\pi}{2}\langle n \rangle$ + a correction term which vanishes in the infinite bandwidth limit due to Anderson's compensation theorem.[2,75,304] In SIAM, conductance can thus also be deduced from the impurity occupancy. Unfortunately, this approach cannot always be generalized to multi-impurity models.

The Kondo (or Abrikosov-Suhl) resonance for $\delta = 0$ can be *approximately* described as a Lorentzian peak:

$$A(\omega) = \frac{2}{\Gamma \pi} {\rm Re} \left[\sqrt{\frac{i\Gamma_K}{\omega + i\Gamma_K}} \right], \tag{6.37}$$

where the Kondo resonance width Γ_K is proportional to the Kondo temperature T_K, $\Gamma_K = k_B T_K / 0.206\pi$.[213,215] It might be noticed that since $1/0.206\pi \approx 1.5$, extracting Kondo

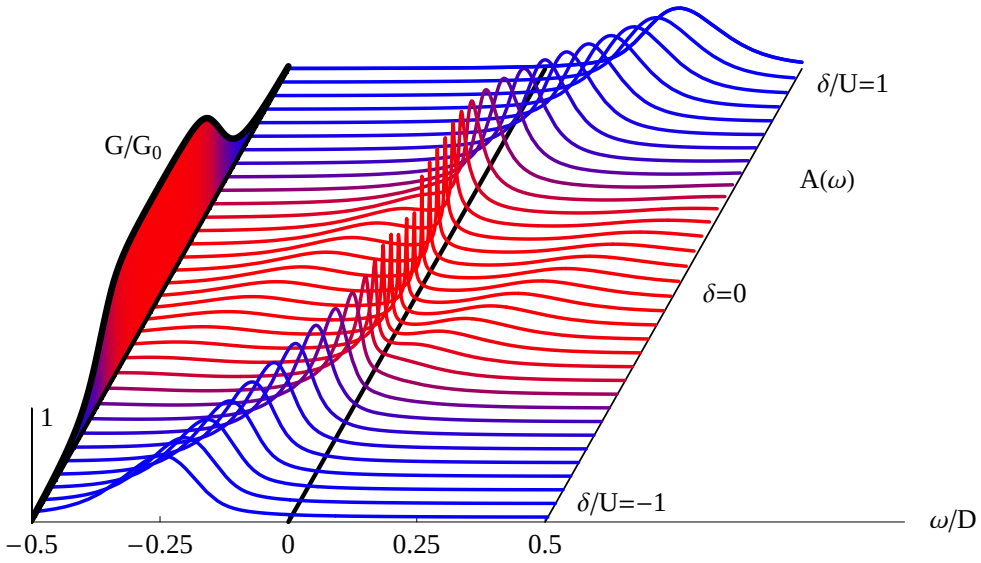

Figure 6.11: Spectral function $A(\omega)$ and conductance through a quantum dot described by SIAM for a range of parameters δ with $U/D = 0.5$, $\Gamma/U = 0.08$. Color of each spectral function corresponds to the value of the conductance.

temperature from the peak width by equating $\Gamma_K = k_B T_K$ leads to a significant error; nevertheless, this procedure is helpful when one is interested only in the scale of T_K. It should also be observed that the weight of the quasiparticle peak in the spectral function is low (of the order T_K/Γ). Finally, I remark that the Lorentzian form is found only asymptotically for $\omega \ll T_K$; for $\omega \gtrsim T_K$ the tails are long and very slowly (logarithmically) decaying.[305]

For $\delta \neq 0$, the peak is displaced from the Fermi level by approximately $2T_K \operatorname{cotan} \delta_{\mathrm{qp}}$.[2] For $\delta \to \pm U/2$, the Kondo peak merges with Hubbard satellites at $\omega = \epsilon_d$ or $\omega = \epsilon_d + U$. These features can be clearly observed in the spectral function sweep in Fig. 6.11.

The effect of the Zeeman field on the impurity spectral function is presented in Fig. 6.12. For $B \sim T_K$, the main effect is the reduction of the Kondo peak amplitude, while the true splitting of the peak becomes noticeable only for $B \gtrsim 3T_K$.

The effect of the Zeeman field on the conductance is demonstrated in Fig. 6.13: as the field B increases past the Kondo temperature T_K, the Kondo resonance splits in two so that the value of the spectral function at $\omega = 0$ decreases and drives the conductance to small values. It can be observed that the effect of the magnetic field to the zero-temperature conductance is similar to the effect of non-zero temperature to the conductance in the absence of the magnetic field.

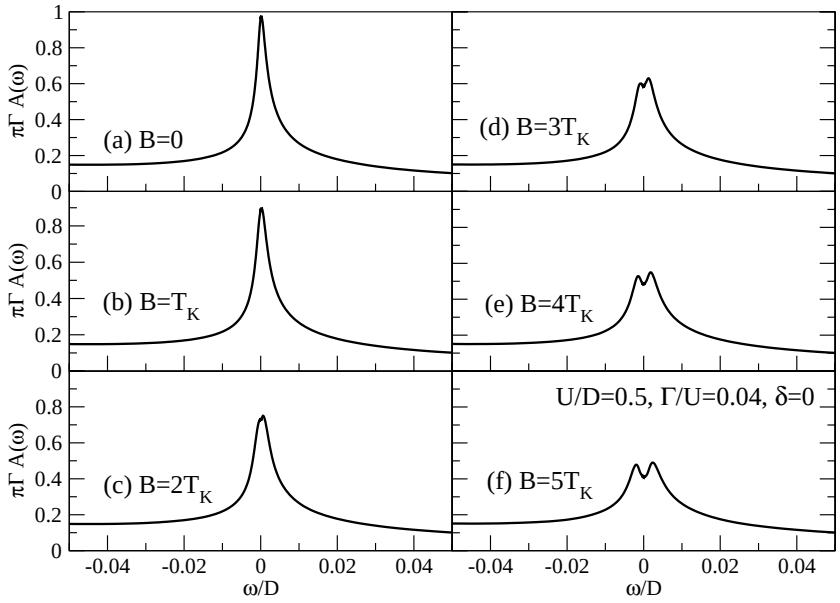

Figure 6.12: Effect of the magnetic field on the impurity spectral function for the single-impurity Anderson model. In the subfigures, the field B stands for $g\mu B$, while the temperature T_K stands for $k_B T_K$.

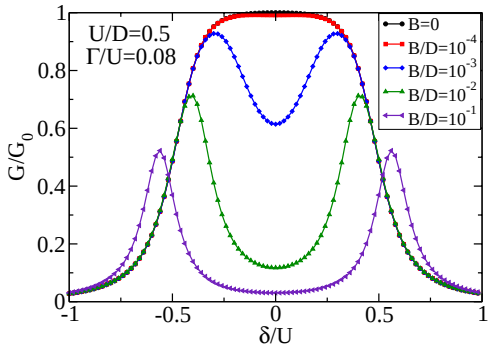

Figure 6.13: Conductance through a QD described by the SIAM in magnetic field of increasing strength. Conductance is computed from extracted spin-dependent quasiparticle scattering phase shifts $\delta_{\mathrm{qp},\sigma}$.

Comparison of different conduction bands

In Fig. 6.14 we plot the conductance as a function of the gate voltage for three different hybridization strengths Γ, and for a) linear dispersion $\epsilon_k = Dk$ ($\Gamma(\epsilon) = \Gamma$) and b) (co)sine dispersion $\epsilon_k = D \sin k$ ($\Gamma(\epsilon) = \Gamma\sqrt{1-\epsilon^2}$). Differences are clearly minimal. The results agree well in the Kondo plateau and for large δ, while the differences are largest in the *VF* regime (the flanks of the Kondo plateau) where the relevant energy scale is high. In the Kondo regime, the Kondo temperature is set by the hybridization strength on the scale of the Kondo temperature itself, i.e. essentially by the hybridization strength at the Fermi level $\Gamma(\epsilon = 0)$. For the same $\Gamma(\epsilon = 0)$, T_K will be roughly the same, since only the effective bandwidth D_{eff} will be affected by the shape of the conduction band dispersion.

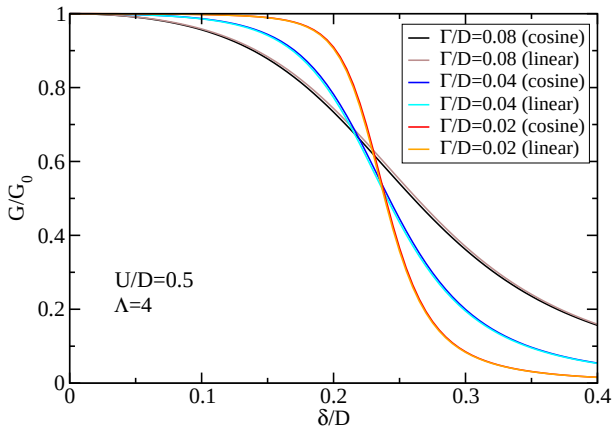

Figure 6.14: Comparison of the conductance sweeps obtained for two different types of conduction band: linear dispersion ("flat-band") and cosine dispersion (tight-binding chain).

Chapter 7

Properties of two-impurity models

Magnetic and transport properties of systems of several magnetic impurities, such as multiple quantum dots or clusters of magnetic adatoms, depend on several elements. At low temperatures, these systems tend to lower their energy and entropy by at least two different mechanisms: by magnetic ordering and by Kondo screening. If both processes occur on the same temperature scale, the resulting competition may lead to non-trivial physics. In the two-impurity Kondo (2IK) model, for example, a quantum critical phase transition at $J \sim T_K$ separates two different regimes: strongly bound local magnetic singlet for $J \gg T_K$ and two separate Kondo singlets for $J \ll T_K$.[20,21,153,155,306–308] Exactly at the transition point, the 2IK model has an unstable non-Fermi liquid (NFL) fixed point.[20,21,111,112,309] The role of the antiferromagnetic (AFM) exchange interaction was also intensely studied in the context of double quantum dots (DQD).[16,19,93,181,182,310–319] Since electron hopping between the dots implies charge transfer between the conduction channels, the 2IK quantum critical phase transition is replaced by a smooth cross-over; the NFL behavior may nevertheless be observed at finite temperatures.[93]

Two mechanisms can contribute to the effective exchange interaction between the dots: the conduction-band mediated Ruderman-Kittel-Kasuya-Yosida (RKKY) interaction[320–322] and the super-exchange mechanism due to the inter-dot electron hopping.[301] RKKY magnetic coupling arises when the magnetic moment on one impurity induces spin polarization in the band which then affects other impurities. Due to recent advances in nanotechnology, the effects of the RKKY interaction on transport properties became directly observable.[18] One should note the double role of the conduction electrons in multi-impurity models; on one hand, they mediate the indirect RKKY exchange interaction,[320] on the other hand, they provide a Kondo screening channel.

RKKY exchange interaction may be ferromagnetic (FM). This occurs, in particular, for small inter-impurity distance, especially when the two impurities couple to the same Wannier orbital of the conduction band.[51] At temperatures on the scale of the RKKY exchange constant, impurity spins align, i.e. they order ferromagnetically; this is followed by a (multi-stage) freezing out of their local moment as they become screened by the conduc-

tion electrons.[152] This scenario was corroborated by numerical studies of the 2IK Kondo model[154] and of the Alexander-Anderson model.[156]

In this chapter, we study the phenomena induced by the interplay between the Kondo effect and the inter-impurity exchange interaction in two different realizations of two-impurity QIMs. The first consists of parallel quantum dots embedded between conduction leads. The second consists of two quantum dots in the side-coupled configuration: one dot is embedded directly between two conduction leads while the second is side-coupled to the first. The ordering is FM in the first case and AFM in the second. Our results complement recent studies which show that AFM and FM interactions lead to different transport properties of DQD systems.[323–325]

It is important to treat the problems with competing processes using suitable methods. It was remarked early on that a number of methods that are applicable for the single-impurity QIMs fail for the two-impurity models;[306] either they do not take into account certain important diagrams or they are mathematically intractable. In light of this, NRG is clearly the method of choice since it is unbiased and capable of resolving conflicting effects.[181]

7.1 General properties of double quantum dot systems

In this section we review some general properties of models of two quantum dots ($i = 1, 2$) embedded between two conduction leads ($\alpha = L, R$). We describe the dots as Anderson impurities (operators $d^\dagger_{i\mu}$), while the conduction leads are represented by two Wilson hopping Hamiltonians (operators $f^\dagger_{j\alpha\mu}$, where j is the site index along the chain). Let us consider the following impurity Hamiltonian $H_{\rm imp}$ and coupling Hamiltonians H_c (in the following, sums over repeated spin indexes are implied):

$$\begin{aligned} H_{\rm imp} &= \sum_{i=1,2} \left[\delta_i \left(n_i - 1\right) + \frac{U}{2}(n_i - 1)^2 \right] - t(d^\dagger_{1\mu} d_{2\mu} + \text{h.c.}) \\ H_{\rm c} &= - \sum_{i=1,2;\alpha=L,R} t_{i\alpha} d^\dagger_{i\mu} f_{0\alpha\mu} + \text{h.c.} \end{aligned} \tag{7.1}$$

Here $t_{i\alpha}$ are the hopping constants $t_{i\alpha} = 2(\Gamma_{i\alpha} D/\pi)^{1/2}$ resulting from the transformation to the hopping Hamiltonian form. We define even and odd conduction channels by symmetric and antisymmetric combination of conduction electron states, so that for the first sites of the Wilson chains we obtain

$$f^\dagger_{e,\mu} = \tfrac{1}{\sqrt{2}} \left(f^\dagger_{0L\mu} + f^\dagger_{0R\mu} \right) \qquad f^\dagger_{o,\mu} = \tfrac{1}{\sqrt{2}} \left(f^\dagger_{0L\mu} - f^\dagger_{0R\mu} \right) \tag{7.2}$$

and rewrite the coupling Hamiltonian as

$$H_{\rm c} = - \sum_i \left(t_{e,i} d^\dagger_{i\mu} f_{0,e,\mu} + t_{o,i} d^\dagger_{i\mu} f_{0,o,\mu} \right) + \text{h.c.} \tag{7.3}$$

with $t_{e/o,i} = 1/\sqrt{2}(t_{Li} \pm t_{Ri})$. Clearly, in the case of left-right symmetry where each impurity couples to the left and right electrode with the same coupling constant, the problem reduces to a single channel QIM just like in the single impurity case.[46] In general, however, these models are genuine two-channel QIMs.

We now set $\delta_1 = \delta_2 = \delta$ and diagonalize $H_{\rm imp}$; the eigenstates are given in Table 7.1 for reference purposes. Each eigenstate is denoted by its quantum numbers (Q, S, S_z, r); Q is the charge, S, S_z are the spin and its component, while r numbers different states with the same Q, S, S_z quantum numbers (sometimes r is called the seniority quantum number). In the absence of the magnetic field, S_z is irrelevant and will be omitted from now on; we thus use (Q, S, r). Each (Q, S, r) multiplet is then $(2S+1)$-fold degenerate.

In the $U \gg t$ limit, state $(0, 0, 2)$ is an inter-impurity singlet $1/\sqrt{2}(d^\dagger_{1\downarrow} d^\dagger_{2\uparrow} - d^\dagger_{1\uparrow} d^\dagger_{2\downarrow})$ with energy $-J$ where $J = 4t^2/U$, and state $(0, 0, 3)$ is an excitonic state $1/\sqrt{2}(d^\dagger_{1\downarrow} d^\dagger_{1\uparrow} + d^\dagger_{2\downarrow} d^\dagger_{2\uparrow})$ with energy $U + J$.

(Q, S)	State (with maximum $S_z = S$)	Energy
$(-2, 0)$	$1,\ 1$	$-2\delta + U$
$(-1, \frac{1}{2})$	$1,\ \frac{1}{\sqrt{2}}\left(d^\dagger_{1\uparrow} + d^\dagger_{2\uparrow}\right)$	$-\delta - t + U/2$
	$2,\ \frac{1}{\sqrt{2}}\left(d^\dagger_{1\uparrow} - d^\dagger_{2\uparrow}\right)$	$-\delta + t + U/2$
$(0, 0)$	$1,\ \frac{1}{\sqrt{2}}\left(d^\dagger_{1\downarrow} d^\dagger_{1\uparrow} - d^\dagger_{2\downarrow} d^\dagger_{2\uparrow}\right)$	U
	$2,\ \frac{1}{\sqrt{A_2}}\left(d^\dagger_{1\downarrow} d^\dagger_{1\uparrow} + B_2\left(d^\dagger_{1\downarrow} d^\dagger_{2\uparrow} - d^\dagger_{1\uparrow} d^\dagger_{2\downarrow}\right) + d^\dagger_{2\downarrow} d^\dagger_{2\uparrow}\right)$	$U/2 - \frac{1}{2}\sqrt{U^2 + 16t^2}$
	$3,\ \frac{1}{\sqrt{A_3}}\left(d^\dagger_{1\downarrow} d^\dagger_{1\uparrow} + B_3\left(d^\dagger_{1\downarrow} d^\dagger_{2\uparrow} - d^\dagger_{1\uparrow} d^\dagger_{2\downarrow}\right) + d^\dagger_{2\downarrow} d^\dagger_{2\uparrow}\right)$	$U/2 + \frac{1}{2}\sqrt{U^2 + 16t^2}$
$(0, 1)$	$1,\ d^\dagger_{1\uparrow} d^\dagger_{2\uparrow}$	0
$(1, \frac{1}{2})$	$1,\ \frac{1}{2}\left(d^\dagger_{1\downarrow} d^\dagger_{1\uparrow} d^\dagger_{2\uparrow} - d^\dagger_{1\uparrow} d^\dagger_{2\downarrow} d^\dagger_{2\uparrow}\right)$	$\delta - t + U/2$
	$2,\ \frac{1}{2}\left(d^\dagger_{1\downarrow} d^\dagger_{1\uparrow} d^\dagger_{2\uparrow} + d^\dagger_{1\uparrow} d^\dagger_{2\downarrow} d^\dagger_{2\uparrow}\right)$	$\delta + t + U/2$
$(2, 0)$	$1,\ d^\dagger_{1\downarrow} d^\dagger_{1\uparrow} d^\dagger_{2\downarrow} d^\dagger_{2\uparrow}$	$2\delta + U$

State number r	A_r	B_r
2	$4 + \frac{U\left(U + \sqrt{16t^2 + U^2}\right)}{4t^2}$	$\frac{U + \sqrt{16t^2 + U^2}}{4t}$
3	$4 + \frac{U\left(U - \sqrt{16t^2 + U^2}\right)}{4t^2}$	$\frac{U - \sqrt{16t^2 + U^2}}{4t}$

Table 7.1: Eigenstates and eigenenergies for decoupled double quantum dot

In the particle-hole symmetric point ($\delta = 0$), for any t/U the ground state is $(0, 0, 2)$, while the first excited state is the triplet state $(0, 1, 1)$. All other states are at least $U/2$ higher in energy. For $U \gg \Gamma$ and $U \gg t$, the occupation of each dot is $n \sim 1$ and low-energy excitations are spin fluctuations.[326] The effective Hamiltonian takes the form of a

two-impurity Kondo model:

$$H = J\mathbf{S}_1 \cdot \mathbf{S}_2 + \mathbf{s}_e \cdot (J_{e1}\mathbf{S}_1 + J_{e2}\mathbf{S}_2) + \mathbf{s}_o \cdot (J_{o1}\mathbf{S}_1 + J_{o2}\mathbf{S}_2)\,. \tag{7.4}$$

The $\mathbf{S}_i$ are spin operators associated with the dots and

$$\mathbf{s}_{e/o} = \sum_{\mu,\mu'} f^\dagger_{0,e/o,\mu}(\tfrac{1}{2}\boldsymbol{\sigma}_{\mu\mu'})f_{0,e/o,\mu'} \tag{7.5}$$

are the spin operators of the Wannier orbitals in even and odd channels to which the impurities couple. To leading order, we have $J = 4t^2/U$ and $\rho J_{\alpha,i} = 8\Gamma_{\alpha,i}/\pi U$. In general, the Hamiltonian also features a channel-changing scattering terms which involve the operator

$$\mathbf{s}_{e-o} = \sum_{\mu,\mu'} f^\dagger_{0,e,\mu}(\tfrac{1}{2}\boldsymbol{\sigma}_{\mu\mu'})f_{0,o\mu'}. \tag{7.6}$$

These terms are especially important in the case of the double quantum dots coupled in series between two conduction leads. Such systems, however, are not discussed at length in this dissertation.

We may also rewrite the Hamiltonian in terms of the eigenstates of H_{imp}:[188,327]

$$H_{\text{imp}} = \sum_\alpha E(\alpha)|\alpha\rangle\langle\alpha| \tag{7.7}$$

$$H_C = \sum_{e/o,\mu,\alpha,\beta} t_{e/o,\mu|\beta\to\alpha}\ |\alpha\rangle\langle\beta|\ f_{0,e/o/\mu} + t^*_{e/o,\mu|\beta\to\alpha} f^\dagger_{0,e/o,\mu}\ |\beta\rangle\langle\alpha|. \tag{7.8}$$

Multi-indexes α and β stand for quantum numbers (Q, S, S_z, r) and the effective hopping coefficients

$$t_{e/o,\mu|\beta\to\alpha} = \sum_i t_{e/o,i}\langle\alpha|d^\dagger_{i,\mu}|\beta\rangle \tag{7.9}$$

correspond to electrons hopping from the conduction band to the dots.

7.2 Double quantum dot: parallel configuration

In this section we study systems of parallel QDs coupled to the same single-mode conduction channel. Since a unified treatment is possible for any number of dots, we will discuss the general N-impurity case whenever possible and specialize to $N = 2$ where needed. The motivation for such models comes primarily from experiments performed on systems of several QDs connected in parallel between source and drain electron reservoirs; these systems can be modelled in the first approximation as several Anderson impurities embedded between two tight-binding lattices as shown schematically in Fig. 7.1. Assuming that the coupling to the left and right electrode is symmetric, only symmetric combinations of conduction electrons play a role (see Sec. 7.1) and the use of a single channel model is justified.

In fact, our model is relevant more generally for any system where RKKY interaction is ferromagnetic, for example to clusters of magnetic adatoms on metallic surfaces.[14,328,329]

We model the parallel QDs using the following Hamiltonian, which we name the "N-impurity Anderson model":

$$H = H_{\text{band}} + H_{\text{dots}} + H_{\text{c}}. \tag{7.10}$$

Here $H_{\text{band}} = \sum_{k\mu} \epsilon_k c^\dagger_{k\mu} c_{k\mu}$ is the conduction band Hamiltonian. $H_{\text{dots}} = \sum_{i=1}^{N} H_{\text{dot},i}$ with

$$\begin{aligned} H_{\text{dot},i} &= \delta\,(n_i - 1) + \frac{U}{2}\,(n_i - 1)^2 \\ &= \epsilon_d n_i + U n_{\uparrow i} n_{\downarrow i} \end{aligned} \tag{7.11}$$

is the N-impurity quantum dot Hamiltonian. Finally,

$$H_{\text{c}} = \frac{1}{\sqrt{N_c}} \sum_{k\mu i} \left(V_k d^\dagger_{i\mu} c_{k\mu} + \text{H.c.} \right) \tag{7.12}$$

is the coupling Hamiltonian, where N_c is the normalization constant (number of states in the conduction band). We assume a constant density of states in the band, $\rho = 1/(2D)$, and a constant hybridization strength Γ. Note that for $N = 1$ this model coincides with the SIAM discussed in Sec. 6.3.

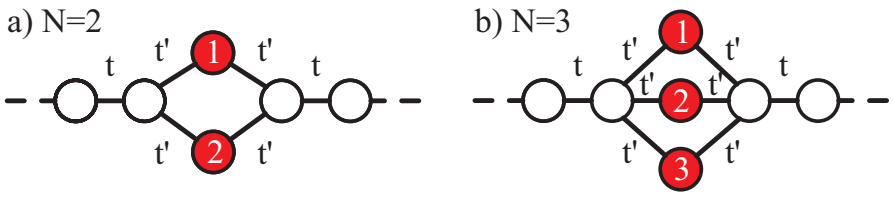

Figure 7.1: Systems of parallel QDs. The tight-binding hopping parameter t determines the half-width of the conduction band, $D = 2t$, while parameter t' is related to the hybridization Γ by $\Gamma/D = (t'/t)^2$.

The discussion of this model is structured as follows: 1) using the generalized Schrieffer-Wolff transformation we show that the effective Hamiltonian in the local moment regime is the N-impurity $S = 1/2$ Kondo model; 2) we show that the ferromagnetic RKKY interaction locks the spins into a state of maximal total spin, $S = N/2$; 3) we study the single-channel $S = N/2$ Kondo screening of this collective spin in which half a unit of spin is screened; 4) we demonstrate the robustness of this behavior by studying the stability of the system with respect to various perturbations and we explore the quantum phase transitions driven by these perturbations.

7.2.1 Low-temperature effective models

We will demonstrate that the low-temperature effective model for the multiple impurity system is the $S = N/2$ Kondo model:

$$H = H_{\rm band} + J_K \mathbf{s} \cdot \mathbf{S}, \tag{7.13}$$

where $\mathbf{s}$ is the local-spin density in the Wannier orbital in the conduction band that couples to *all* N impurities, $\mathbf{S}$ is the collective impurity $S = N/2$ spin operator and J_K is the anti-ferromagnetic spin-exchange interaction that can be derived using the Schrieffer-Wolff transformation. The value of J_K will be shown to be independent of N.

Let us consider the different time scales of the N-impurity Anderson problem, focusing on the (nearly) symmetric case $\delta \ll U$ well within the Kondo regime, $U/(\Gamma\pi) \gg 1$. The shortest time scale, $\tau_U \sim \hbar/U$, represents charge excitations. The longest time scale is associated with the Kondo effect (magnetic excitations) and it is given by $\tau_K \sim \hbar/T_K$ where T_K is the Kondo temperature of *single-impurity* Anderson model,

$$T_K = 0.182U\sqrt{\rho J}\exp(-1/\rho J), \tag{7.14}$$

with $\rho J = 8\Gamma/\pi U$. As we will show later, there is an additional time scale $\tau_J \sim \hbar/J_{\rm RKKY}$, originating from the *ferromagnetic* RKKY dot-dot interactions:

$$J_{\rm RKKY} \sim U(\rho J_K)^2 = \frac{64}{\pi^2}\frac{\Gamma^2}{U}. \tag{7.15}$$

From the condition for a well developed Kondo effect, $U/(\Gamma\pi) \gg 1$, we obtain $J_{\rm RKKY} \ll U$. We thus establish a hierarchy of time scales $\tau_U \ll \tau_J \ll \tau_K$.

Based on the three different time-scales, we predict the existence of three distinct regimes close to the particle-hole symmetric point. The *local moment* regime is established at $T \sim T_1^*$, where $T_1^* = U/\alpha$ and α is a constant of the order one.[30] In this regime the system behaves as N independent spin $S = 1/2$ impurities. At $T \sim T_F^*$, where $T_F^* = J_{\rm RKKY}/\beta$ and β is again a constant of the order one, spins bind into a high-spin $S = N/2$ state. With further lowering of the temperature, at $T \sim T_K$ the $S = N/2$ object experiences the Kondo effect which screens half a unit of spin (since there is a single conduction channel) to give a ground-state spin of $S - 1/2 = (N-1)/2$.

7.2.2 Schrieffer-Wolff transformation for multiple impurities

For $T < T_1^*$, SIAM can be mapped using the Schrieffer-Wolff transformation (SWT) to the Kondo model, see Sec. 6.3.1. In this subsection we show that for multiple impurities a generalized SWT can be performed and that below T_1^*, the N-impurity Anderson model maps to the N-impurity $S = 1/2$ Kondo model. Furthermore, the exchange constant is shown to be the same as in the single impurity case, i.e. it does not depend on N.

In the first approximation, each impurity can be considered independent due to the separation of time scales. Therefore, we choose the generator $\mathcal{S}$ in the SWT to be the sum $\mathcal{S} = \sum_i \mathcal{S}_i$ of generators $\mathcal{S}_i$, where $\mathcal{S}_i$ for each impurity has the same form as in the single-impurity case:

$$\mathcal{S}_i = \sum_{k\mu\alpha} \frac{V_k}{\epsilon_k - \epsilon_\alpha} n^\alpha_{i,-\mu} c^\dagger_{k\mu} d_{i\mu} - \text{H.c.} \tag{7.16}$$

with $\epsilon_\pm = \delta \pm U/2$ and $n^+_{i,-\mu} = n_{i,-\mu}$, $n^-_{i,-\mu} = 1 - n_{i,-\mu}$. The resulting effective Hamiltonian given by

$$H_{\text{eff}} = H_0 + \frac{1}{2}[S, H_c] \tag{7.17}$$

features $\mathcal{O}(V_k^2)$ effective interactions with the leading terms that can be cast in the form of the Kondo antiferromagnetic exchange interaction

$$H_{\text{ex}} = \sum_i J_K \mathbf{s} \cdot \mathbf{S}_i, \tag{7.18}$$

where $\mathbf{S}_i$ is the $S = 1/2$ spin operator on impurity i defined by $\mathbf{S}_i = \sum_{\alpha\alpha'} d^\dagger_{i\alpha}(1/2\boldsymbol{\sigma})d_{i\alpha'}$ and the exchange constant is

$$J_K \equiv 2|V_{k_F}|^2 \left(\frac{1}{|\delta - U/2|} + \frac{1}{|\delta + U/2|} \right). \tag{7.19}$$

This result is identical to J_K obtained for a single impurity, see Sec. 6.3.1.

In addition to the expected impurity–band interaction terms, SWT produces impurity–impurity interaction terms. In the p-h symmetric $\delta = 0$ case, these additional terms can be written as

$$\Delta H_{\text{eff}} = 2\frac{|V_{k_F}|^2}{U} \left(\sum_{i=1}^{N} n_i - N \right) h_{\text{hop}}, \tag{7.20}$$

where

$$h_{\text{hop}} = \sum_{i<j,\mu} \left(d^\dagger_{i\mu} d_{j\mu} + d^\dagger_{j\mu} d_{i\mu} \right). \tag{7.21}$$

Since the on-site charge repulsion favors states with single occupancy of each impurity, the term in the parenthesis in Eq. (7.20) is on the average equal to zero. Furthermore, if on each site charge fluctuations are small, $\langle n_i^2 \rangle - \langle n_i \rangle^2 \sim 0$, hopping between the sites is suppressed and the term h_{hop} represents another small factor. The Hamiltonian ΔH is thus not relevant: impurities are indeed independent.

On departure from the p-h symmetric point ($\delta \neq 0$), ΔH_{eff} generalizes to

$$\Delta H_{\text{eff}} = 2\frac{U|V_{k_F}|^2}{U^2 - 4\delta^2} \left(\left(\sum_{i=1}^{2} n_i - N \right) - 2N\frac{\delta}{U} \right) h_{\text{hop}}. \tag{7.22}$$

For moderately large δ/U this Hamiltonian term still represents only a small correction to Eq. (7.18). However, for strong departure from the p-h symmetric point, close to the *VF* regime (i.e. $\delta \to U/2$), $\Delta H_{\rm eff}$ becomes comparable in magnitude to $H_{\rm ex}$ and generates hopping of electrons between the impurities.

The above discussion leads us to the conclusion that just below T_1^* the effective Hamiltonian close to the p-h symmetric point is

$$H_{\rm eff} = H_{\rm band} + \sum_i J_K \mathbf{s} \cdot \mathbf{S}_i. \tag{7.23}$$

If the dots are described by unequal Hamiltonians $H_{{\rm dot},i}$ or have unequal hybridizations V_k^i, then the mapping of the multi-impurity Anderson model to a multi-impurity Kondo model still holds, however with different effective exchange constants J_K^i.

7.2.3 RKKY interaction and ferromagnetic spin ordering

The RKKY interaction is expected to be ferromagnetic as shown by the following qualitative argument. We factor out the spin operators in the effective Hamiltonian Eq. (7.23):

$$H_{\rm eff} = H_{\rm band} + J_K \mathbf{s} \cdot \sum_i \mathbf{S}_i. \tag{7.24}$$

Spins $\mathbf{S}_i$ are aligned in the ground state since such orientation minimizes the energy of the system. This follows from considering a spin chain with N sites in a "static magnetic field" $J_K\mathbf{s}$. The assumption of a static magnetic field is valid due to the separation of relevant time scales, $\tau_K \gg \tau_J$. Impurity states with $S < N/2$ are clearly excited states with one or several "misaligned" spins.

The inter-dot spin-spin coupling is a special case of the RKKY interaction, therefore a characteristic functional dependence given by

$$J_{\rm RKKY} \propto U(\rho J_{\rm K})^2 = \frac{64}{\pi^2}\frac{\Gamma^2}{U} = \frac{16 V_{k_F}^4}{D^2 U}, \tag{7.25}$$

is expected. The factor U in front of $(\rho J_K)^2$ plays the role of a high-energy cut-off, much like the $0.182U$ effective-bandwidth factor in the expression for T_K, Eq. (7.14); this is due to the fact that Anderson impurities behave as local moments only for temperatures below $T_1^* \propto U$.

Using the Rayleigh-Schrödinger perturbation theory we calculated the singlet and triplet ground state energies E_S and E_T to the fourth order in V_k for the two-impurity case (see the Appendix in Ref. 51). The RKKY exchange parameter is defined as $J_{\rm RKKY} = E_S - E_T$; positive value of $J_{\rm RKKY}$ corresponds to ferromagnetic RKKY interaction. For $U/D \lesssim 0.1$, the prefactor of $(\rho J_K)^2$ in the expression (7.25) is indeed found to be linear in U. Together with the prefactor the perturbation theory leads to[51]

$$J_{\rm RKKY} = 0.62U(\rho J_K)^2 \quad \text{for} \quad U/D \ll 1, \tag{7.26}$$

which, as we will show later, fits very well our numerical results. The RKKY interaction becomes fully established for temperatures below T_J which is roughly one or two orders of magnitude smaller than T_1^* (T_J is defined in the Appendix of Ref. 51). Since the RKKY interactions in the first approximation do not depend much on the number of impurities, for $N > 2$ the exchange interaction between each pair of impurities has the same strength as in the two impurity case. Therefore, for temperatures just below T_J, the effective Hamiltonian for the N-impurity Anderson model becomes

$$H_{\text{eff}} = H_{\text{band}} + J_K \mathbf{s} \cdot \sum_i \mathbf{S}_i - J_{\text{RKKY}} \sum_{i<j} \mathbf{S}_i \cdot \mathbf{S}_j. \tag{7.27}$$

When the temperature drops below a certain temperature T_F^*, the spins align and form a state of maximum spin $S = N/2$. The transition temperature T_F^* is generally of the same order as J_{RKKY}, i.e. $T_F^* = J_{\text{RKKY}}/\beta$, where β is an N-dependent constant of the order one. This relation holds if $T_F^* \ll T_J$.[51]

In conclusion, for $T \lesssim T_F^*$ the states with total spin less than $N/2$ can be neglected, and the system behaves as if it consisted of a single spin $\mathbf{S}$ of magnitude $S = N/2$. The effective Hamiltonian at very low temperatures is therefore the $S = N/2$ Kondo model

$$H_{\text{eff}} = H_{\text{band}} + J_K \mathbf{s} \cdot \mathbf{S}, \tag{7.28}$$

where $\mathbf{S} = \mathcal{P}\left(\sum_i \mathbf{S}_i\right)\mathcal{P}$ and $\mathcal{P}$ is the projection operator on the subspace with total spin $S = N/2$. Other multiplets are irrelevant at temperatures below T_F^*. We point out that the Kondo temperature for this model is given by the formula for SIAM, Eq. (7.14), irrespective of the number of dots N, since the FM interaction only leads to moment ordering, while the exchange interaction of the collective spin is still given by the same J_K.

It should be mentioned that if the exchange constants J_K^i for different impurities are different, there will be some mixing between the spin multiplets. The simple description of impurities as a collective $S = N/2$ spin still holds even for relatively large differences, but in general the virtual excitations to other spin multiplets must be taken into account. This is studied in detail for the case of two dots in Section 7.2.9.

7.2.4 Numerical results

We choose the parameters U and Γ well within the Kondo regime, $U/(\Gamma\pi) \gg 1$. The relevant energy scales are then well separated ($T_K \ll T_F^* \ll T_1^*$) which enables clear identification of various regimes and facilitates analytical predictions (see also Section 7.2.1).

In Fig. 7.2 we show temperature dependence of magnetic susceptibility and entropy for $N = 1, 2, 3$ and 4 systems. As the temperature is reduced, the system goes through the following regimes:

1. At high temperatures, $T > T_1^*$, the impurities are independent and each is in the *free orbital regime* (*FO*) (states $|0\rangle$, $|\uparrow\rangle$, $|\downarrow\rangle$ and $|2\rangle$ on each impurity are equiprobable). Each dot then contributes 1/8 to $\mu_{\rm eff} = T\chi/(g\mu_B)^2$ for a total of $\mu_{\rm eff} = N/8$. The entropy approaches $S_{\rm imp} = N \ln 4$ since all possible states are equally probable.[30]

2. For $T_F^* < T < T_1^*$ each dot is in the *local-moment regime* (*LM*) (states $|\uparrow\rangle$ and $|\downarrow\rangle$ are equiprobable, while the states $|0\rangle$ and $|2\rangle$ are suppressed). Each dot then contributes 1/4 to $\mu_{\rm eff}$ for a total of $N/4$. The entropy decreases to $S_{\rm imp} = N \ln 2$.

3. For $T_K < T < T_F^*$ and $N \geq 1$ the dots lock into a high spin state $S = N/2$ due to ferromagnetic RKKY coupling between local moments formed on the impurities. This is the *ferromagnetically frozen regime* (*FF*)[152] with $\mu_{\rm eff} = S(S+1)/3 = N/2(N/2+1)/3$. The entropy decreases further to $S_{\rm imp} = \ln(2S+1) = \ln(N+1)$.

4. Finally, for $T < T_K$, the total spin is screened from $S = N/2$ to $\tilde{S} = S - 1/2 = (N-1)/2$ as we enter the *strong-coupling regime* (*SC*) with $\mu_{\rm eff} = \tilde{S}(\tilde{S}+1)/3 = (N-1)/2[(N-1)/2+1]/3$. The remaining $S - 1/2$ spin is a complicated object: a $S = N/2$ multiplet combination of the impurity spins antiferromagnetically coupled with a spin-1/2 cloud of the lead.[152] In this regime, the entropy reaches its minimum value of $S_{\rm imp} = \ln(2\tilde{S}+1) = \ln N$.

N	Kondo temperature T_K/D	LM-FO temperature T_F^*/D
1	1.20×10^{-12}	-
2	1.23×10^{-12}	1.87×10^{-5}
3	1.29×10^{-12}	2.11×10^{-5}
4	1.32×10^{-12}	2.32×10^{-5}

Table 7.2: Kondo temperatures for different numbers of quantum dots N corresponding to plots in Fig. 7.2.

In Fig. 7.2, atop the NRG results we additionally plot the results for the magnetic susceptibility of the $S = N/2$ Kondo model obtained using the Bethe-Ansatz (BA) method. For $T < T_F^*$ nearly perfect agreement between the N-impurity Anderson model and the corresponding $S = N/2$ SU(2) Kondo model are found over many orders of magnitude. This agreement is used to extract T_K of the multiple-impurity Anderson model. The fitting is performed numerically by the method of least-squares; in this manner very high accuracy of the extracted T_K can be achieved. The results in Table 7.2 point out the important result of this work that the T_K is nearly independent of N, as predicted in Section 7.2.3. In this sense, the locking of spins into a high-spin state does not, by itself, weaken the Kondo effect;[18,324] however, it does modify the temperature-dependence of the thermodynamic and transport properties.[98,99]

It is instructive to follow transitions from *FO* to *LM* and *FF* regimes through a plot combining the temperature dependence of the magnetic susceptibility and of other thermodynamic

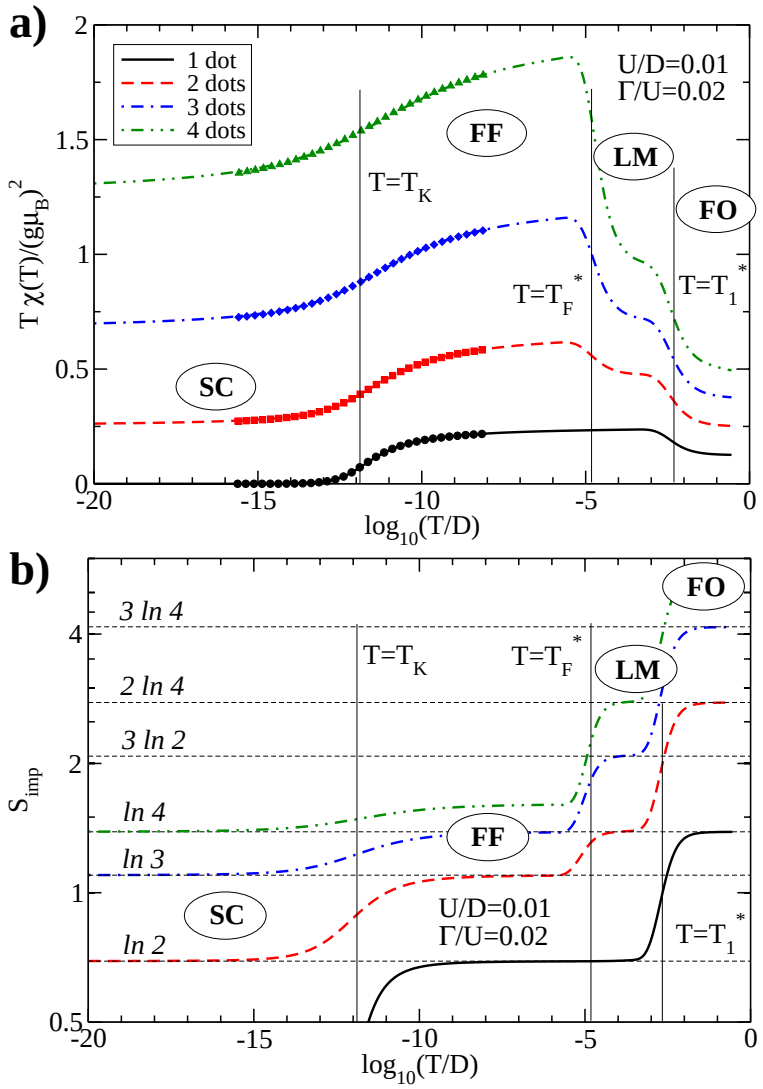

Figure 7.2: a) Temperature-dependent susceptibility and b) entropy of the N-dot systems calculated using the NRG. The symbols in the susceptibility plots were calculated using the thermodynamic Bethe Ansatz approach for the corresponding $S = N/2$ SU(2) Kondo models ($\bullet$ $S = 1/2$, $\blacksquare$ $S = 1$, $\blacklozenge$ $S = 3/2$, $\blacktriangle$ $S = 2$).

quantities, as presented in Fig. 7.3. Charge fluctuations $\langle(\delta n)^2\rangle$ show a sudden drop at $T \sim T_1^*$ representing the *FO-LM* transition. In contrast, the magnitude of the total spin S increases in steps: $S = 1/2$, $(\sqrt{7}-1)/2$ and 1; these values are characteristic for doubly occupied DQD in the *FO*, *LM* and *FF* regime, respectively.

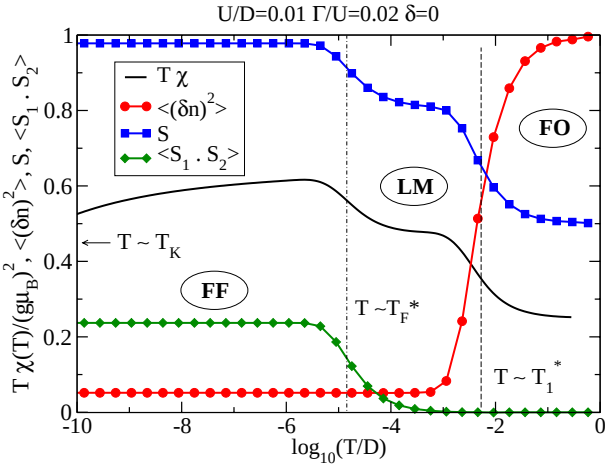

Figure 7.3: Temperature-dependence of susceptibility, charge fluctuations $\langle(\delta n)^2\rangle$, total spin S and the spin-spin correlations $\langle \mathbf{S}_1 \cdot \mathbf{S}_2\rangle$ of the 2-dot system.

The *LM-FF* transition temperature T_F^* can be deduced from the temperature dependence of the spin-spin correlation function. In the *FF* regime the spins tend to align, which leads to $\langle \mathbf{S}_1 \cdot \mathbf{S}_2\rangle \to\sim 1/4$ as $T \to 0$, see Fig. 7.3. The transition from 0 to 1/4 occurs at $T \sim T_F^*$. We can extract T_F^* using the (somewhat arbitrary) condition

$$\langle \mathbf{S}_1 \cdot \mathbf{S}_2\rangle(T_F^*) = 1/2\langle \mathbf{S}_1 \cdot \mathbf{S}_2\rangle(T \to 0). \tag{7.29}$$

In section 7.2.7 we show that this condition is in very good agreement with $T_F^* = J_{\mathrm{RKKY}}/\beta$ obtained by determining the explicit inter-impurity AFM coupling constant J_{12}, defined by the relation $J_{\mathrm{RKKY}} + J_{12} = 0$ that destabilizes the high-spin $S = N/2$ state. The extracted T_F^* transition temperatures that correspond to plots in Fig. 7.2 are given in Table 7.2. We find that they weakly depend on the number of impurities, more so than the Kondo temperature. The increase of T_F^* with N can be partially explained by calculating T_F^* for a spin Hamiltonian $H = -J_{\mathrm{RKKY}} \sum_{i<j} \mathbf{S}_i \cdot \mathbf{S}_j$ for N spins decoupled from leads. Using Eq. (7.29) we obtain $T_F^* \approx 1.18\ J_{\mathrm{RKKY}}$ for $N = 2$, $T_F^* \approx 1.36\ J_{\mathrm{RKKY}}$ for $N = 3$ and $T_F^* \approx 1.55\ J_{\mathrm{RKKY}}$ for $N = 4$.

By performing NRG calculations of T_F^* for other parameters U and Γ and comparing them to the prediction of the perturbation theory, we found that the simple formula (7.26) for J_{RKKY} agrees very well with numerical results.

The effect on thermodynamic properties of varying U while keeping Γ/U (i.e. ρJ_{K}) fixed is illustrated in Fig. 7.4 for 2- and 3-dot systems. Parameters Γ and U enter expressions for $T_F^* = J_{\mathrm{RKKY}}/\beta$ and T_K only through the ratio Γ/U, apart from the change of the effective

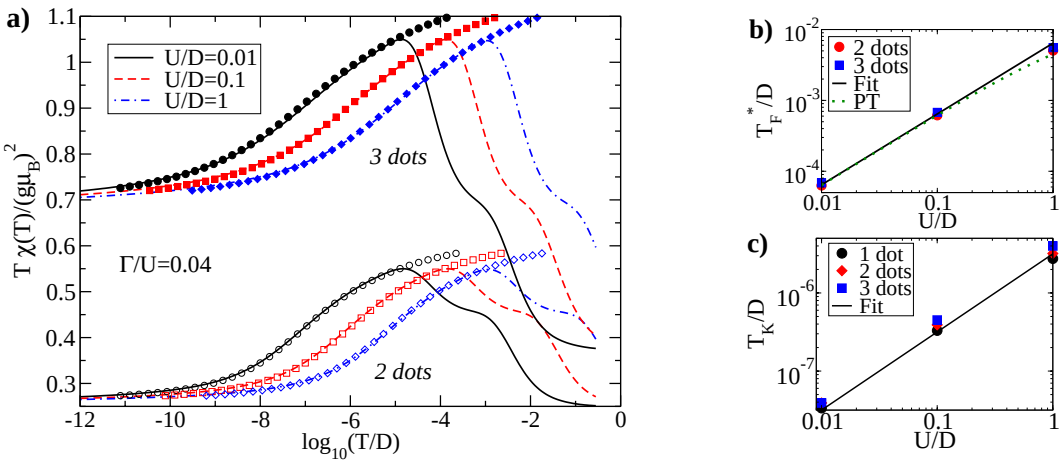

Figure 7.4: a) Temperature-dependent susceptibility of the 2 and 3-dot systems with the same Γ/U ratio. Open (filled) symbols are Bethe-Ansatz results for the $S = 1$ ($S = 3/2$) Kondo model. b) Comparison of *LM-FF* transition temperature T_F^* with predictions of the perturbation theory, Eq. (7.26). c) Comparison of calculated T_K with the Haldane's formula, Eq. (7.14).

bandwidth proportional to U, see Eq. (7.14) and (7.26). This explains the horizontal shift towards higher temperatures of susceptibility curves with increasing U, as seen in Fig. 7.4a. NRG results and BA results for the Kondo models with $S = 1$ and $S = 3/2$ show excellent agreement for $T < T_F^*$. In Figs. 7.4b and 7.4c we demonstrate the nearly linear U-dependence of T_F^* and T_K, respectively.

In Fig. 7.5 we show the effect of varying Γ/U while keeping U fixed. In this case, T_1^* stays the same, T_F^* is shifted quadratically and T_K exponentially with increasing Γ/U. Fig. 7.5b shows the agreement of T_F^* with expression (7.26), while Fig. 7.5c shows the agreement of the extracted values of T_K with formula (7.14).

We note that for $N \geq 2$, eventual coupling to an additional conduction channel would lead to screening by additional half a unit of spin[152,154] and the residual ground state spin would be $S - 1 = N/2 - 1$. This may occur, for example, due to a small asymmetry in the coupling to the source and drain (left and right) electrodes; the two screening channels are formed by the even and odd linear combinations of the conduction electrons from both electrodes. For $N \geq 3$ and three channels (due to weak coupling to some third electrode), three half-units of spin would be screened, and so forth. These additional stages of Kondo screening would, however, occur at much lower temperatures; all our findings still apply at temperatures above subsequent Kondo cross-overs.

In systems of multiple QDs, an additional screening mechanism is possible when after the first Kondo cross-over, the residual interaction between the remaining spin and the Fermi liquid quasi-particles is antiferromagnetic.[174] This leads to an additional Kondo cross-over at temperatures that are exponentially smaller than the first Kondo temperature, as

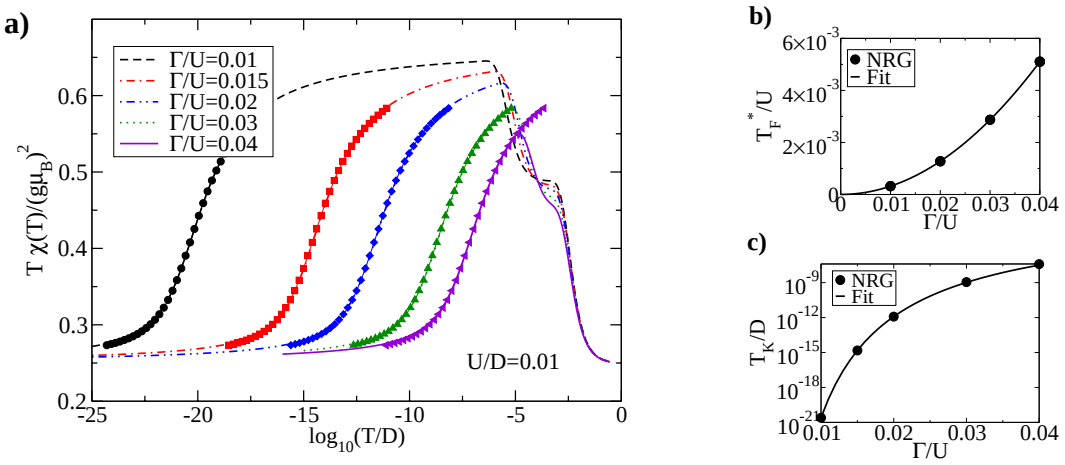

Figure 7.5: a) Temperature-dependent susceptibility of the 2-dot system for equal e-e repulsion $U/D = 0.01$ and for different hybridization strengths Γ. Symbols represent the Bethe-Ansatz susceptibility for the $S = 1$ Kondo model with corresponding T_K. b) Comparison of calculated and predicted T_F^*, Eq. (7.26). c) Fit of T_K to the Haldane's formula, Eq. (7.14).

discussed in Sec. 7.3.3. In parallelly coupled systems, the residual interaction between the remaining spin and the Fermi liquid quasi-particles is, however, ferromagnetic as can be deduced from the splitting of the NRG energy levels in the *SC* fixed point:[99] the *SC* fixed point is stable.

7.2.5 Stability of $N = 2$ systems with respect to various perturbations

The following subsections are devoted to the effect of various physically relevant perturbations for the $N = 2$ system. We generalize the Hamiltonians to

$$\begin{aligned} H_{\rm imp} &= \sum_i H_{{\rm dot},i} + U_{12}(n_1 - 1)(n_2 - 1) + t_{12} \sum_\mu \left(d_{1\mu}^\dagger d_{2\mu} + {\rm H.c.} \right) + J_1 2 \mathbf{S}_1 \cdot \mathbf{S}_2 \\ H_{{\rm dot},i} &= \delta_i (n_i - 1) + \frac{U}{2}(n_i - 1)^2 \\ H_{\rm c} &= \sum_{i,\mu} t_i \left(d_{i\mu}^\dagger f_{e,\mu} + {\rm H.c.} \right). \end{aligned} \tag{7.30}$$

We will study different perturbation terms separately. It will be shown that *FF* regime and the ensuing $S = 1$ Kondo effect are fairly robust against perturbation of increasing strength; very strong perturbations, however, lead to quantum phase transitions (QPTs) from the $S = N/2$ state. QPTs are triggered by the competition between various effects

(such as magnetic ordering and Kondo screening) when the two relevant energy scales become comparable.

Some of the results will be easier to understand if $H_{\rm imp}$ and $H_{\rm c}$ are transformed to symmetric and antisymmetric (gerade/ungerade) basis states [for $J_{12}=0$]:

$$g^\dagger_\mu = \tfrac{1}{\sqrt{2}}\left(d^\dagger_{1\mu}+d^\dagger_{2\mu}\right), \quad u^\dagger_\mu = \tfrac{1}{\sqrt{2}}\left(d^\dagger_{1\mu}-d^\dagger_{2\mu}\right). \tag{7.31}$$

We define the asymmetry in coupling of dots to the band by Δt by $t_1 = t+\Delta$ and $t_2 = t-\Delta t$ and the difference in on-site energies $\Delta\delta$ by $\delta_{1,2} = \delta \pm \Delta\delta$. The transformed Hamiltonian reads:

$$\begin{aligned} H_{\rm imp}+H_{\rm c} = {} & (\delta - t_{12})(n_g-1) + (\delta+t_{12})(n_u-1) \\ & + \left(\frac{U+U_{12}}{4}\right)(n_g-1)^2 + \left(\frac{U+U_{12}}{4}\right)(n_u-1)^2 \\ & + \left(\frac{U+3U_{12}}{4}\right)(n_g-1)(n_u-1) + (-U+U_{12})\,\mathbf{S}_g\cdot\mathbf{S}_u \\ & + \left(\frac{-U+U_{12}}{2}\right)\left(g^\dagger_\uparrow g^\dagger_\downarrow u_\uparrow u_\downarrow + u^\dagger_\uparrow u^\dagger_\downarrow g_\uparrow g_\downarrow\right) \\ & - 2t\left(f^\dagger_{e,\mu} g_\mu + \text{h.c.}\right) \\ & - 2\Delta_t\left(f^\dagger_{e,\mu} u_\mu + \text{h.c.}\right) + \Delta\delta\left(g^\dagger_\mu u_\mu + \text{h.c.}\right) + \text{const.} \end{aligned} \tag{7.32}$$

The hopping t_{12} leads to hybridization between the atomic levels and results in the formation of "molecular orbitals" with energies $\epsilon_{u,g} = \delta \pm t_{12}$. We observe that for $\Delta t = 0$, only symmetric (gerade) level is coupled to the leads. In addition, for $\Delta\delta = 0$, the two levels are "decoupled", i.e. there is no one-electron hopping from g to u.

7.2.6 Variation of the on-site energy levels

Deviation from the particle-hole symmetric point

A small departure from the p-h symmetric point does not destabilize the $S=1$ Kondo behavior: the magnetic susceptibility curves still follow the BA results even for δ/U as large as 0.4, see Fig. 7.6a. The triplet state is destabilized for some critical value δ_c, beyond which the $S=1$ Kondo effect does not occur.

In the asymmetric SIAM, the *VF* regime is characterized by $\mu_{\rm eff} = 1/6$, see Sec. 6.3. For two uncorrelated dots in the *VF* regime, we expect $\mu_{\rm eff} \sim 1/3$. In Fig. 7.6a we plotted a number of susceptibility curves for parameters δ in the proximity of the singlet-triplet transition. While there is no clearly-observable *VF* plateau, the value of $\mu_{\rm eff}$ is indeed near 1/3 between T_1^* and $T_2^*(\delta_c)$.

In Fig. 7.6b we compare calculated T_K with analytical predictions based on the results for the single impurity model.[31] For $\delta \neq 0$, we use the SWT results for exchange J_K and

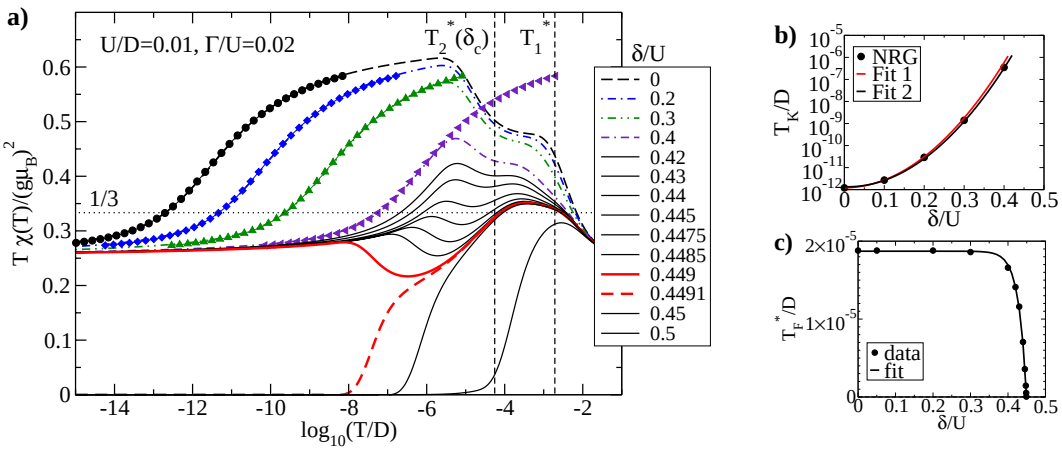

Figure 7.6: a) Temperature-dependent susceptibility of the 2-dot systems on departure from the p-h symmetric point. Symbols are fits to the universal susceptibility obtained using the Bethe-Ansatz method for the $S = 1$ Kondo model. b) Calculated and predicted Kondo temperature (fit 1), Eq. (7.34). For comparison we also plot T_K given by Eq. (7.14), which shows expected discrepancy for large δ/U (fit 2). c) Calculated T_F^* and the fit to an exponential function.

potential scattering K, see Sec. (6.3.1). The effective $\tilde{J}_{\rm K}$ that enters the expression for the Kondo temperature is[31]

$$\tilde{J}_{\rm K} = J_{\rm K}\left[1 + (\pi\rho K)^2\right], \tag{7.33}$$

and the effective bandwidth $0.182U$ is replaced by $0.182|E_d^*|$. The Kondo temperature is now given by

$$T_K = 0.182|E_d^*|\sqrt{\rho\tilde{J}_{\rm K}}\exp\left(-1/(\rho\tilde{J}_{\rm K})\right). \tag{7.34}$$

This analytical estimate agrees very well with the NRG results: for moderate δ/U, the results obtained for asymmetric single impurity model also apply to the multi-impurity Anderson model.

In Fig. 7.6c we show the δ-dependence of the *LM-FF* transition temperature T_F^*. Its value remains nearly independent of δ in the interval $\delta \lesssim 0.4U$ and then it suddenly drops. More quantitatively, the dependence on δ can be adequately described using an exponential function

$$T_F^*(\delta) = T_F^*(0)\left[1 - \exp\left(\frac{\delta - \delta_c}{\lambda}\right)\right] \tag{7.35}$$

where $T_F^*(0)/D = 1.8 \times 10^{-5}$ is the transition temperature in the symmetric case, $\delta_c/D = 0.45$ is the critical δ and $\lambda/D = 2.1 \times 10^{-2}$ is the width of the transition region. Exchange interaction $J_{\rm RKKY}$ does not depend on δ for $U/D = 0.01 \ll 1$, which explains constant value of $T_F^*(\delta)$ for $\delta \lesssim 0.4U$. At a critical value δ_c, T_F^* goes to zero and for still higher δ the spin-spin correlation becomes antiferromagnetic. Since the ground-state spins are different, the triplet and singlet regime are separated by a QPT at $\delta = \delta_c$. This transition is induced

by charge fluctuations which destroy the ferromagnetic order of spins as the system enters the *VF* regime. The exponential dependence arises from the grand-canonical statistical weight factor $\exp[\delta(n-2)/(k_BT)]$, where n is the number of the electrons confined on the dots. The transition is of the first order, since for equal coupling of both impurities to the band there is no mixing between the $n=2$ triplet states and the $n=0$ singlet state.[174]

For δ slightly lower than the critical δ_c, the effective moment $\mu_{\rm eff} = T\chi(T)/(g\mu_B)^2$ shows a rather unusual temperature dependence. It first starts decreasing due to charge fluctuations, however with further lowering of the temperature the moment ordering wins over, $\mu_{\rm eff}$ increases and at low-temperatures approaches the value characteristic for the partially screened $S=1$ moment, i.e. $\mu_{\rm eff} = 1/4$.

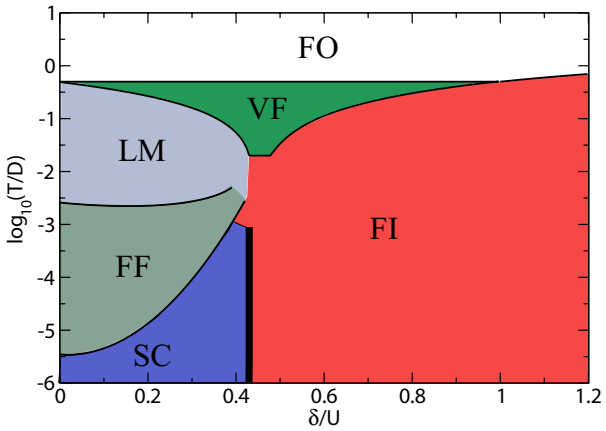

Figure 7.7: "Phase diagram" for the two-impurity Anderson model. Compare with the diagram for the single-impurity model, Fig. 6.7.

The "phase diagram" for the two-impurity model that schematically represents the flow between the fixed points is shown in Fig. 7.7. In comparison with the analogous diagram for the single-impurity model (Fig. 6.7), there are two notable differences: an additional ferromagnetically-frozen fixed point region *FF* appears, and the strong coupling *SC* and frozen impurity *FI* regimes no longer correspond to the same line of fixed points, but are, instead, separated by the quantum phase transition that was described above. Note that in general, there may exist several qualitatively different intermediate-temperature high-spin and low-temperature strong-coupling fixed points. For $N \geq 3$, there might in principle exist (for $\delta \neq 0$) additional ferromagnetically-frozen regimes with $S = n/2$, where $n < N$ is the occupancy of the impurities near such fixed-points. The system would then make a transition from such $FF(n)$ regime to a $SC(n)$ regime with residual spin $S = (n-1)/2$. Since the $SC(n)$ fixed points have different spin, the system will go through cross-overs or true quantum phase transitions as δ is increased toward $U/2$ at zero-temperature. There can be at most $N-1$ such transitions, since there are N *SC* fixed points with residual spin ranging from 0 to $(N-1)/2$ in steps of $1/2$, where $SC(N-1)$ should be identified with the *FI* fixed point. It turns out (results not shown), that for $N=3$ there are indeed two

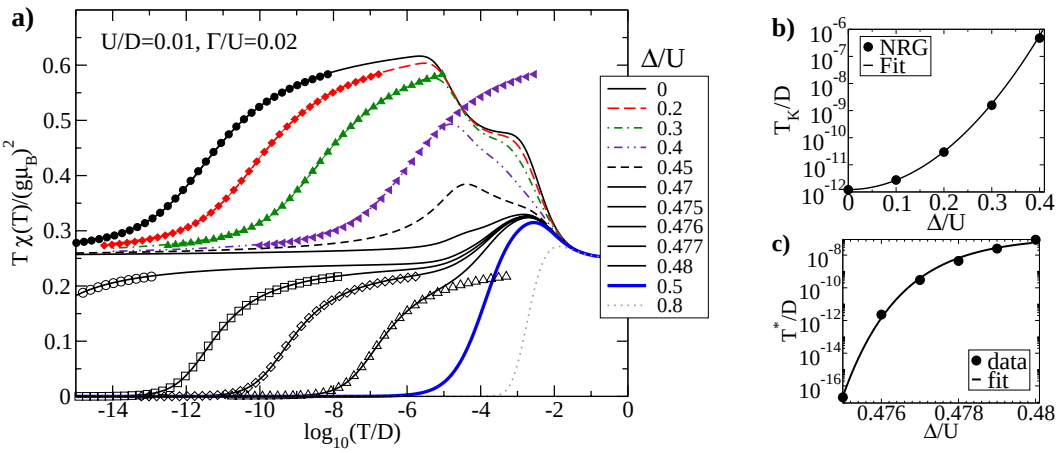

Figure 7.8: a) Temperature-dependent susceptibility of the 2-dot system with unequal (detuned) on-site energies, $\delta_1 = \Delta$, $\delta_2 = -\Delta$. Full symbols present Bethe-Ansatz results of the equivalent $S = 1$ Kondo model, while empty symbols are BA results of a $S = 1/2$ Kondo model. b) Comparison of calculated and predicted Kondo temperature, see Eqs. (7.14) and (7.36). c) The Kondo temperature of the S=1/2 Kondo screening on the singlet side of the transition and a fit to Eq. (7.37).

quantum phase transitions and, surprisingly, the same holds for $N = 4$ and $N = 5$ as well. The conductance through N parallel quantum dots is shown in Subsection 7.2.10.

Splitting of the on-site energy levels

We next consider the 2-dot Hamiltonian with unequal on-site energies δ_i and focus on the case $\delta_{1,2} = \pm\Delta$. This model is p-h symmetric under a generalized p-h transformation $c^\dagger_{k\mu} \to c_{k,-\mu}$, $d^\dagger_{1\mu} \to d_{2,-\mu}$, $d^\dagger_{2\mu} \to d_{1,-\mu}$; the total occupancy of both dots is thus exactly 2 for any Δ. We can therefore study the effect of the on-site energy splitting while maintaining the p-h symmetry. This perturbation induces hybridization between gerade and ungerade levels, see Eq. (7.32). Susceptibility curves are shown in Fig. 7.8a for a range of values of Δ. For Δ up to some critical value $\Delta_c \approx 0.47$ the 2-dot Anderson model remains equivalent to the $S = 1$ Kondo model for $T < T^*_F$. A singlet-triplet transition of the Kosterlitz-Thouless type[71,174] occurs at $\Delta = \Delta_c$.

Even though the two dots are now inequivalent, the Schrieffer-Wolff transformation yields the same J_K for both spin impurities. We obtain

$$J_K = 2|V_{k_F}|^2 \left(\frac{1}{|\Delta - U/2|} + \frac{1}{|\Delta + U/2|} \right). \tag{7.36}$$

Due to the p-h symmetry no potential scattering is generated. In Fig. 7.8b calculated T_K are plotted in comparison with analytical result from Eqs. (7.14) and (7.36). The agreement is excellent.

The properties of the systems with $\delta \neq 0$ and $\Delta \neq 0$ become markedly different near respective singlet-triplet transition points. For $\delta \neq 0$, the transition is induced by charge fluctuations which suppress magnetic ordering and, due to equal coupling of both dots to the band, the transition is of first order. For $\Delta \neq 0$ the transition is induced by depopulating dot 2 and populating dot 1 while the total charge on the dots is maintained, which leads to the transition from an inter-impurity triplet to a local spin-singlet on the dot 1. Since there is an asymmetry between the dots, the transition is of the Kosterlitz-Thouless type.[174]

The Kondo temperature of the $S = 1/2$ Kondo screening near the transition on the singlet side, T^*, is approximately given by

$$\log T^*/D = -\alpha - \beta \exp\left(-\frac{\Delta - \tilde{\Delta}}{\lambda}\right). \tag{7.37}$$

We obtain $\alpha \approx 7$, $\beta \approx 2.8$, $\tilde{\Delta}/D \approx 0.477$ and $\lambda/D \approx 1.5 \times 10^{-3}$. This expression is consistent with the cross-over scale formula $T^* \propto \exp[-T_K/J_{12}]$ for a system of two fictitious spins, one directly coupled to the conduction band and the other side-coupled to the first one with exchange-interaction J_{12} that depends exponentially on Δ: $J_{12} = T_K/\beta \exp[(\Delta - \tilde{\Delta})/\lambda]$.

7.2.7 Inter-impurity interaction

Inter-impurity exchange interaction

By introducing an explicit exchange interaction J_{12} between the localized spins on the dots, the strength of the RKKY interaction, J_{RKKY}, can be directly determined. We study the two-impurity Anderson model with

$$H_{\mathrm{dots}} = \sum_{i=1}^{2} H_{\mathrm{dot},i} + J_{12}\mathbf{S}_1 \cdot \mathbf{S}_2,$$

where $J_{12} > 0$. As seen from Fig. 7.9, for J_{12} above a critical value J_c, the RKKY interaction is compensated, local moments on the dots form a singlet state rather than the triplet which in turn prevents formation of the $S = 1$ Kondo effect. The phase transition is of the first order.[174] Using Eq. (7.29), we obtain $T_F^*/D \approx 1.87 \times 10^{-5}$ for the non-perturbed problem with the same U and Γ, while $J_c/D \approx 1.68 \times 10^{-5}$. Taking into account the definition $T_F^* = J_{\mathrm{RKKY}}/\beta$, where $\beta \sim 1$, we conclude that J_{RKKY} agrees well with the critical value of J_c, i.e. $J_c = J_{\mathrm{RKKY}}$. The perturbation theory prediction of $J_{\mathrm{RKKY}}/D = 1.6 \times 10^{-5}$ also agrees favorably with numerical results.

As long as $J_{12} < J_c$, even for $J_{12} > T_K$, the $S = 1$ Kondo effect survives and, moreover, T_K remains unchanged, determined only by the value of ρJ_{K} as in the $J_{12} = 0$ case. The

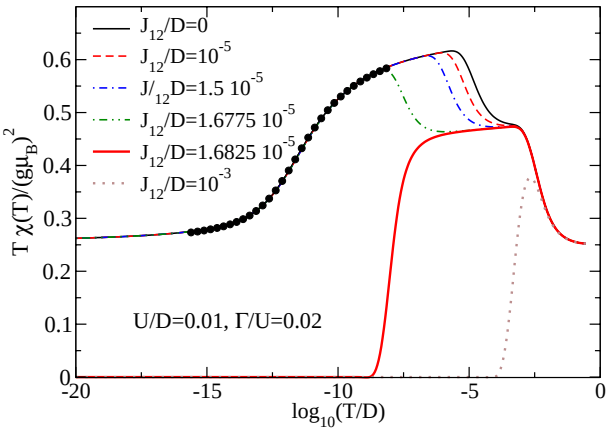

Figure 7.9: Temperature-dependent susceptibility of the 2-dot systems for different antiferromagnetic inter-impurity couplings J_{12}. Circles are Bethe-Ansatz results for the susceptibility of the $S = 1$ Kondo model with the Kondo temperature which is equal for all cases where $J_{12} < J_c$.

only effect of increasing J_{12} in the regime where $J_{12} < J_c$ is the reduction of the transition temperature into the triplet state, which is now given by $T_F^* \sim J_{\rm eff}/\beta$ with the effective inter-impurity interaction $J_{\rm eff} = J_{\rm RKKY} - J_{12}$.

Hopping between the impurities

We now study the two-impurity Anderson model with hopping between the dots:

$$H_{\rm dots} = \sum_{i=1}^{2} H_{{\rm dot},i} - t_{12} \sum_{\mu} \left(d_{1\mu}^\dagger d_{2\mu} + d_{2\mu}^\dagger d_{1\mu} \right), \tag{7.38}$$

This model can be viewed also as a single-channel version of the Alexander-Anderson model[330] in the limit of zero separation between the impurities. This perturbation shifts gerade and ungerade levels in opposite direction, i.e. it induces tunnel splitting, see Eq. (7.32). Such tunable tunnel splitting has been experimentally studied in Refs. 313, 331, 332. The magnetic-susceptibility curves are shown in Fig. 7.10 for several values of the hopping parameter.

In the presence of interaction U there are two contributions to the energy of the low-lying states: "kinetic energy" proportional to t_{12} and "magnetic energy" due to an effective antiferromagnetic exchange $J_{\rm AFM} = 4t_{12}^2/U$, which is second-order in t_{12}. Even though the kinetic energy is the larger energy scale, the Kondo effect is largely insensitive to the resulting level splitting. Instead, the Kondo effect is destroyed when $J_{\rm AFM}$ exceeds $J_{\rm RKKY}$, much like in the case of explicit exchange interaction between the dots which was discussed in the previous subsection. We should emphasize the similarity between the curves in

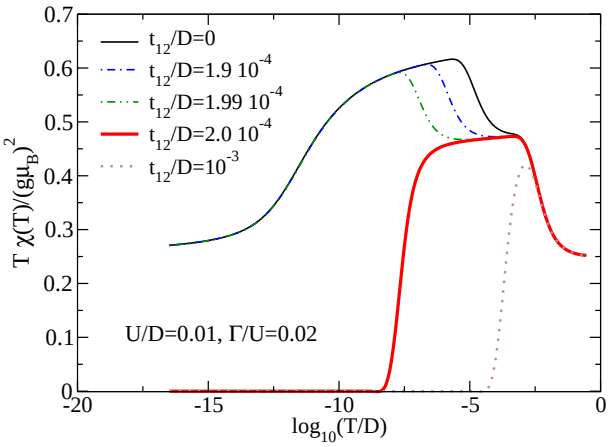

Figure 7.10: Temperature-dependent susceptibility of the 2-dot systems with inter-dot tunneling coupling t_{12}. For $t_{12}/D \approx 2 \times 10^{-4}$, we have $J_{\rm AFM}/D \approx 1.6 \times 10^{-5}$, which agrees well with the critical value of $J_c/D \approx 1.7 \times 10^{-5}$ found in the case of an explicit exchange interaction between the dots, see Fig. 7.9.

Figs. 7.9 and 7.10. In the wide-band limit $U \ll D$, $J_{\rm RKKY}/D \approx 0.62 \times (64/\pi^2)\ (\Gamma^2/U)$, therefore the critical $t_{12,c}$ is given by $t_{12,c} \approx \Gamma$ and it does not depend on U.

7.2.8 Inter-impurity electron repulsion

We study the effect of the inter-impurity electron repulsion (induced by capacitive coupling between the two parallel QDs) by turning on the U_{12} term:

$$H_{\rm dots} = \sum_{i=1}^{2} H_{dot,i} + U_{12}(n_1 - 1)(n_2 - 1). \tag{7.39}$$

This perturbation breaks $\mathrm{SU(2)_{iso}}$ symmetry to $\mathrm{U(1)_{charge}}$, see Sec. 2.3.4. Results in Fig. 7.11 show that the inter-impurity repulsion is not an important perturbation as long as $U_{12} < U$. Finite U_{12} only modifies the Kondo temperature and the temperature T_1^* of the *FO-LM* transition, while the behavior of the system remains qualitatively unchanged. Note that T_F^* is unchanged since U_{12} equally affects both the singlet and the triplet energy. For $U_{12} > U$ the electrons can lower their energy by forming on-site singlets and the system enters the *charge-ordering regime*.[184]

The system behaves in a peculiar way at the transition point $U_{12} = U$ where U_{12} and U terms can be combined using isospin operators as

$$U/2\left(4(I_1^z)^2 + 4(I_2^z)^2\right) + U_{12} 4 I_1^z I_2^z = 2U(I^z)^2. \tag{7.40}$$

Note also that exchange and two-electron hopping terms drop of the Hamiltonian in the gerade/ungerade basis, see Eq. (7.32). We now have an intermediate temperature fixed

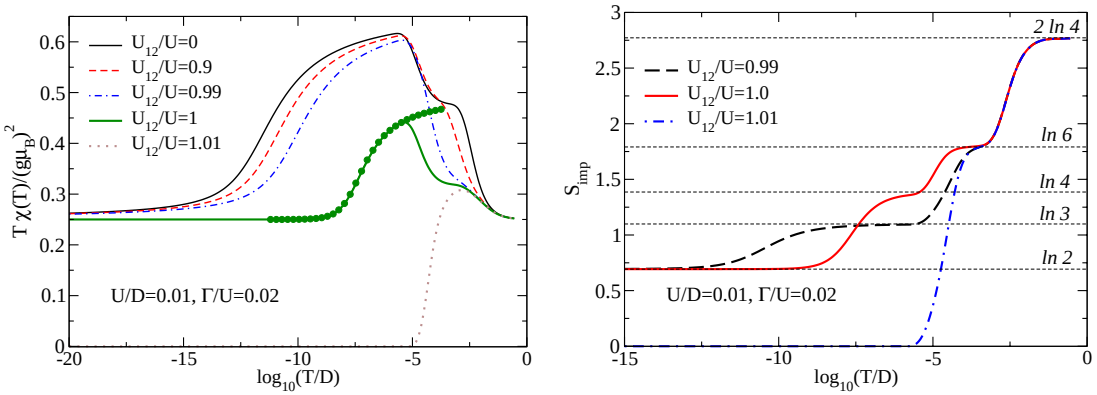

Figure 7.11: a) Temperature-dependent susceptibility of the 2-dot systems for different inter-impurity electron-electron repulsion parameters U_{12}. Circles are the Bethe-Ansatz results for the $S = 1/2$ Kondo model which fit the NRG results in the special case $U_{12} = U$. b) Temperature-dependent entropy of the 2-dot systems for different inter-impurity electron-electron repulsion U_{12}.

point with a six-fold symmetry of states with $I_z = 0$ as can be deduced from Eq. (7.40) and the entropy curve in Fig. 7.11b).

While the $\mathrm{SU}(2)_{\mathrm{iso}}$ isospin symmetry is broken for any $U_{12} \neq 0$, a new orbital $\mathrm{SU}(2)_{\mathrm{orb}}$ pseudo-spin (approximate) symmetry appears at the special point $U_{12} = U$. For two impurities we can define an orbital pseudo-spin operator as

$$\mathbf{O} = \sum_{\mu} \sum_{i,j=1,2} d^{\dagger}_{i\mu} (1/2\boldsymbol{\sigma}_{ij}) d_{j\mu}, \tag{7.41}$$

where $\boldsymbol{\sigma}$ is the vector of the Pauli matrices. Note that the orbital pseudo-spin and isospin operators do not all commute, therefore the full orbital pseudo-spin and isospin SU(2) symmetries are mutually exclusive. The quantum dots Hamiltonian H_{dots} commutes for $U_{12} = U$ with all three components of the orbital pseudo-spin operator; the decoupled impurities thus have orbital $\mathrm{SU}(2)_{\mathrm{orb}}$ symmetry. Furthermore, pseudo-spin $\mathbf{O}$ and spin $\mathbf{S}$ operators commute and the symmetry is larger, $\mathrm{SU}(2)_{\mathrm{spin}} \otimes \mathrm{SU}(2)_{\mathrm{orb}}$. In fact, the set of three S^i, three O^i and nine operators $S^i O^j$ are the generators of the SU(4) symmetry group of which $\mathrm{SU}(2)_{\mathrm{spin}} \otimes \mathrm{SU}(2)_{\mathrm{orb}}$ is a subgroup. The six degenerate states are the spin triplet, orbital singlet and the spin singlet, orbital triplet[149] which form a SU(4) sextet (the notation is $|S, S_z, O, O_z\rangle$):

$$\begin{aligned}
|1,1,0,0\rangle &= |\uparrow,\uparrow\rangle, & |0,0,1,1\rangle &= |\uparrow\downarrow,0\rangle,\\
|1,0,0,0\rangle &= 1/\sqrt{2}\,(|\uparrow,\downarrow\rangle + |\downarrow,\uparrow\rangle), & |0,0,1,0\rangle &= 1/\sqrt{2}\,(|\uparrow,\downarrow\rangle - |\downarrow,\uparrow\rangle),\\
|1,-1,0,0\rangle &= |\downarrow,\downarrow\rangle, & |0,0,1,-1\rangle &= |0,\uparrow\downarrow\rangle.
\end{aligned}$$

It should be noted that the orbital pseudo-spin eigenstates $|0,0,1,\pm 1\rangle$ can be combined

into an isospin triplet eigenstate $|S=0,I=1,I_z=0\rangle = 1/\sqrt{2}\,(|\uparrow\downarrow,0\rangle + |0,\uparrow\downarrow\rangle)$ and an isospin singlet eigenstate $|S=0,I=0\rangle = 1/\sqrt{2}\,(|\uparrow\downarrow,0\rangle - |0,\uparrow\downarrow\rangle)$. This recombination is possible because I_z ($U(1)_{\rm charge}$ charge operator) commutes with both the Hamiltonian (see Eq. (7.40)) and the orbital pseudo-spin operators.

The coupling of impurities to the leads, however, breaks the orbital symmetry. Unlike the model studied in Ref. 184, our total Hamiltonian H is not explicitly SU(4) symmetric, and unlike in the model studied in Ref. 194, in our system this symmetry is not dynamically (re)established on the scale of the Kondo temperature. No SU(4) Kondo effect is therefore expected. Instead, as the temperature decreases the degeneracy first drops from 6 to 4 and then from 4 to 2 in a $S=1/2$ SU(2) Kondo effect (see the fit to the BA result in Fig. 7.11). There is a residual two-fold degeneracy in the ground state. Perturbation theory (Appendix in Ref. 51) shows that the sextuplet splits in the fourth order perturbation in the coupling to the band, V_k. The spin-triplet states and the state $|S=0,I=0\rangle$ form the new four-fold degenerate low-energy subset of states, while the states $|S=0,I=1,I_z=0\rangle$ and $|S=0,O=1,O_z=0\rangle$ have higher energy. The remaining four states can be expressed in terms of molecular-orbitals u and g:

$$\begin{aligned} |1,1,0,0\rangle &= g_\uparrow^\dagger u_\uparrow^\dagger |0\rangle, \\ |1,0,0,0\rangle &= 1/\sqrt{2}\left(u_\uparrow^\dagger g_\downarrow^\dagger + g_\uparrow^\dagger u_\downarrow^\dagger\right)|0\rangle, \\ |1,-1,0,0\rangle &= g_\downarrow^\dagger u_\downarrow^\dagger |0\rangle, \\ |S=0,I=0\rangle &= 1/\sqrt{2}\left(u_\uparrow^\dagger g_\downarrow^\dagger - g_\uparrow^\dagger u_\downarrow^\dagger\right)|0\rangle. \end{aligned} \tag{7.42}$$

The four remaining states are therefore a product of a spin-doublet in the gerade orbital and a spin-doublet in the ungerade orbital. Due to the symmetry of our problem, only the gerade orbital couples to the leads, while the ungerade orbital is entirely decoupled. The electron in the gerade orbital undergoes $S=1/2$ Kondo screening, while the unscreened electron in the ungerade orbital is responsible for the residual two-fold degeneracy.

7.2.9 Unequal coupling to the continuum

We finally study the Hamiltonian that allows for unequal hybridizations $\Gamma_i = \pi\rho|V^i_{k_F}|^2$. We set $V_k^2 = \alpha V_k^1$, i.e. $\Gamma_2 = \alpha^2\Gamma_1$. The effective low-temperature Hamiltonian can be now written as

$$H_{\rm eff} = H_{\rm band} + \mathbf{s}\cdot\sum_{i=1}^{2} J_{{\rm K},i}\mathbf{S}_i - J^{\rm eff}_{\rm RKKY}\mathbf{S}_1\cdot\mathbf{S}_2. \tag{7.43}$$

with $J_{K,2} = \alpha^2 J_{K,1}$ and with the effective RKKY exchange interaction given by a generalization of Eq. (7.25)

$$J^{\rm eff}_{\rm RKKY} = 0.62U\rho^2 J_{{\rm K},1}J_{{\rm K},2} = \alpha^2 J_{\rm RKKY}, \tag{7.44}$$

where $J_{\rm RKKY}$ is the value of RKKY parameter at $\alpha = 1$. In our attempt to derive the effective Hamiltonian we assume that in the temperature regime $T \lesssim J^{\rm eff}_{\rm RKKY}$ the two

moments couple into a triplet. Since the two Kondo exchange constants $J_{\mathrm{K},i}$ are now different, we rewrite H_{eff} in Eq. (7.43) in the following form

$$H_{\mathrm{eff}} = H_{\mathrm{band}} + \mathbf{s}\cdot\left(\frac{J_{\mathrm{K},1}+J_{\mathrm{K},2}}{2}\left(\mathbf{S}_1+\mathbf{S}_2\right)\right) + \mathbf{s}\cdot\left(\frac{J_{\mathrm{K},1}-J_{\mathrm{K},2}}{2}\left(\mathbf{S}_1-\mathbf{S}_2\right)\right) - J^{\mathrm{eff}}_{\mathrm{RKKY}}\mathbf{S}_1\cdot\mathbf{S}_2. \tag{7.45}$$

Within the triplet subspace, $\mathbf{S}_1+\mathbf{S}_2$ is equal to the new composite spin 1, which we denote by $\mathbf{S}$, $\mathbf{S}_1-\mathbf{S}_2$ is identically equal to zero, and $\mathbf{S}_1\cdot\mathbf{S}_2$ is a constant $-1/4$. As a result, the effective J_{K} is simply the average of the two exchange constants:

$$J_{\mathrm{K,eff}} = \frac{J_{\mathrm{K},1}+J_{\mathrm{K},2}}{2}. \tag{7.46}$$

Susceptibility curves for different α are shown in Fig. 7.12. Note that T_K determined using Eq. (7.14) combined with the naive argument given in Eq. (7.46) fails to describe the actual Kondo scale for $\alpha \lesssim 0.4$ as seen from Fig. 7.13. This is due to admixture of the singlet state, which also renormalizes J_K, even though the singlet is separated by $J^{\mathrm{eff}}_{\mathrm{RKKY}} \gg T_K$ from the triplet subspace. Note however, that $J^{\mathrm{eff}}_{\mathrm{RKKY}}$ is well described by the simple expression given in Eq. (7.44) as shown in Fig. 7.13.

By performing a second-order RG calculation (see Appendix D), which takes the admixture of the singlet state into account, we obtain T_K as a function of α which agrees very well with the NRG results, see Fig. 7.13. The following effective low-temperature Kondo Hamiltonian is used:

$$H_{\mathrm{eff}} = H_{\mathrm{band}} + J_1\mathbf{s}\cdot\mathbf{S}_1 + J_2\mathbf{s}\cdot\mathbf{S}_2 - J^{\mathrm{eff}}_{\mathrm{RKKY}}\left(\mathbf{S}_1\cdot\mathbf{S}_2 - 1/4\right), \tag{7.47}$$

where I have added a non-significant additive constant $J_{\mathrm{RKKY}}/4$. Introducing spin-1 operator $\mathbf{S}$ defined by the following Hubbard operator expressions: $S_z = X_{\uparrow\uparrow} - X_{\downarrow\downarrow}$, $S^+ = \sqrt{2}\left(X_{\uparrow 0} + X_{0\downarrow}\right)$ and $S^- = (S^+)^\dagger$, we obtain

$$\begin{aligned} H = {} & H_{\mathrm{band}} + \tilde{J}\mathbf{s}\cdot\mathbf{S} + J^{\mathrm{eff}}_{\mathrm{RKKY}}X_{SS} \\ & + \Delta\big(s_z(X_{0S}+X_{S0}) + s^+(X_{\downarrow S} - X_{S\uparrow}) \\ & + s^-(X_{S\downarrow} - X_{\uparrow S})\big), \end{aligned} \tag{7.48}$$

where index S denotes the singlet state and we have

$$\begin{aligned} \tilde{J} &= \frac{J_1+J_2}{2} = J_0(1+\alpha^2)/2, \\ \Delta &= \frac{J_1-J_2}{2} = J_0(1-\alpha^2)/2. \end{aligned} \tag{7.49}$$

Equations (D.4) reduce to two equations for $\tilde{J}$ and Δ

$$\begin{aligned} \delta\tilde{J} &= \rho_0|\delta D|\left[\frac{\tilde{J}^2}{D} + \frac{\Delta^2}{D+J^{\mathrm{eff}}_{\mathrm{RKKY}}}\right], \\ \delta\Delta &= -2\rho_0\frac{|\delta D|}{D}\Delta\tilde{J}. \end{aligned} \tag{7.50}$$

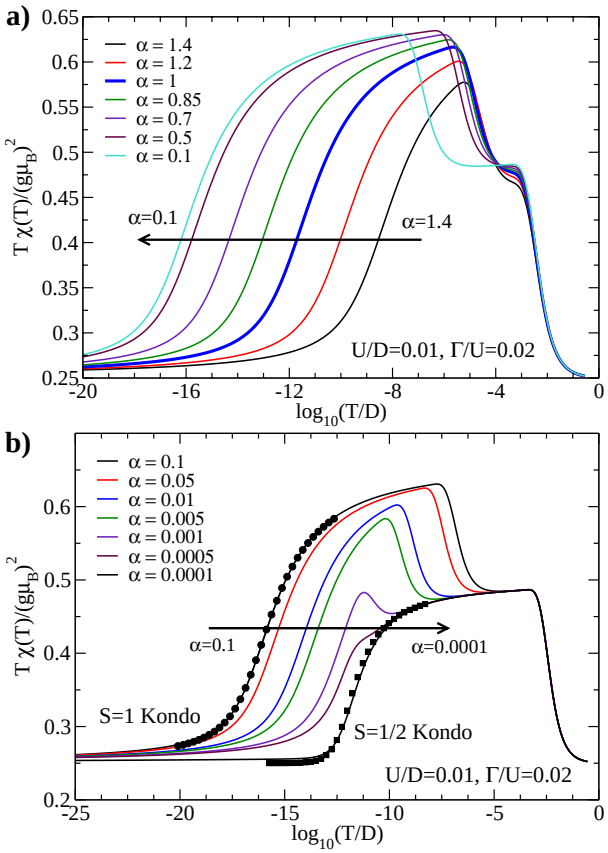

Figure 7.12: Temperature-dependent susceptibility of the 2-dot system with unequal coupling to the leads, $\Gamma_2 = \alpha^2\Gamma_1$. a) The range of α where T_K is decreasing. b) The range of α where T_K is increasing again. Circles (squares) are BA results for the $S = 1$ ($S = 1/2$) Kondo model. The arrows indicate the evolution of the susceptibility curves as the parameter α decreases.

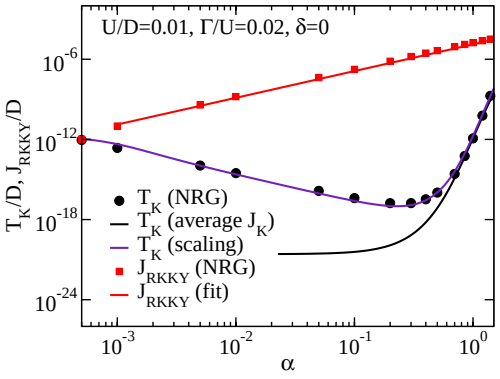

Figure 7.13: Comparison of calculated and predicted Kondo temperature T_K and effective exchange interaction $J^{\rm eff}_{\rm RKKY}$. Average $J_{\rm K}$ corresponds to Eq. (7.46), scaling result is obtained numerically as described in the text. Fit to $J^{\rm eff}_{\rm RKKY}$ corresponds to Eq. (7.44).

from which ensue the following scaling equations

$$\begin{aligned} \frac{d\tilde{J}}{dl} &= -\rho_0 \tilde{J}^2 - \rho_0 \frac{\Delta^2 D}{D + J^{\text{eff}}_{\text{RKKY}}}, \\ \frac{d\Delta}{dl} &= -2\rho_0 \Delta \tilde{J}, \end{aligned} \tag{7.51}$$

where $l = \log D$. The initial bandwidth D is the effective bandwidth $D_{\text{eff}} = 0.182U$ for the Anderson model and we take $\tilde{J}(l = \log D_{\text{eff}}) = \tilde{J}$ and $\Delta(l = \log D_{\text{eff}}) = \Delta$ with $\tilde{J}$ and Δ taken from Eq. (7.49). We integrate the equations numerically until $\tilde{J}$ starts to diverge. The corresponding cut-off D defines the Kondo temperature.

For extremely small α, $J^{\text{eff}}_{\text{RKKY}}$ eventually becomes comparable to the Kondo temperature, Fig. 7.13. For that reason the ferromagnetic locking-in is destroyed and the system behaves as two $S = 1/2$ doublets, one of which is screened at $T_K^1 = T_K(J_{\text{K},1})$ as shown in Fig. 7.12b.

7.2.10 Conductance of parallel quantum dot systems

Using the spectral-function and the quasiparticle-scattering phase-shift methods, I have computed the conductance through the system of N parallel quantum dots. The results for $N = 1, 2, 3$ were computed using both methods and they agree up to the expected errors associated with spectral function calculations in NRG. For $N = 4$ and $N = 5$, only the phase-shift method was used. The results are shown in Fig. 7.14.

The results for $N = 2$ reflect the quantum phase transition discussed in Subsection 7.2.6. The conductance at the transition point drops in a discontinuous manner for $\sim 0.2G_0$. At this point, the occupancy changes only slightly, however the spin-spin correlations flip from positive to negative (not shown). In the $\delta < \delta_c$ regime, the low-temperature fixed points lie on a line of $S = 1$ Kondo model strong-coupling fixed points with $S = 1/2$ residual spin, while for $\delta > \delta_c$, the low-temperature fixed points lie on a line of free-impurity fixed points. In the $\delta > \delta_c$ regime, the conductance goes through a maximum of conductivity near $\delta = U/2$. When magnetic field is applied, it has a strong effect on the Kondo plateau for $\delta < \delta_c$, while it affects the narrow peak for $\delta > \delta_c$ only weakly unless the field is extremely large.

The results for $N = 3$ reflect two different quantum phase transitions. The conductance exhibits a discontinuous jump by $\sim 0.2G_0$ at $\delta = \delta_{c1}$, then the conductance decreases in the narrow interval $\delta_{c1} < \delta < \delta_{c2}$ to 0. This is followed by a sudden jump from zero conductivity to unitary conductivity at δ_{2c}, then the conductance slowly decreases toward 0. The first transition point at δ_{c1} is similar to the transition in the $N = 2$ case: occupancy is affected only slightly, while the spin-spin correlations change sign. The second transition point at δ_{c2} is quite different: the occupancy changes by exactly 1 electron, while the spin-spin correlations appear continuous. Since a change of electron occupancy by 1 corresponds, by the Friedel sum rule, to a $\pi/2$ phase shift in electron scattering, this explains the change of conductance from 0 to G_0.

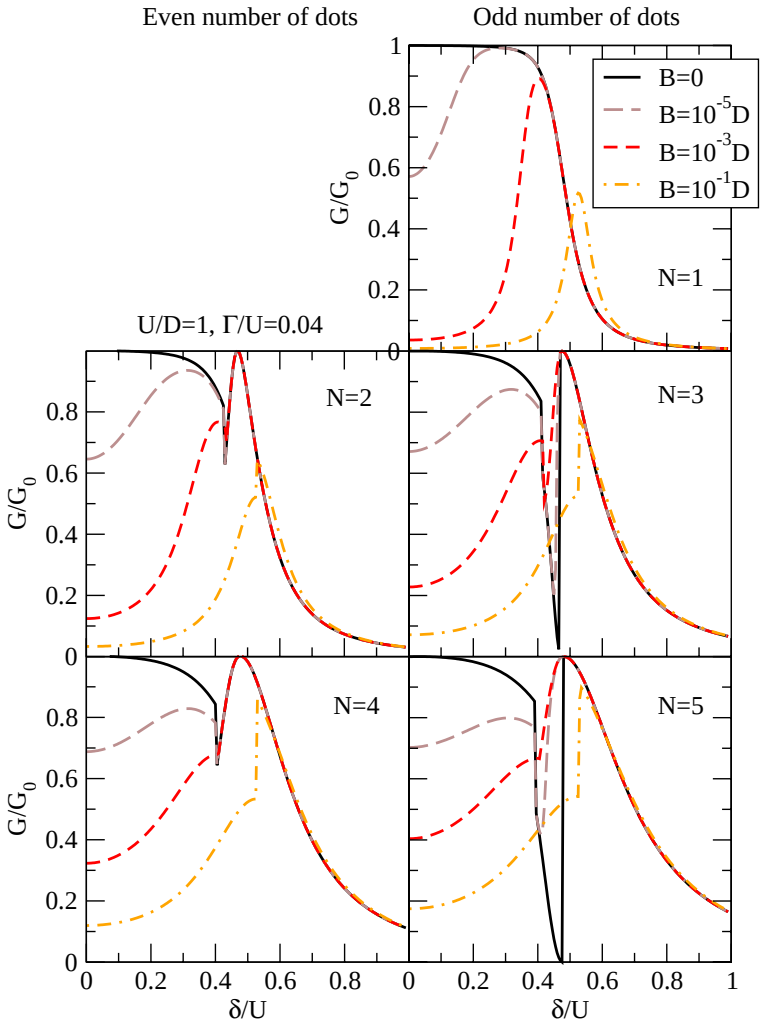

Figure 7.14: Conductance through the system of N parallel quantum dots as a function of the gate voltage for a range of magnetic fields. Results shown are obtained using the phase-shift method. $\Lambda = 4$; 200 NRG iterations were performed to reach the zero temperature limit. For the most demanding $N = 5$ calculation, up to 5000 states were retained in the NRG truncation.

For both $N = 2$ and $N = 3$, the phase transitions are replaced by smooth cross-overs when the impurity-band coupling constants are made unequal.

The conductances of $N = 4$ and $N = 5$ are similar to $N = 2$ and $N = 3$, respectively. There are no additional discontinuities in the conductance as a function of the gate voltage. It turns out that for all $N \geq 3$ with symmetric coupling to the band, there are precisely two phase transitions of the same types that occur for $N = 3$. The second transition corresponds to a change of total electron number by $N-2$. Since for $N = 4$ the occupancy changes by two electrons, the phase shift is π and the quantum phase transition is not mirrored by a discontinuity in the conductance, thus the conductance is similar to that of $N = 2$. For $N = 5$, the occupancy change by three electrons leads to a $3\pi/2$ phase shifts and there is again a conductance jump from 0 to G_0, like for $N = 3$. These results can be generalized for arbitrary $N \neq 1$: for odd N, there are two quantum phase transitions and two conductance discontinuities, while for even N there are also two quantum phase transition, but a single conductance discontinuity.

7.3 Double quantum dot: side-coupled configuration

We now study the DQD system in the side-coupled configuration. The first QD is embedded between source and drain electrodes while the second QD is coupled to the first through a tunneling junction; there is no direct coupling of the first QD to the conduction bands. The Hamiltonian is

$$H = H_{\text{band}} + H_{\text{dots}} + H_{\text{c}} \tag{7.52}$$

where $H_{\text{band}} = \sum_{k\mu} \epsilon_k c^\dagger_{k\mu} c_{k\mu}$ and H_{dots} and H_{c} are the impurity and coupling Hamiltonians

$$\begin{aligned} H_{\text{dots}} &= \sum_{i=1}^{2} H_{\text{dot},i} - t \sum_{\mu} \left(d^\dagger_{1\mu} d_{2\mu} + \text{H.c.} \right), \\ H_{\text{c}} &= 1/\sqrt{N_c} \sum_{k\mu} V_k (d^\dagger_{1\mu} c_{k\mu} + \text{H.c.}), \end{aligned} \tag{7.53}$$

where $H_{\text{dot},i} = \delta(n_i - 1) + U/2(n-1)^2$. For simplicity, we choose the on-site energies and Coulomb interactions to be equal on both dots (the effect of the on-site energy splitting is studied in Ref. 188). Coupling between the dots is described by the inter-dot tunnel coupling t.

By changing the gate voltage and the inter-dot tunneling rate, the system can be tuned to a non-conducting spin-singlet state, the usual Kondo regime with odd number of electrons occupying the dots, the two-stage Kondo regime with two electrons, or a valence-fluctuating state associated with a Fano resonance; these regimes are shown in the phase diagram of the system in Fig. 7.15. We will first study the case of large t with wide regimes where the conductance is enhanced due to the Kondo effect, separated by low-conductance regimes

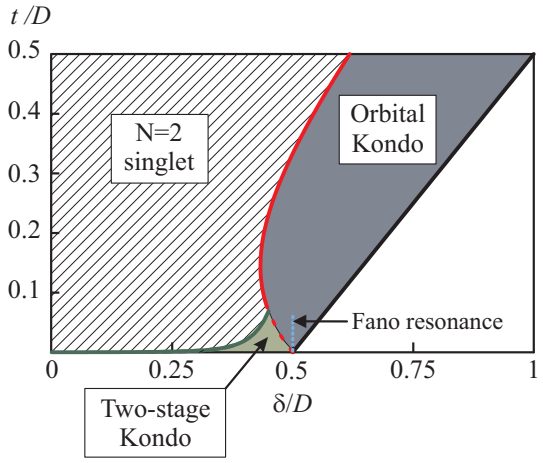

Figure 7.15: The phase diagram of the side-coupled DQD. $U/D = 1$, $\Gamma/D = 0.03$. Grey area represents Kondo regime where $S \sim 1/2$, $\langle n \rangle \sim 1$ and $G/G_0 \sim 1$. In shaded area, called spin-singlet regime, where $S \sim 0$ and $\langle n \rangle \sim 2$, there is strong antiferromagnetic spin-spin correlation and $G/G_0 \sim 0$. The two-stage Kondo regime is discussed in Subsection 7.3.3.

where localized spins on DQD are antiferromagnetically (AFM) coupled. In the case of small t we will study the *two stage Kondo regime* where the two local moments are screened at different Kondo temperatures.[158,174,183,188]

7.3.1 Strong inter-dot coupling

Conductance and correlation functions

The conductance through the DQD at different values of t is shown in Fig. 7.16 as a function of the gate voltage δ. The conductance is enhanced for a wide range of δ due to the Kondo effect. To better understand multidot problems in the case of strong inter-dot coupling, it is helpful to rewrite the total Hamiltonian in terms of the eigenstates. The eigenvalue diagram in Fig. 7.17 represents the gate-voltage dependence of the multiplet energies $E(Q, S, r)$ of the isolated DQD. From this diagram we can read off the ground state and the excited states for each parameter δ.

Such eigenvalue diagrams are a very useful tool to study multi-impurity and multi-level systems. The Kondo effect tends to occur whenever the ground state of the system is degenerate and there are excited states with $Q' = Q \pm 1$, $S' = S \pm 1/2$. Ranges where these conditions are fulfilled appear in the form of triangular level crossings such as ABC in Fig. 7.17. Here, these intervals are given approximately by $\delta_1 < |\delta| < \delta_2$, where $\delta_1 = t(2\sqrt{1 + (U/4t)^2} - 1)$ and $\delta_2 = U/2 + t$. These estimates are obtained from the lowest energies of states with zero, one and two electrons on the isolated DQD, see Table 7.1. The widths of conductance plateaus (measured at $G/G_0 = 1/2$) are therefore approximately

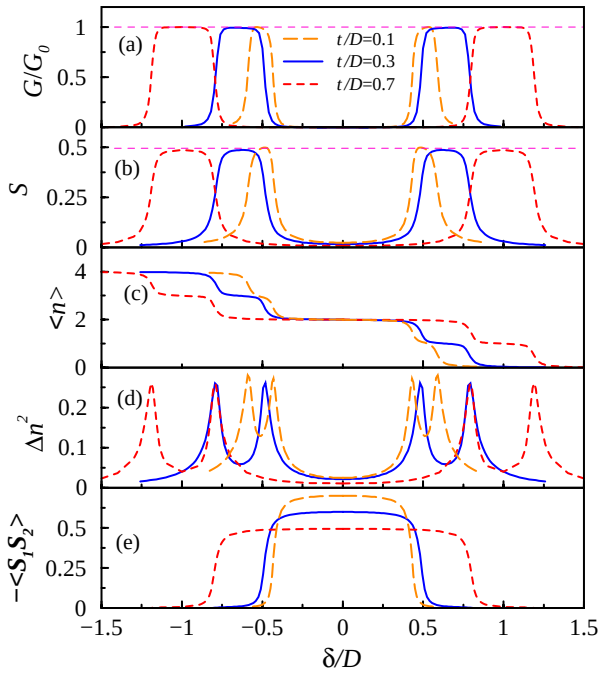

Figure 7.16: Conductance and correlation functions of DQD. Besides different values of t, indicated in the figure, other parameters of the model are $\Gamma/D = 0.03$ and $U/D = 1$. Temperature is $T/D = 10^{-9}$, which for all parameters used corresponds to a zero temperature limit. In particular, in the Kondo plateaux $T \ll T_K$ for all δ.

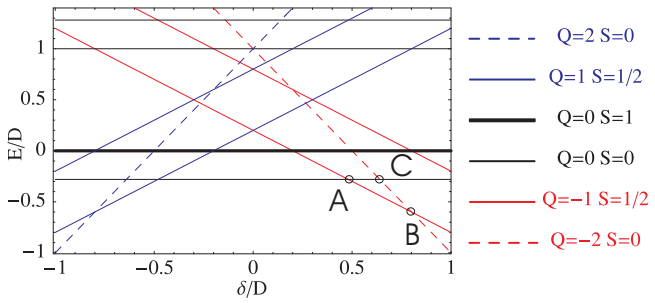

Figure 7.17: Eigenvalue diagram for isolated DQD system. The diagram is symmetric, since for $\delta \to -\delta$, $E(Q,S,r) \to E(-Q,S,r)$. Points A and B correspond to valence-fluctuation regions when the charge on the dot changes, while point C corresponds to the center of the Kondo regime, when the Kondo temperature is the lowest. Parameters are $U/D = 1$ and $t/D = 0.3$.

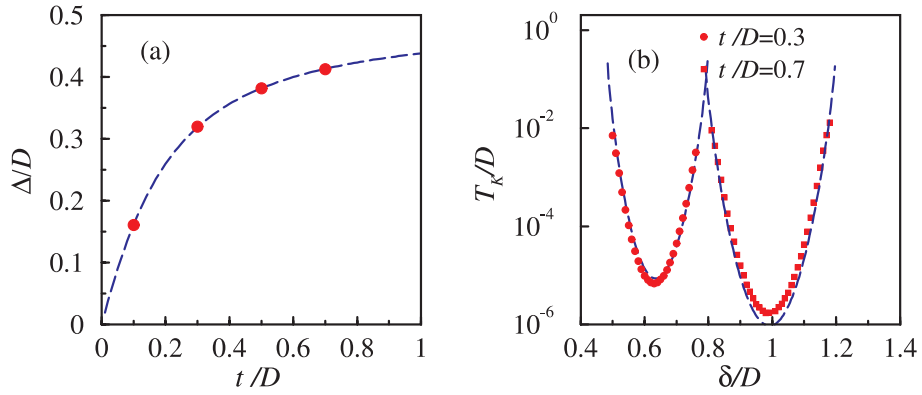

Figure 7.18: a) The width of conductance peak Δ vs. t as obtained from NRG calculations (full circles), compared with the analytical result as given in the text (dashed line). b) Kondo temperatures T_K vs. δ as obtained from the widths of Kondo peaks (full circles). Analytical estimate, Eq. 7.55, is shown using dashed lines. The rest of parameters are identical to those in Fig. 7.16.

given by

$$\Delta = U/2 + 2t(1 - \sqrt{1 + (U/4t)^2}). \tag{7.54}$$

Note that in the limit of large t, $\Delta \simeq U/2$, and in the limit of large U, $\Delta \simeq 2t$. Comparison of conductance-peak widths with the analytical estimate Δ is shown in Fig. 7.18a.

We now confirm the presence of the Kondo effect by considering various correlation functions. In Fig. 7.16b we show S, calculated from expectation value $\langle \mathbf{S}_{\rm tot}^2 \rangle = S(S+1)$, where $\mathbf{S}_{\rm tot} = \mathbf{S}_1 + \mathbf{S}_2$. S reaches value 1/2 in the regime where $G/G_0 = 1$ which indicates that high conductance is associated with the presence of local moment on the DQD. The average occupancy $\langle n \rangle$ in this regime approaches odd-integer values 1 and 3, Fig. 7.16c. Transitions between regimes of nearly integer occupancies are rather sharp; they are visible as regions of enhanced charge fluctuations measured by $\Delta n^2 = \langle n^2 \rangle - \langle n \rangle^2$, as shown in Fig. 7.16d. Finally, we show in Fig. 7.16e spin-spin correlation function $\langle \mathbf{S}_1 \cdot \mathbf{S}_2 \rangle$. Its value is negative between two separated Kondo regimes where conductance approaches zero, i.e. for $-\delta_1 < \delta < \delta_1$, otherwise it is zero. This regime further coincides with $\langle n \rangle \sim 2$. Each dot thus becomes nearly singly occupied and spins on the two dots form a local singlet due to effective exchange coupling $J \approx 4t^2/U$.

In Fig. 7.18b we present Kondo temperatures T_K vs. δ extracted from the widths of Kondo peaks in spectral functions. NRG results fit well the expression obtained using the generalized SWT (see Sec. 6.3.1 and Appendix C):

$$T_K = 0.182U\sqrt{\rho J}\exp[-1/\rho J] \tag{7.55}$$

with

$$\rho J = \frac{2\Gamma}{\pi}\left(\frac{\alpha}{|E(-1,\tfrac{1}{2},0) - E(-2,0,0)|} + \frac{\beta}{|E(-1,\tfrac{1}{2},0) - E(0,0,0)|}\right), \tag{7.56}$$

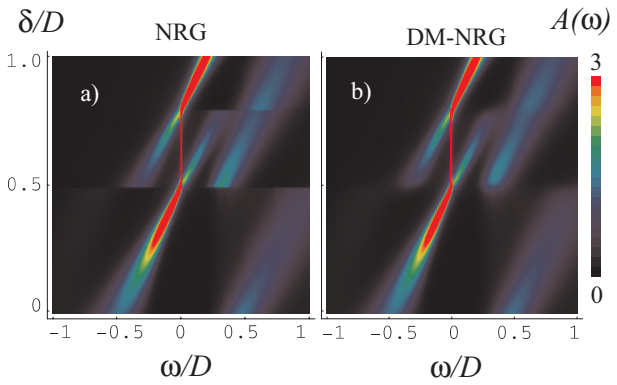

Figure 7.19: Zero-temperature spectral function $A_1(\omega)$ sweeps for $t/D = 0.3$. a) Spectral function calculated using the conventional NRG approach. b) Spectral function calculated using the DM-NRG approach. Note that the vertical line, representing the Kondo peak, has been artificially broadened. Its true width is T_K.

where

$$\alpha = |\langle -1, \tfrac{1}{2}, \tfrac{1}{2}, 0 | d_\uparrow^\dagger | - 2, 0, 0, 0 \rangle|^2 = 1/2,$$
$$\beta = |\langle 0, 0, 0, 0 | d_\downarrow^\dagger | - 1, \tfrac{1}{2}, \tfrac{1}{2}, 0 \rangle|^2 = \frac{\left(4t + U + \sqrt{16t^2 + U^2}\right)^2}{8\left(16t^2 + U\left(U + \sqrt{16t^2 + U^2}\right)\right)}. \tag{7.57}$$

Spectral function

Spectral function calculations using the conventional NRG approach fail for this model: the spectral functions manifest spurious discontinuities and the normalization sum rule is violated for some choices of model parameters.[188] Correct results can be, however, obtained using the DM-NRG technique[188,206] presented in Sec. 3.9. In Fig. 7.19 we present sweeps of $A_1(\omega)$ calculated using both approaches. In vast regions of the plot the results are in perfect agreement. The differences appear for those values of δ where the ground state changes. Three characteristic spectral functions calculated using the DM-NRG are shown in Fig. 7.20.

Features in the spectral function sweeps can be easily interpreted using eigenvalue diagram in Fig. 7.17. At low temperatures and for constant δ, spectral function $A(\omega)$ will be high whenever the energy difference $\Delta E = E_1 - E_0$ between the ground state (0) and an excited state (1) is equal to $+\omega$ (particle excitations, $Q_1 = Q_0 + 1$, $S_1 = S_0 \pm \frac{1}{2}$) or to $-\omega$ (hole excitations, $Q_1 = Q_0 - 1$, $S_1 = S_0 \pm \frac{1}{2}$). At $\delta = 0$ two broad peaks are seen located symmetrically at $\omega \sim \pm\delta_1$ (see Fig. 7.19 and Fig. 7.20 at $\delta = 0$). At this point the model is p-h symmetric and therefore $E(Q, S, r) = E(-Q, S, r)$ for all Q, S, r. Consequently, the spectrum is also symmetric, $A_1(\omega) = A_1(-\omega)$. With increasing δ, the particle excitation energy $E(1, \frac{1}{2}, 0) - E(0, 0, 0)$ increases and the corresponding peak quickly washes out. The hole excitation energy $E(-1, \frac{1}{2}, 0) - E(0, 0, 0)$ decreases and the peak gains weight.

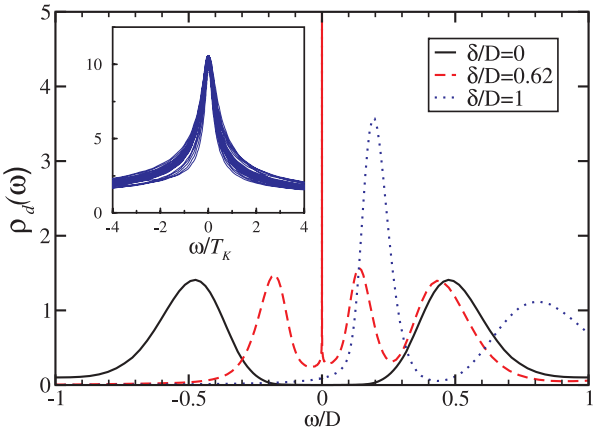

Figure 7.20: Three zero-temperature spectral functions $A_1(\omega) = \rho_d(\omega)$ for $t/D = 0.3$: at the p-h symmetric point $\delta = 0$, in the Kondo regime $\delta/D = 0.62$ and in the empty-orbital regime $\delta/D = 1$. *Inset*: Scaling of spectral functions $A_1(\omega/T_K)$ in the Kondo region $0.52 < \delta < 0.76$. Parameters are as in Fig. 7.16.

At $\delta = \delta_1$, $E(0,0,0) = E(-1,\frac{1}{2},0)$ (point A in Fig. 7.17) and the system enters the Kondo regime: a sharp many-body resonance appears which remains pinned at the Fermi level throughout the Kondo region (see Fig. 7.19 and Fig. 7.20 at $\delta/D = 0.62$). Kondo effect occurs since the ground state is a doublet, $S = 1/2$, and there are excited states with $S' = 0, 1$, $Q' = Q \pm 1$. The high-energy peaks at $\omega = E(0,0,0) - E(-1,\frac{1}{2},0) > 0$ and $\omega = E(-1,\frac{1}{2},0) - E(-2,0,0) < 0$ in the spectral function are also characteristic: they correspond to particle and hole excitations that are at the heart of the Kondo effect.

In the case of the DQD we also see additional structure for $\delta_1 < \delta < \delta_2$: a broad peak at $\omega = E(0,1,0) - E(-1,\frac{1}{2},0)$ which corresponds to virtual triplet excitations from the ground state. These excitations could also be taken into account in the calculation of the effective exchange interaction, Eq. (7.56), however due to their high energy, they only lead to an exponentially small difference in the Kondo temperature, which may be neglected.

In the inset of Fig. 7.20 we show scaling of Kondo peaks vs. ω/T_K. In the case of perfect scaling, all curves should exactly overlap. However, Kondo temperatures of different peaks differ by almost four orders of magnitudes, as seen in Fig. 7.18b. Moreover, Kondo peaks become asymmetric near the edges of the Kondo region, i.e. for $\delta \gtrsim \delta_1$ and $\delta \lesssim \delta_2$. Note also that for each point in Fig. 7.18b there is a respective spectral function presented in the inset of Fig. 7.20.

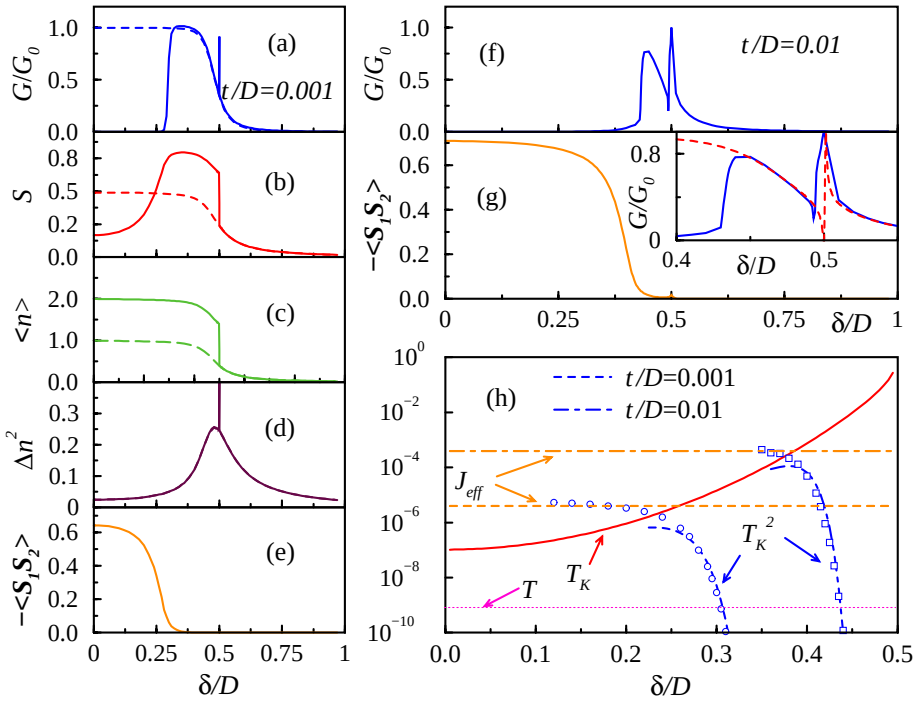

Figure 7.21: Conductance and correlation functions at $t/D = 0.001$ (a,...,e), $t/D = 0.01$ (f,and g) and a blow-up of f) in the inset of g). Dashed lines in a) represent G/G_0 and b) S of a single quantum dot with otherwise identical parameters. Dashed line in c) represents $\langle n_1 \rangle$ of DQD, and finally dashed line in the inset of g) represents the semi-analytical model described in the text. In h) a schematic plot of different temperatures and interactions is presented as explained in the text. NRG values of the gap in $A_1(\omega)$ at $\omega = 0$ and $T \ll T_K^{(2)}$ are presented with open circles and squares for $t/D = 0.001$ and 0.01 respectively. Values of J and analytical results of $T_K^{(2)}$ are presented with dashed and dot-dashed lines for $t/D = 0.001$ and 0.01 respectively. For analytical estimates of $T_K^{(2)}$ different values of $c_1 = 2.2$ and 1.3, respectively, were used. Other parameters of the model are $\Gamma/D = 0.03, U/D = 1$.

7.3.2 Weak inter-dot coupling: the Fano resonance

We now turn to the case of weak inter-dot coupling, $t/U \ll 1$. Unless otherwise specified, we choose the effective temperature T to be finite, $T \sim 10^{-9}D$, i.e. we stop the NRG iteration after a predetermined number of iterations. It should be noted that $T = 0$ results may be misleading for some models and parameter ranges, since the temperature scale where the system crosses over to its $T = 0$ fixed point may be extremely low, much lower than the experimentally relevant temperature. For the following discussion it will become clear that the side-coupled DQD is an example of such system.

One may naively expect that in the small t limit we obtain essentially identical conductance as in the single-dot case, since dot 2 is expected to be decoupled and play no role. As δ decreases below $\delta \sim U/2$, G/G_0 indeed follows results obtained for the single-dot case, Fig. 7.21a. In the case of DQD, however, a sharp asymmetric resonance appears around $\delta = U/2$. It has the form of a Fano resonance and it coincides with the sudden jump in S, $\langle n \rangle$, as well as with the spike in Δn^2, Figs 7.21b,c, and d.

In the context of quantum transport, the Fano effect[333] is most easily described as an interference between a resonant and a non-resonant (direct, background) transport channel[182] or, equivalently, between a narrow and a broad resonance. Fano effect leads to a characteristic Fano line-shape of the resonance in the transmission function, *the Fano resonance*, which can be parametrised as

$$T = \frac{(q+\epsilon)^2}{1+\epsilon^2} = 1 + \frac{q^2 - 1 + 2q\epsilon}{1+\epsilon^2}, \tag{7.58}$$

where $\epsilon = (E - E_0)/(\Gamma/2)$ is a rescaled energy, E_0 is the resonance position, Γ its width, while q is the Fano parameter that determines the form of the resonance. Physically, q is the ratio between resonant and direct scattering probability. In the limit $q \to \infty$, the Fano resonance goes into the Breit-Wigner (Lorentzian) resonance, while in the $q \to 0$ limit it has the appearance of a symmetric dip.

Fano resonances have been detected in QDs and SETs,[334,335] in QDs embedded in Aharonov-Bohm interferometers[336] and in quantum wires with side-coupled QD.[337]

In our case, the Fano resonance is a consequence of a sudden charging of the nearly decoupled dot 2, as its energy ϵ crosses the Fermi level at $\epsilon_F = 0$. Meanwhile, the electron density on the dot 1 remains a smooth function of δ, as seen from $\langle n_1 \rangle$ in Fig 7.21c. This can be qualitatively understood from a simple noninteracting model

$$H = \epsilon_1 |1\rangle\langle 1| + \epsilon_2 |2\rangle\langle 2| + t\left(|1\rangle\langle 2| + \text{h.c.}\right). \tag{7.59}$$

Using the Green's function method (Sec. 4.1) we obtain the following expression for conductance

$$G = G_0 \frac{4\epsilon_2^2 (t')^4}{\epsilon_2^2(\epsilon_1^2 + 4(t')^4) - 2\epsilon_1\epsilon_2 t^2 + t^4}, \tag{7.60}$$

where t' is the coupling of impurity 1 to the leads in the tight-binding description. Conductance is clearly zero when the on-site energy ϵ_2 of the side-coupled dot crosses the Fermi level. If the levels are shifted using the gate-voltage ($\epsilon_1 = V_g$ and $\epsilon_2 = V_g - \Delta$, where Δ is the detuning parameter), we find that $G = 0$ at $V_g = \Delta$ and $G = G_0$ at $V_g = \frac{1}{2}(\Delta + \sqrt{\Delta^2 + 4t^2})$. The width of the Fano resonance is proportional to the energy difference between these extrema:

$$w = \tfrac{1}{2}(\sqrt{\Delta^2 + 4t^2} - \Delta) \sim \frac{t^2}{\Delta} + \mathcal{O}(t^4). \tag{7.61}$$

In the interacting case, we may improve this calculation using a simple model. We will consider the total Hamiltonian H in the $t = 0$ limit exactly and then couple the two subsystems using perturbation theory. For $t = 0$, the exact Green's function of impurity 1 at $\omega = 0$ is

$$\mathcal{G}_1^0 = 1/(i\Gamma - \Gamma\cot\phi) = -\frac{\cos\phi\sin\phi}{\Gamma} - i\frac{\sin^2\phi}{\Gamma} = -\frac{\sin\phi}{\Gamma}e^{i\phi}, \tag{7.62}$$

where ϕ is the scattering phase shift for single impurity model. This is simply an expression of the Friedel sum rule[304] and follows from (all quantities are evaluated at $\omega = 0$)

$$2i\phi = \ln\left(\mathcal{G}^R(0)[\mathcal{G}^A(0)]^{-1}\right) \text{ or } \phi = \arg\mathcal{G}^R(0) \tag{7.63}$$

and

$$\mathrm{Im}\,\Sigma = \Gamma, \tag{7.64}$$

i.e. the imaginary part of the self-energy is due only to hybridization.[315,338] Near $\delta = U/2$, the conductance of SIAM is $G \approx G_0/2$, thus $\phi \sim \pi/4$. Impurity 2 is decoupled and its Green's function is known exactly. The effect of impurity 2 in the $t \neq 0$ is taken into account using perturbation theory and the full Green's function is obtained from the Dyson's equation

$$\mathcal{G}_1 = \mathcal{G}_1^0 + \mathcal{G}_1^0\Sigma\mathcal{G}_1 = \frac{\mathcal{G}_1^0}{1 - \Sigma\mathcal{G}_1^0} = \mathcal{G}_1^0/(1 - t^2\mathcal{G}_1^0\mathcal{G}_2^0), \tag{7.65}$$

since the self-energy is $\Sigma = t^2\mathcal{G}_2^0$. For the Fano resonance at $\epsilon = \delta - U/2 \sim 0$, we keep only the low-energy pole in the Green's function of impurity 2,

$$\mathcal{G}_2^0(\omega) \approx \tfrac{z}{\omega - \epsilon + i\eta}, \tag{7.66}$$

where $z = \frac{1}{2}$ for $\epsilon < 0$ and $z = 1$ for $\epsilon > 0$. The conductance $G = G_0\pi\Gamma(-1/\pi\mathrm{Im}\,\mathcal{G}_1)$ is

$$G = G_0\frac{2\Gamma^2\epsilon^2\sin^2\phi}{z^2t^4 + 2\Gamma^2\epsilon^2 - z^2t^4\cos(2\phi) - 2zt^2\epsilon\Gamma\sin(2\phi)}. \tag{7.67}$$

Results of the NRG calculation are compared to the prediction from Eq. 7.67 in the inset of Fig. 7.21g. We see that general features are adequately described, but there are subtle

differences due to non-perturbative electron correlation effects. Numerically calculated Fano resonance is wider than the semi-analytical prediction and G does not drop to zero. In particular, from Eq. 7.67 it follows that $G = 0$ at $\delta = U/2$ (or $\epsilon = 0$) and $G = G_0$ at $\delta = U/2 + t^2 \tan\phi/\Gamma$. These details are not corroborated by NRG results which show, for example, *maximal* conductance at $\epsilon = 0$.

With increasing t, the width of the resonance increases, as shown for $t/D = 0.01$ in Fig. 7.21f. For $t \gtrsim 0.1$, the resonance merges with the Kondo plateau and disappears (see Fig. 7.16a).

7.3.3 Weak inter-dot coupling: the two-stage Kondo effect

The *two-stage Kondo effect* is a generic name for successive Kondo screening of the impurity local moments at different temperatures.[69–71,75,152,174,183,188] This term has been used in two different (but closely related) contexts: 1) two step screening of $S = 1$ spin in the two-channel case,[152] 2) two step screening of two local moments in the single-channel case.[70,71,174] In the first case, the first-stage Kondo screening is an underscreened $S = 1$ Kondo effect which reduces the spin to 1/2, while the second-stage Kondo screening is a perfect-screening $S = 1/2$ Kondo effect which leads to a spin singlet ground state.[70,233] In the second case, at a higher Kondo temperature $T_K^{(1)}$ the Kondo effect occurs on the more strongly coupled impurity; the Fermi liquid quasiparticles associated with the Kondo effect on the first impurity participate in the Kondo screening of the second impurity on an exponentially reduced Kondo temperature scale $T_K^{(2)}$.[174,183,188] The first case is relevant when the ground state is a triplet, while the second case occurs when the ground state is a singlet, but there is a nearby excited triplet state.[71] In fact, the two cases are connected through a quantum phase transition which occurs at the degeneracy point between the singlet and triplet state;[71,174] this also demonstrates the connection between the two-stage Kondo effect and the "singlet-triplet" Kondo effect.[70]

In the case of the side-coupled DQD, the inter-impurity exchange interaction is antiferromagnetic and it is given by the superexchange expression

$$J = \frac{t}{2}\left(\sqrt{\left(\frac{U}{t}\right)^2 + 16} - \frac{U}{t}\right) \approx \frac{4t^2}{U}. \tag{7.68}$$

The two-stage Kondo effect of the second type occurs when $J < T_K$, where $T_K = T_K^{(1)}$ is the Kondo temperature of the SIAM that describes impurity 1 (without impurity 2).[183,188] The second Kondo crossover then occurs at

$$T_K^{(2)} = c_2 T_K^{(1)} \exp(-c_1 T_K^{(1)}/J). \tag{7.69}$$

Constants c_1 and c_2 are of the order of 1 and they are problem-dependent. The spectral function $A_1(\omega)$ of impurity 1 increases at $\omega \sim T_K^{(1)}$, but then drops at $\omega \sim T_K^{(2)}$, i.e. there

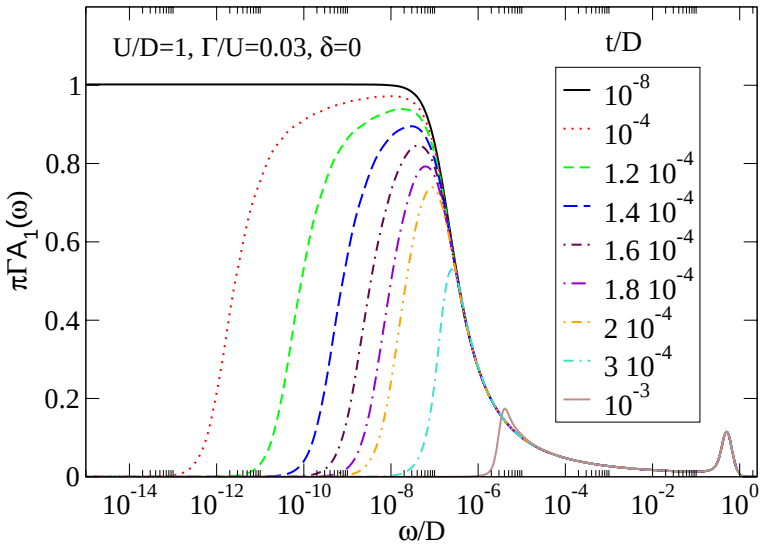

Figure 7.22: Spectral function on the directly coupled impurity 1 for a range of values of the interdot hopping parameter t.

is a gap in the spectral function and the system is non-conducting at zero temperature, Fig. 7.22. In magnetic susceptibility plots, the two-stage Kondo effect manifests as two successive decreases of the susceptibility which both have the form of the universal $S = 1/2$ Kondo susceptibility curves; the first from 1/2 to 1/4 occurs at $T \sim T_K$ and the second from 1/4 to 0 at $T_K^{(2)}$,[183] Fig. 7.23.

If, however, $J > T_K$, the impurity spins bind in a singlet before any Kondo effect can occur. There is again a gap of width J in the spectral function and conductance is zero for $T < J$. It should be noted that from the zero-temperature conductance plots alone we cannot determine if the system underwent two-stage Kondo screening or if a local singlet was formed; in fact, the $T = 0$ fixed point is the same in both cases and, moreover, the two regimes are continuously connected.[174]

Equipped with this theory, we now return to the description of the results presented in Fig. 7.21a for $\delta < U/2$. Just below $\delta < U/2$, $J < T_K^{(1)}$ and the system is in the two-stage Kondo regime. In the range of δ where T falls in the interval given by $T_K^{(2)} \ll T \ll T_K^{(1)}$, the conductance is high. For still lower δ, $T < T_K^{(2)}$ and the conductance decreases. Finally, for lowest δ, $J > T_K^{(1)}$ and the system is in the local singlet regime where the conductance is zero. NRG results for the gap in the spectral function $A_1(\omega)$ calculated at $T = 0$ (open circles and squares) follow analytical results for $T_K^{(2)}(\delta)$ when $J < T_K^{(1)}$ and they approach J when $J > T_K^{(1)}$, as expected, see Fig. 7.21h.

As shown in Fig. 7.21a for $0.3D \lesssim \delta < U/2$, G/G_0 calculated at $T = 10^{-9}D$ follows results obtained in the single quantum dot case and approaches value 1. The spin quantum number S in Fig. 7.21b reaches the value $S \sim 0.8$, consistent with the result obtained for a system

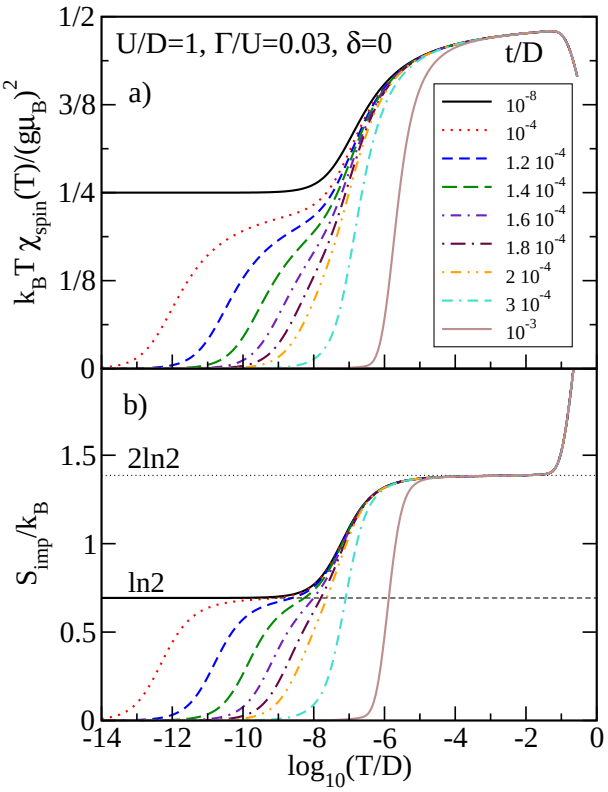

Figure 7.23: Spin susceptibility and specific heat of the side-coupled double quantum dot for a range of values of the interdot hopping parameter t. We begin to enter the two-stage Kondo regime for $t/D \lesssim 1.8\ 10^{-4}$.

of two decoupled spin-1/2 particles, where $\langle \hat{\mathbf{S}}^2 \rangle = 3/2$. This result is also in agreement with $\langle n \rangle \sim 2$ and the small value of the spin-spin correlation function $\langle \mathbf{S}_1 \cdot \mathbf{S}_2 \rangle$, presented in Fig. 7.21c and 7.21e respectively.

With further decreasing of δ, G/G_0 suddenly drops to zero at $\delta \lesssim 0.3D$. This sudden drop is approximately given by $T \sim T_K^{(2)}(\delta)$, see Figs. 7.21a and h. At this point a gap opens in $A_1(\omega)$ at $\omega = 0$, which in turn leads to a drop in the conductivity. The position of this sudden drop in terms of δ is rather insensitive to the chosen T, as apparent from Fig. 7.21h.

Below $\delta \lesssim 0.25D$, which corresponds to the condition $J \sim T_K^{(1)}(\delta)$, also presented in Fig. 7.21h, the system crosses over from the two-stage Kondo regime to a regime where spins on DQD form a singlet. In this case S decreases and $\langle \mathbf{S}_1 \cdot \mathbf{S}_2 \rangle$ shows strong antiferromagnetic correlations, Figs. 7.21b and e. The lowest energy scale in the system is J, which is supported by the observation that the size of the gap in $A_1(\omega)$ (open circles in Figs. 7.21h) is approximately given by J. The main difference between $t/D = 0.001$ and $t/D = 0.01$ comes from different values of $J = 4t^2/U$. Since in the latter case J is larger, the system enters the AFM singlet regime at much larger values of δ, as can be seen from comparison

of Figs. 7.21g and f. Consequently, the regime of enhanced conductance shrinks.

7.4 Double quantum dots in magnetic field

In Fig. 7.4 I plot the conductance through the double quantum dot systems of different coupling topologies as a function of the inter-dot exchange coupling J and of the applied magnetic field B. The parameters entering the corresponding quantum impurity models are chosen so that U and Γ are the same in all cases. The effect of the magnetic field on the conductance through the double quantum dot depends strongly on the type of the Kondo effect which occurs in the system.

In the side-coupled DQD, two-stage Kondo screening occurs when $J < T_K^{(1)}$. In this regime, the conductance is unitary if $T_K^{(2)} \ll B \ll T_K^{(1)}$, but it drops to zero for $B \ll T_K^{(2)}$ and for $B \gg T_K^{(1)}$. This is clearly visible in Fig. 7.4a. For the smallest values of J shown, $T_K^{(2)}$ is essentially zero and the conductance is high for B below $T_K^{(1)} \sim 10^{-4}D$. For J of the order of $T_K^{(1)}$, non-monotonous field-dependence of the conductance can be observed with a high-conductance plateau in the range $T_K^{(2)} \ll B \ll T_K^{(1)}$. This plateau evolves for $J > T_K^{(1)}$ into increasingly narrow peak centered near $B \sim J$. For $B = J$, the singlet and the lowest triplet state are degenerate and the system conducts due to the singlet-triplet Kondo effect. This plot therefore clearly establishes the relation between the two-stage Kondo effect and the singlet-triplet Kondo effect : they are the two extreme limits of the same type of behavior related to the near-degeneracy of singlet and triplet states.

In the serially-coupled DQD, the conductance is high in the absence of the field only when $J \sim T_K^{(1)}$. For smaller J, each impurity tends to form a separate Kondo correlated state with the neighboring conduction lead, and the conductance is low. For larger J, the impurities form a strongly-bound inter-impurity spin-singlet state, which again leads to low conductance. For $J \sim T_K^{(1)}$, the system crosses over between these two regimes and the conductance exhibits a unitary peak. It is interesting to note that the related two-impurity Kondo system undergoes a true quantum phase transition with non-Fermi liquid properties at the critical point at $J \sim T_K^{(1)}$, however the charge transfer between the two channels destabilizes this NFL fixed point[93] in the case of the serially-coupled DQD where the exchange interaction is generated by the superexchange mechanism due to the electron hopping ; similar behavior is found in the triple quantum dot system presented in the following chapter. The lowest value of B shown in Fig. 7.4b is much lower than $T_K^{(1)}$, therefore the behavior is similar to the one in the absence of the field, with the exception that the highest conductance does not quite reach the unitary limit. For stronger fields, we obtain the singlet-triplet Kondo effect as in the case of the side-coupled DQD.

The parallel DQD undergoes $S = 1$ Kondo screening for $J < J_{\mathrm{RKKY}}$. The expected very slow (logarithmic) approach to the unitary conductance limit is clearly visible in Fig. 7.4c. For small B, the conductance drops abruptly to zero when J is increased past J_{RKKY},

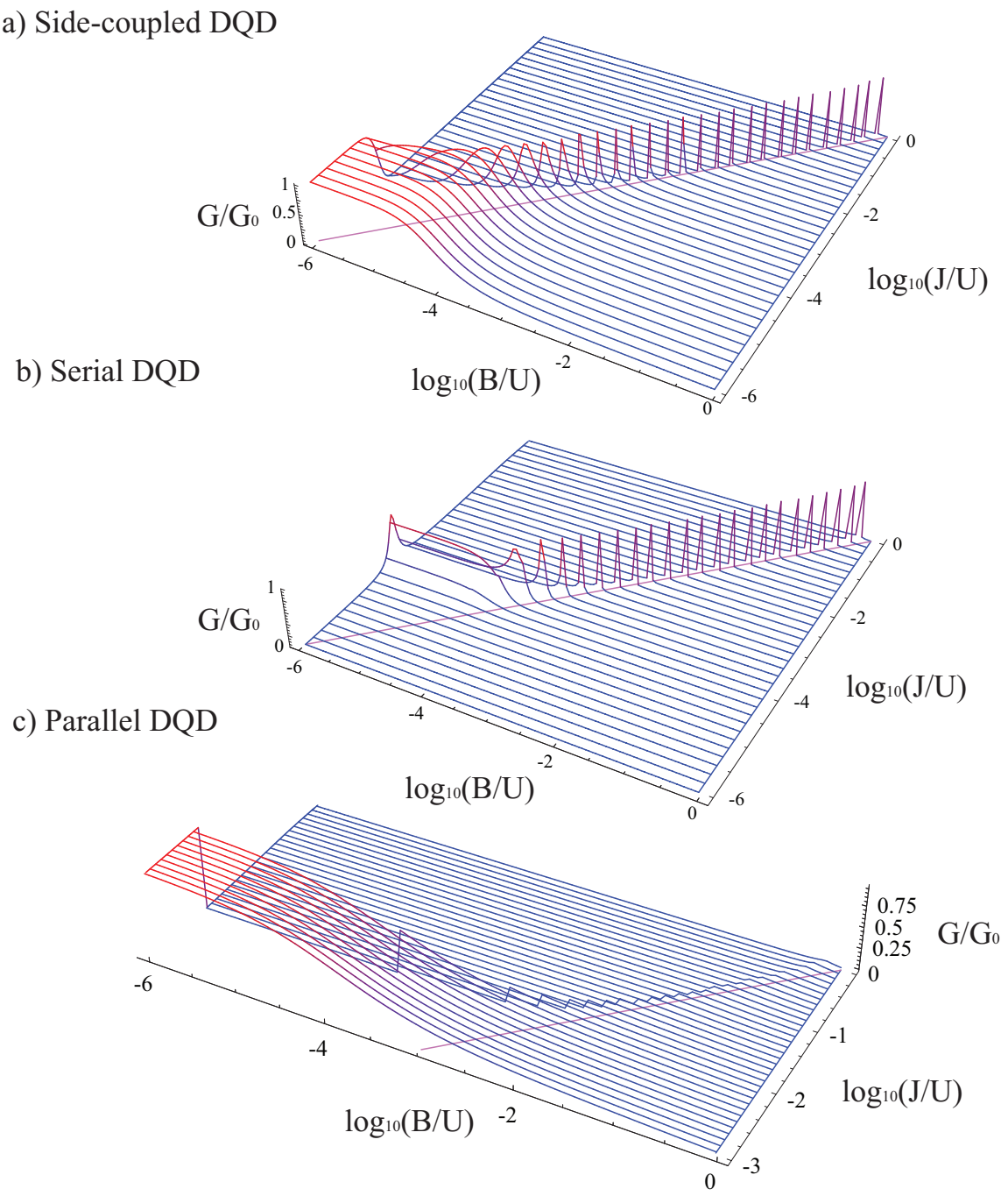

Figure 7.24: Conductance of double quantum dot systems of different coupling topologies as a function of the inter-dot antiferromagnetic exchange interaction J and of the applied magnetic field B. The parameters are the same in all three cases: $U/D = 1$, $\Gamma/D = 0.05$, $\delta = 0$. Conductance is calculated by extracting quasiparticle phase shifts. In the plots for side-coupled and serial DQD, data points with $G/G_0 = 1$ have been added to the singlet-triplet Kondo peaks a posteriori for presentation purposes, therefore the widths of these narrow peaks are, in fact, largely exaggerated.

since the spins bind into a singlet and the Kondo effect no longer occurs. For large B, the decrease in conductance is less pronounced. It should be noticed that there is no singlet-triplet Kondo effect in this system.

Chapter 8

Properties of three-impurity models

While the two-impurity models were intensely studied in the past (and still are), the attention is recently shifting to more complex three-impurity models. Near the particle-hole symmetric point (or, equivalently, at half filling), systems with even or odd number of QDs have radically different behavior due to the distinct properties of integer and half-integer spin states. The half-integer spin states are always degenerate and QD systems with such ground states tend to exhibit some form of the Kondo effect for any coupling strength; the zero-temperature conductance of systems of an odd number of dots will be high. In systems with an even number of QDs, however, the range of half filling is generally associated with Mott-Hubbard insulating behavior.[273] The prototype three-impurity model describes the triple quantum dot (TQD) system in the linear configuration, usually modelled as a three-site Hubbard chain embedded between two non-interacting electron reservoirs (conduction leads). TQD structures have been manufactured in recent years and the analysis of their stability diagrams demonstrates that a description with a Hubbard-like model is indeed a good approximation.[339,340] Models of three Anderson-like impurities have already been studied by a variety of techniques in different temperature regimes.[24,189,190,327,341–347] While many features were previously known, detailed understanding of the underlying microscopic mechanisms emerged only recently.[157,158]

In this chapter I study linear TQDs. The special feature of this system is the presence of two equivalent screening channels (as in the 2CK model) combined with two-stage Kondo screening and/or magnetic ordering. The main message conveyed by this chapter is that the three-dot structures are a promising system for both theoretical and experimental study of NFL physics.[24,158] The relevance of these results is reinforced by the recent detection of the 2CK effect in a system of a QD coupled to leads and to a quantum box:[272] exotic Kondo effects can indeed be detected in semiconductor nanoelectronic devices.

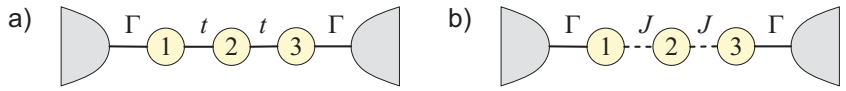

Figure 8.1: a) Model I: the triple quantum dot embedded between two leads. b) Model II: a related system with exchange interaction between the impurities.

8.1 Triple quantum dot: linear configuration

In this section, I consider two different but closely related systems of three Anderson impurities coupled in series between two conduction channels, Fig. 8.1. They are described by the Hamiltonian $H = H_{\rm band} + H_{\rm imp} + H_{\rm c}$, where

$$H_{\rm band} = \sum_{\nu,k,\mu} \epsilon_k c^\dagger_{\nu k\mu} c_{\nu k\mu} \tag{8.1}$$

describes the left and right conduction lead ($\nu = L, R$), and

$$H_{\rm c} = \sum_{k\mu} V_k (c^\dagger_{Lk\mu} d_{1\mu} + c^\dagger_{Rk\mu} d_{3\mu} + {\rm H.c.}) \tag{8.2}$$

describes the coupling of the bands to the left and right impurity (numbered 1 and 3, while 2 is the impurity in the middle, Fig. 8.1). In model I, $H_{\rm imp}$ is the Hubbard Hamiltonian

$$H^{\rm I}_{\rm imp} = \sum_{i=1}^{3} H_{{\rm dot},i} + \sum_{i=1}^{2} \sum_{\mu} t \left(d^\dagger_{i\mu} d_{i+1,\mu} + {\rm H.c.} \right), \tag{8.3}$$

with

$$H_{{\rm dot},i} = \delta(n_i - 1) + \frac{U}{2}(n_i - 1)^2, \tag{8.4}$$

where, as before, δ is the on-site energy (gate voltage), U is the on-site e-e repulsion, $n_i = \sum_\mu d^\dagger_{i\mu} d_{i\mu}$ is the electron number on site i and t is the inter-impurity hopping. Model II is the exchange-only variant of the model I, with

$$H^{\rm II}_{\rm imp} = \sum_{i=1}^{3} H_{{\rm dot},i} + J\mathbf{S}_1 \cdot \mathbf{S}_2 + J\mathbf{S}_2 \cdot \mathbf{S}_3, \tag{8.5}$$

where $\mathbf{S}_i = \sum_{\mu\mu'} d^\dagger_{i\mu} (1/2\boldsymbol{\sigma}_{\mu\mu'}) d_{i\mu'}$ is the spin operator on site i, and J is the exchange constant. We set J to the superexchange value of $J = 4t^2/U$ to relate the two models for $t \ll U$. In two-channel QIMs, two different types of the particle-hole symmetry may be realized, see Sec. 2.3.5 and Refs. 21, 28. For $\delta = 0$, models I and II both have p-h symmetry of the first type. As I show below, this has important consequences on the zero-temperature conductance through the QD molecules.

The ground state of model I is Fermi liquid (FL) for any choice of parameters.[158,189,190] If, however, the impurities are coupled only by exchange interaction, as in model II, the system has a non-Fermi liquid (NFL) ground state of the 2CK type with a residual $\ln 2/2$ zero-temperature entropy.[28,80] Replacing spin exchange interaction with hopping (i.e., going from model II to model I) enables charge transfer between the left and right conduction channels, thereby inducing channel asymmetry[24,93] which drives the system to a FL ground state.[28] Nevertheless, model I exhibits NFL properties in an interval of finite temperatures where the system approaches the (unstable) 2CK fixed point. It will be shown in the following (Sec. 8.1.5) that there is in fact a range of hopping parameters t where this temperature interval is particularly wide. As this interval is entered from above, the conductance through the side dots increases to a half of the conductance quantum, while the conductance through the system remains small. At lower temperatures the conductance through the system increases to the unitary limit as the system crosses over to the FL ground state.

While our main tool will again be NRG, in this section comparisons with other methods are also made. In particular, the zero-temperature conductance will be computed using the sine formula (Sec. 5.2) with energies of the auxiliary ring system obtained using the constrained-path quantum Monte Carlo (CPMC), Sec. 4.3, and with the Gunnarson-Schönhammer variational method (GS), Sec. 4.2. The CPMC calculations were performed on a ring of 100-180 sites. As the number of sites with interaction is small, CPMC produces ground state energies with excellent precision, typically of the order of $\Delta E/E = 10^{-6}$. On the other hand, the constrained number of sites in the ring limits the energy resolution of this approach. With GS, the size of the ring can be increased up to a few thousands sites. While this improves the energy resolution by an order of the magnitude, none of these two methods can compete with NRG which can in principle handle arbitrarily small energy scales. In this section, I discuss both dispersionless bands (NRG calculations) and cosine bands (NRG, CPMC, GS calculations). In the latter case, $\Gamma = 2t'^2/t$, where t' is the coupling between sites 1 and 3 of the TQD and the first sites in left and right tight-binding chains.

8.1.1 Mapping to molecular-orbital levels

For large t/U, the TQD system described by model I behaves as an artificial molecule composed of three atoms (QDs). In the non-interacting $U \to 0$ limit, the molecule has three distinct non-interacting levels: non-bonding (0), bonding (-) and anti-bonding (+) molecular-orbitals (Fig. 8.2) with energies

$$E_{\pm,0} = \pm\sqrt{2}t, 0 \tag{8.6}$$

and effective hybridizations

$$\Gamma_{\pm,0} = \frac{3}{8}\Gamma, \frac{1}{2}\Gamma. \tag{8.7}$$

When interactions are switched on, the non-bonding level remains at $E_0 = 0$, while the other two are symmetrically shifted to $E_\pm \sim \pm(\sqrt{2}t + \frac{5}{16}U) + \mathcal{O}(U^2/t)$ where the U-term is a consequence of the inter-orbital repulsion. The effective intra-orbital e-e repulsion is given by $U_\pm \sim \frac{3}{8}U + \mathcal{O}(U^2/t)$ and $U_0 \sim \frac{1}{2}U + \mathcal{O}[U^3/t^2]$. These molecular orbitals are spatially extended throughout the TQD system even in the presence of interactions. It should be noted that bonding and anti-bonding wavefunctions are symmetric (even parity), while the non-bonding wavefunction is antisymmetric (odd parity), Fig. 8.2.

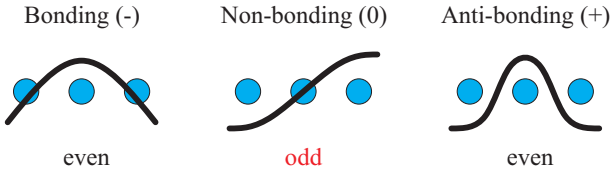

Figure 8.2: Molecular-orbitals in a linear artificial molecule

The energy-level structure of the system can be conveniently represented in the form of the eigenvalue diagram (see also Sec. 7.3.1). In Fig. 8.3 I show the case of both large t/U and small t/U. In the latter case, the description in terms of molecular-orbital levels breaks down. The features in these diagrams will be commented in more detail in the following.

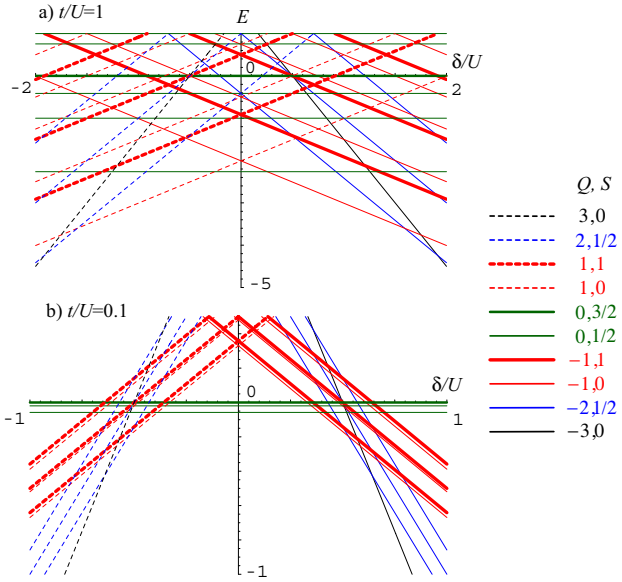

Figure 8.3: The energy-level structure for the decoupled TQD system in the case of a) strong and b) weak inter-impurity tunnel coupling.

8.1.2 Phase diagram and physical regimes

The zero-temperature phase diagram of the TQD system, Fig. 8.4, features several phases with enhanced conductance which will be discussed in this section.

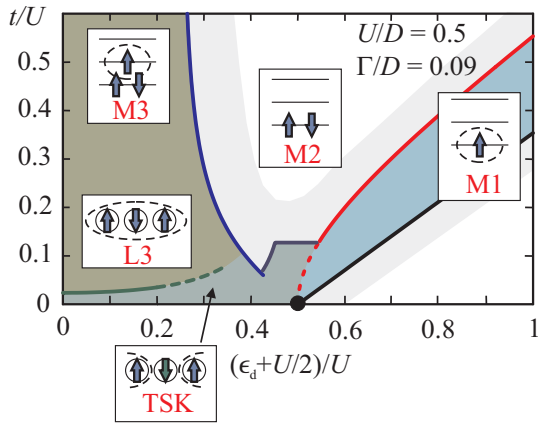

Figure 8.4: M1, M3: *MO* Kondo regime with $\langle n\rangle \sim 1, 3$. M2: non-conductive even-occupancy state. L3: local Kondo regime with $\langle n\rangle \sim 3$. TSK: two-stage Kondo regime. Due to the p-h symmetry, the diagram is mirror-symmetric with respect to the $\delta = 0$ axis; for negative $\delta < 0$ we thus find M4 non-conductive regime and M5 *MO* Kondo regime.

For large t/U, the molecular-orbital levels are filled consecutively by electrons as the gate voltage is swept; this is clearly visible in the diagram a of Fig. 8.3, where the total number of electrons in the ground state $N = Q + 3$ increases in steps of 1 at well separated gate voltages δ. Each molecular orbital can accommodate two electrons, which bind into a spin singlet ($S = 0$ for N even). The ground state is thus a spin doublet ($S = 1/2$) only when the total occupancy N is odd, i.e., when there is a single electron in one of the molecular orbitals. Model I then maps to an effective SIAM and we say that the system is in the *molecular-orbital* (*MO*) Kondo regime (shaded regions labelled 'M1' and 'M3' in Fig. 8.4). The unpaired electron develops local moment for $T \lesssim U_{\rm eff}$, where $U_{\rm eff}$ is U_0 for $Q = 0$ ($N = 3$) or $U_\pm$ for $Q = \pm 2$ ($N = 1, 5$). The local moment is then Kondo screened in the conventional single-channel Kondo effect by the electrons in the leads. Depending on the symmetry of the relevant orbital wave-function (even for bonding and anti-bonding levels and odd for non-bonding level), the Kondo effects occurs either in the even or odd conduction channel formed by the symmetric or antisymmetric combination of conduction band electrons. The Kondo temperatures $T_{\pm,0}$ for levels $(\pm, 0)$ can be determined from Eq. (6.32) with effective parameters $U_{\rm eff}$ and $\Gamma_{\rm eff}$, where $\Gamma_{\rm eff}$ is Γ_0 or $\Gamma_\pm$. Just like in the case of a single-impurity Anderson model, in *MO* Kondo regime the conductance approaches $G = G_0$ for low temperatures, $T \ll T_{\pm,0}$, while for intermediate temperatures $T_{\pm,0} \ll T \ll U_{\rm eff}$ the system is in the Coulomb blockade regime with $G \sim 0$ except along the border lines. Lightly shaded stripes of width $\sim \Gamma_{\rm eff}/2$ represent the transition regions, where $G/G_0 \lesssim 0.5$. Phase 'M2' is a non-conductive even-occupancy singlet regime, where two electrons occupy the same molecular-orbital.

The orbital description breaks down for small t/U. Referring back to Fig. 8.3b, this is reflected in near degeneracy of several many-particle states. The excitation energies are no longer on the scale of $U_{\rm eff}$, but rather on the smaller magnetic scale of the superexchange

interaction, $J = 4t^2/U$. Each impurity then behaves as a separate magnetic moment and the system properties are qualitatively different. We refer to this regime as the *local* regime. The behavior of the system is most easily understood around the p-h symmetric point $\delta = 0$. For decreasing t/U, the *MO* Kondo regime 'M3' is followed by antiferromagnetic spin-chain (*AFM*) Kondo regime 'L3' and two-stage Kondo (*TSK*) regime 'TSK'. In all three regimes, the conductance is unitary below the respective Kondo temperature which is a function of t.

In *AFM* regime, three on-site local moments bind at $T \sim J = 4t^2/U$ into a rigid antiferromagnetic spin-chain with total spin 1/2; this is followed by the screening of the collective spin by the Kondo effect at some lower temperature. Using SWT it can be shown that the collective spin couples more strongly to the odd channel than to the even channel, Fig. 8.5. Consequently the Kondo effect again occurs in the odd channel (see Sec. 6.2), like in the case of the *MO* Kondo effect for the non-bonding molecular orbital. The transition between *MO* 'M3' regime and *AFM* regime is very smooth; it is determined by the competition between kinetic (t) and magnetic ($J = 4t^2/U$) scales.

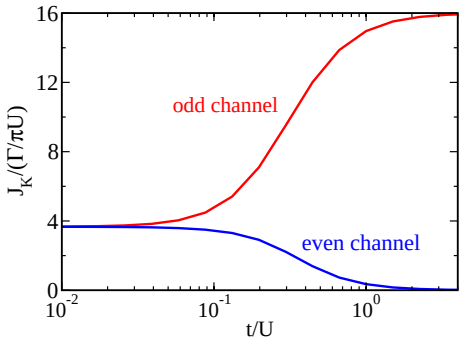

Figure 8.5: The effective Kondo exchange interaction between the ground doublet of the TQD and the conduction band electrons in even and odd channels as a function of the inter-dot tunneling. The results are meaningful only for *MO* and *AFM* regimes, where the lowest-energy doublet is sufficiently separated from the first excited states.

In *TSK* regime, due to very weak coupling of the middle dot, the moments are quenched successively: on left and right dot at the upper Kondo temperature $T_K^{(1)}$, while on middle dot at an exponentially reduced lower Kondo temperature (Sec. 7.3 and Refs. 157, 174, 183, 188):

$$T_K^{(2)} \propto T_K^{(1)} \exp(-cT_K^{(1)}/J). \tag{8.8}$$

The cross-over to the *TSK* regimes occurs for $J \sim T_K^{(1)}$.

Note that all three regimes at $\delta = 0$ become qualitatively similar at sufficiently low temperature: the remaining degree of freedom is one spin 1/2 coupled to two Fermi liquids. The most general effective Hamiltonian describing model I that is allowed by the symmetries is the 2CK model with broken channel symmetry.

It was originally suggested that in the local regime with double occupancy, i.e. for t/U small and $\langle n \rangle \sim 2$, the left and right impurities (1 and 3) tend to form two relatively independent Kondo correlated states, while the central impurity (2) plays no important role.[157] We named this the "double Kondo regime". That hypothesis was based on the analogy with the DQD coupled in series between two leads[315] and the two-impurity Kondo problem.[20] In DQD, the two relevant energy scales are the exchange energy $J = 4t^2/U$ and the Kondo temperature $T_K^{(1)}$; for t/U such that $T_K^{(1)} \lesssim J$, the exchange interaction leads to the formation of an inter-impurity singlet. In TQD, two electrons can reduce their energy by hopping within the TQD, therefore instead of J the relevant scale is the kinetic energy linear in t. We thus postulated the existence of a cross-over at $t \sim T_K^{(1)}$ to a double Kondo phase, where the spin of each electron is screened by electrons from the nearest lead. In reality, using NRG calculations I find that the *TSK* regime actually extends in the region of double occupancy and that there is no "double Kondo regime".

In Table 8.1 I give quantitative relations for lines between different phases of the system. Boundaries between phases 'M1', 'M2', 'M3', and 'L3' are determined in the molecular $\Gamma \to 0$ limit by exact diagonalization and expansion to the lowest non-trivial order. The expressions are in excellent agreement with numerical results for conductance presented in the following section. It should be noted that all transitions are smooth cross-overs; there are no abrupt phase transitions.

Phase 1	Phase 2	Condition
empty	M1	$\delta \sim U/2 + \sqrt{2}t$
M1	M2	$\begin{cases} \delta \sim U/2 + 3t^2/U, & t \lesssim U \\ \delta \sim U/8 + \sqrt{2}t, & t \gtrsim U \end{cases}$
M2	M3, L3	$\begin{cases} \delta \sim U/2 - \sqrt{2}t + 3t^2/U, & t \lesssim U \\ \delta \sim U\left(1/4 + \frac{3}{512}(U/t)^2\right), & t \gtrsim U \end{cases}$
M3	L3	$\sqrt{2}t \sim J$
L3	TSK	$J \sim 2T_{1K}$

Table 8.1: Definitions of boundaries and cross-over regions between various phases in Fig. 8.4. Here $J = 4t^2/U$.

Model II has *AFM* and *TSK* regimes separated by the crossover regime. There is clearly no *MO* regime; instead, the *AFM* regime extends to the region of high J, where the two models describe very different physical systems. Since the left and right conduction channels are not communicating (in the sense that there are no $L \leftrightarrow R$ cotunneling processes), the channel symmetry is maintained and a stable 2CK NFL ground state is expected for all J.

8.1.3 Zero-temperature conductance

In model I with $t = 0$, left and right conduction channels become decoupled and the TQD is clearly not conducting. In contrast, for large t this system can be mapped to SIAM (see above) and is fully conducting at the p-h symmetric point.[157, 190, 348] The p-h symmetry of the first type restrains the phase shifts for the even and odd channel, $\delta_{\rm qp}^{\rm even}$ and $\delta_{\rm qp}^{\rm odd}$, to either 0 or $\pi/2$;[21] the conductance, given by

$$G = G_0 \sin^2(\delta_{\rm qp}^{\rm odd} - \delta_{\rm qp}^{\rm even}), \tag{8.9}$$

can thus be either $G = G_0$ or $G = 0$. Consequently, there are only two possibilities: either the conductance is $G = G_0$ down to the $t \to 0^+$ limit, or there is a quantum phase transition to a zero conductance state at some small t. I will show that for $T \ll T_K^{(2)}$ the TQD is also fully conducting in the *TSK* regime for any $t \neq 0$ and that the transition from *AFM* to *TSK* regime is not a phase transition. Weak perturbations from the p-h symmetric point are marginal, therefore the TQD is expected to have an extended region of high $T = 0$ conductance as a function of the gate voltage.

In Fig. 8.6 I present the zero-bias conductance G along with the total occupancy $\langle n \rangle$ as a function of the gate voltage for a range of t and for fixed $U/D = 0.5$ and $\Gamma/D = 0.09$. The conductance is calculated with various methods, as explained in the introduction to this section.

For $t/U \gtrsim 0.2$, the system is in the *MO* regime. As the occupancy monotonically decreases from 6 (full TQD) to 0 (empty TQD), the conductance exhibits well resolved peaks when occupancy is odd and valleys when occupancy is even.[7, 349] In this regime, the conductance obtained with CPMC and GS methods shows good agreement, and the Hartree-Fock method gives reasonably good results.

The local regime emerges for $t/U \lesssim 0.2$. The conductance is unitary near the p-h symmetric point, while in the charge transfer region, $\delta \sim U/2$, the conductance exhibits humps separated by dips. In this range the CPMC method is no more applicable since due to the computational restrictions on the system size, its energy resolution is insufficient to describe the small Kondo scale.

It should be noted that the TQD is fully conducting at the p-h symmetric point for any t and as t/U is reduced the system goes continuously through three different Kondo regimes.

8.1.4 Correlation functions

In Fig. 8.7 I show the ground state expectation values of charge fluctuations $(\delta n_i)^2 = n_i^2 - \langle n_i \rangle^2$ and spin-spin correlations between neighboring $\mathbf{S}_1 \cdot \mathbf{S}_2$ and between side impurities $\mathbf{S}_1 \cdot \mathbf{S}_3$ at the p-h symmetric point as a function of t. These calculations were performed using NRG ($\Lambda = 4$, Campo-Oliveira discretization, truncation with energy cut-off at $12\omega_N$ or at most 2000 states kept).

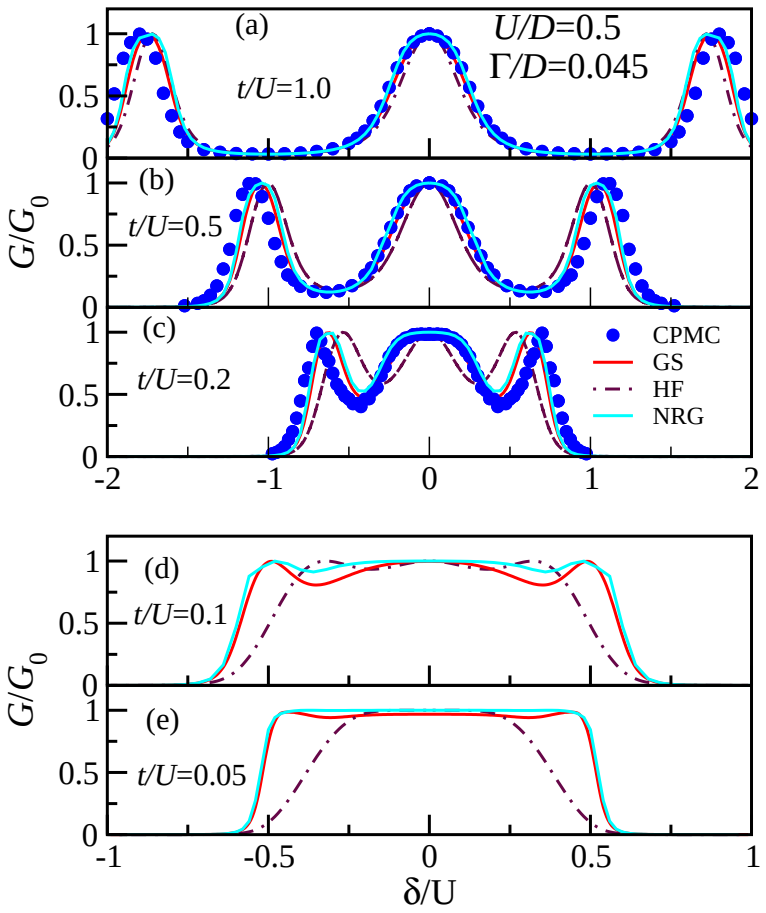

Figure 8.6: Conductance G/G_0 and occupancy $\langle n \rangle$ as a function of the gate voltage for various inter-dot hopping parameters t. Note that the energy scale in panels (d) and (e) is different. Error bars of CPMC are smaller than the size of circles. For comparison the Hartree-Fock (HF) results are also shown.

For model I, the smooth cross-over from *MO* to *AFM* regime, predicted to occur on the scale of $t_1 \sim U/2\sqrt{2}$ (Table 8.1) is reflected in the decrease of charge fluctuations and the increase of spin-spin correlations. The cross-over from *AFM* to *TSK* regime occurs when $J \sim T_K^{(1)}$ or $t_2 \sim \sqrt{T_K^{(1)} U}/2$: as t decreases past t_2 the spin-spin correlations tend toward zero as the spins decouple. For model II, the results in the *TSK* regime match closely those of model I, while in the *AFM* regime near $t \sim t_1$ the differences become notable. Large values of $J \gg \Gamma$ suppress charge fluctuations on side-dots, $(\delta n_1)^2 \to 0$, while local moments on impurities tend to form a well developed *AFM* spin-chain (for comparison, in isolated three-site spin chain $\langle \mathbf{S}_1 \cdot \mathbf{S}_2 \rangle = -1/2$ and $\langle \mathbf{S}_1 \cdot \mathbf{S}_3 \rangle = 1/4$).

If U/Γ is smaller, the local moments on sites 1 and 3 are less well developed since the charge fluctuations are larger, Fig. 8.7b. The characteristic values of the spin correlation functions in the *AFM* regime then cannot be attained. Consequently, the boundaries between various

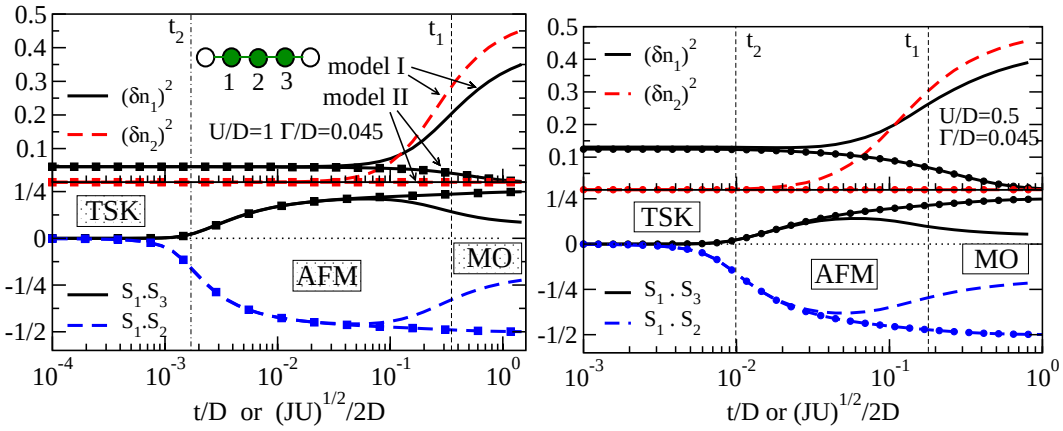

Figure 8.7: Charge fluctuations and spin-spin correlations of model I (lines without symbols) and model II (lines with symbols) as a function of the inter-dot coupling t (for model I) or corresponding $J = 4t^2/U$ (for model II) at the p-h symmetric point. Left panel corresponds to $U/D = 1$, right panel corresponds to $U/D = 0.5$. The molecular-orbital (MO) regime is characterized by large on-site charge fluctuations, the antiferromagnetic spin-chain regime (AFM) by negative spin correlations of neighboring spins 1-2 and positive correlation of spins 1-3, and the two-stage Kondo regime (TSK) by vanishing spin correlations.

regimes are more fuzzy.

We now focus on the local regime with double occupancy, Fig. 8.8 (for reference, results at $\epsilon_d = 0$ are shown in panel b). For small t, I find $\langle c^\dagger_{1\mu} c_{3\mu}\rangle \sim 0$ (not shown) and $\mathbf{S}_1 \cdot \mathbf{S}_3 \sim 0$, which implies that sites 1 and 3 are uncorrelated: the second electron equally occupies symmetric and antisymmetric orbitals $1/\sqrt{2}(c_{1\mu} \pm c_{3\mu})$. This implies that both left and right sites are independent and both form a valence fluctuating state with the neighboring lead. The electron on the central site then undergoes Kondo screening by coupling antiferromagnetically with the quasiparticles from each valence fluctuating state. The screening of spins thus occurs in two stages. The first stage corresponds to the behavior found in the strongly asymmetric Anderson model with $\delta \to U/2$, thus the screening has exponential temperature dependence and is not Kondo-like. The second stage, however, is Kondo-like screening: although δ is near $U/2$ on the central site also, the effective hybridization is very small.

8.1.5 Thermodynamic properties

In Fig. 8.9a we plot the impurity contribution to the magnetic susceptibility and entropy at the p-h symmetric point for $U/D = 1$ and a range of t calculated using NRG ($\Lambda = 4$, $\bar{\beta} = 0.75$, Campo-Oliveira discretization, typically the truncation energy cut-off is set at $12\omega_N$ and up to 3500 states are kept). The ground state of model I is nondegenerate,

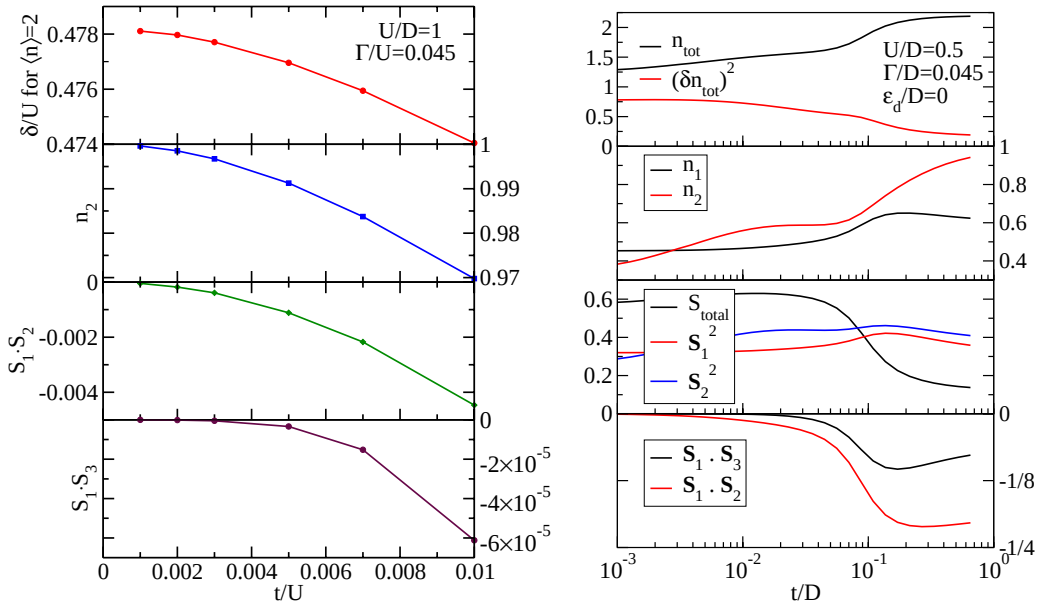

Figure 8.8: a) Properties of the TQD at double occupancy, $\langle n_{\rm tot}\rangle = 2$. b) Correlation functions as a function of the inter-dot coupling t/D for $\epsilon_d = 0$.

$s_{\rm imp} = 0$, and the impurities are fully screened for all t. In *MO* regime the system undergoes single-channel Kondo screening with T_K that increases with t and becomes constant for $t \gg U$, see Fig. 8.10. In this regime the system is well described by effective SIAM with parameters U_0 and Γ_0.

In *AFM* regime, the binding of spins is most clearly discernible in the curves calculated at $t/D = 0.05$ which show a kink in $s_{\rm imp}$ at $3\ln 2$ (local moment formation), followed by an exponential decrease to $s_{\rm imp} = \ln 2$ at $T \sim 4t^2/U$. The Kondo screening in *AFM* regime is of single-channel type for $t/D \gtrsim 0.02$. Between $t/D = 0.02$ and t_2 there is a *cross-over regime* with NFL-like properties. Here magnetic ordering competes with the single-channel Kondo screening of left and right impurity. The magnetic moment is rapidly quenched at $T \sim T_{\rm scr} \sim J$, yet the entropy does not go to zero but exhibits a $\ln 2/2$ NFL plateau.. At still lower temperature T_Δ, NFL fixed point is destabilized by the channel asymmetry and the system crosses over to the FL ground state characteristic of the conventional Kondo model. Note that in this regime $T_{\rm scr}$ is high while T_Δ is low (Fig. 8.10), making this range suitable for experimental study of NFL physics.

In *TSK* regime, the left and right impurity are screened by the single-channel Kondo effect at temperature $T_K^{(1)}$ that is nearly the same for all $t \lesssim t_2$ (Fig. 8.10). The susceptibility is reduced from $\sim 3/4$ to $1/4$ and the entropy from $3\ln 2$ to $\ln 2$. The central impurity is screened by the 2CK effect at $T_K^{(2)}$, below which the system is near the NFL fixed

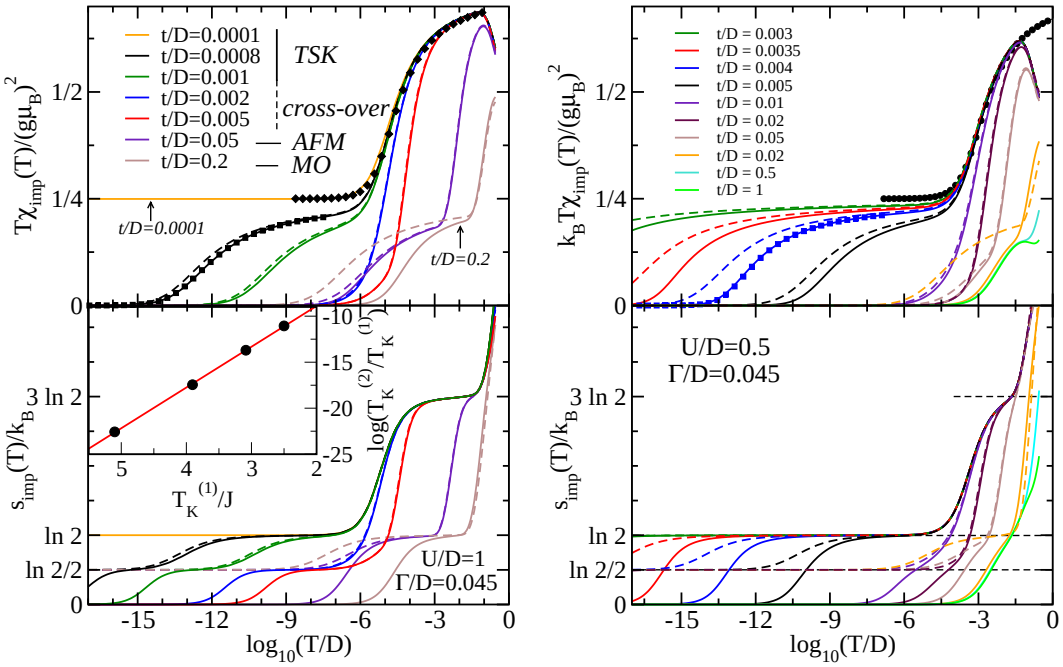

Figure 8.9: Impurity magnetic susceptibility and entropy at $\delta = 0$ for model I (full lines) and model II (dashed line) with $J = 4t^2/U$. Left panel corresponds to $U/D = 1$, right panel to $U/D = 0.5$. Lozenges ♦ are a fit to Bethe-Ansatz results for one-channel Kondo model (multiplied by two and shifted by 1/4) and squares ■ are a fit to NRG results for 2CK model. *Inset:* $T_K^{(2)} = aT_K^{(1)} \exp(-bT_K^{(1)}/J)$ scaling of the second Kondo temperature of model I. $a = 0.97$, $b = 4.4$, $T_K^{(1)}/D \approx 1.0\ 10^{-5}$.

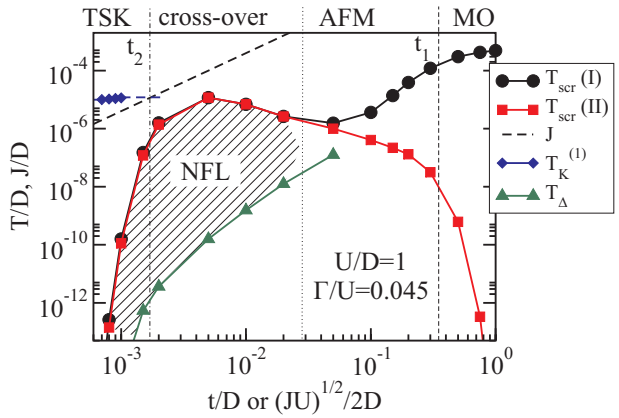

Figure 8.10: Cross-over scales of models I and II as functions of the inter-dot coupling. The magnetic screening temperature $T_{\rm scr}$ is defined by $T_{\rm scr}\chi(T_{\rm scr})/(g\mu_B)^2 = 0.07$; it is equal to the Kondo temperature when screening is due to the single-channel Kondo effect. T_Δ is here defined as $s_{\rm imp}(T_\Delta)/k_B = \ln 2/4$.

point with $\ln 2/2$ entropy. In the inset to Fig. 8.9 we show that $T_K^{(2)}$ scales as $T_K^{(2)} \propto T_K^{(1)} \exp(-cT_K^{(1)}/J)$, as expected for the TSK effect.[174,183,188]

Model II has a stable NFL ground state. For low J, it has a *TSK* regime where the the Kondo temperature $T_K^{(2)}$, determined by J, is lower than that of the corresponding model I, set by $\max\{J_1, J_2\} = J_1 > J$ (Fig. 8.10). In the *crossover regime* physical properties of model II for $T > T_\Delta$ match closely those of model I. In *AFM* regime, the Kondo temperature is a non-monotonous function of J. The energy required to break the doublet spin-chain state increases with J and the effective Kondo exchange constant $J_K \propto \Gamma/J$ decreases. T_K therefore decreases exponentially with increasing J. In contrast, the Kondo temperature of model I in *MO* regime increases monotonically with t and becomes constant for very large t.

The spin-1/2 degree of freedom responsible for NFL behavior is either the collective spin of the three impurities forming a magnetic chain (in *AFM* regime) or the spin of the central impurity (in *TSK* regime). In the cross-over regime, the distinction between the two cases is lost.

For smaller e-e repulsion U, Fig. 8.9b, the cross-over regime is not well developed. Furthermore, the difference between models I and II is accentuated. As previously commented, the models differ in that in model I electrons can cotunnel between one lead to another. The smaller U is, the more likely such tunneling events are, and the larger the channel asymmetry is. Hence, the $\ln 2/2$ plateau in the entropy curve disappears as T_Δ becomes comparable to $T_K^{(2)}$. For constant Γ, U thus controls the degree of the channel symmetry breaking.

8.1.6 Fixed points

NRG eigenvalue flows show that for any $t \neq 0$ (i.e. for *MO*, *AFM* and *TSK* regimes alike), the model I at $\delta = 0$ ultimately flows to the same strong coupling FL fixed point. The spectrum is a combination of two FL spectra: one for odd-length and one for even-length free electron Wilson chain.[29] By performing the calculation in a basis with well defined parity, it can be ascertained that odd channel gathers a $\pi/2$ phase shift, while even channel has zero phase shift. The fixed point eigenvalues of a single chain for $\Lambda = 2$ are

$$\begin{aligned} \eta_j^* &= 0.6555129, 1.976002, 3.999881, \Lambda^4, \Lambda^5, \ldots, \quad N \text{ odd}; \\ \hat{\eta}_j^* &= 1.296385, 2.825966, 5.656852, \Lambda^{7/2}, \Lambda^{9/2}, \ldots, \quad N \text{ even}. \end{aligned} \tag{8.10}$$

The predicted fixed point spectrum fits very well the computed NRG energy levels.

The finite-size spectrum of the unstable intermediate-temperature fixed-point of model I is in agreement with the boundary conformal field theory predictions for the 2CK model[80] (Fig. 8.11). The same fixed point is obtained as the stable zero temperature fixed point for all J in model II. In Fig. 8.12 we plot the NRG eigenvalue flow of model II in the

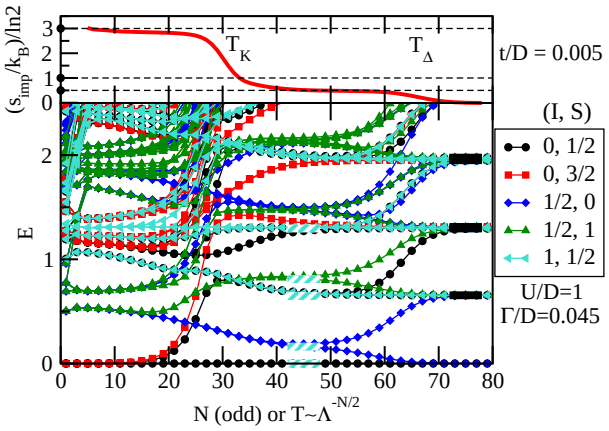

Figure 8.11: NRG eigenvalue flow for odd-length Wilson chains of model I ($\Lambda = 2$, $z = 1$) in the cross-over regime (below) and the corresponding impurity entropy (above). The states are classified according to the total isospin and total spin quantum numbers, (I, S). The low-energy fixed point is a combination of one odd-length and one even-length Wilson chain free-electron spectrum (black full stripes). The black full strips are at energies $0.655 = \eta_1^*$, $1.296 = \hat{\eta}_1^*$, $1.311 = 2\eta_1^*$, $1.952 = \eta_1^* + \hat{\eta}_1^*$, $1.967 = 3\eta_1^*$ and $1.976 = \eta^* 2$. The intermediate-temperature unstable fixed point is the 2CK NFL fixed point. Red hatched strips are at energies (after rescaling by 1.296) 0, 1/8, 1/2, 5/8, 1, as predicted by the boundary conformal field theory approach to the 2CK problem.[80]

TSK regime for both even and odd iteration N. At intermediate temperatures ($N \sim 15$ to $N \sim 35$), the system behaves effectively as a FL with a (nearly) free local moment. This agrees with the qualitative picture of the first stage Kondo effect leading to local Fermi liquid systems, the quasiparticles of which then screen the non-compensated spin on the impurity 2. It may be noted that there is no even/odd alternation in the finite size spectrum at the 2CK fixed point, similar to the case of the single-impurity 2CK model.

The characteristic $0, 1/8, 1/2, 5/8, 1, 1+1/8, \ldots$ sequence of excitation energies in the 2CK model NFL fixed point can be reproduced using free Majorana fermion field theory with appropriately twisted boundary conditions.[76,105,111] The conduction band electrons are of four different types (spin $\mu = \uparrow$ or $\downarrow$, channel $\alpha = L$ or R). We further decompose electrons (Dirac fermions) into real and imaginary parts (Majorana fermions, Appendix F) to obtain eight Majorana fermions in total.[76] These have SO(8) symmetry (see Sec. 2.3). Using bosonization into charge, spin, flavor, and spin-flavor bosons,[109,111] followed by some transformations and the refermionization, it can be shown that the NFL fixed point corresponds to the boundary conditions where three of eight Majorana fermions are twisted and the free conduction band SO(8) symmetry is broken down to SO(3) × SO(5).[76,111]

The spectrum of a system of finite size with one type of free Majorana electrons with periodic boundary conditions (Ramond sector) is[165]

$$E_{\mathrm{R}} = \frac{\pi v_F}{L} k, \quad k = 1, 2, 3, \ldots, \tag{8.11}$$

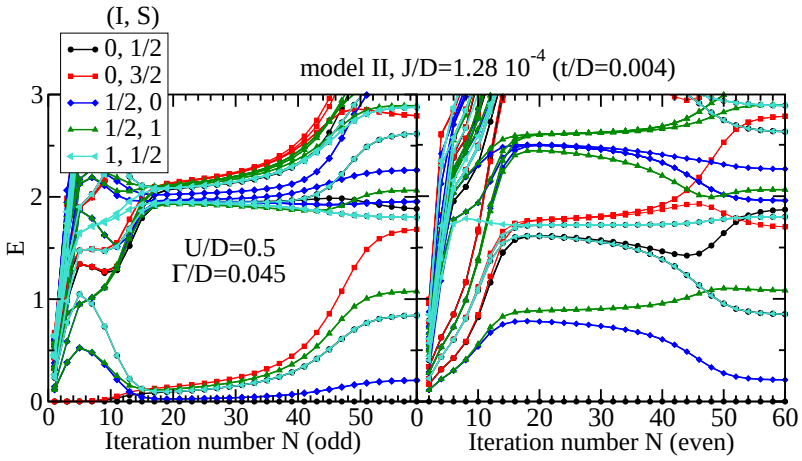

Figure 8.12: NRG eigenvalue flow of model II ($\Lambda = 4$, $z = 1/6$) for odd and even-length Wilson chains. Note that there is no even/odd alternation in the finite size spectrum at the 2CK NFL fixed point.

and with anti-periodic boundary conditions (Neveu-Schwartz sector) is

$$E_{\rm NS} = \frac{\pi v_F}{L} k, \quad k = 1/2, 3/2, 5/2, \ldots. \tag{8.12}$$

Furthermore, the difference in the ground state (vacuum) energy between the two sectors is

$$E_{0,\rm R} - E_{0,\rm NS} = \frac{\pi v_F}{L} \frac{1}{16}. \tag{8.13}$$

Taking into account the twisted boundary conditions, the spectrum is generated by taking three Majorana fermions from one sector and five Majorana fermions from the other.[111] The construction can be presented in a pictorial manner, Fig. 8.13. To obtain the correct degeneracies, one must take into account that the ground state degeneracy of N zero-energy Majorana modes is $2^{[N/2]}$, where $[x]$ denotes the integer part of x. This approach leads to correct energies and degeneracies of the 2CK fixed point.

8.1.7 Robustness of the NFL regime

In model I, the channel symmetry is broken intrinsically by the inter-impurity hopping, which contributes a left-right cotunneling term of the form $J_{\rm LR}\mathbf{S}\cdot(\mathbf{s}_{\rm LR}+\mathbf{s}_{\rm RL})$ to the effective 2CK Hamiltonian. Here $\mathbf{s}_{\rm LR}$ is the left-right spin operator[24]

$$\mathbf{s}_{\rm LR} = \sum_{kk'\mu\mu'} c^\dagger_{Lk\mu}(1/2\boldsymbol{\sigma}_{\mu\mu'})c_{Rk'\mu'}. \tag{8.14}$$

The impurities then couple to a symmetric and antisymmetric (even and odd) combination of channels with exchange constants $J_{\rm S,A} = J_{\rm avg} \pm J_{\rm LR}$. The effective model at intermediate

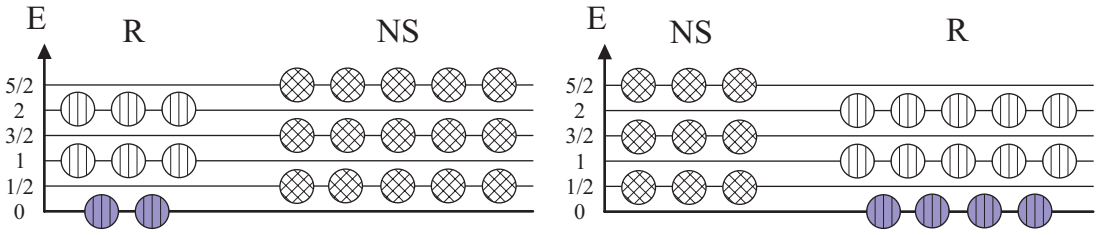

(a) $E = 0$, degeneracy 2

(b) $E = 1/8$, degeneracy 4

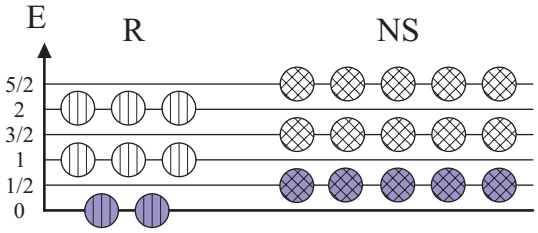

(c) $E = 1/2$, degeneracy 10

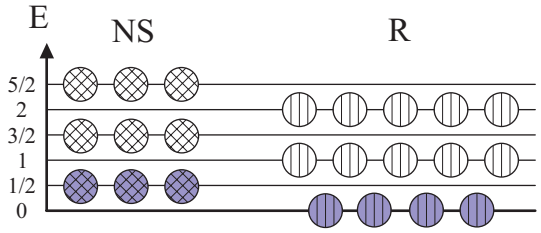

(d) $E = 5/8$, degeneracy 12

Figure 8.13: Schematic representation of the excitation spectrum of the two-channel Kondo model fixed point.

temperature is

$$H_{\text{eff}} = \sum_{k\mu} \sum_{\nu=S,A} \epsilon_k g^\dagger_{k\mu\nu} g_{k\mu\nu} + \sum_{\nu=S,A} J_\nu \mathbf{s}_\nu \cdot \mathbf{S}. \tag{8.15}$$

with

$$g_{k\mu S} = \frac{1}{\sqrt{2}}(c_{k\mu L} + c_{k\mu R}), \quad g_{k\mu A} = \frac{1}{\sqrt{2}}(c_{k\mu L} - c_{k\mu R}), \quad \mathbf{s}_\nu = \sum_{kk'\mu\mu'} g^\dagger_{k\mu\nu}(1/2\boldsymbol{\sigma}_{\mu\mu'}) g_{k'\mu'\nu}. \tag{8.16}$$

Index $\nu = S, A$ here runs over the two effective Fermi-liquid channels. It must be emphasized that these do not correspond to two decoupled semi-infinite conduction leads, but rather to even and odd combinations of the former. Despite its weakness, the channel asymmetry destabilizes the NFL state and leads to the FL fixed point characteristic of the one-channel Kondo model. Since $J_S > J_A$, the second stage Kondo effect occurs in the even channel. As the first stage Kondo effect led to $\pi/2$ phase shifts in both channels, the additional shift of $\pi/2$ in the even channel gives total zero phase shift in this channel (recall that the phase shifts are defined modulo π), while odd channel quasiparticles still experience $\pi/2$ phase shift. This is consistent with the NRG eigenvalue flows presented in the previous subsection.

The asymmetry parameter

$$A = \Delta/\mathcal{J}^2 \tag{8.17}$$

with $\Delta = \rho(J_S - J_A) = 2\rho J_{LR}$ and $\mathcal{J} = \rho(J_S + J_A)/2 = \rho J_{avg}$ determines the cross-over scale[11]

$$T_\Delta / T_K \approx A^2. \tag{8.18}$$

Estimating J_S and J_A for $t/D = 0.005$ using the Schrieffer-Wolff transformation we obtain $A^2 \sim 10^{-6}$, to be compared with $T_\Delta/T_{scr} \sim 10^{-5}$ determined by the NRG calculation. The discrepancy appears due to competing magnetic ordering and Kondo screening (and emerging two-stage Kondo physics); simple scaling approach fails in this case.

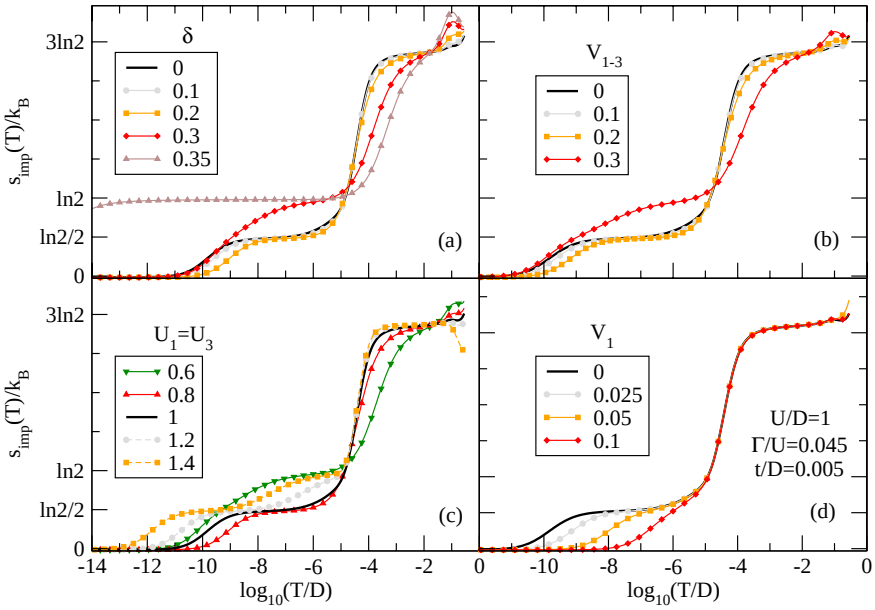

Figure 8.14: Effect of various perturbation terms on the impurity contribution to the entropy. (a) Particle-hole symmetry breaking $\delta \neq 0$. (b) Parity breaking $H' = V_{1-3}(n_1 - n_3)$ (note that the channel asymmetry is not affected by this form of parity breaking). (c) Unequal e-e repulsion $U_1 = U_3 \neq U_2$. (d) "Dangerous" perturbation that breaks channel symmetry $H' = V_1 n_1$.

It is instructive to study the effect of various additional perturbation terms on the stability of the $\ln 2/2$ NFL plateau in the temperature dependence of the impurity contribution to the entropy. We focused on the cross-over regime, which occurs for $U/D = 1$ and $\Gamma/U = 0.045$ around $t/D = 0.005$. We find a high degree of robustness with respect to the p-h symmetry breaking up to $\delta/U \approx 0.2$, Fig. 8.14a, left-right symmetry (parity) breaking up to $V_{1-3}/U \approx 0.2$, Fig. 8.14b, and unequal e-e repulsion parameters, Fig. 8.14c and more detailed 8.15. In this last case we notice that when $U_1 = U_3$ is decreased, the system is pushed towards the *AFM* regime,[158] since the fluctuations on sites 1 and 3 increase and $T_K^{(1)}$ decreases below J. If, however, $U_1 = U_3$ is increased, the system goes into the two-stage Kondo regime since $T_K^{(1)}$ is higher than J. In this latter case, there will still be a $\ln 2/2$ NFL plateau, however the relevant temperature interval is shifted to considerably lower temperatures and becomes narrower.[158] The most dangerous perturbation is the channel-

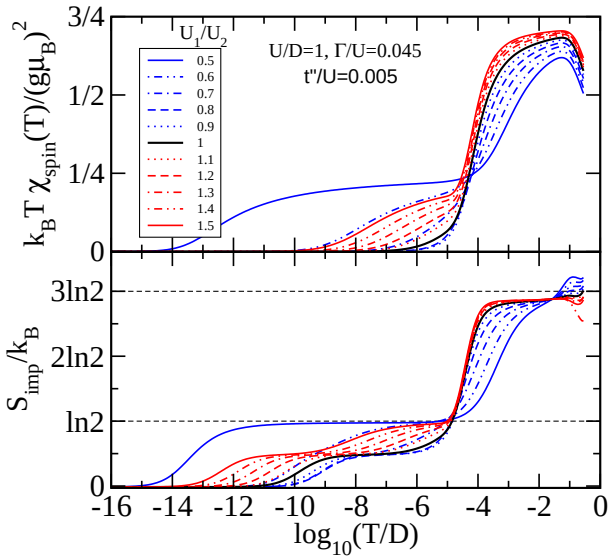

Figure 8.15: Impurity magnetic susceptibility and entropy for the TQD for a range of $U_1 = U_3$, while U_2 is held constant. $\delta = 0$

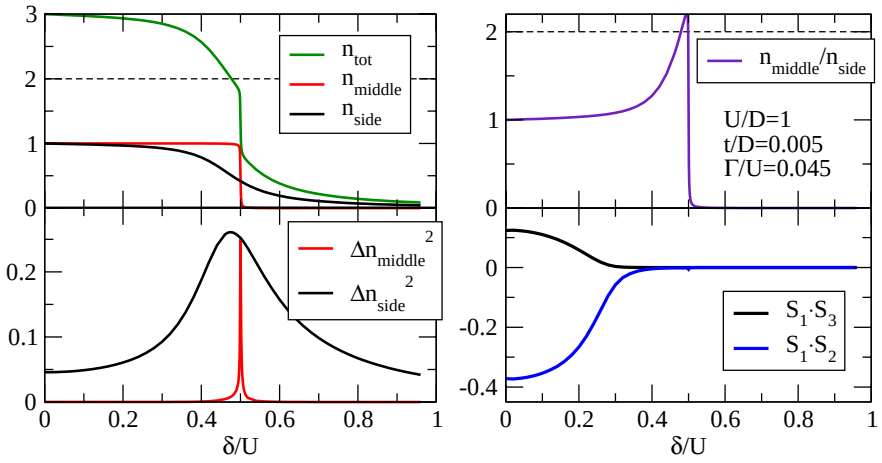

Figure 8.16: Site occupancy, charge fluctuations and spin correlations as a function of the on-site energy δ.

symmetry breaking, Fig. 8.14d, which rapidly wipes out the NFL plateau. It should be noted, however, that those asymmetries of the device that break the left-right symmetry can be corrected using gate voltages in experimental realizations of the three-impurity model where the on-site energies and inter-dot tunneling parameters can be controlled independently.

It is interesting to follow the behavior of correlation functions as the gate voltage δ is swept, Fig. 8.16. We observe that the occupancy of side (left and right) dots decreases and the charge fluctuations increase as we move towards the valence fluctuation regime of the side

dots; the occupancy of the central dot is hardly affected due to its weak effective coupling. An important consequence is the reduction of the spin correlations: the rigid spin chain breaks near $\delta = 0.3U$ and the system enters the two-stage Kondo regime, as is visible in Fig. 8.14a.

8.1.8 Temperature dependence of conductivity

Measuring the differential conductance in a three-terminal configuration (see the insets in Fig. 8.17) provides an experimental probe into the NFL behavior. The qualitative temperature dependence of the zero-bias conductance through the system can be inferred in a very rough approximation from the frequency dependence of the spectral functions. The conductance through the system is given by $G_{\rm serial}/G_0 \approx 4(\pi\Gamma A_{13})^2$ (Ref. 350) and the conductance through a side dot in three-terminal configuration by $G_{\rm side}/G_0 \approx \pi\Gamma A_1$.[351] The appropriately normalized spectral densities are shown in Fig. 8.17 for the cases of cross-over regime with a NFL region and *AFM* regime with no discernible NFL behavior. In the NFL region ($t/D = 0.005$ and $T_\Delta \lesssim T \lesssim T_{scr}$), the conductance $G_{\rm side} \sim 1/2G_0$, while $G_{\rm serial} \sim 0$. The increase of the conductance through the system at $T \lesssim T_\Delta$ is concomitant with the cross-over from NFL to FL fixed point, since charge transfer (or, equivalently, channel asymmetry) destabilizes the NFL fixed point like in the two-impurity case.[93] In the *AFM* regime with no NFL region, both conductances increase below the same temperature scale, i.e. at $T \lesssim T_{scr}$. Measuring $G_{\rm side}$ and $G_{\rm serial}$ could therefore serve as an experimental probe for observation of NFL physics.

In $A_1(\omega)$, the Hubbard peak at $U/2$ corresponds to adding an electron to the site, while the "magnetic-excitation" peak at J appears when, after adding an electron, the electron with the opposite spin hops from the impurity into the band. This breaks the AFM spin chain, increasing the energy by J, see Fig. 8.18. The magnetic peak evolves into a "molecular-orbital" peak at the energy of the non-bonding orbital (for t in *MO* regime) or into the Kondo peak of the side dot [for t in *TSK* regime, see Fig. (8.19)]. It may also be observed that the approach to the $\omega = 0$ limit is different in FL and NFL cases.

8.1.9 Conclusion

In a wide range of gate voltages around the p-h symmetric point, the TQD system has a FL ground state with high conductance at $T = 0$. The different regimes exhibit different approaches to this fixed point. At finite T, the system has NFL properties which can be detected by measuring $G_{\rm side}$ and $G_{\rm serial}$ in a three-terminal configuration. The most likely candidate for observing this 2CK behavior is the cross-over regime with competing magnetic ordering and Kondo screening, $J \sim T_K$. In this regime the NFL behavior occurs in a wide temperature range and it is fairly robust against various perturbation that do not additionally increase the channel asymmetry.

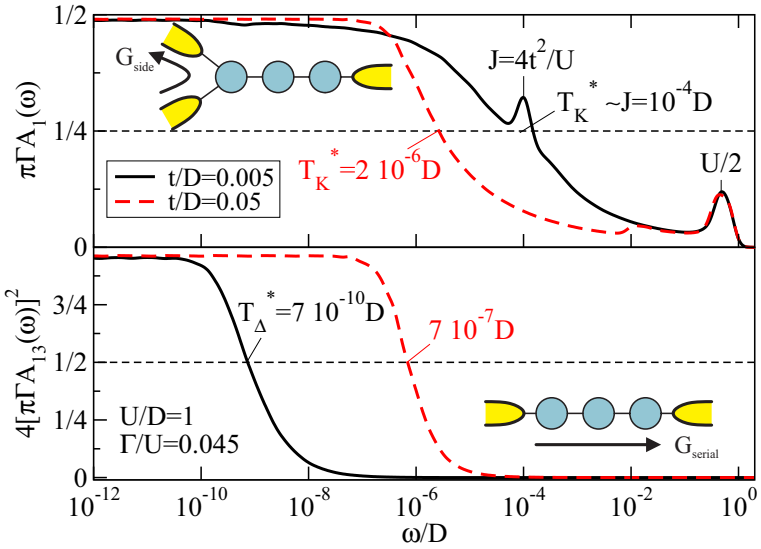

Figure 8.17: Dynamic properties of model I in the AFM (dashed lines) and in the cross-over regime (full lines). Upper panel: on-site spectral function $A_1(\omega)$ of the left dot. Lower panel: out-of-diagonal spectral function $A_{13}(\omega)$ squared. Temperature T^*_Δ is of order T_Δ, T^*_K is of order $T_{\rm scr}$.

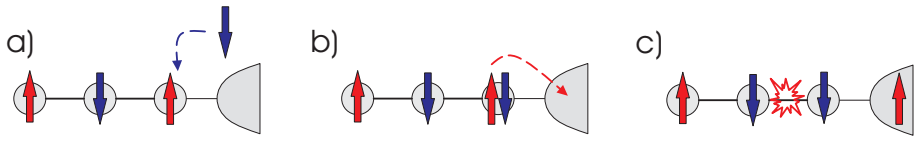

Figure 8.18: The schematic representation of the process leading to a peak at $\omega = J$ in the spectral function $A_1(\omega)$.

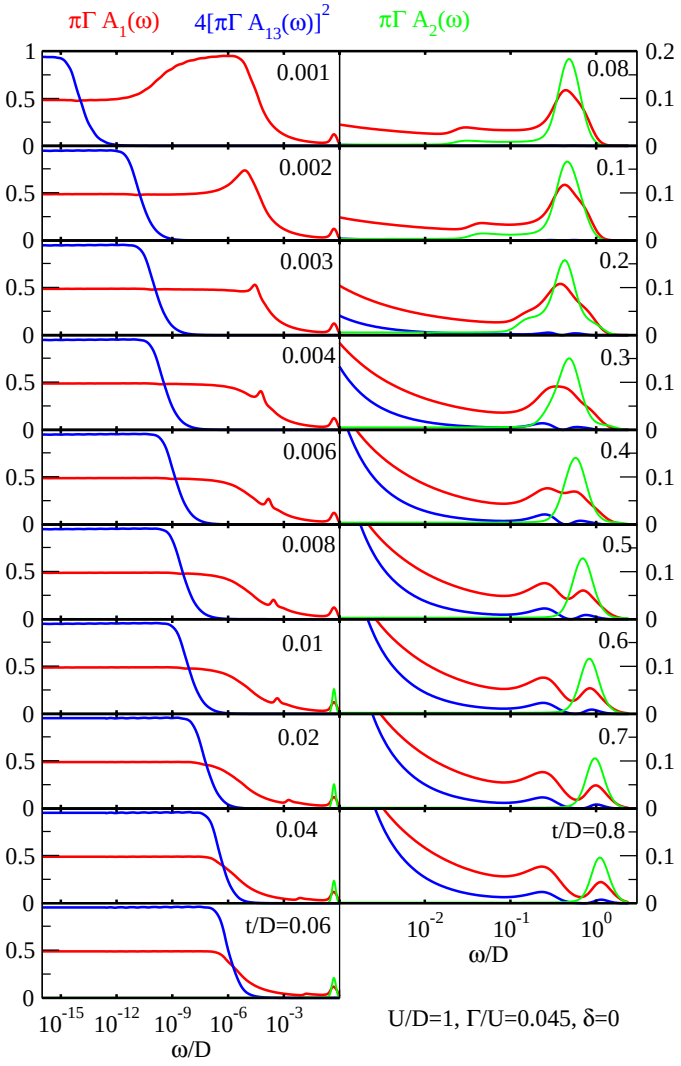

Figure 8.19: The evolution of the spectral functions from the *TSK* regime through *cross-over* to the *AFM* regime.

Part III

Scanning tunneling microscopy and adsorbates

Chapter 9

Scanning tunneling microscopy

The scanning tunneling microscope (STM) was invented by G. Binnig and H. Rohrer in 1982.[352] It brought unprecedented resolution in imaging of surfaces of conducting samples and quickly became one of the prominent tools in surface science. In this chapter I briefly review some of the applications of the scanning tunneling microscopy (Sec. 9.1), describe the construction of a low-temperature STM (Sec. 9.2) and give some background information on ultra-high vacuum systems (Sec. 9.3) and sample preparation (Sec. 9.4). Finally, in Section 9.5 I show some examples of images obtained with the new instrument.

9.1 Applications of the scanning tunneling microscopy

A number of good comprehensive review articles and books on scanning tunneling microscopy and related topics were published in the past.[353–360] These cover general aspects of imaging of clean and adsorbate-covered surfaces, tunneling theory and interpretation of STM images, scanning tunneling spectroscopy and STM hardware. In addition, there is a number of reviews of more specialized subject matters such as imaging of metal surfaces,[361] tunneling theory,[362] interaction of surface states with nanostructures,[363] high resolution image interpretation,[364,365] chemical identification via inelastic tunneling spectroscopy,[366,367] manipulation of atoms[368] and molecules[369] and single-molecule chemistry.[370] In this section I thus only review topics that I personally find particularly interesting.

An important research field where STMs find use is surface chemistry and catalysis of molecules. This domain of research has many immediate applications; some notable examples are organic light emitting diodes, thin film transistors and molecular electronics (the use of single molecules as building blocks of electric circuits[371,372]). In Table 9.1 I list some combinations of organic molecules and surfaces where successful imaging was performed. Topographical STM images of molecules sometimes exhibit atomic scale features. A particularly good example are planar molecules where the molecular "height" is typically 2 Å and the internal structure is visible with $\sim$ 0.4 Å corrugation.[373] Such

planar molecules are highly interesting for molecular electronics; they typically have a central aromatic π board and spacer-groups ("legs") that lift the molecular backbone from the surface.[374,375] Generally, internal structure features agree well with simple Hückel molecular-orbital calculations:[373,376] image contrast is similar to calculated valence charge density. In addition, STM can be used to determine a number of important properties[377] such as adsorbate orientation and binding site,[378,379] diffusion rates,[380–386] molecular conformations,[375,376,387,388] conductance of molecules[389–391] and growth and crystallization of molecules on surfaces.[375,392]

Molecule	Surface	Reference
C_2H_2	Cu(211)	393
C_2H_2	Cu(100)	394,395
butene	Pd(110)	396
CO	Cu(211)	397
CO	Cu(111)	398,399
C_6H_6, CO	Rh(111)	400
benzene	Ag(110)	401
benzene	Pt(111)	378
naphthalene	Pt(111)	379
azulene	Pt(111)	388
xylene	Pd(111)	402
anthracene	Ag(110)	403
pentacene	Cu(111)	404
sexiphenyl	Ag(111)	405
pyridone	Cu(110)	406
pyridine	Cu(100)	394
pyrollidine	Cu(100)	407
Cu-PC	Cu(100)	373
Cu-PC	Al_2O_3/NiAl(110)	408
β-carotene	Cu(111)	409
decacyclene	Cu(110)	375
HtBDC	Cu(110)	410
coronene	Ag(111)	411
TB-PP	Au(111)	412
PTCDA	Ag(110)	413
Lander	Cu(110)	375,414
C_{60}	Au(111)	415
C_{60}	Au(110)	416
C_{60}	Ag(100)	417,418

Table 9.1: Observation of molecules on different surfaces

Using magnetic tips, one can study magnetic ordering on atomic scale,[419,420] magnetic vortex cores,[421] and magnetic hysteresis.[422] An emerging field is combining STM with electron spin resonance spectroscopy to detect the presence of localized spins on surfaces;[423,424] in this type of experiments, the STM is operated in a magnetic field and the high-frequency components of the tunneling current are monitored to detect spin precession. From measured Larmor frequency, the gyromagnetic ratio of the spin entity can be inferred.[424]

Especially important is the tunneling spectroscopy which provides information on local density of states (spectral functions)[425] with high spatial and energy resolution. It was applied to systems which exhibit the Kondo effect,[4,5,269,426–429] superconductors,[430–435] and artificial atomic chains,[436] to name just a few. It is even possible to study vibrational properties of single molecules[395,401,407,437,438] and magnetic properties of single atoms,[439] spin chains[440,441] and magnetic islands.[442] A new trend is to study molecules on a thin oxide layer grown on metal surfaces, for example Al_2O_3 on NiAl(110) surface.[408,443] Since

the oxide is a tunneling barrier, the molecule is coupled to the metal conduction band very weakly. This decreases the hybridization broadening of molecular-orbital electronic levels; in addition, vibrational states become better defined.[443] Very accurate tunneling spectroscopy can then be performed.[408]

The tip of the STM can also be used to perform manipulations. It is possible to perform lateral and vertical manipulations of single atoms[393,397,444–449] and molecules,[369,397,450–453] and to controllably induce reversible conformation changes of adsorbed molecules.[387] Atoms can be extracted from the native substrate by controlled tip crash.[454] Finally, using STM surface reactions can be studied at the single molecule level.[370,394,396,429,438,455–457]

I conclude this short review section by remarking that atomic-scale imaging is also possible using atomic force microscope (AFM)[458–461] which also allows measuring of chemical-bonding forces between two atoms.[462]

9.2 Construction of the low-temperature STM

We have undertaken the construction of an ultra-high-vacuum (UHV) liquid-helium-cooled low-temperature (LT) STM (Fig. 9.1) to complement an existing room-temperature (RT) instrument Omicron UHV STM-1. The design constraint for the new LT STM was to accept the Omicron sample plates in order to retain compatibility with the existing equipment, and that the LT STM be housed in the same vacuum system. The long-term goal is to achieve capabilities comparable to those of similar systems developed at the Freie Universität Berlin[463] and commercialized by SPS-Createc GmBH, i.e. vertical and horizontal stability of $\sim 1\,\mathrm{pm}$ at $6\,\mathrm{K}$.

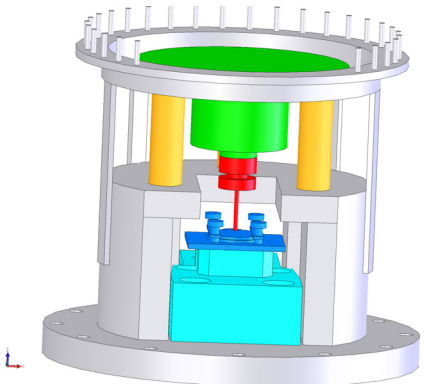

Figure 9.1: Schematic drawing of the modified Besocke type STM scanner. Piezo tubes are shown in yellow, the ramp disk in green, the tip holder and the tip in red, the sample plate in dark blue and the sample clamping support in light blue.

9.2.1 The cryostat

In low-temperature STMs, either the sample or the entire STM head with the sample can be cooled down to low temperatures. The advantage of the latter approach is enhanced stability, reduced transfer of impurities from hot to cold surfaces (i.e. to the sample), and, most importantly, better energy resolution in tunneling spectroscopy. Several cryostat types are used. Liquid-helium (LHe) bath cryostats are commonly used,[463] but it is also possible to cool down an STM using flow cryostats.[464–467]

We have used a bath LHe cryostat (Fig. 9.2a) based on the original design by G. Meyer.[463] It consists of a 4 l LHe reservoir suspended on a long thin-walled stainless-steel tube (neck) which reduces losses through thermal conduction. The STM head itself is suspended on three springs from the cold copper plate on the bottom of this reservoir. The head is surrounded by a nickel-plated copper radiation shield which is solidly bolted to the LHe reservoir. At the bottom of the radiation shield chamber, there is a gold-plated copper plate that faces oppositely mounted plate which holds magnets; this assembly enables the system of the tube, reservoir and radiation shield to play the role of a large magnetically damped pendulum which reduces the transfer of the environmental horizontal vibrations to the STM head. Liquid helium reservoir is enclosed in a larger (5.3 l) liquid nitrogen (LN2) shroud whose main purpose is to reduce losses via radiation transfer from the vacuum chamber walls at room temperature to the LHe part of the system. In addition, there is a thermal link (copper braid) from the LN2 reservoir to the top of the LHe neck to provide heat sinking to LN2 temperature; in this manner, the temperature gradient on the longer portion of LHe reservoir neck is significantly smaller (furthermore, thermal conductivity coefficients are lower at reduced temperatures). An additional nickel-plated copper radiation shield is bolted to the bottom of the LN2 reservoir which provides another layer of radiation shielding for the STM head. Care was taken to reduce any openings in the shields as much as possible: radiation losses radiation losses are one of the main limiting factors both for the ultimate working temperature of the STM head and for the cryogen (in particular LHe) consumption. To reduce radiation losses in the vertical direction (i.e. radiation from the RT top wall of the UHV chamber to the LHe reservoir), a number of radiation plates are soldered to the LHe neck. Finally, there is a thermal link (three 100 μm high-purity Au wires) between the cold finger and the baseplate of the STM. This link proved to be crucial to reduce the ultimate temperature of the STM head and to provide thermal stability in time. It is very important how the thermal link wires are installed: at low temperatures, the thermal conductivity of very pure gold is high and an important source of thermal resistance is the contact resistance. Contact resistance depends on materials on both sides of the junction; it is lowest in the case of homogeneous junctions (the same material on both sides) when the thermal impedance is matched. Even for homogeneous junctions, the differences are large: the conductance of gold-gold contacts is 20 times larger than that of copper-copper contacts.[468,469] It is interesting to note that the majority of heat is carried across the interface by thermal waves (phonons) rather than by electrons.[468,470] Thermal conductance increases linearly with the applied pressure so

the contacts must be tight.

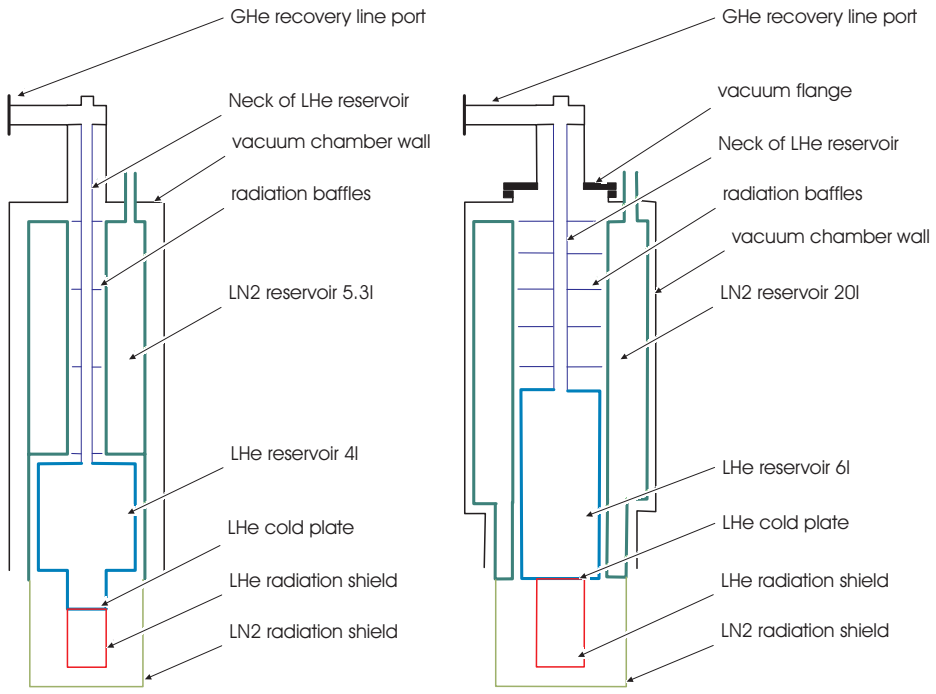

(a) Old cryostat (b) New cryostat

Figure 9.2: Schematic drawings of the currently used and newly constructed LHe bath cryostat.

The holding times in the fully assembled system with this cryostat are 14 h for LN2 and 26 h for LHe (provided that LN2 reservoir is never empty). The ultimate temperature of the STM head is 5.9 K as measured on the sample holder stage using a Si diode (LakeShore DT471). The cool-down time of the STM from RT to LN2 temperature is approximately one day, and it takes further 15 h to go down from LN2 to the lowest attainable temperature.

In 2005, the construction of a new improved LHe bath cryostat was undertaken (Fig. 9.2b). It was designed to solve a number of problems that we experience with the existing cryostat. To assist design decisions, I have developed a simple Mathematica package Krio (`http://auger.ijs.si/nano/krio`) for building thermal models of cryogenic systems. As input, it takes a list of parts of the system and thermal links (radiation, conduction) between them. The equations are then set up automatically and numerically solved. Temperature dependencies of thermal conductivity coefficients are taken into account. As output, we obtain ultimate temperatures of all parts and thermal currents between them. Using this package, one can easily identify critical elements which can then be optimized. One of the interesting results is that the surface emissivity of reservoirs and radiation shields is the most important element. Emissivity can be reduced by polishing and plating of large

surfaces, or by wrapping them in gold-plated mylar sheets (as long as this does not spoil the ultimate pressure in the vacuum system and reduce the pump-down time excessively).

In the new cryostat, the cryogen reservoirs are significantly larger (6 l for LHe and 20 l for LN2), which should improve holding time. The volume inside the LHe cryoshield is enlarged to allow easier mounting of the STM head, better access for maintenance and neater routing of the instrumentation wiring. The cryostat is assembled from separate LHe insert and an external vacuum chamber with the LN2 reservoir; in this manner, LHe part of the cryostat can be pulled out for installation of wiring and repairs (should the need arise). There are additional vacuum flanges to improve flexibility of the system and the possibility of adjusting the tilt of the LHe neck has been added. The cryostat was manufactured by Vacutech, Ljubljana. At the time near the completion of this dissertation, the first tests of the cryostat are being planned.

9.2.2 The STM head

The STM head we have built is based on modified Besocke-beetle type STM head:[471,472] the modification consists in having a fixed sample, while the main piezo tube is mobile on a ramp disk that can be coarsely positioned both horizontally and vertically using three supporting piezoelectric tubes,[463,473] while in the original design the scanner was fixed and the sample plate mobile.[471] The main parts for the head were purchased from Createc GmBH, however the STM head was heavily adapted to accommodate samples mounted on Omicron-type sample holders (Fig. 9.1). In addition, we used a different design for magnetic eddy-current damping of vertical vibrations. The fully assembled STM head is shown in Fig. 9.3.

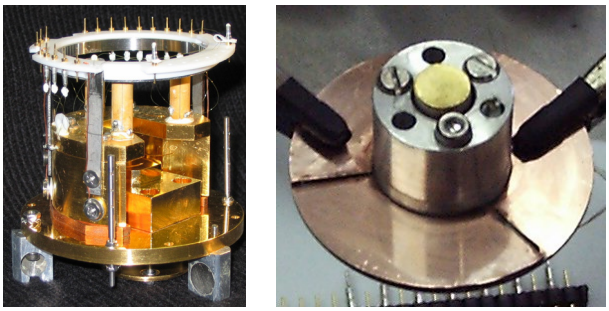

Figure 9.3: Pictures of the assembled low-temperature STM head (left) and the ramp disk (right).

Piezoelectric tubes with longitudinally quartered electrodes on the outside and a single continuous electrode on the inside wall are used.[474,475] The coarse piezo tubes are Staveley Sensors EBL #2 (PZT-5A), $L = 18.5\,\mathrm{mm}$ long, $D = 6.4\,\mathrm{mm}$ wide, $t = 0.5\,\mathrm{mm}$ wall thickness; the central piezo is Staveley Sensors EBL #2 (PZT-5A), $L = 10.3\,\mathrm{mm}$, $D = 6.4\,\mathrm{mm}$,

$t = 0.5\,\mathrm{mm}$.[476] Some properties of this piezoceramic are given for reference purposes in Table 9.2. To drive the piezotubes laterally, bipolar symmetric voltages on opposing segments of the outer (X, Y) electrodes are used, while the tubes are extended by applying voltage to the inner electrode (Z). For this purpose we use a high-voltage amplifier manufactured by Createc that is based on high-slew rate (up to $1000\,\mathrm{V}/\mu\mathrm{s}$) Apex PA85 MOSFET operational amplifiers.

To move the main piezo scanner with respect to the sample surface and to perform the coarse approach of the tip to the surface, stick-slip technique is used to move the ramp disk.[471, 473, 477] Saw-tooth like voltage profiles are typically used, but cycloidal[477] and parabolic[473] profiles are more effective. Both the amplitude and the frequency of the driving signal are important[473] and they must be carefully determined for different temperatures at which the system is operated.

We repoled the piezo tubes after observing that the ramp disk plate was running askew during rotation. This is achieved by applying high voltage (600 V, positive on outside electrodes, negative on inside electrodes) for a long time (several hours), while the piezos are moderately heated using an incandescent bulb held in close proximity. No appreciable deviations during rotation were observed after repoling. It should be noted that piezo tubes can depole with time due to aging and thermal cycling and even during normal use since scanning is equivalent to applying an ac field to the piezoelectric; taking the depoling field value from Table 9.2, we obtain a depoling voltage value of 350 V rms for our tubes.

Property	Value	Units
d_{31}	-1.73	Å/V at 293 K
d_{33}	3.80	Å/V at 293 K
d_{31}	-0.31	Å/V at 4.2 K
d_{33}	0.69	Å/V at 4.2 K
Y, Young's modulus	6.3	$10^{10}\mathrm{N/m^2}$
AC depoling field	7	kV/cm rms
Dielectric constant K_3^T	1725	
Curie temperature	350	°C
Thermal conductivity	1.5	W/m K
Density	7.5	$\mathrm{g/cm^3}$

Table 9.2: EBL #2 material properties. Source: Staveley Sensors.

During normal operation, the outer coarse piezos are used to scan over the surface area in X and Y directions, while the main central piezo is used for vertical displacements; in this mode of operation, the vertical and horizontal displacements are approximately decoupled. The vertical expansion of a piezotube is given by

$$\Delta Z = \frac{d_{31} L}{t} V_Z, \tag{9.1}$$

where d_{31} is the piezoelectric coefficient, L tube length and t wall thickness. This gives 35 Å/V piezo constant in Z direction at room temperature and 6.4 Å/V at LHe temperature for the central piezo tube. Horizontal displacement is given by[353,475]

$$\Delta X, \Delta Y = \frac{0.9 d_{31} L^2}{\mathrm{D}\ t} V_X, \tag{9.2}$$

where D is the diameter of the tube. For the central piezo this gives 52 Å/V piezo constant at RT and 9.2 Å/V piezo constant at LHe temperature, while for the coarse piezos we obtain 170 Å/V at RT and 30 Å/V at LHe.

The piezoelectric behavior of the tubes, as well as the mechanical resonance frequencies of the tubes themselves and of the scanner as a whole, can be studied by measuring the double piezo response: one electrode (or a pair) is used to excite the piezo, another to measure the response.[478–480] An example of such measurements is shown in Fig. 9.4. The lowest resonance frequency is found to be ~ 900 Hz. This lowest mechanical resonance frequency limits the highest scanning speed attainable.[478]

Capacitance of a piezo tube is

$$C = \frac{2 K_3^T \epsilon_0 \pi L}{\ln \mathrm{OD/ID}} \tag{9.3}$$

where $\mathrm{ID} = d$ and $\mathrm{OD} = d + t$ are inner and outer diameter, K_3^T is the dielectric constant and ϵ_0 is the vacuum permittivity. This gives $C = 4.2$ nF for the central piezo and $C = 7.5$ nF for coarse piezos. This is more than the capacitance of the wires, so measuring the capacitance is a reliable test to determine if the wires make contact to the electrodes when the system is already assembled. As a quick test, one can manually apply a high voltage ramp to a pair of electrodes (e.g., 200 V in one second) and observe the transient current which should rise to a few μA.

For assembling parts that need to be glued together, we used special two-component epoxy glue which is sold as leak sealant by vacuum components companies ("epoxy patch" from Caburn). Once cured, this glue has very low degassing rate and is suitable for ultra-high vacuum applications. Excellent adhesion to sufficiently rough surfaces can be achieved and the joints are very strong, especially if the curing process is performed at elevated temperatures. Cured glue can withstand bake-out temperatures up to 125 °C; at higher temperatures it becomes softer.

The STM tip holder is attached at the center of the central piezo tube using a magnet that is glued in a metal plated ceramic receptacle which, in turn, is glued to the end of the main piezo tube. The tips are made of etched tungsten wire (see below); the wire segment is inserted into a syringe tube and crimped.

We first attempted to wire the head using 50 μm thick polyimide-insulated (HML) high-purity copper wire (California Fine Wire Company) but this proved to be troublesome, especially in the initial stages of our work when the system had to be repeatedly disassembled for modifications and tuning. The wires tend to break near the soldering points where

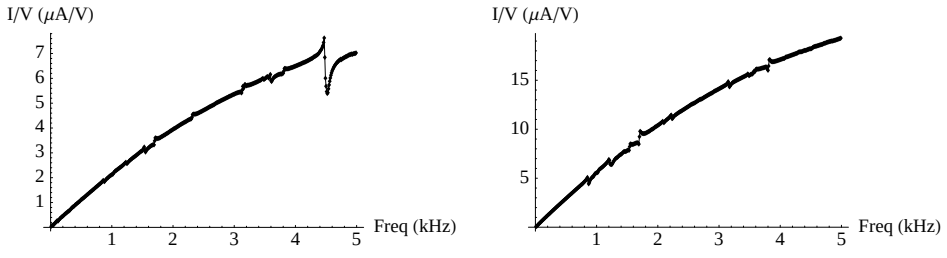

(a) A2-C2

(b) A1-C1

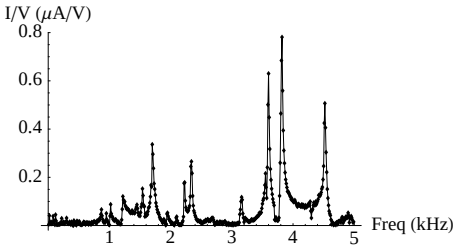

(c) C1-A2

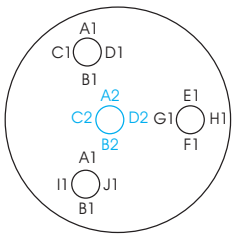

(d) Electrical wiring of a Besocke type STM

Figure 9.4: Double piezoelectric response for various electrode combinations. The first electrode given in subfigure captions is being excited, the second is used to take measurements.

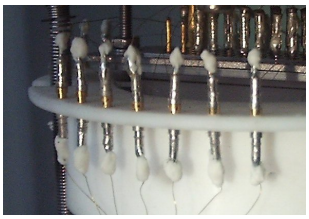

(a) Glued solder joints

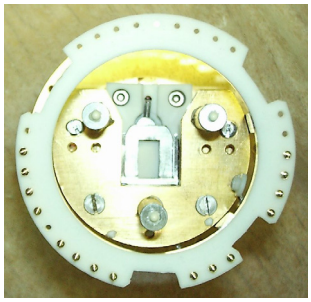

(b) PTFE assembly 1

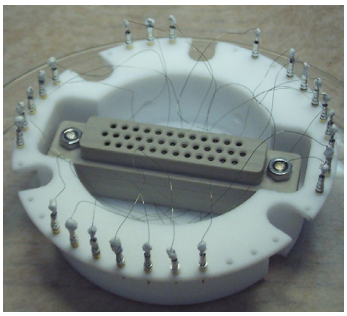

(c) PTFE assembly 2

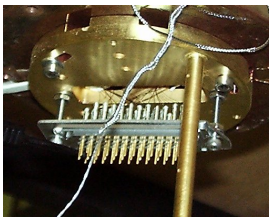

(d) Connector on the cold plate

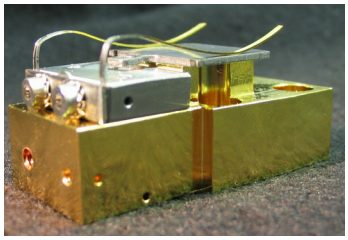

(e) Omicron sample plate holder

(f) STM head in cryoshield

(g) Heat sink

Figure 9.5: Close-up pictures of some elements of the STM system and of wiring.

the insulation is stripped and the mechanical strength of the wire reduced; in addition, we observed that the wires tend to thin down during soldering, perhaps by the action of the soldering flux. Later we opted for 75 μm and 100 μm 0.45Ni-0.55Cu (constantan) wires which are much more robust. Furthermore, we developed the practice of putting a small drop of epoxy glue on the soldering points (Fig. 9.5a); the glue embeds the uninsulated part of the wire and plays the role of a stress relief. Due to small confines of our present LHe cryoshield, we had to be meticulous about the routing of the wires from the STM head to the connector at the cold plate to avoid tangling of the wires and to prevent that the wires touch the shield and bring in more environmental vibrations. We decided to use multiple stages: the signal wires first go from attachment points (piezos, Si diode, sample holder) to pins on a PTFE ring tightly attached to the guarding ring of the STM head (Fig. 9.5b), from there to pins on another PTFE ring fixed to the bottom of the cold plate (Fig. 9.5c), and from this ring to the connector (Fig. 9.5d). Using pins and sockets provides for easier maintenance. In addition, the wires are neatly coiled and, in a sense, become part of the spring suspension system (see below). From the connector at the cold plate, 150 μm polyimide-insulated stainless steel (SS316) wires take the signals to the RT connector at the top of the cryostat; stainless steel wires are chosen for their low heat conductivity and (relatively) low electrical resistance of $\sim 150\,\Omega$. We test all cables for mutual shorts at > 400 V and for shorts to the ground at > 300 V.

All signal wires must be properly thermally anchored. In the presently used cryostat, the wires are anchored on the cold plates of the LN2 and LHe reservoirs: they are glued in epoxy and embedded between two very thin mica plates over ~ 1 cm length (Fig. 9.5g). These plates are then glued to the cold plates. There is no heat sink at the top of the cryostat as we do not have access to that area. In the new cryostat, the wires will be thermally anchored to LN2 temperature at the top of the LN2 reservoir using gold-plated copper bobbins (LakeShore Cryotronics, Inc.) and at the LHe cold plate at the bottom of the cryostat using beryllium oxide heat sink blocks (LakeShore), so that the temperature gradient from LN2 to LHe temperature will occur over a much longer length of wires (~ 1 m).

For soldering we use lead-free silver-tin alloy Castolin 157 in conjunction with Castolin 157N liquid flux. This combination is useful not only for soldering wires, but also for assembling metallic parts, in particular stainless steel parts where excellent bond strengths are achieved. It is very important to remove flux residue as it is etching. In addition, we observed that the flux reacts at high temperatures with the epoxy glue to produce insoluble conducting black goo which can lead to short circuits.

9.2.3 Bandwidths, resolution and vibrations

For an estimated ~ 10 nF capacitance of the piezotube and the internal and external wires, and $\sim 300\,\Omega$ of resistance of a pair of wires, we estimate the RC time constant to be of the order of 3 μs. For a 512×512 STM image recorded in one minute, assuming equal forward

and backward scanning speed, the point-to-point mean time is $\sim 100\,\mu$s. The RC constant is thus not a limiting factor. Neither is the 60 kHz bandwidth of the high-voltage amplifier that drives the piezo tubes, nor the $< 5\,\mu$s conversion period of the D/A converters. We are therefore limited essentially by the bandwidth of the tunneling current preamplifier (for example, 1.2 kHz at 10^9 V/A in the low-noise mode) and by the mechanical resonances of the scanner (which are also of the order of 1 kHz).[478]

There is no intrinsic resolution limit in STM comparable to the diffraction limit of optical and electron microscopes. STM is essentially a counting apparatus: we measure the number of electrons that tunnel through the barrier in a unit of time. The wavelength of electrons concerned plays no role in this regard (beyond the fact that transmission probability is a function of electron energy/momentum). It is useful to remember that 1 nA roughly corresponds to $\sim 10^9$ electrons per second. At $\sim$ 1 kHz bandwidth, the relevant time interval is 1 ms, i.e. 10^6 electrons. Considering the tunneling as a Poissonian process, the shot noise is $\sim 1/\sqrt{10^6} = 10^{-3}$ of the signal amplitude, i.e. 1 pA. Johnson-Nyquist noise at 1 GΩ impedance at 1 kHz is lower by an order of the magnitude even at room temperature. Finally, the intrinsic noise of the current amplifier (Femto DLPCA-200) is declared to be $4.3\,\mathrm{fA}/\sqrt{\mathrm{Hz}}$, i.e. ~ 0.1 pA at $\sim$ 1 kHz bandwidth. In usual circumstances, electronic noise is not a limiting factor since it is much smaller than the set-point tunneling current (provided, of course, that the system is properly shielded from external electromagnetic interference). Instead, lateral resolution is limited by the width of the tunneling current flux, i.e. by the atomistic details of the STM tip over which one has little control. Vertical resolution is chiefly limited by the tip-sample vibration amplitude, which also affects lateral resolution. For good results, stable tip and stable STM scanner are thus essential.

In order to reduce the noise due to external electromagnetic interference in the tunneling signal, it is important to place the current amplifier as close to the tunneling junction as possible. A convenient choice is to connect it directly to the BNC feed-through at the top of the cryostat. The connection between the feed-throughs and the STM head is currently made using shielded twisted-pair cable; one wire is used for the tunneling current, the other for the bias voltage applied to the sample. A possible improvement would be to use two separate insulated coaxial cables for these two signals and to make a common ground at the input of the current amplifier. The two coaxial cables can then be twisted to eliminate the 50 Hz power line noise. It is recommended to wire the tunneling signal separately from the high-level signals used to drive the piezo-tubes to reduce noise coupling.

External cables for high-level signals also need to be properly shielded to prevent that they pick up high-frequency electromagnetic interferences from the environment and radiate them in the STM head. Shielded paired data transmission cables (liycy) are a good choice. A pair of wires is used to carry a pair of signals that are connected to the opposite electrodes of a piezo tube.

Another important aspect is correct grounding. Shields on cables should be grounded at one point only to prevent the noise currents from flowing.[481] For ungrounded circuits (such as the STM junction), the best shield connection point is at the current amplifier

(amplifier common terminal).[481] Shields around amplifiers should also be connected to amplifier common terminals.[481] All grounds should be solidly connected (soldered, bolted) to avoid hard-to-diagnose problems later on.

The vacuum chamber, pumps and other vacuum equipment is always grounded to a safety ground. It is appropriate to use separate signal grounds for all STM wiring and to connect the two grounds at a single point at the main power inlet box of the laboratory, thus avoiding possible ground loops and, more importantly, common ground impedance coupling problems.[481] Unfortunately, this is not always practicable nor economical, since floating vacuum electrical feed-throughs are more expensive. By trial and error, we largely succeeded in eliminating the 50 Hz power line noise. We also find that it helps significantly to power the STM electronics through an insulation transformer; even better solution would perhaps be a dual conversion online uninterruptible power supply (online UPS) which is an excellent filter for removing line noise.

To monitor noise levels, it is very useful to perform real-time spectral analysis of the tunneling current signal. Since the frequencies of interest are in the audible frequency range, the signal can be fed to an audio input of a personal computer via a high-impedance buffer (since audio inputs typically have relatively low input impedance). While this provides a convenient and inexpensive way to perform spectral analysis, one should nevertheless note that the frequency response in the consumer-grade audio cards is non-flat and that such inputs typically have a high-pass filter which prevents to observe noise below 10 Hz which also affects the operation of an STM in a significant manner. Typically, we observe that spectra contain some 50 Hz noise and higher harmonics, as well as sharp peaks attributed to mechanical resonances. Using a loudspeaker directed to the UHV chambers which is driven by a frequency generator, it is also possible to study the transfer of acoustic vibrations from the environment to the STM junction.

Most importantly, the stability of the system can be quantified by imaging flat crystalline surfaces such as Cu(111) (Fig. 9.6a) and calculating the standard deviation of the topographical z signal along a line profile in the fast scanning direction (Fig. 9.6b, first three rows) and along the slow scanning direction (Fig. 9.6a, last two rows). The heights can be calibrated accurately from the known step height, 210 pm (Fig. 9.6b, first row). The standard deviation of the height on the lower part is $\sigma = 1.2$ pm and $\sigma = 1.5$ pm. To calculate these values, the image was leveled using the three-point procedure[482] and a polynomial background of second order was subtracted from each segment of the line profile (Fig. 9.6b, second and third row). The line profile along the slow scanning profile (Fig. 9.6b, fourth line) exhibits more irregularities. The standard deviation is higher, $\sigma = 4$ pm. After performed additional image processing (step line correction[482] and subtraction of the polynomial background of third order from the line profile, see fig. 9.6b, last line), the calculated standard deviation is $\sigma = 2$ pm.

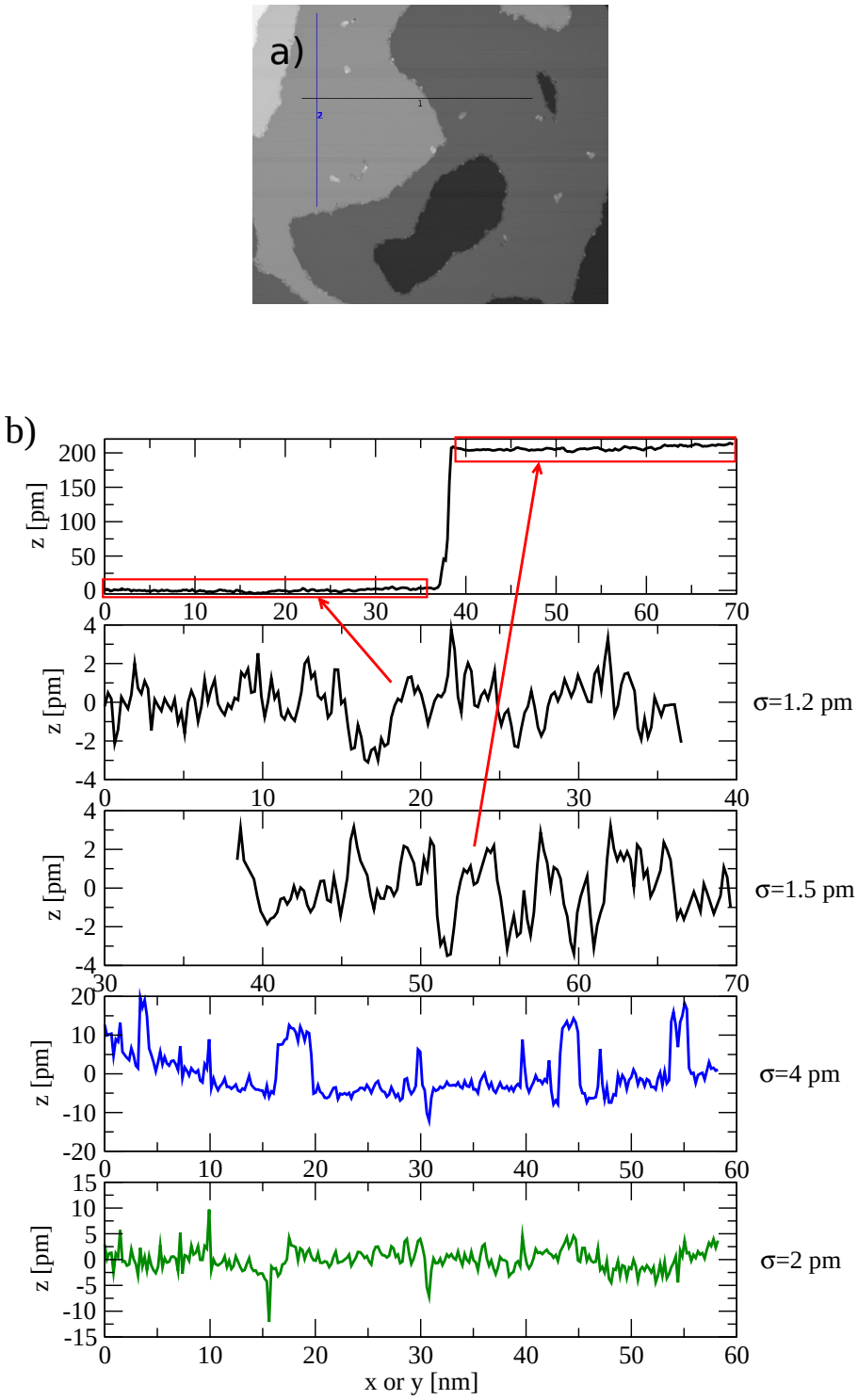

Figure 9.6: Determination of the stability of the system from line profiles on flat surfaces. Cu(111), $U = 943\,\mathrm{mV}$, $I = 0.38\,\mathrm{nA}$, image size $(108\,\mathrm{nm})^2$, 328 ms per line.

9.2.4 Vibration isolation

To reduce transfer of environmental vibrations to the STM chamber, the entire vacuum system is suspended on pneumatic vibration isolators (Melles Griot self-leveling vibration isolators) which provide both vertical and horizontal isolation. Their resonance frequencies are around 1 Hz and transmissibility is below 6% and 10% for horizontal and vertical vibrations, respectively, at 5 Hz which is the typical frequency of vibrations in buildings.

The STM head is suspended on stainless steel springs and its oscillations are damped by eddy current damping.[353] This setup very effectively damps the high frequency (acoustic) range of environmental vibrations that are transferred through the springs. The relation between the axial load F, and the deflection Δ of a spring with coil diameter D, number of coils n, and wire diameter d is $F = S\Delta$, where S is the *stiffness* or *rate* of the spring:

$$S = \frac{Gd^4}{8nD^3} \tag{9.4}$$

where G is the shear modulus of elasticity (modulus of rigidity). Elastic properties of some materials used in STM applications are listed in Table 9.3. For packed springs the length of the spring $L = nd$ and $S = Gd^5/8LD^3$.

Material	Modulus of rigidity G [10^{10} N/m^2]	Young modulus Y [10^{10} N/m^2]	Thermal expansion coefficient α [10^{-6} K^{-1}]
Aluminum	2.6	7	23
Platinum	6.1	16.8	9
Gold	2.7	7.8	14
Silver	3	8.3	19.6
Copper	4.8	13	17
Iron	8.2	21.1	12
Music wire	8	21	
Stainless steel	6.7		17.3
Tungsten	16.1	41.1	4.5

Table 9.3: Shear modulus (rigidity modulus), and Young modulus of elasticity for a selection of wire materials. The values are given for room temperature. Sources: CRC Handbook of chemistry and physics, and `http://www.matweb.com`.

Let us consider the force exerted on the base plate of the STM if the attachment point of the spring oscillates as $\Delta = \Delta_0 \sin(\omega t)$. It is clear that a hard string will transfer vibrations more efficiently than a soft spring. The transfer of vibrations depends on the damping of the STM head using the eddy-current damper. We define the Q factor as

$$Q \equiv \frac{\omega_0}{2\gamma}. \tag{9.5}$$

Here $\omega_0 = \sqrt{S/m}$ is the eigenfrequency of the vertical vibrations of the STM head of mass m, while γ is the damping rate. The transfer function of this mechanical system is (Ref. 353; note that the power of ω_0 in Eq. (10.17) in the book must be corrected to 4)

$$K(\omega) = \sqrt{\frac{{\omega_0}^4 + 4\gamma^2\omega^2}{(\omega_0 - \omega^2)^2 + 4\gamma^2\omega^2}}. \tag{9.6}$$

If there is no damping, the transfer function at high frequencies is $K(\omega) \approx (\omega_0/\omega)^2$. With damping, we have $K(\omega_0) \approx Q$ and $K(\omega) \approx (1/Q)(\omega_0/\omega)$ for $\omega > Q\omega_0$.[353] A Q value of $3 - 10$ is usually chosen as a compromise between the suppression of resonance and the suppression of high-frequency vibrations.[353] Clearly, harder spring means higher Q if damping is left unchanged.

Spring rate of typical coils used to suspend an STM head ($d = 0.5\,\mathrm{mm}$, $D = 4\,\mathrm{mm}$, $L = 10\,\mathrm{cm}$, stainless steel) is $S \sim 300\,\mathrm{N/m}$. For three coils, we have a total stiffness of roughly $1000\,\mathrm{N/m}$.

It may be noted that a set of 25 copper wires of $d = 100\,\mu\mathrm{m}$ diameter, each rolled into a spring of diameter $D = 3\,\mathrm{mm}$ with $n = 20$ loops has a stiffness of $S \sim 30\,\mathrm{N/m}$. For a thicker wire of $d = 200\,\mu\mathrm{m}$, the stiffness is $S \sim 450\,\mathrm{N/m}$, which is comparable to the stiffness of the suspension springs, but probably still acceptable. The idea here is to use the wires as part of the suspension system. The wires must be firmly mechanically attached to the baseplate of the STM and only then routed to the final electrical connection point (piezo electrodes, leads of thermometric diode, etc.). It is not a good idea to connect the wires directly to their final connection point since in that case different forces are exerted to various parts of the instrument; if all wires are fixed on the baseplate, the differences are effectively compensated and the STM head tends to vibrate as a whole. The worst case scenario is if the wires are routed directly to the scanner, since environment vibrations then translate into sample-tip distance oscillations.

9.2.5 Tip preparation and characterization

Regarding the tip, three factors are important for reliable STM operation: the tip must have high flexural resonant frequencies to allow high scanning rate, it must have a sharp apex (ideally a single site of closest atomic approach) and it must be clean so that a series resistance is not present.[483] There is a large number of STM tip preparation recipes. Two types of tips are most commonly used: etched tungsten (W) tips and mechanically cut platinum/iridium (0.9Pt/0.1Ir) tips. W tips can be made very sharp, they are suitable for tough samples due to their hardness which prevents deformations and erosion during imaging, but their lifetime in air is short because of W oxidation.[484,485] The resistance of a tungsten oxide layer can easily be much higher than the desired tunnel gap resistance; such a tip would crash before the set tunneling current can be obtained.[483] In addition, tunneling spectroscopy of metal surfaces using oxidized tips shows a spectrum characteristic

of a semiconductor.[486] Pt/Ir tips, on the other hand, are oxide free and can be used in air for very flat surfaces, but they are not suitable for highly corrugated surfaces.[484,487] These tips are prepared by cutting the wire with scissors. The reproducibility is low: the method "relies on operator's skill rather than on controllable parameters".[487]

Other types of tips are also sometimes used. Ni tips are oxide free,[487] while Co tips form a homogeneous thin oxide layer which prevents further oxidation.[488] Both can be reproducibly prepared by etching. Furthermore, they are ferromagnetic, so they can be used to perform spin-polarized tunneling microscopy.

We mostly used W tips. We prepare them from polycrystalline tungsten wire of 99.95% purity with a diameter of 0.25 mm or 0.38 mm. We electrochemically etch[485,489] the wire in a (typically) 2 N solution of KOH at a depth of a few millimeters beneath the surface. W wire is the anode and we use a ring of Au wire as the cathode. With an etching current of 10 mA, the process takes around 10 min. We use a home-made electronic device to accelerate the shutdown of the tunneling current when the wire starts to break apart since a short cutoff time is necessary to obtain a sharp tip.[489,490] As mechanical cutting of W introduces defects, it is a good idea to remove the damaged material by etching away a few millimeters of the wires.[491] W tips are robust with respect to dipping in liquids and even dropping if the very end of the tip is untouched.[491] It was found, however, that ultrasonic cleaning[485] or exposing the tip to a jet of water from a perpendicular direction bends the tip apex. It is important that etching and rinsing be performed using clean and dust-free liquids; we observed that tips are often covered with dust particles, often even near the tip apexes, Fig. 9.7.

As etched, the tips are always chemically contaminated. Using ESCA, we have detected K containing crystallites, while other groups reported existence of thin carbonaceous phases.[484,485,492] Above all, the tip is always coated with a layer of tungsten oxide. These contaminants can be removed by etching in concentrated HF.[486] Since a new oxide layer would form on a time scale of several days[483,484,492] (a contradicting report of Ekvall et al.[491] maintains that no traces of oxides were formed for more than one month), it is best to perform the HF treatment just prior to introducing the tip in the UHV system. The tip is exposed for 10 s to concentrated HF, then immediately rinsed with deionized water and dried with pure isopropanol (IPA). All tungsten oxides are soluble in concentrated HF, while tungsten itself should be inert to attack by HF.[486] Nevertheless, it is found that the tip sharpness is reduced after prolonged HF etching.[485] On the other hand, short HF treatments do not remove the insulating layer entirely.[491] It is thus very important to perform further in-situ preparation of the tip using either ion bombardment[483] or annealing;[484,485,493] unfortunately such treatments are not currently possible in our system since we do not have the possibility to change tips in situ using a manipulator. Finally, and most importantly, the tips can be improved by intentionally crashing them in a soft metal surface (such as Cu or Ag) in a controlled manner and applying a large potential for a short time;[486] the tip apex is then expected to be covered by sample atoms. We found that such crashing treatment was required for all our tips to achieve stable operation and

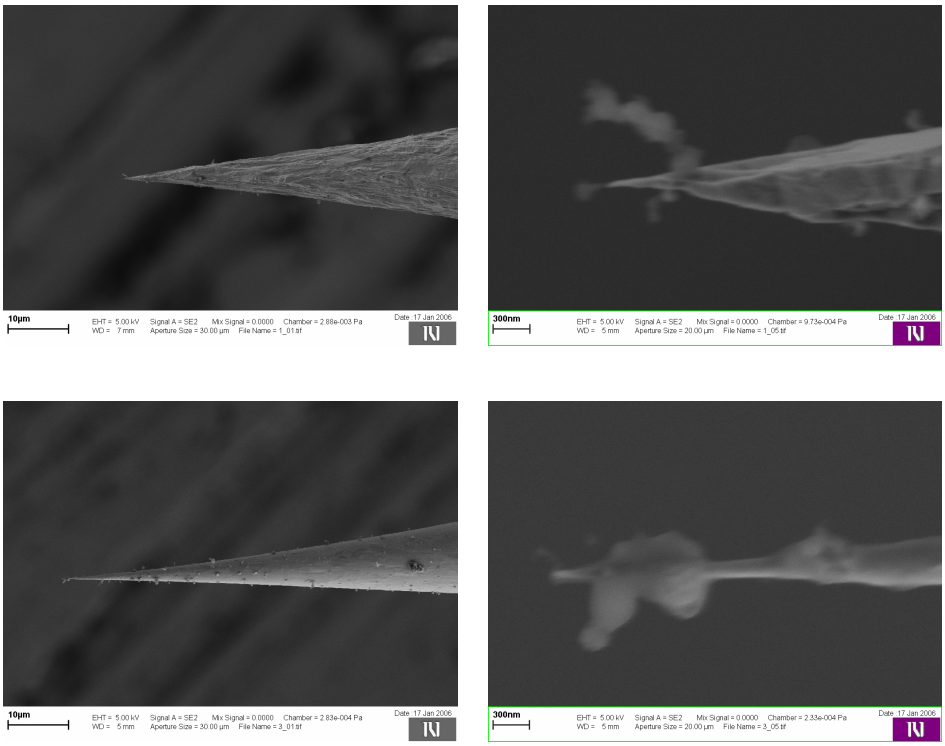

Figure 9.7: SEM images of two different electrochemically etched W tip with contamination: large-scale overview (left) and zoom to the apex region (right).

atomic resolution.

It is characteristic for bad tips to show an oscillating tunneling current when the tip is held stationary. Often the oscillations have the appearance of a series of current spikes between regions where the current is close to zero: a spike appears when a break is produced in an oxide layer and metallic region is exposed.[486]

The control of STM tip shape, bulk and surface composition is of extreme importance. To characterize a tip, an optical microscope can be used to eliminate tips that are bent on a large scale, while SEM and TEM can be used to obtain information on the apex region. With the resolution of the SEM, it is not really possible to distinguish a sharp tip from a blunt one.[491] Only using TEM is it possible to study the very apex of the tip; one can even detect a possible insulating layer.[491] A cheap alternative to TEM characterization is the use of the field-emission from the tip apex to determine the effective apex curvature.[492]

9.2.6 Sample transfer mechanism

Due to budget constraints, instead of using standard but costly manipulators, a specialized sample transfer mechanism has been constructed (Fig. 9.8). Its purpose is to convey the

sample from the central chamber (where the sample storage carousel is located) to the STM head. It has three degrees of freedom: linear motion to insert the sample in the STM, vertical motion to let go the sample once it is properly fixed by the pair of clamps in the STM head, and rotation to suitably orient the sample. The mechanism is affixed in the narrow space of the flange neck in the UHV chamber where the STM is housed. The mechanism is operated using a wobble stick, as well as by linear and rotary feed-throughs that are located in other parts of the vacuum system and connected to the mechanism by thin stainless steel braided wires.

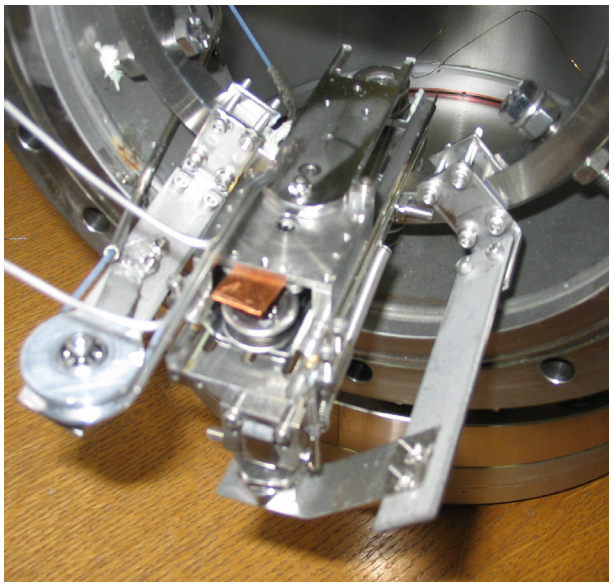

Figure 9.8: Sample transfer mechanism

A major difficulty in mechanical assemblies operated in UHV systems is friction which increases quickly as the oxide layers wear off, resulting in cold welds. Often even a single motion cycle can lead to a grinding halt. It is interesting to note that similar problems arise in the space technology. The solution consists in using light-load designs that rely on UHV-compatible ball bearings; direct rubbing of components must be avoided. If this is not possible, hard coating improves the situation considerably. We have experienced excellent results with TiN coating which eliminated cold welding; in addition, it has low coefficient of friction that does not increase with motion cycles in a perceptible manner.

Vacuum-related mechanical problems can easily remain undetected during prototype construction at ambient conditions, therefore early testing in UHV is recommended.

9.3 Ultra-high vacuum system

An important development in vacuum technology was the invention of copper gasket seals by Wheeler in 1962;[494] this was the first reliable seal for achieving ultra high vacuum

(UHV), defined as pressure below 10^{-7} Pa (or 10^{-9} mbar). Pressures as low as 10^{-14} Pa have since been measured in the laboratory.[495] It is interesting to note that this is still several orders of magnitude higher than the vacuum in the deep space.[496]

Use of UHV is important to study reactive surfaces with strong chemisorption of molecules; at the limit pressure of 10^{-9} mbar it takes 10^3 s to cover a surface with a monolayer of contaminants if the sticking coefficient c_S is unity (oxygen sticking coefficient for polycrystalline Cu at RT is quite low, $\sim 10^{-3}$,[497] it is even lower for smooth single crystal Cu surfaces;[498] for more reactive metals and for semiconductors, it can be considerably higher). Obtaining UHV is rather demanding: the experimental set-up needs to be constructed from suitable materials, be extremely clean and have small surface area, and vacuum pumping must be performed in multiple stages (rotation or diaphragm fore pumps, turbomolecular pumps, and gettering ion and sublimation pumps when high vacuum is attained). Furthermore, the entire vacuum systems needs to be "baked" to remove adsorbed water, hydrocarbons, CO and CO_2.[499] These species have a surface lifetime in the range of seconds to hours and therefore hinder rapid pump-down; in contrast, species with longer lifetime remain stuck to the surfaces, while species with shorter lifetime are quickly desorbed and pumped out of the system.

Mean free path (for example of air molecules) at $p = 10^{-9}$ mbar is $\lambda \sim 50$ km, therefore gas molecules collide with chamber walls more often than they do with each other. The corresponding Knudsen number $\mathrm{Kn} = \lambda/d \gg 1$ (here d is the characteristic size of, e.g., a tube) and the flow characteristics are well within the free molecular flow regime.[500] The pressure can vary from chamber to chamber and even from point to point inside a single chamber; it is important where the pressure reading is taken. It is worth noting that the number of gas molecules adsorbed on the walls of the chambers is higher than the number of flying molecules; at low pressure the surface area of the system is thus more important than the volume.

Conservation of mass equation for gas in the chamber is[494]

$$V\frac{\mathrm{d}p}{\mathrm{d}t} = L + QA - Sp, \tag{9.7}$$

where V and A are the system volume and surface area, L is the leak rate, Q is the outgassing rate per unit area and S is the pumping speed. To obtain UHV, it is essential that $L \ll QA$, i.e. all seals must be tight and there must be no virtual leaks inside the system (there will always be some permeation of the atmospheric helium and hydrogen[501]). The ultimate pressure is then

$$p_\infty = \frac{QA}{S}. \tag{9.8}$$

Note that the system volume drops out of this equation; it does affect, however, the pump-down time. Usually the maximum value of the pumping speed S is limited by available space if not budget. Furthermore, the theoretical maximum pumping speed is approximately proportional to the chamber surface area A (for example $44\,\mathrm{ls^{-1}cm^{-2}}$ for

H_2 at 300 K).[494, 495] To reduce the ultimate pressure it is therefore necessary to reduce the out-gassing rate Q by suitable choice of materials and by baking the system.[501]

The entire UHV system is schematically represented in Fig. 9.9.

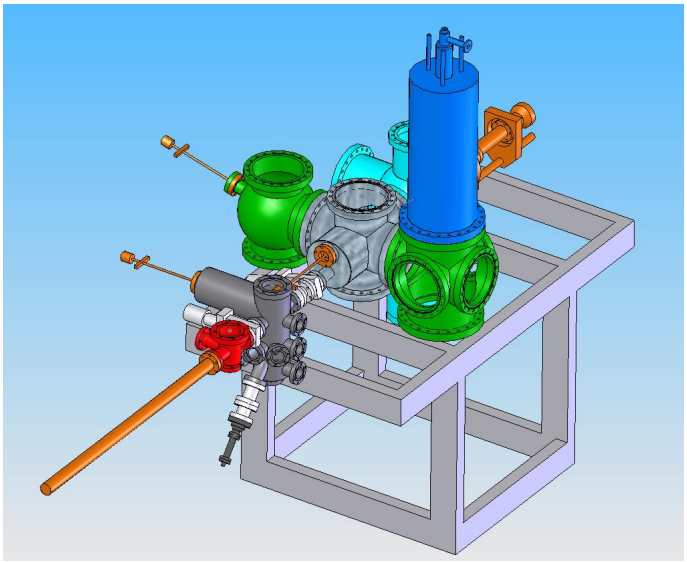

Figure 9.9: Schematic representation of the UHV system with room-temperature STM (in the green chamber to the left) and LHe low-temperature STM (in the green chamber to the right) with cryostat (blue), manipulators and wobble-sticks for handling the samples (orange and red), sample storage chamber (textured gray), sample preparation chamber (gray) with a Knudsen evaporation source (dark gray) and a sample analysis chamber (cyan). The system is mounted on a solid frame (light gray) which is carried on four pneumatic isolation cylinders (not shown).

To check the composition of the residual gas, we use a quadrupole mass spectrometer (QMS) to record mass spectra. Residual gases can then be identified by referring to mass spectra cracking pattern tables which list largest peaks for common substances. The background gases at the ultimate pressure are typically hydrogen and trace amounts of low-weight hydrocarbons (CH_x), nitrogen, oxygen and argon. As a rule of thumb, if the oxygen peak (32) is higher than the argon peak (40), there is a leak from the atmosphere. When the STM is cooled down to LHe temperatures, the pressure drops further due to the cryopumping action of the cold cryostat walls. The residual gas inside the radiation shields consists essentially of He atoms; the sample stays clean for days, if not months. For reference purposes, I list largest peaks in QMS spectra for different vacuum conditions in Tables 9.4.

UHV is dynamically maintained by pumping the system using titanium sublimation getter pump and ion pumps; the main purpose of the latter is to provide pumping for rare gases and methane which are not pumped by sublimation pumps. We bake the system at 105 °C; this relatively low temperature has been chosen to prevent softening of the glue used in

m/q	Species	Intensity $/10^3$
1	H	0.4
2	H_2	2.7
12	C	0.1
15	CH_3	0.1
16	CH_4, O	0.2
17	HO	0.25
18	H_2O	0.8
26	C_2H_2	<0.1
28	N_2, CO	1.25
32	O_2	<0.05

(a) Before bake-out

m/q	Intensity
1	0.6
2	4
15	0.3
16	0.4
17	0.6
18	1.5
28	0.5

(b) Empty cryostat

m/q	Intensity
2	2
15	0.3
16	0.3
18	0.3
28	0.5

(c) LN2 in cryostat

Table 9.4: Typical peaks in mass spectra (a) before bake-out ($p = 2 \times 10^{-7}$ mbar) and (b,c) after bake-out in the case of (b) empty cryostat reservoirs ($p = 5 \times 10^{-10}$ mbar) and (c) with LN2 ($p = 1.9 \times 10^{-10}$ mbar) in the cryostat reservoirs. m/q is the mass/charge ratio of ionized particles that is measured by QMS.

the assembly of the low-temperature STM head. During bake-out, the system is covered with ironing table fabric cover which has very good thermal insulation properties in the relevant temperature range and is straightforward to install due to its light weight. A single radiative infrared bake-out heater with a fan is used. In addition, we have taped heater cables on vacuum chambers: these are used to perform small bake-outs after sample preparation processes such as sputtering which lead to increased contamination levels in the system.

9.4 Preparation of clean surfaces and evaporation of materials

For STM work, sample surfaces of good quality are required. Ideally, the surface would be atomically flat with the same chemical composition as the bulk of the crystal. In reality, all surfaces (with the possible exception of some layered compounds that can easily be cleaved) are contaminated (oxidized) and rough. The samples must therefore be cleaned by ion sputtering and annealed.[502] Ion sputtering is a process of removing surface atoms by bombarding the surface with ions of high kinetic energy (we use Ar accelerated to 1 keV).[503] Even if the surface is flat and ordered before sputtering, ion bombardment disrupts the crystal lattice and the sample must be annealed. Unfortunately, annealing brings contaminant atoms from the bulk to the surface by enhanced diffusion; in copper,

for example, the most problematic species is sulphur. Cleaning must therefore be repeated in cycles of sputtering and annealing. In this manner, a decreasing gradient of contaminant concentration is achieved in the near-surface region of the bulk and the surface can be made relatively clean. During the last cleaning cycles the acceleration voltage can be decreased as the surface is already relatively flat; it should be just high enough to sputter off the contaminants without damaging the surface excessively. Annealing temperature may also be decreased.

The cleaning process was automatized to relief us from tedious manual work. Computer regulates the sample temperature (through Oxford Instruments ITC4 temperature controller) and acceleration voltage and filament current controls of the ion gun. During annealing, the ion current is shut down by setting the acceleration voltage to zero and the emission current is reduced by decreasing the filament current to improve the life-time of the emission cathode. To calibrate the temperature control, we measured the surface temperature using an optical pyrometer. As our pyrometer works in the near-IR range, we constructed view-ports into which we mounted ZnSn plates; ZnSn is transparent both to IR and to visible light, therefore the laser beam pointer of the pyrometer can be aimed at the surface and the temperature read-out performed.

Single-crystal copper samples with (111) and (211) surfaces were used in this work. Originally, we had the samples cut using wire saw from ingots and polished mechanically; results were modest and required extensive in-situ preparation. In addition, circular disk sample geometry proved problematic for mounting on Omicron sample plates. We later used purchased samples of square shape with mounting steps on edges (MaTeck GmbH, Germany, and Surface Preparation Laboratory, Netherlands). These samples are cut using spark erosion and polished with high orientational accuracy (to within $0.1\,^\circ$) and to very low surface roughness (average roughness $R_a \sim 30\,\mathrm{nm}$); a few cycles (~ 10) of sputtering and annealing were sufficient to obtain large atomically flat terraces with little defects on new samples.

To monitor the composition and crystal order of the surface we use Auger electron spectroscopy (AES) and low-energy electron diffraction (LEED). In AES, we irradiate the surfaces with high-energy (of the order of 3 keV) electrons which knock out core-state bound electrons. The resulting core-level holes are filled by electrons from higher energy outer-shell orbitals of the same atom and the difference in energy is carried away by a third electron which is ejected from the atom (Auger process); it is these latter electrons that are measured in AES after they leave the surface. With our equipment (Omicron SpectaLEED) we can detect electrons in the 50 eV to 1 keV range: electrons in this range have a very short escape length, therefore they originate from the topmost surface layers. As the energy differences are characteristic of the element where the Auger process had occurred, surface composition and chemistry (bonding state) can be probed in this manner. Our main use of AES is to measure the level of the surface contamination. An example of AES spectrum is given in Fig. 9.10. Typical contaminants on metal samples are oxygen, carbon and nitrogen, and sulphur on some lower grade Cu samples.

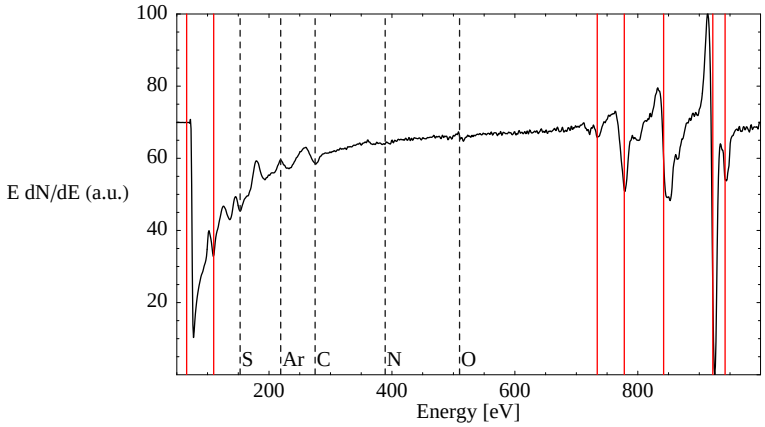

Figure 9.10: Auger electron spectrum of a relatively clean Cu sample, captured with Omicron SpectaLEED electron optics and Stanford Research SR830 lock-in amplifier, and smoothed using Savitzky-Golay smoothing filter which preserves positions of spectral peaks and their width (in contrast, moving average filters tend to reduce height and increase width). Red vertical lines correspond to positions of Cu peaks. Some O, C, and S contamination can also be observed.

In LEED, low-energy electrons ($E \sim 100\,\mathrm{eV}$) are emitted in the form of a narrow beam perpendicularly on a surface. Due to wave-particle duality, diffraction occurs and elastically back-scattered electrons are observed on a phosphorescent screen. In a simple approximation, the LEED pattern corresponds to the Fourier transform of the charge density in the surface region projected to a two-dimensional plane in real space. If the surface is perfectly ordered, the pattern corresponds to the two-dimensional reciprocal lattice of the surface atomic layer(s). In the presence of disorder, peaks will be smeared and the background intensity increased. From the shape of smearing, it is possible to distinguish the type of disorder (chemical inhomogeneity, structural inhomogeneity, etc.) When interpreting spectra, one should take into account that the lateral coherence length ($\Delta r_c \approx 10\,\mathrm{nm}$ at $E \sim 100\,\mathrm{eV}$) is much smaller than the beam spot ($\lesssim 1\,\mathrm{mm}$). The pattern is thus an incoherent average of diffraction patterns over a large number of small areas. Examples of LEED spectra are given in Fig. 9.11.

To evaporate metals in vacuum, atomic beam sources are used.[504–506] Such a source consists of a container where a determined vapor pressure of a substance is sustained. The vapors exit through a well-defined opening and a set of apertures. A directional beam is obtained if the source is operated in the regime where the Knudsen number (ratio of the mean free path to the diameter of the aperture) is greater than unity. The angular distribution of the molecular effusion from the source is then described by the Knudsen's equation

$$dN = \frac{\mathrm{d}\Omega}{4\pi} n\bar{v}B\cos\theta \tag{9.9}$$

where B is source area, n is the particle density in the source, and $\bar{v}$ is the mean molecular

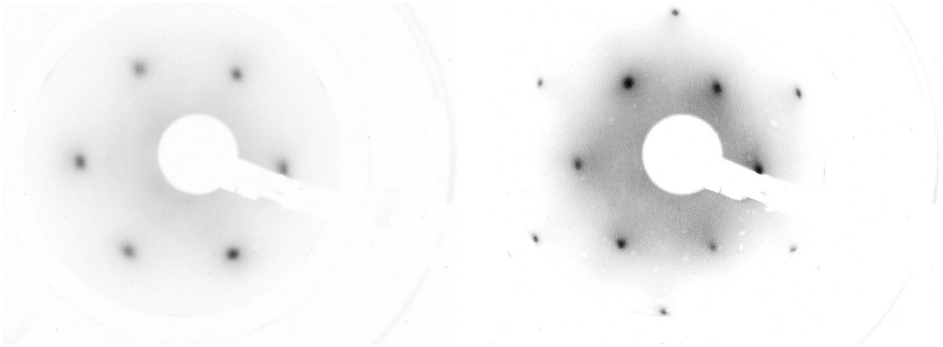

(a) $E = 143$eV (b) $E = 183$eV

Figure 9.11: LEED patterns of relatively clean Cu(111) samples. Color photographs of the fluorescent screen were converted to gray-scale and inverted, so that dark spots correspond to original bright spots.

velocity of the atoms in the source.[505] A fairly uniform beam is obtained using a collimator tube. If the vacuum is high enough, the atoms propagate in straight lines and the deposited material has sharp boundaries. This approach is also applicable to compounds; a beam of single molecules (and possibly small clusters) is obtained in this manner. We used Omicron EFM3 Knudsen source with home-made stainless steel crucibles with nozzles to deposit copper-phthalocyanine (CoPC) molecules on metal samples. While this electron bombardment heating Knudsen source is designed for evaporation of metals, it is nevertheless possible to evaporate high-melting-point substances such as CoPC.

9.5 Sample STM images

In this section, examples of images obtained using the new low-temperature STM are shown. They demonstrate that the instrument is capable of achieving atomic resolution on low-corrugation metal surfaces.

9.5.1 Atomic resolution

The first topographic image with atomic resolution that we have obtained was that of Cu(111) surface, Fig. 9.12. The lattice constant of copper is $a = 3.6\,\text{Å}$. On the (111) surface, the nearest-neighbor inter-atomic distance is $\sqrt{2}/2a = 2.5\,\text{Å}$, the next-nearest-neighbor distance is $\sqrt{6}/2a = 4.4\,\text{Å}$ and the step height is $\sqrt{3}/3a = 2.1\,\text{Å}$.

We also obtain atomic resolution on more corrugated Cu(211)$\equiv$ (3(111) $\times$ (100)) surface, Fig. 9.13. This vicinal surface is strongly anisotropic and the top-most atoms form narrow

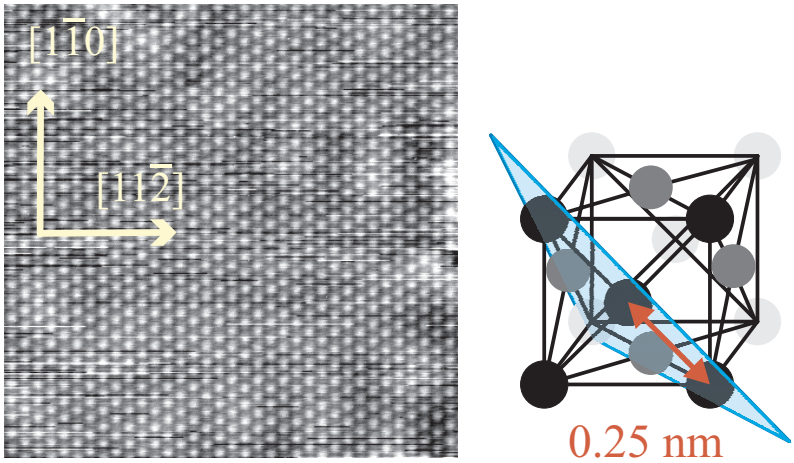

Figure 9.12: Topographic image of Cu(111) surfaces exhibiting atomic resolution (left). $V = 190\,\mathrm{mV}$, $I = 2.2\,\mathrm{nA}$, $77 \times 77\,\mathrm{Å}^2$, $T = 25\,\mathrm{K}$. The drawing represents the (111) plane in the f.c.c. lattice (right).

(111)-facets separated by (100)-steps of monoatomic height.[397,463,507,508] The inter-row distance is 6.35 Å and the inter-atomic separation in the top-most atomic rows is 2.5 Å. On large scale images, one can observe that adatom rows form on top of the regular Cu(211) surfaces along the [01$\bar{1}$] directions, giving the surface a filamentary appearance, Fig. 9.13a. Individual missing surface atoms and single adatoms can be resolved, Fig. 9.13b. At higher resolution, individual protrusion are resolved in the top-most rows, Fig. 9.13c. The distance between the protrusions does not correspond to the expected inter-atomic distance of 2.5 Å; it is possible that only every second atom is imaged.

9.5.2 Spontaneous tip restructuring

The atomistic details of the STM tip apex change in time either spontaneously by relaxation and atomic diffusion processes, or during scanning due to atomic forces exerted between the tip and the sample and due to the strong electronic flux in the apex region. Such dynamic tip effect can be observed in STM images where contrast is changed in parts of images, Fig. 9.14. The slow scanning direction is top to bottom, and the fast scanning direction is left to right. Especially interesting is the left image. In the upper half of the image, double tip effects can be observed: adsorbates are imaged as deformed elliptical depressions with a protrusion in the center. The image of the substrate is smeared and underlying atomic lattice is not clearly resolved. The tip condition is then improved and rather good atomic resolution is obtained in a narrow band. This is followed by a band of intermediate tip condition with deformed adsorbate images and only rough atomic raster, then the tip is improved again for a few scan lines and we finally return to the same bad tip condition as in the upper part of the image.

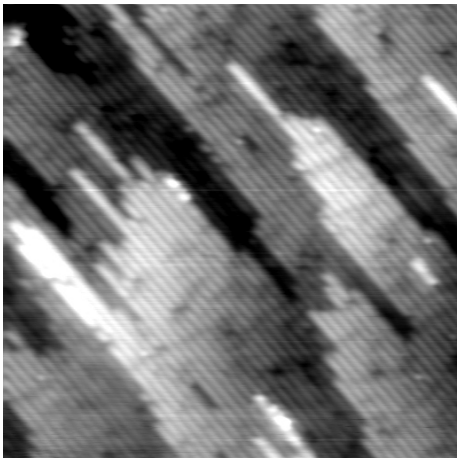

(a) $V = 805\text{mV}$, $I = 0.6\text{nA}$, $300 \times 300\text{Å}^2$

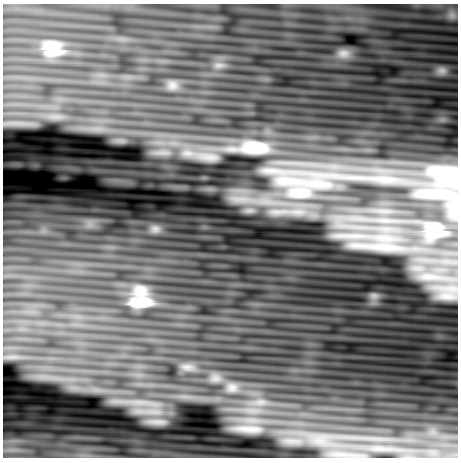

(b) $V = 805\text{mV}$, $I = 0.6\text{nA}$, $300 \times 300\text{Å}^2$

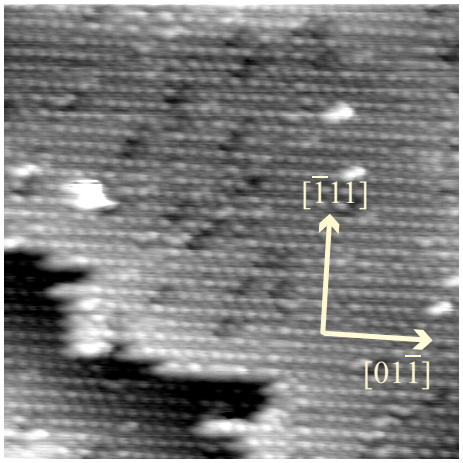

(c) $V = 805\text{mV}$, $I = 0.76\text{nA}$, $200 \times 200\text{Å}^2$

Figure 9.13: Topographic images of Cu(211) surfaces exhibiting atomic resolution. $T = 7\,\text{K}$.

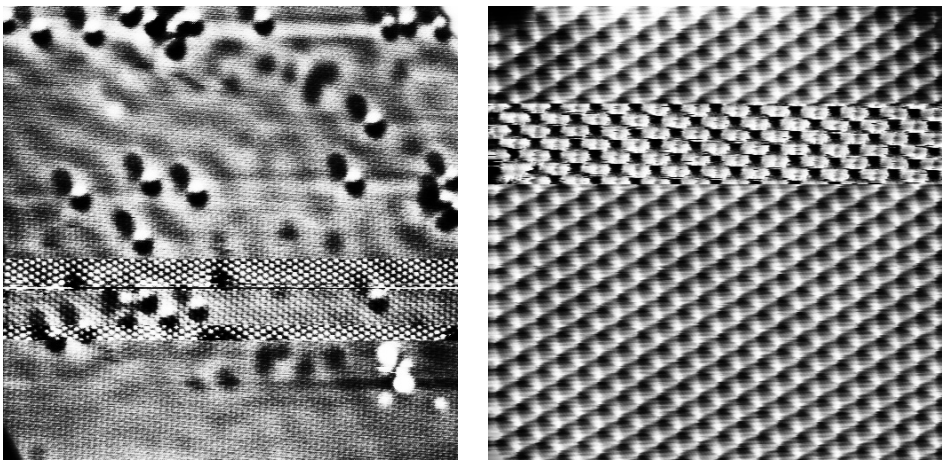

(a) $U = 200$mV, $I = 1$nA, $T = 25$K (b) $U = 313$V, $I = 0.96$nA, $T = 25$K

Figure 9.14: Examples of images taken with unstable tips

9.5.3 Surface-electron standing waves

Copper has a gap of 5.1 eV at the Fermi energy in the (111) direction, but there is a Cu(111) surface state band which starts at 450 mV below the Fermi level as can be inferred from photoemission studies and tunneling spectroscopy.[426] Surface states decay exponentially in the normal direction but are extended in the transverse direction. On close-packed noble metal surfaces, such as (111) surfaces of face-centered cubic lattices, the electrons move almost freely in two lateral dimensions and the the band is highly isotropic. The motion of this two-dimensional electron gas on surfaces is hindered by different kinds of obstacles, such as step edges, dislocations, point defects and adsorbates. Scattering at these obstacles perturbs the surface state charge density and leads to wave-like patterns that can be observed using STM.[509–511] The observed patterns are electron standing waves, which are often claimed to be Friedel oscillations. Strictly speaking, true Friedel oscillations are *charge* density ($\rho(\mathbf{r})$) oscillations around impurities.[512] What we observe on topographic STM images are rather energy-resolved charge-density ($n(\mathbf{r}, E)$) Friedel oscillations.[513] The two quantities are related by

$$\rho(\mathbf{r}) = -e \int_{-\infty}^{E_F} n(\mathbf{r}, E) \mathrm{d}E, \tag{9.10}$$

where E_F is the Fermi energy.

We have observed standing waves around impurities on Cu(111), Fig. 9.15. On highly symmetric surfaces such as Cu(111) scattering on adsorbed atoms is isotropic to a good approximation, thus the patterns are circular. At the Fermi level, surface state electrons have a wavelength of approximately 14 inter-atomic distances, but one should recall that

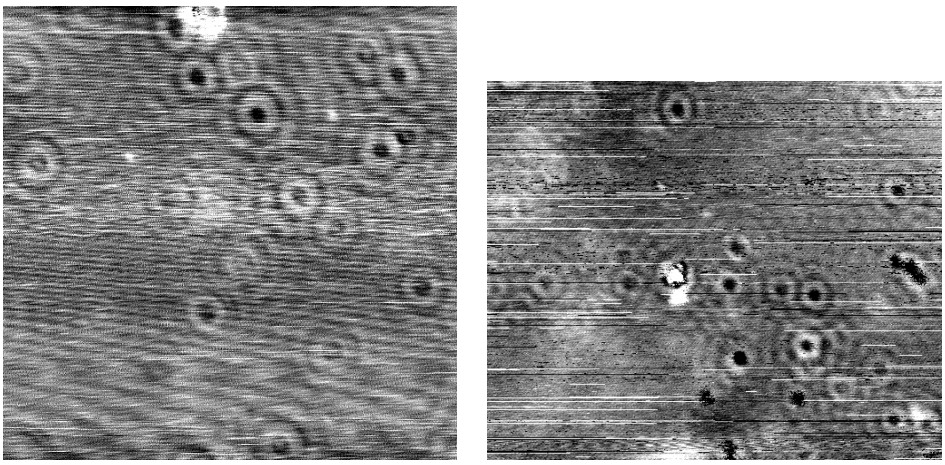

(a) $U = 98$mV, $I = 0.56$nA, $T = 25$K

(b) $U = 89$mV, $I = 0.76$nA, $T = 25$K

Figure 9.15: Standing waves around impurities on Cu(111) surface.

in local density ($|\psi(r)|^2$) wavelength looks half as long. The problem of surface standing waves can be formulated as a scattering problem in two dimensions. The two-dimensional scattering matrix T is:[514]

$$T(E) \propto e^{i\delta(E)} \sin \delta(E), \tag{9.11}$$

where δ is the s-wave phase shift of the electrons that are scattered at the defect. δ is a complex number; imaginary part accounts for absorption of the scattered wave to the bulk. This expression is used in the Dyson's equation $G = G_0 + G_0 T G_0$ to obtain the Green's function, from which we extract the local density of states (spectral function) at a given point:

$$A(E, r) = -\frac{1}{2\pi} \mathrm{Im}\, [G(r, r, E)] \approx_{kr>1} A_0(E) \left[1 + \frac{1}{2\pi^2} \mathrm{Re} \left(\frac{e^{2i\delta} - 1}{2i} \frac{e^{2ikr}}{kr} \right) \right], \tag{9.12}$$

where k is the energy dependent wave-number of the surface-state electrons, and $A_0(E)$ is the spectral function of the unperturbed 2DEG. This equation is valid in the far field of the scatterer.

9.5.4 Molecules on surfaces

On many occasions, we have imaged Cu(111) terraces covered with individual molecules, Fig. 9.16. Each molecule is imaged as a depression surrounded by a protruding ring. The molecules were not deposited intentionally; these are rather molecules which are difficult to eliminate in the sample cleaning process, most likely CO molecules which are a notorious

contaminant species on Cu(111) surfaces. CO adsorbs on the top site with carbon atom down[515] and it is imaged as a depression by clean metallic tips. The origin of the protruding ring are Friedel oscillations around the adsorbed molecule.

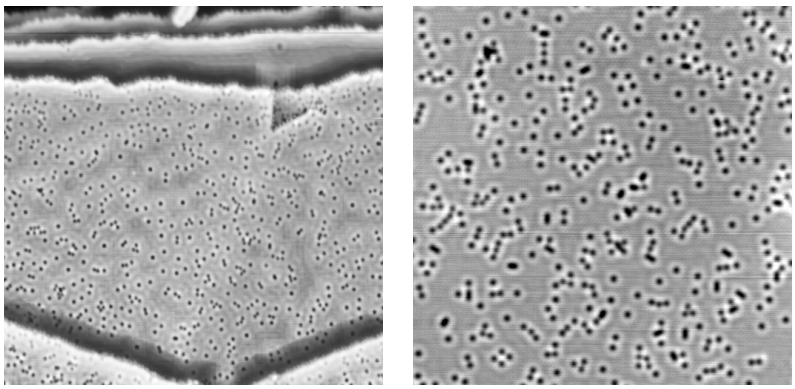

(a) $U = 211$mV, $I = 1$nA, $T = 25$K

(b) $U = 636$mV, $I = 1$nA, $T = 25$K

Figure 9.16: Cu(111) covered with a low concentration of CO molecules.

We also observed in some cases that the molecules are displaced under the effect of the tip, Fig. 9.17. The molecules appear to be pushed away from the tip during successive line scans, which leads to appearance of worm-like linear structures; each such line corresponds to a single molecule being displaced. It should be noticed that not all molecules seem to be moved by the tip; some are immobile and imaged as depressions (black spots) without any artifacts. Later, when we attempted to perform controlled manipulations, it was confirmed that some molecules are indeed more easily displaced than others. It is likely that some molecules are trapped by subsurface impurities which lead to stronger binding, or that there are in fact two different molecular species on the surface.

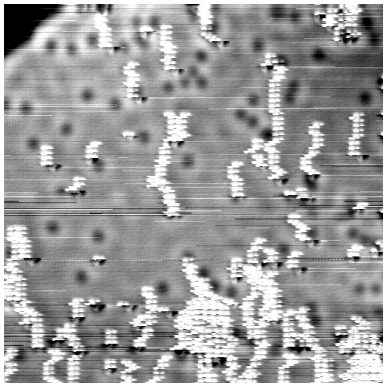

Figure 9.17: Cu(111) covered with a low concentration of CO molecules. $U = 501$mV, $I = 0.96$nA, $T = 25$K.

Chapter 10

Clusters of magnetic adatoms and surface Kondo effect

Magnetic nanostructures are attractive candidate systems for data recording applications (information *storage* in a magnetic medium) and for spintronics (information *processing* using spin degrees of freedom). Studies of magnetic properties of clusters of magnetic impurities elucidate how magnetism appears as the system size is increased.[516,517] Properties of small clusters adsorbed on surfaces depend strongly on their size and geometry, as well as on their coupling to the substrate. Due to surface interactions the inter-atomic distances and cluster shapes may be very different from free clusters in vacuum;[518,519] the adatoms in the smallest clusters (2-10 atoms) are often found to be planar and in registry with the surface atoms.[517] Furthermore, in addition to bonding interaction (roughly equivalent to electron hopping in the context of quantum dots) and direct exchange interaction, there will always be some substrate-mediated long-range indirect interaction between constituent atoms (indirect hopping, RKKY exchange interaction).

Co, Fe, Mn and their dimers on NiAl(110) were studied using STS by Lee et al.[520] Single adatoms have spin-split single-electron resonances of *sp* character that can be easily observed in STS spectra. Spin-splitting originates from the exchange interaction with the spin-polarized, partially filled $3d$ states. When two such adatoms are brought together, the hybridization of these *sp* resonances depends of the sign of the magnetic interaction between the atoms. In the case of AFM coupling two spin-degenerate states are expected, while in the case of FM coupling four exchange-split resonances should appear. The spectral resolution in STS is sufficient to discern between the two possibilities: all three dimers were found to be ferromagnetic. This demonstrates that STM can be used to study internal magnetic coupling in metal clusters even without a spin-polarized tip.

The Kondo effect that occurs in the systems of magnetic impurities on metal surfaces is of special importance; using a low-temperature STM it is possible for the first time to study a single magnetic adatom in interaction with a continuum of states in the substrate.[4,5] In bulk Kondo systems we are in fact considering an ensemble average over a macroscopic

number of impurities with random inter-impurity interactions. The Kondo resonance has been observed, for example, using high-resolution photo-electron spectroscopy that averages over a typical surface area of $1\,\mathrm{mm}^2$.[521] An STM, however, has atomic resolution in space and $< 1\,\mathrm{meV}$ resolution in energy: with STM, magnetic impurities can be characterized both spectroscopically and in space. By measuring the difference of the $\mathrm{d}I/\mathrm{d}V$ signal at the minimum and the maximum of the Fano resonance resulting from the Kondo effect, it is possible to locate spin centers in magnetic molecules with atomic precision.[15] In $Co(CO)_4$ complexes, for example, the Fano spectral signature is well visible when the tip is positioned above the center where the cobalt atom is located and it decays within a radius of $2.5\,\text{Å}$.[15]

Another field of study focuses on the effects of magnetic impurities on correlated materials such as superconductors. It has been shown, for example, that a magnetic adatom (Fe) on a conventional BCS superconductor (Nb) breaks Cooper pairs, as expected.[430]

In this chapter I focus on the Kondo effect induced by magnetic adatoms and clusters. In Section 10.1 I review known experimental results, while in Section 10.2 I briefly present effective phenomenological and microscopic models in common use. Finally, in Section 10.3 I present results of my NRG calculations of the tunneling current affected by the presence of impurities; this section also provides the link to the first part of this dissertation.

10.1 Review of experimental results on surface Kondo effect

Following the seminal work of Madhavan et al.[4] and Li et al.,[5] the surface Kondo effect has been detected in a large number of adsorbate/surface systems in which the magnetic moment is carried either by single atoms or by magnetic ions embedded in molecules; an overview of some measured Kondo temperatures in various systems is given in Table 10.1. It should be noted that experimentalists define the Kondo temperature as the half-width of the Fano resonance. The half-width is only proportional (but not equal) to the Kondo temperature. Since the coefficient of proportionality varies from case to case, published values only indicate the *scale* of the true Kondo temperature. Another complication is that extracting the half-width of the Fano resonance by fitting depends on the background-subtraction procedure. These facts should be taken into account when using published values of T_K in theoretical work. Kondo temperatures are seen to cover a wide interval from much above the room temperature to temperatures below the experimentally achievable range; this merely reflects the exponential dependence of T_K on the microscopic parameters.

Surface	Adatom/complex	Kondo temperature	Reference
Au	Co in bulk	$300 - 700\,\mathrm{K}$	$4, 522$
Au(111)	Co	$70\,\mathrm{K}$	$4, 523$
Au(111)	Co_2	$\ll 6\,\mathrm{K}$	523
Ag(111)	Co	$92\,\mathrm{K}$	$514, 524$
Cu	Co in bulk	$\sim 500\,\mathrm{K}$	525
Cu(111)	Co	$53 \pm 3\,\mathrm{K}$	426
Cu(111)	Co embedded	$405 \pm 35\,\mathrm{K}$	526
Cu(111)	Co	$54 \pm 2\,\mathrm{K}$	525
Cu(100)	Co	$88 \pm 4\,\mathrm{K}$	525
Cu(100)	$Co(CO)_2$	$165 \pm 21\,\mathrm{K}$	15
Cu(100)	$Co(CO)_3$	$170 \pm 16\,\mathrm{K}$	15
Cu(100)	$Co(CO)_4$	$283 \pm 36\,\mathrm{K}$	15
Cu(100)	$(Co(CO)_2)_2$	$138 \pm 21\,\mathrm{K}$	15
Cu(100)	$(Co(CO)_2)_2$	$176 \pm 13\,\mathrm{K}$	15
Au(111)	CoPC	$\ll 5\,\mathrm{K}$	429
Au(111)	d-CoPC	$208\,\mathrm{K}$	429
Cu(100)	Fe	$< 60\,\mathrm{K}$	15
Cu(100)	$Fe(CO)_4$	$140 \pm 23\,\mathrm{K}$	15
Au(111)	Ti	$70\,\mathrm{K}$	527
Au(111)	Ni	$100 \pm 20\,\mathrm{K}$, mixed valent	$13, 527$
Au(111)	Ni_2	$42 \pm 5\,\mathrm{K}$	13
Ag(100)	Ti	$40\,\mathrm{K}$	528
Ag(111)	Ce	$580\,\mathrm{K}$	5
Au(111)	V, Cr, Mn, Fe	$< 6\,\mathrm{K}$	527
Au(111)	Cr	$\ll 7\,\mathrm{K}$	14
Au(111)	Cr_3, equilateral	$50\,\mathrm{K}$	14

Table 10.1: Kondo temperatures for surface Kondo effect on metals.

10.1.1 Kondo effect in a single magnetic adatom

A magnetic impurity (transition metal such as Co or lanthanide such as Ce) adsorbed on the surface of a normal metal (usually a noble metal such as Cu, Ag or Au) induces a characteristic narrow ($\sim 10\,\mathrm{mV}$ for Co/Cu) anti-resonance-like structure near the Fermi level in the electronic surface local density of states (LDOS). The characteristic asymmetric line shape resembles that of a Fano resonance;[4] it should be contrasted with resonances of non-magnetic adatoms which are typically much broader (hundreds of mV). The resonance is spatially centered on the impurity atom and decays over a lateral distance of $\sim 10\,\text{Å}$, where the spectrum becomes identical to the one obtained on a clean surface.[426] The resonance line shape tends to become more symmetric as the tip is moved radially outward; for Co/Au(111) a symmetric dip is observed at a distance of $4\,\text{Å}$.[4] The observed features do not depend on the tip used.[4,5]

The simplest interpretation of these results is that the adatom magnetic moment is Kondo screened and that the observed asymmetric feature in the tunneling spectrum is related to the Kondo resonance. Since the *d*-orbitals of magnetic adsorbates are both spatially well localized within the adatom and far away in energy from the Fermi level, it is reasonable to assume that the majority of the tunneling current at small bias is carried by the *sp*-like states resulting from the hybridization of the substrate states with the adatom electronic levels (in particular adatom valence *s* levels). A good indication that this is true is the independence of the tunneling spectra on the tip-sample distances.[4,426,427,525] What the STM probes is thus, in a very simple approximation, the LDOS of the conduction band electrons at the position of the impurity local moment (or, more accurately, at the position of the tip apex), and not the LDOS of the impurity *d*-level. The hybridization of an impurity site featuring a resonance in its spectral function with a continuum band induces a sharp anti-resonance in the LDOS of the continuum band at the position of the impurity; it is this anti-resonance that we observe in the experiments with magnetic adatoms. Using NRG (see Ref. 529 and Sec. 10.3), it can be shown that for asymmetric single-impurity Anderson model, the anti-resonance indeed has an asymmetric shape similar to that of the Fano model. This point of view is more than a restatement of the conventional description of the origin of the Fano resonance as an interference between two tunneling channels;[4,530] I find it conceptually cleaner to describe the anti-resonance as a feature of the substrate LDOS with the effects of the impurity *d*-orbital taken into account, rather than as an interference phenomenon between the tunneling in *unperturbed* substrate band and the indirect tunneling through the perturbing impurity. The distinction between the two perspectives becomes unmistakable when the impurity *d*-level is modeled as a Kondo impurity. In this case, there is no hybridization to the *d*-level at all, only exchange interaction; nevertheless, a Kondo anti-resonance appears in the spectral function of the conduction band (see Fig. 6.2). Of course, if part of the tunneling current actually does flow directly through the impurity *d* level, the asymmetry is enhanced even further as described by the Fano model.[529]

Recently, the Kondo resonance has also been "directly" observed in the system of a Mn

adatom on an Al_2O_3 island formed on NiAl(110) surface:[439] a narrow conductance peak with Lorentzian shape was observed near zero bias. The magnetic ion is not directly interacting with the substrate electrons; instead, the interaction is mediated by an oxide film. More importantly, the tunneling mechanism is most likely different: in this case, the electrons tunnel from the STM tip to the Mn adatom, and then they tunnel anew through the oxide layer. This two-step tunneling process strongly depends on the impurity spectral function and is, in fact, very similar to the transport phenomena in quantum dots weakly coupled to two electron reservoirs that were the subject of the first Part of this dissertation. When a magnetic field is applied, the peak decreases in amplitude and then splits:[439] this is a conclusive demonstration that the origin of the resonance is the Kondo effect.

Kondo temperature increases with the number of atoms surrounding the impurity.[525,526,531] For example, for Co/Cu(111) the coordination number $Z = 3$ and the Kondo temperature is $T_K = 54\,\mathrm{K}$, while for Co/Cu(100) $Z = 4$ and $T_K = 88\,\mathrm{K}$.[525] Furthermore, impurities in the bulk have significantly higher T_K than adatoms, while $T_K = 405\,\mathrm{K}$ of an impurity embedded in the surface layer ($Z = 9$) interpolates between T_K for adsorbed Co atoms and the bulk T_K of Co/Cu ($Z = 12$).[526] A higher number of neighbors implies stronger hybridization and thus higher T_K. Knorr et al.[525] have proposed a phenomenological model $J\rho \propto Z$ which provides a reasonable fit.

Sharp features in LDOS at one focus of an elliptical quantum corral can be coherently projected by the surface-state electrons to the other focus: this effect has been nicknamed "quantum mirage".[426,532] The experiment is a clear demonstration of the wave nature of electrons. From a semi-classical point of view, the mirage effect occurs due to the property of an ellipse that the sum of the path lengths from the foci to an arbitrary point on the ellipse is constant; if a scatterer is placed at one focus, all scattered waves will interfere constructively at the other focus.[426] The corral behaves as a resonant cavity and the sharp spectral feature projected is the Kondo/Fano resonance of the magnetic Co atom in the focus. As expected, the mirage vanishes when the magnetic adatom is displaced from the focus. A scattering theory that accounts quantitatively for these results was developed by Fiete et al.[533,534]

10.1.2 Dimers of Kondo impurities

Dimers of magnetic adatoms are in many respects similar to the systems of double quantum dots that were the subject of the first part of this dissertation. The insight developed in studying quantum dots can also be applied to understand magnetic structures on surfaces. We saw the important role played by the various inter-impurity interactions. Dimers provide a convenient playground where the pair-wise interactions between Kondo impurities can be studied as a function of their separation.[329]

In quantum corrals formed by Co atoms, the Kondo effect signature is present around each adatom;[426] at the mean inter-atom distance of 10 Å the adatoms thus behave to a large extent as independent Kondo impurities. Other studies of Co/Au(111) show that

the spectral line shape does not change in the presence of other Co atoms for inter-atom separation down to as low as 6 Å,[4] however the Kondo resonance abruptly disappears for Co-Co separations less than 6 Å.[523]

In another type of experiment, interaction effects between Co impurities on Au(111) remained small as Co coverage was increased to 1 ML,[427] however the fraction of atoms that exhibited the Kondo effect was reduced. This experiment indicates that long-range RKKY interactions between Co atoms are weak. On the other hand, two focal magnetic adatoms in quantum mirage experiments interact quite strongly with one another (the Kondo resonances were perturbed)[426] which hints that the surface-state electrons mediated RKKY interaction can be significantly amplified by constructing a suitable resonant cavity. Calculations of inter-impurity interaction between two magnetic atoms located at the foci of an elliptical quantum corral indicate that the quantum corral eigenmode mediated exchange interaction is ferromagnetic.[535,536]

Madhavan et al. have studied the evolution in electronic properties of Ni/Au(111) as two Ni atoms are merged to form a dimer.[13] In free Ni_2 molecules, the inter-atomic exchange interaction is ferromagnetic.[537] For inter-atom distance $d > 12$ Å the adatoms do not interact. Hybridization effects become observable at $d \sim 7$ Å. For $d \geq 4$ Å the Kondo temperature is 100 ± 20 K, but it drops sharply at the closest separation of 3.4 Å. Using LSDA calculations, they explained their findings by impurity energy level shifts; the system is moved from valence-fluctuation regime to a regime with stronger local moment and strongly reduced T_K.

Recently, a study of Co dimers on Cu(100) was performed[329] which sheds more light on this problem. It was shown that for $d \geq 5.7$ Å, the resonance features recover their $d \to \infty$ form, while for $d = 2.56$ Å (compact dimer) the tunneling spectrum is featureless; finally, for intermediate $d = 5.12$ Å a strongly perturbed anti-resonance was found, which is broadened compared to the spectrum of the isolated Co atom. An antiferromagnetic coupling $J \sim 16$ meV at $d = 5.12$ Å was extracted, which should be compared with $k_B T_K^0 = 7.6$ meV for Co/Cu(100). This system is thus near the critical point at $J \sim 2k_B T_K^0$. For the compact dimer, the RKKY interaction is ferromagnetic, binding the spins to $S = 1$, and it appears that the (upper) Kondo temperature is pushed below the temperature range of the experiment.

10.1.3 Trimers of Kondo impurities

Jamneala et al.[14] have studied trimers of Cr atoms, a frustrated antiferromagnetic system. Cr has $3d^5 4s^1$ configuration with large atomic magnetic moment and strong inter-atomic bonding.[14] Cr_3 clusters can be reversibly switched between two configuration with different electronic behavior. One has a resonance near ϵ_F, the other a featureless spectrum; in the original experiment, the atomic positions of atoms could not be resolved. It was proposed that the isosceles trimer shows the Kondo effect since it has magnetic moment, while a compact symmetric trimer does not since the spins sum up to zero.[14] This description in

terms of classical spins is questionable: quantum mechanically, in a triangle we have an octuplet of states which split into a quartet and two degenerate doublets. The original interpretation has been superseded by different theories.[37,38,538] It appears possible that in the symmetric trimer exotic Kondo effect with non-Fermi liquid behavior leads to an increased T_K.[37,38]

10.1.4 Kondo effect in adsorbed molecules

Kondo effect also occurs in adsorbed molecules containing a magnetic ion, for example in $Co(CO)_n$ molecular complexes.[15] The spectral features were related to the Kondo effect by observing that the resonance remained pinned at the Fermi level when the number of ligands was changed. Similar behavior was observed in binuclear cobalt carbonyls, which consist of two cobalt atoms and a number of carbonyl groups.

The coupling between the spin of individual cobalt adatoms with their surroundings can be controlled by attachment of molecular ligands (here CO molecules). A reasonable fit was obtained using $J\rho = J_0 + cn$, where n is the number of ligands. The exchange interaction J and the Kondo temperature increase due to two factors: increased hybridization between the orbital which carries spin and the conduction band, and delocalization of the d electrons which decreases the on-site Coulomb repulsion. This implies that by choosing appropriate ligands, the Kondo temperature can be controlled by modifying the chemical environment of the spin center.[15]

A similar experiment was performed on cobalt phthalocyanine (CoPC) molecules on Au(111).[429] In free CoPC molecule, the Co atom has unpaired d electron with magnetic moment. As 8 hydrogen atoms were removed from the PC backbone, the molecule became more strongly chemically bound to the surface and the Kondo temperature increased.

10.1.5 Kondo effect in metal clusters on nanotubes

Odom et al.[539] have studied small cobalt clusters on metallic single-walled carbon nanotubes (CNTs) with STM. On small nanotube pieces, quantum box effects were detected. A peak near E_F was observed above the center of Co clusters which disappeared over a distance of 2 nm from the cluster. Control experiments were performed with non-magnetic Ag atoms and on semi-conducting CNTs: no resonance was visible in either case, which is consistent with the hypothesis of the Kondo physics.

10.2 Theory of the surface Kondo effect

STM probes Fermi-level LDOS of the sample at the position of the tip,[425] i.e. the extended sp wave functions rather than the well localized d or f orbitals,[5,513,540] see Fig. 10.1. In a

first approximation, we may thus assume that the STM current is due only to tunneling into the conduction band and we may neglect direct tunneling into the impurity d or f level.[427] This holds approximately even when the tip is directly above the atom; in this case the adatom sp orbitals that protrude into the vacuum are strongly hybridized with the conduction band of the substrate.[541] To understand the origin of the Fano resonances in the tunneling spectra measured over magnetic impurities, we must thus study the effect of the impurity on the continuum states.

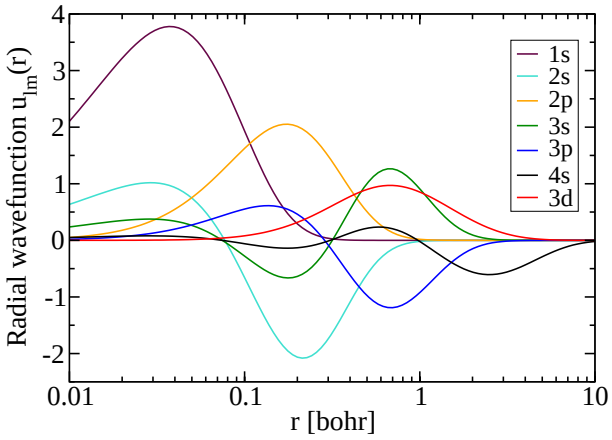

Figure 10.1: Radial wavefunctions of free Co atom in [Ar]$4s^2 3d^7$ configuration computed using Hartree-Fock code.[542] Note that the horizontal (radial) scale is logarithmic. The orbital that extends the furthest outward is $4s$.

10.2.1 Effective quantum impurity models

Magnetic impurities can be modeled as asymmetric Anderson model in the Kondo regime, but not far from the valence-fluctuation regime (see Sec. 6.3). This model can be mapped at low temperatures onto the Kondo model (Sec. 6.3.1 and Ref. 298). A simple approximation for the effective Kondo exchange interaction J is[30]

$$J \propto \frac{|V_{dk}|^2}{\min(|\epsilon_d|, |\epsilon_d + U|)}. \tag{10.1}$$

Here ϵ_d is the energy of the impurity d level, U is the on-site Coulomb repulsion, and $V_{d,k}$ are hybridization matrix elements between the d level and the continuum of states. Only $V_{d,k}$ for k on the scale of T_K are important in the formation of the Kondo resonance, i.e. $V_{d,k}$ is determined by bulk and surface states with energies of the order of 10 mV from the Fermi level. Generally the relevant d level lies below the Fermi energy, while $U \gg |\epsilon_d|$, thus ϵ_d sets the scale of J.

The effective (half-)bandwidth must be appropriately defined. It must be emphasized that the effective bandwidth is not necessarily related to the width of either the bulk conduction

band or the surface-state band. In fact, we have $D_{\rm eff} \sim \min(D_b, D_s, U, E_d^*)$, where D_b is the half-bandwidth of the bulk band and D_s the half-bandwidth of the surface-state band (if both are at play), U is the Coulomb repulsion and E_d^* is the renormalized impurity energy which is usually the relevant energy scale in the valence-fluctuation regime (Sec. 6.3). E_d^* is the solution of transcendental equation[31]

$$E_d^* = \epsilon_d - \frac{\Gamma}{\pi} \ln\left(\frac{U}{-E_d^*}\right). \tag{10.2}$$

There are some indications that magnetic impurities on surfaces indeed are mixed valent (for example Ni/Au(111)[527]). One must thus be very careful when extracting $D_{\rm eff}$ and J from experimentally determined T_K.

Measured temperature dependence of the resonance-width agrees with theoretical predictions of broadening for Kondo impurities in the Fermi liquid (FL) regime.[429, 528] In the FL regime, one can make the following approximation, which holds in the particle-hole symmetric case:[94, 228, 528, 543]

$$\begin{aligned} A(\omega,T) &= -\frac{1}{\pi}\mathrm{Im}\, G^R(\omega,T) = \frac{1}{\pi}\frac{\Sigma^I(\omega)}{(\omega-(\epsilon_d+\Sigma^R(\omega)))^2+\Sigma^I(\omega)^2}, \\ \Sigma^R(\omega,T) &\sim -\epsilon_d, \\ \Sigma^I(\omega,T) &\sim \Gamma + \gamma(\omega,T), \\ \gamma(\omega,T) &= c\Gamma\left[\left(\frac{\omega}{k_B T_K}\right)^2 + \pi^2\left(\frac{T}{T_K}\right)^2\right], \end{aligned} \tag{10.3}$$

where $A(\omega,T)$ is the impurity spectral function at temperature T, Σ is the self-energy, and the coefficient c is $\pi^2/32 \approx 0.3$. A simple approximation for the resonance line-width is then[528]

$$\mathrm{FWHM} = 2\sqrt{(\pi k_B T)^2 + 1/c(k_B T_K)^2}. \tag{10.4}$$

Fermi liquid theory is actually valid only for $\omega, T \ll T_K$. For $\omega, T \sim T_K$, logarithmic corrections should be taken into account. Furthermore, the value of c is not a constant and it is different from $c = \pi^2/32$ if there is no particle-hole symmetry; since in general the system is indeed asymmetric [for example $\epsilon_d = -0.84\,\mathrm{eV}$ and $U = 2.84\,\mathrm{eV}$, i.e. $\delta/U = 0.2$ for Co/Au(111)[522]], large systematic errors are introduced in the determined value of T_K if an arbitrary value for c is used [$c = 1/2$ is often used for historical reasons[528]].

10.2.2 Fano model of interfering discrete and continuum channels

Fano originally studied the interference between a discrete and a continuum channel in the context of atomic physics for discrete auto-ionized states.[333] He has shown that such interference produces a characteristically asymmetric line shape in spectra. It should be noted that the Fano effect is not, per se, a quantum mechanical effect; it is a wave interference

effect that also arises in purely classical systems. Fano resonance can appear whenever there is an interference between a narrow and a wide spectral feature (resonance); see, for example, Sec. 7.3.2 where a Fano resonance appears in the context of side-coupled double quantum dot system. The observation of a Fano-like resonance near the Fermi level in a tunneling spectrum is by itself not a proof of Kondo effect. It must be shown that the narrow spectral feature responsible for the Fano resonance is the Kondo resonance, i.e. is of many-particle origin. A possible test is a measurement of the temperature dependence of the spectral features which should follow the universal Kondo temperature dependence and, in particular, the resonance should gradually disappear above T_K.[528] The results of such temperature-dependent measurements are unfortunately confounded by the fact that the spectral resolution of the tunneling spectroscopy itself is of the order of k_BT, therefore the logarithmic decrease of the amplitude of the Kondo resonance cannot be accurately followed for $T > T_K$. A better test is thus the splitting of the Kondo resonance in strong magnetic field.[439]

The experimental spectra can be fitted with a Fano line

$$\frac{(q+\epsilon)^2}{1+\epsilon^2} = 1 + \frac{q^2 - 1 + 2q\epsilon}{1+\epsilon^2} \tag{10.5}$$

where $\epsilon = (E - E_0)/(\Gamma/2)$ is a rescaled energy, E_0 is the resonance position, Γ its width, with parameter q that is typically between 0 and ~ 1.[541] The Fano line-shapes are plotted in Fig. 10.2 for a range of parameter q. Fits to Fano line shape reproduce the dip structure, the asymmetry and the shift in the minimum from E_F.[426] Small $q \ll 1$ corresponds to small coupling of the discrete state to the tunnel-current carrying continuum states, while large $q \gg 1$ would imply strong tip-impurity coupling, either directly (tunneling of electrons into the localized d-orbital) or indirectly (tunneling of electrons to the d-orbital via the conduction band).[427] The intermediate value $q \sim 1$ means that such coupling is small, yet significant. As we move away from the impurity, q decreases,[4] and the line shape becomes more symmetric (for $q = 0$, the line shape is a symmetric dip). Presently used models have difficulties in reproducing this feature.[541,544,545]

10.2.3 Microscopic theory

Systems described by the quantum impurity models exhibit universality: their low temperature properties are described by a small number of parameters, often only two – the Kondo temperature and the quasiparticle scattering phase shift. In contrast, the line shapes found in the tunneling spectra measured over magnetic adatoms on surfaces are markedly dissimilar. It turns out that they depend on the details of the substrate-electronic-structure induced quantum interference phenomena.

Phenomenological impurity models discussed in the previous section account well for the observed features. To gain more insight, theoretical predictions of the effective parameters starting from microscopic theories were performed.[522,530,544–546] In particular, sophisticated

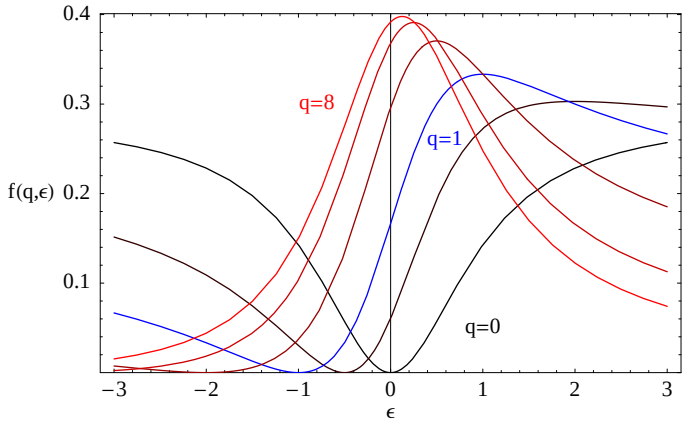

Figure 10.2: Fano resonance lines for a range of parameter q. I plot function $f(q,\epsilon) = c\frac{(q+\epsilon)^2}{1+\epsilon^2}$, where c is some q-dependent normalization constant. Note that $f(-q,-\epsilon) = f(q,\epsilon)$, therefore the Fano lines for negative q are mirror reflections of those for positive q.

methods to calculate the hybridization matrix elements $V_{d,k}$ were sought for;[544,545] it was found early that these parameters are very sensitive to the details of the band structure,[522] which unfortunately reduces the predictive power of simple theories. In addition, the d-level is shifted in energy by the surface potential; due to exponential dependence of T_K on ϵ_d, a modest atomic level shift can lead to a big change in the Kondo temperature. To complicate matters further, in addition to the Kondo effect, the LDOS around the impurity is affected by the Friedel oscillations induced by the adatom.[522]

When a cobalt atom is adsorbed on a metal surface, its outmost s-wave electrons either gets transferred to the metal conduction band or to its own d orbital, therefore Co tends to form $[\mathrm{Ar}]3d^9$ electronic configuration on a Cu surface, i.e. it has a single d-orbital hole and $S = 1/2$.[522,544] In addition, there are good reasons to believe that the relevant d-orbital is $d_{3z^2-r^2}$ and that the orbital motion is quenched by the broken symmetry at the surface (incidentally, this implies that the gyromagnetic ratio is $g \approx 2$). From this follows that the Co adatom can indeed be roughly modeled using the single impurity Anderson model. Ujsaghy et al. have studied the parameters that enter the effective model for cobalt on Au(111).[522] These can be used as simple modeling parameters and are given for reference purposes in Table 10.2. On-site Coulomb repulsion was taken to be proportional to the LSDA Stoner splitting. For the band cutoff (bulk and (111) surface bands of Au) an assumed value of $D = 5.5\,\mathrm{eV}$ can be used (the effective bandwidth is controlled by U and ϵ_d anyhow). With these parameters, we get T_K which is of the expected order of the magnitude.

Parameter	Value
Broadening $\Delta = \pi\|V\|^2\rho$	0.2 eV
On-site Coulomb repulsion U	2.84 eV
Orbital energy ϵ_d	-0.84 eV
Band cutoff D	5.5 eV

Table 10.2: Effective parameters for the Anderson model of Co/Au(111).[522]

10.2.4 Surface-state electrons or bulk conduction band electrons

One of the main difficulties in microscopic modelling of the surface Kondo effect is determining the hybridization constants that enter the expression for the Kondo exchange interaction. Both bulk Bloch waves and surface-state electrons can play a role and, generally, both do. Most experiments are performed on the (111) facets of noble metals where bulk electrons coexist with Shockley surface-state electrons.[547] In recent years, the question about which are predominant was widely debated. Clearly, the presence of the adatom induces mixing between the bulk and surface states[525,545] and the d-level couples to the hybridized mixture of bulk and surface states; we may still be interested in the predominant character (bulk vs. surface) of these hybridized states. The available experimental results suggests a more important role of bulk states even on (111) surfaces.[524,525,547,548] Recent studies based on DFT calculations also indicate much larger contribution from bulk states in Co/Cu(111) system.[545]

The problem of a magnetic impurity on a surface is a two-band, but single channel problem, since only one effective channel couples to the impurity. In this respect it is similar to the quantum dot coupled to two distinct leads, but to a single channel of symmetric combination of wave-functions. If there are two bands coupled to a single $S = 1/2$ impurity orbital, a suitable effective model would be

$$\begin{aligned} H = &\sum_{\mathbf{k}\mu} \epsilon^b_{\mathbf{k}} c^\dagger_{b,\mathbf{k}\mu} c_{b,\mathbf{k}\mu} + \sum_{\mathbf{k}\mu} \epsilon^s_{\mathbf{k}} c^\dagger_{s,\mathbf{k}\mu} c_{s,\mathbf{k}\mu} + H_{\text{impurity}} \\ &+ \sum_{\mathbf{k}\mu} V^b_{\mathbf{k}} \left(d^\dagger_\mu c_{b,\mathbf{k}\mu} + \text{H.c.} \right) + \sum_{\mathbf{k}\mu} V^s_{\mathbf{k}} \left(d^\dagger_\mu c_{s,\mathbf{k}\mu} + \text{H.c.} \right) . \end{aligned} \tag{10.6}$$

with, for example, $H_{\text{impurity}} = \sum_\mu \epsilon_d d^\dagger_\mu d_\mu + U n_\uparrow n_\downarrow$. For definiteness we have assumed that the first band b corresponds to the substrate bulk band (3D), while the second band s corresponds to the surface-state band (2D). We assume that both bands are isotropic, the first in three-dimensions and the second in two-dimensions, i.e. $\epsilon^n_{\mathbf{k}}$ depends only on $k = |\mathbf{k}|$. It should be noted that k in 3D and k in 2D are not comparable. In particular, the Fermi moments are different, $k^b_F \neq k^s_F$.

We can furthermore safely assume that $V^s_{\mathbf{k}}$ depends solely on the magnitude of $\mathbf{k}$, but not on its direction, i.e. only the s-wave symmetric combination of surface-state electrons

couples to the dot. For $V^b_{\mathbf{k}}$ such an approximation cannot be made since the hybridization clearly strongly depends on the direction of $\mathbf{k}$. Nevertheless, we can compute the suitable angular averages of $V^b_{\mathbf{k}}$ and label them by V^b_k. The impurity only couples to the one-dimensional manifold of direction-averaged combinations of states. We then transform from momentum-space to energy-space by defining $a_\epsilon = (d\epsilon_k/dk)^{-1/2} a_k$ when $\epsilon = \epsilon_k$. We obtain (sums over repeated spin indexes are implied)

$$H = \int_{-D_b}^{D_b} \epsilon a^\dagger_{b,\epsilon\mu} a_{b,\epsilon\mu} \mathrm{d}\epsilon + \int_{-D_s}^{D_s} \epsilon a^\dagger_{s,\epsilon\mu} a_{s,\epsilon\mu} \mathrm{d}\epsilon + H_{\mathrm{impurity}} + \int_{-D_b}^{D_b} [\rho_b(\epsilon)]^{1/2} V_b(\epsilon) \left(d^\dagger_\mu a_{b,\epsilon\mu} + \mathrm{H.c.} \right) \mathrm{d}\epsilon + \int_{-D_s}^{D_s} [\rho_s(\epsilon)]^{1/2} V_s(\epsilon) \left(d^\dagger_\mu a_{s,\epsilon\mu} + \mathrm{H.c.} \right) \mathrm{d}\epsilon. \tag{10.7}$$

Now comes the crucial step: at each energy ϵ, the impurity couples only to the "symmetric" combination

$$f_{\epsilon\mu} = \frac{\rho_b^{1/2} V_b a_{b,\epsilon\mu} + \rho_s^{1/2} V_s a_{s,\epsilon\mu}}{\sqrt{\rho_b V_b^2 + \rho_s V_s^2}}, \tag{10.8}$$

while it is decoupled from the "antisymmetric" combination:

$$g_{\epsilon\mu} = \frac{\rho_b^{1/2} V_b a_{b,\epsilon\mu} - \rho_s^{1/2} V_s a_{s,\epsilon\mu}}{\sqrt{\rho_b V_b^2 + \rho_s V_s^2}}. \tag{10.9}$$

We choose a new cut-off $D = \max(D_b, D_s)$, define $\rho V^2 \equiv \rho_s V_s^2 + \rho_b V_b^2$, and write the effective single-channel Anderson model:

$$H = \int_{-D}^{D} \epsilon f^\dagger_{\epsilon\mu} f_{\epsilon\mu} \mathrm{d}\epsilon + H_{\mathrm{impurity}} + \int_{-D}^{D} \sqrt{\rho V^2} \left(d^\dagger_\mu f_{\epsilon\mu} + \mathrm{H.c.} \right) \mathrm{d}\epsilon. \tag{10.10}$$

Thus $\rho|V|^2$ and consequently ρJ are additive quantities.

10.3 NRG calculations

Numerical renormalization group is a powerful technique for computing spectral functions (local densities of states) in problems where many-particle effects are important and need to be properly taken into account. It may be applied in the field of tunneling spectroscopy whenever the problem can be reduced to a quantum impurity problem with a small number of impurity orbitals and one or two conduction channels. NRG is particularly suited for studying the physics of Kondo impurities adsorbed on surfaces where the relevant magnetic orbital is typically a single d-level and there may be a small number of broad sp-derived levels near the Fermi level, while all other atomic levels away from the Fermi level

are irrelevant: such atoms can be accurately modeled by some multi-level Anderson-like impurity model.

To my knowledge, the impurity *sp* orbitals are entirely neglected in all phenomenological as well as most microscopic theories that had been applied to the surface Kondo problem, even though these orbitals may modulate the density of states that the *d*-level couples to. Furthermore, these orbitals can carry a portion of the tunneling current when the STM tip is located directly above the impurity atoms. The closer the energy of these orbitals is to the Fermi level, the more important role they play.

In this section I show by NRG calculations that a) the anti-resonance in the differential conductance is a direct consequence of the resonance on the *d*-level, b) the anti-resonance diminishes and splits in applied magnetic field, c) the form of the anti-resonance depends in an essential way on the proportions of the tunneling current that flows in the adsorbate *s*-level and in the substrate band, d) the *s*-level modulates the density of states to which the impurity couples, therefore the changes in the *s*-level energy can drive the Kondo temperature to extremely small values.

The tunneling current is given by (see Sec. 5.3.2)

$$I = \frac{e}{h} \sum_{\mu} \int \mathrm{d}\epsilon \, (f_{\mathrm{substrate}}(\epsilon) - f_{\mathrm{tip}}(\epsilon)) \, \mathrm{Tr}[\mathbf{\Gamma}^{\mathrm{tip},\mu}(\epsilon) \mathrm{Im}\, \mathbf{G}^{r\mu}(\epsilon)]. \tag{10.11}$$

Here $\mathbf{\Gamma}^{\mathrm{tip}}$ is the hybridization matrix between the STM tip states and the adsorbate levels, while $\mathbf{G}^r$ is the retarded Green's function matrix of the adsorbate. At zero temperature, the Fermi-Dirac distribution functions become $f_{\mathrm{substrate}}(\epsilon) = \theta(\epsilon_F - \epsilon)$, $f_{\mathrm{tip}}(\epsilon) = \theta(\epsilon_F + eV - \epsilon)$, where ϵ_F is the Fermi level and V the voltage drop in the gap between the STM tip and the adsorbate; for $V > 0$ electrons flow from the tip to the sample. We then obtain

$$\mathrm{d}I/\mathrm{d}V = -G_0/2 \sum_{\mu} \mathrm{Tr}[\mathbf{\Gamma}^{\mathrm{tip},\mu}(\epsilon) \mathrm{Im}\, \mathbf{G}^{r\mu}(\epsilon)]_{\epsilon=\epsilon_F+eV}. \tag{10.12}$$

The imaginary part of the Green's function $\mathbf{G}^r$ is essentially orbitally-resolved local density of states of the impurity, while the hybridization matrix $\mathbf{\Gamma}^{\mathrm{tip}}$ encodes both the density of states in the tip and the tunneling probability to various orbitals. The tunneling probability depends on the orbitals at play: the tunneling to the *d*-level is expected to be negligible or small, while the tunneling to the *s*-level is substantial. In addition, part of the tunneling current inevitably flows directly into the substrate states. This possibility is not taken into account in Meir-Wingreen formula and therefore neither in Eqs. (10.11) and (10.12). In Bardeen's theory, the tip-substrate current is proportional to a square of the surface integral over a separation surface between the tip and the sample[353]

$$M = -\frac{\hbar^2}{2m} \int_{\Sigma} (\chi^* \nabla \psi - \psi \nabla \chi^*) \cdot \mathrm{d}\mathbf{S}, \tag{10.13}$$

where ψ is the sample conduction band wave-function and χ the tip wave-function. The simplest approximation consists of assuming that the tip-substrate wave-function overlap

is largest at the position of the impurity atom. From the perspective of NRG calculations, this approximation corresponds to assuming that the tip probes the Wannier orbital f_0 of the Wilson chain[529] . The idea here is to consider f_0 as part of the impurity system; Eq. (10.12) then still applies, but the trace over impurity orbitals is extended to include the f_0 orbital. The tunneling current then flows to some linear combination of orbitals, described by an operator such as $h_\mu^\dagger \propto t_s d_{s\mu}^\dagger + t_{f_0} f_{0\mu}^\dagger$, where t_s and t_{f_0} are the tunneling amplitudes for tunneling in either the s-level or in the substrate electron band.[529, 530]

Equation (10.12) simplifies to

$$\mathrm{d}I/\mathrm{d}V = G_0/2 \sum_\mu \pi[\Gamma^{\mathrm{tip}}(\epsilon) A_{h,\mu}]_{\epsilon=\epsilon_F+eV}, \tag{10.14}$$

where $\Gamma^{\mathrm{tip}}(\epsilon) = \pi\rho_{\mathrm{tip}}(\epsilon)(t_s^2 + t_{f_0}^2)$. We take t_s and t_{f_0} to be energy-independent in the relevant energy range around the Fermi level, but this assumption may be relaxed. It should be emphasized that in this formalism the sum over different tunneling paths is performed coherently and that all quantum interference effects are taken into account. The quantity of central interest is thus the spectral function of the effective "orbital h", $A_{h,\mu}$.

Before focusing on the two-level impurity model, we first study the conventional description of the surface Kondo effect using a single d-level Anderson model:[30]

$$\begin{aligned} H_{\mathrm{imp}} &= \delta(n_d - 1) + \frac{U}{2}(n_d - 1)^2, \\ H_{\mathrm{c}} &= \left(\frac{2\Gamma D}{\pi}\right)^{1/2} \sum_\mu \left(d_\mu^\dagger f_{0\mu} + \mathrm{H.c.}\right). \end{aligned} \tag{10.15}$$

By writing the coupling Hamiltonian H_{c} in this form, we assumed that the d-level hybridizes with the conduction band orbital centered at the impurity site, f_0. Furthermore, we assume that when the STM tip is directly above the adsorbate the tunneling current flows only to f_0, i.e. $h_\mu^\dagger = f_{0\mu}^\dagger$. The impurity d-level spectral functions and the conduction band LDOS (or, equivalently, the spectral function of the f_0 orbital) are shown in Fig. 10.3.

In the absence of the impurity, the conduction band LDOS is flat near the Fermi level, $A_{f_0}(\omega) = 1/(2D)$. When the impurity is introduced, the impurity spectral function is mirrored in the conduction band LDOS. The following relation holds for a flat band at $T = 0$:[548]

$$A_{f_0}(\omega) = A_0 \left(1 - \pi\Gamma A_d(\omega)\right). \tag{10.16}$$

The conduction band LDOS is thus exactly zero at the Fermi level in the case of symmetric Anderson model ($\delta = 0$). When the Anderson impurity is asymmetric ($\delta \neq 0$), the Kondo resonance is also asymmetric and so is the anti-resonance, similar to what is found in the experimental tunneling spectra.

It is known that applied magnetic field splits the Kondo resonance. This is expected to be reflected in a diminished Fano anti-resonance for small fields, and a double dip anti-resonance for strong fields, Fig. 10.4. To this date no experimental results of such splitting

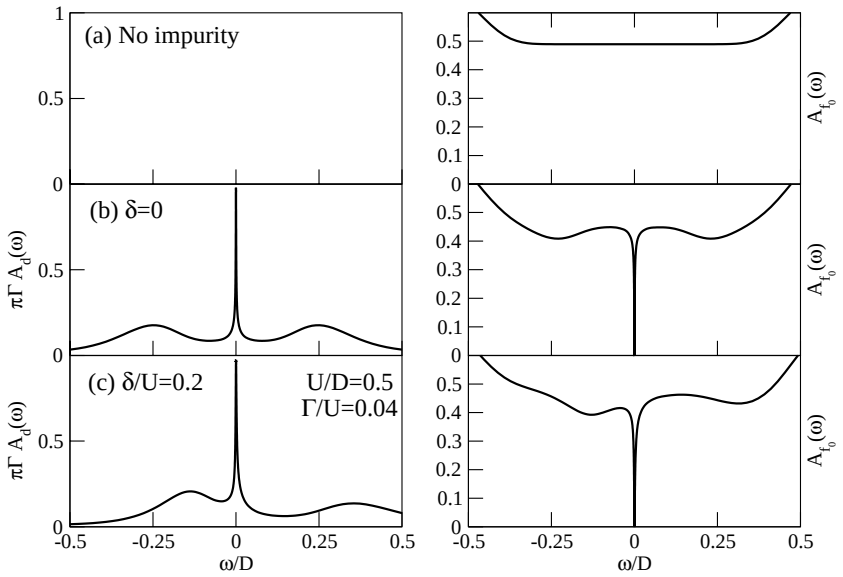

Figure 10.3: Impurity and conduction band spectral functions without an impurity (top), with a symmetric impurity (center) and with an asymmetric Anderson impurity (bottom).

have been reported, however the Kondo resonance splitting was observed in a somewhat different setting with a magnetic impurity adsorbed on an insulating island grown on metallic surface.[439]

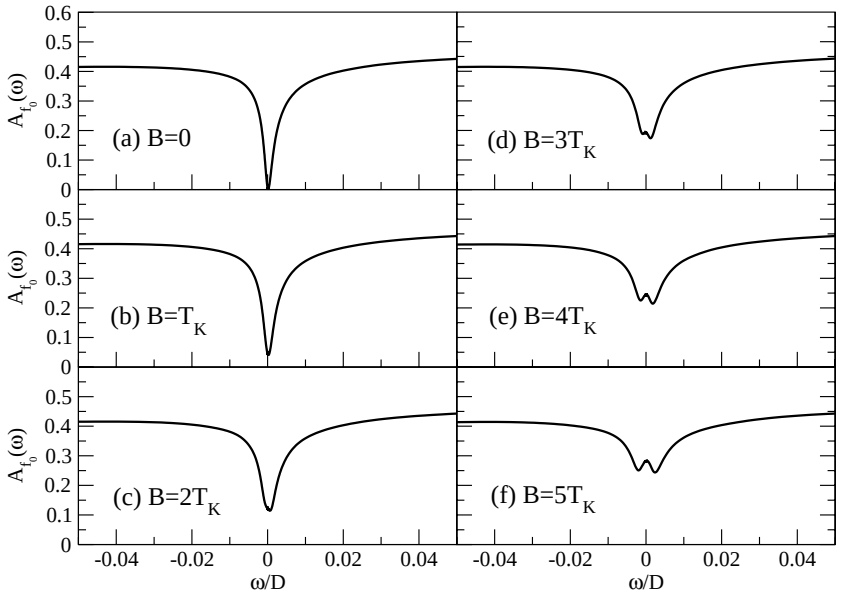

Figure 10.4: Effect of the magnetic field on the conduction band spectral function for the single-impurity Anderson model. See the impurity spectral function counterpart in Fig. 6.12.

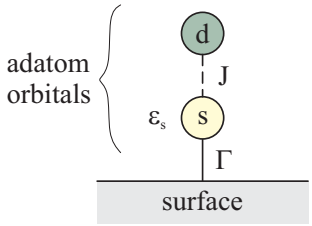

Figure 10.5: The two-orbital single-impurity model.

We now turn to the two-orbital model represented graphically in Fig. 10.5. The d-orbital may be described by a single spin operator $\mathbf{S}_d$ like in the Kondo model; since we neglect tunneling to d-levels, this is a good approximation. The s-level is described as a non-interacting level. Initially we assume that the d-level interacts via exchange interaction only with the s-level. The corresponding Hamiltonian is thus

$$\begin{aligned} H_{\rm imp} &= \epsilon_s \sum_\mu d^\dagger_{s\mu} d_{s\mu} + J \mathbf{S}_d \cdot \mathbf{S}_s \\ H_{\rm C} &= \left(\frac{2\Gamma D}{\pi}\right)^{1/2} \sum_\mu \left(d^\dagger_{s\mu} f_{0\mu} + \text{H.c.} \right) . \end{aligned} \tag{10.17}$$

Here $\mathbf{S}_s = \frac{1}{2}\sum_{\mu\nu} d^\dagger_{s\mu} \boldsymbol{\sigma}_{\mu\nu} d_{s\nu}$ is the spin operator of s-orbital. (I note that models of this type have been recently studied in the context of double quantum dots[549]). The hybridization of the s-level with the conduction band electrons is expected to be strong, therefore parameter Γ is large.

We first consider the case when the s-level is centered at the Fermi level, Fig. 10.6. In the absence of the adatom, the conduction band LDOS is (assumed) flat near the Fermi level (green line in Fig. 10.6b). When only the s-level is taken into account by setting $J = 0$, the broad resonance in $A_s(\omega)$ is reflected in a broad anti-resonance in $A_{f_0}(\omega)$ (blue lines in Fig. 10.6a,b). When exchange interaction is switched on, the Kondo effect leads to a narrow dip $A_s(\omega)$ in the broad s-level resonance (compare with Fig. 6.2), and this anti-resonance is reflected in a resonance in $A_{f_0}(\omega)$ (black lines in Fig. 10.6a,b). The spectroscopic signature of the Kondo effect will depend in an essential way on the respective proportion of the tunneling current that flows to the s-level or directly to the conduction band. A range of spectral functions for different combinations is shown in Fig. 6.2c,d. The full range of possible Fano line-shapes can be obtained, ranging from a symmetric dip ($q = 0$ for $h = s$) to a symmetric peak (q large for $h = f_0$). In other words, the Fano parameter q can take an arbitrary value.

Since in the simplest two-level model, the local moment couples only to the s-orbital, the spectral function of the s-level near the Fermi level determines the Kondo temperature T_K. It is highest when $\epsilon_s = 0$, and it rapidly drops to very small values as the s-level is shifted from the Fermi level, Fig. 10.7. Two effects in the $A_h(\omega)$ for $h \propto s + f_0$ are noteworthy. The Fano line-shape changes (parameter q increases), even though the combination h is kept

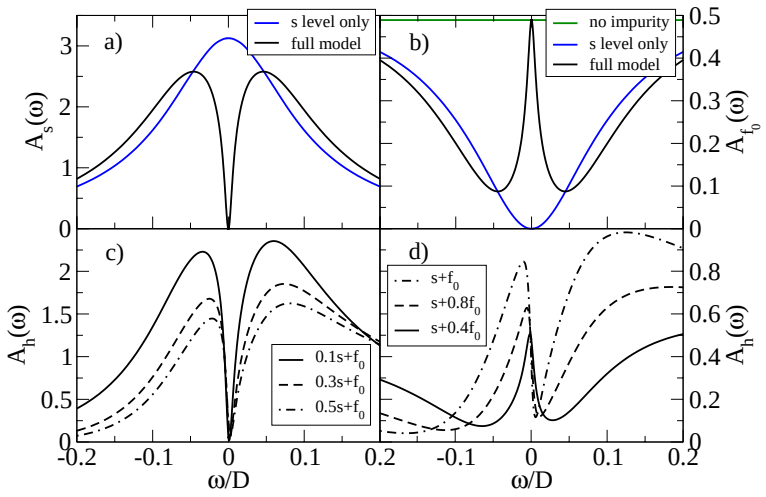

Figure 10.6: Spectral functions in the two-level model for a magnetic adatom. a) s-level spectral function. b) f_0 Wannier orbital spectral function. c) and d) spectral functions for a linear combination of the s-level and the f_0-orbital.

constant; this is another indication that the line-shape strongly depends on the microscopic details of the problem. We also notice that the spectral peak in $A_h(\omega)$ is shifted to higher energies as compared to the spectral peak in $A_s(\omega)$ and spectral dip in $A_{f_0}(\omega)$. This is a quantum effect resulting from coherent addition of various tunneling processes. This suggests that parameter extraction from experimental spectroscopic measurements is model dependent and that obtaining "true" microscopic parameters is difficult.

We now relax the assumption that the d-level interacts only with the s-orbital electrons. We add a perturbation term $H' = J_{df}\mathbf{S}_d \cdot \mathbf{S}_{f_0}$ and study the effect of different ratios of J and J_{df} while keeping the sum constant, Fig. 10.8. The most notable effect is the strong reduction of the Kondo temperature, which drops to zero when the moment couples only to band electrons. The origin of this behavior is the depletion of the conduction band LDOS near the Fermi level due to the hybridization with the s-orbital.[549] When ϵ_s is shifted from 0 for large J_{df}, the Kondo temperature increases again since the conduction band LDOS at Fermi level increases (results not shown).

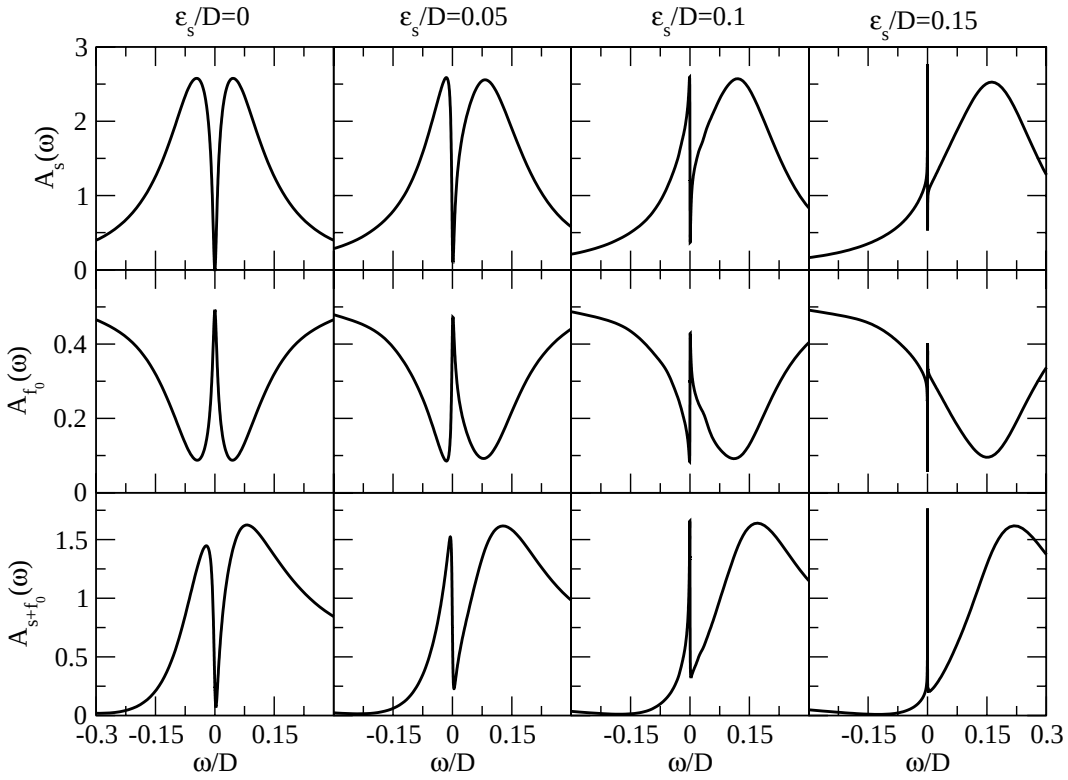

Figure 10.7: Spectral functions in the two-level model for a range of s-level energies ϵ_s.

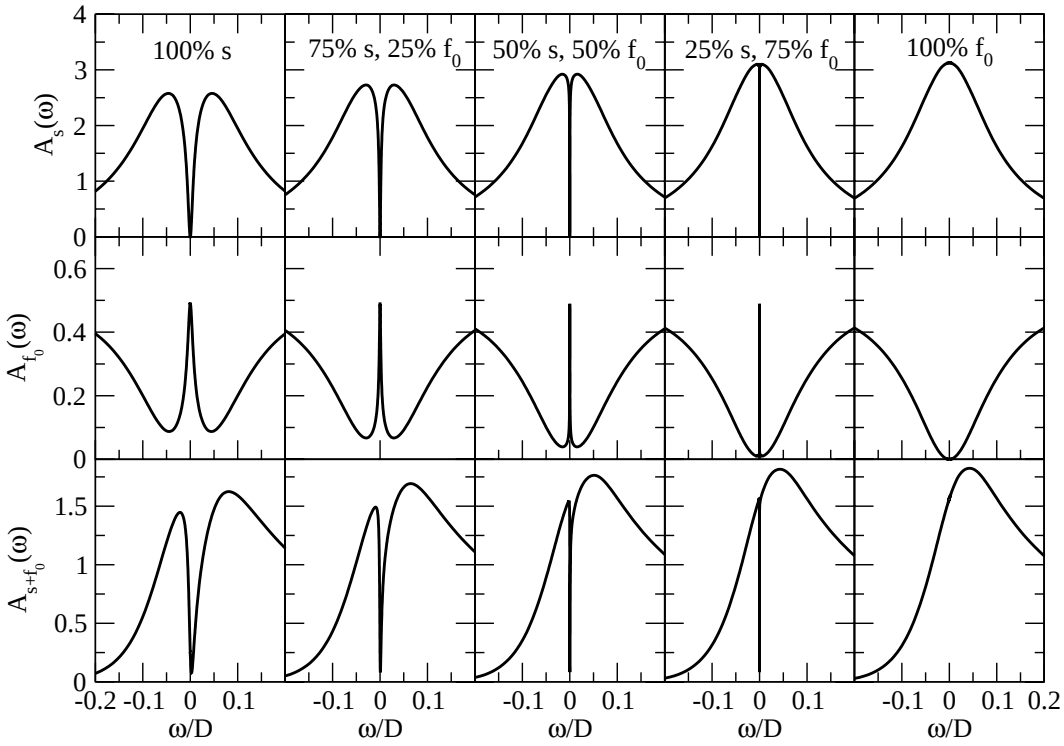

Figure 10.8: Spectral functions in the two-level model for different proportions of coupling of the magnetic impurity to either the s-level or to the conduction band electron Wannier orbital f_0.

Part IV

Conclusion

Chapter 11

Conclusions

This concluding chapter provides a concise summary of the main ideas, techniques and results contained in this dissertation and suggests some possible directions for further research.

Quantum impurity models

Quantum impurity models describe a variety of different physical systems in which an impurity with internal degrees of freedom is coupled to a continuum of states in its environment. Notable examples are magnetic impurity ions in bulk metal samples or on their surfaces, and nanostructures such as systems of coupled quantum dots. The origin of their unusual behavior are the internal degrees of freedom which may lead to anomalously strong scattering at low temperatures – the Kondo effect. At high temperatures, the models exhibit asymptotic freedom and can be studied by perturbation theory, while the strong coupling regimes at low temperatures are generally non-perturbative. In the case of magnetic impurities, the Kondo effect leads to the screening of the local moment and the impurity becomes effectively non-magnetic. In addition, a characteristic narrow Kondo resonance emerges near the Fermi level and it strongly affects the low-temperature transport properties of the system.

The models discussed in this dissertation feature at most two continua of states (two channels). Two-channel free-electron bands have internal SO(8) symmetry; the coupling to the impurity reduces this symmetry to some subgroup of SO(8). The behavior of quantum impurity models strongly depends on the symmetry of the problem; the most unusual effects tend to occur in highly symmetric cases. Particularly important symmetry groups are $\mathrm{SU}(2)_{\mathrm{spin}}$ related to the isotropy in spin space, $\mathrm{SU}(2)_{\mathrm{iso}}$ related to charge conservation and particle-hole symmetry, and $\mathrm{SU}(2)_{\mathrm{flavor}}$ related to the symmetry between the two channels, as well as their various subgroups.

Since impurities may be considered as point-like, they effectively couple to a one-dimensional continuum of states (or, possibly, to a finite number of such continua). Furthermore, when the continuum density of states does not exhibit any irregularities at the Fermi level, the dispersion can be linearized in the relevant low-energy range. Quantum impurity models then reduce to one-dimensional effective field theories with characteristic properties such as the spin-charge separation. Their low-temperature fixed points can be Fermi liquid or non-Fermi liquid in character. An important tool to study the fixed-points and their vicinity is the boundary conformal field theory. It provides an intuitive picture of the Kondo effect: the impurity degrees of freedom disappear from the problem, their only effect is to modify the boundary conditions for the scattering of continuum particles.

While much is already known about the symmetries of quantum impurity models and the relation between the symmetries and the stability of various fixed points, a comprehensive study of the possible non-trivial non-Fermi liquid fixed points in models that are relevant to the transport through nanostructures would be highly desirable. In this context, it is worth noting that the boundary conformal field theory approach allows, in principle, to systematically study all the fixed points of models with purely local interactions.

Renormalization group

The renormalization group idea is a way of understanding the different types of behavior of a system at different energy scales and how they are related. The RG notions of renormalizability, universality and dimensional transmutation are closely related; quantum impurity models often exhibit universal behavior that depends only on a handful of parameters. In the high-temperature perturbative regime, impurity models can be described by simple cut-off renormalization theories (scaling) which, however, fail as the strong coupling regime is approached.

Wilson's numerical renormalization group (NRG) is a non-perturbative approach to performing RG transformations. A new flexible implementation of this method ("NRG Ljubljana") was coded in Mathematica and C++ for performing calculations of the properties of quantum impurity problems that are relevant for studying quantum transport through nanostructures.

NRG consists of the logarithmic discretization of the bands, followed by the iterative diagonalization of a series of Hamiltonians. The logarithmic discretization (or, more accurately, the neglect of higher Fourier modes in each energy interval) is clearly an approximation; nevertheless, it is shown a posteriori that this is a good approximation even for relatively large values of the discretization parameter Λ. For complex multi-impurity and multi-channel problems, it is imperative to take into account all the symmetry elements of the problem at hand to reduce the computational demands. In "NRG Ljubljana", computer algebra system Mathematica was used to automate the generation of code for various types of symmetries; for large symmetry groups, such as $\mathrm{SU}(2)_{\mathrm{iso}} \times \mathrm{SU}(2)_{\mathrm{spin}} \times \mathrm{Z}_2$, manual

derivation of various coefficients becomes intractable.

The iterative diagonalization consists of successively adding sites from the hopping Hamiltonian and performing exact diagonalizations. The result of the diagonalization (eigenvalues and eigenvectors) at iteration N constitutes a description of the original problem on the energy scale $\propto \Lambda^{-N/2}$. Since the number of states in the calculation would grow exponentially with the number of iterations, a truncation to a finite number of sites is performed after each diagonalization. This is a good approximation, since at each RG transformation only the lowest-lying eigenstates are renormalized.

Using NRG, one can compute many important physical quantities. Much information can be extracted from the finite-size spectra alone: for example, one can identify the fixed points of the problem and study cross-overs between them. Furthermore, one can extract effective Hamiltonians that describe the behavior of the system near fixed points and determine if various perturbations are relevant, marginal or irrelevant. From finite-size spectra, static thermodynamics quantities (such as susceptibilities and entropy) can also be obtained. In addition, it is possible to calculate correlation functions (such as charge fluctuations and spin-spin correlations) and dynamic quantities (such as spectral functions and dynamic spin susceptibilities). In the density-matrix NRG method, the reduced density matrix is used in the spectral function calculations so that the true ground state of the system is taken into account also at higher excitation energies.

With the recent resurgence of the interest in impurity models, the NRG technique is also experiencing significant development. Especially important are improvements in spectral function calculations, which make NRG a very capable impurity solver in the dynamic mean-field theory of extended correlated systems.

Other methods for impurity models

In addition to NRG, Gunnarsson-Schönhammer variational method and Quantum Monte Carlo can be applied to study quantum impurity models.

In the variational method, a trial wave-function which takes into account the suppression of charge fluctuations in the Anderson model is used as an Ansatz. Suitable wave-function is constructed by projecting the Hartree-Fock wave-function to subspaces with different occupancy of the impurity orbitals. The method can be improved by considering the parameters of an effective quasiparticle Hamiltonian to be variable. Variational energy minimization problem is then solved iteratively.

In auxiliary-field (determinantal) Quantum Monte Carlo (QMC), a problem of lattice fermions is transformed to an Ising-model-like classical model using Trotter decomposition and Hubbard-Stratonovich transformation, followed by the integration over fermion degrees of freedom. In the Constrained Path QMC, the fermionic minus-sign problem is alleviated by restricting the calculation to one of the two degenerate halves of the Slater

determinant space.

It would be interesting to implement the variational method using logarithmic discretization of the conduction band; it seems possible that a better description of low energy scales could be achieved. Another promising direction would be the development of the variational Anstaz that took into account the degrees of freedom which become decoupled from the Fermi liquid electron system at low energies: this might overcome the problems when the method is applied to singular Fermi liquid systems. Finally, it would be very interesting to implement a variational approach in terms of Majorana fermions that could possibly be able to describe non-Fermi liquid systems.

Quantum transport theory

Transport through a system of quantum dots and tunneling spectroscopy of magnetic adsorbates on a metallic surface are closely related problems; they can both be modeled using quantum impurity models.

Zero-temperature conductance through an interacting region can be calculated from quasiparticle scattering phase shifts if the ground state of the system is Fermi liquid. This approach is based on the Landauer-Büttiker formalism. The scattering phase shifts can be easily extracted from NRG finite-size spectra by making use of the known quantum numbers of the excitations.

For Fermi-liquid systems, the $T = 0$ conductance can also be obtained using the "sine formula" by calculating the difference in energies of two auxiliary ring systems with embedded impurity region for periodic or anti-periodic boundary conditions. This approach is especially suitable when used in conjunction with the variational method which provides ground state energies with good accuracy.

Finally, the conductance can be calculated from spectral functions using the Meir-Wingreen formula. The advantage of this approach is that the temperature dependence of the conductance can be inferred from the energy dependence of the spectral functions.

Further research in the transport theory could be centered at non-equilibrium, time-dependent and finite-temperature properties of impurity systems. While the basic transport formalism is well developed, calculations of non-equilibrium properties of correlated system is still a formidable problem. The recently developed time-dependent NRG technique appears very promising in this respect.

Single-impurity models

The characteristic property of the paradigmatic quantum impurity model – the Kondo model – is screening of the magnetic moment below the Kondo temperature T_K. At very

low temperature, $T \ll T_K$, the system behaves as a local Fermi liquid; its interacting nature is seen in the non-trivial Wilson ratio $R = 2$. Without additional potential scattering, the behavior of Kondo systems is universal and described by universal functions of T/T_K. In the presence of potential scattering, the low-temperature fixed points are parameterized by an additional quantity, the quasiparticle phase shift $\delta_{\rm qp}$.

In the two-channel Kondo model, the over-screening of the impurity spin leads to non-Fermi liquid (NFL) behavior. The impurity has residual ground state entropy of $k_B \ln 2/2$ and the system has an unusual spectrum $0, 1/8, 1/2, 5/8, 1, 1+1/8$, etc.. NFL fixed point is destabilized by channel asymmetry and the system crosses over to a Fermi liquid ground state at some lower temperature.

Single-impurity Anderson model describes formation of local moments in systems such as magnetic impurities (d-orbital) or quantum dots. Near particle-hole symmetric point, the system flows with decreasing temperature from the free-orbital regime (spin and charge fluctuations) to valence-fluctuation regime (charge fluctuations between two values) to local-moment regime (spin fluctuations only), and it ends up in the strong-coupling regime where the local moment is screened; the behavior of the system can be summarized in a kind of "phase diagram" as a function of the on-site energy and the temperature. At sufficient low temperature, the single-impurity Anderson model can be mapped to Kondo model using the Schrieffer-Wolff transformation, which projects out charge fluctuations from the problem.

Charge fluctuations on the impurity site are given for small Γ/U by a universal function $\langle q^2 \rangle = (4/\pi)(\Gamma/U)$. The departure of the charge fluctuations on the first site of the Wilson's chain, $\langle q_f^2 \rangle$, from the non-interacting value of $1/2$ demonstrates that the impurity indeed induces correlated behavior in the band. The charge-charge correlation function $\langle q q_f \rangle$ is negative for large Γ/U and positive for $\Gamma/U \lesssim 1$. The spin-spin correlation function $\langle \mathbf{S} \cdot \mathbf{S}_f \rangle$ is negative due to effective antiferromagnetic interaction between the impurity moment and the conduction band electrons. It tends toward zero as the hybridization Γ is decreased which demonstrates that the Kondo screening cloud is an extended object.

The spectral function on the impurity site in the Kondo regime features two broad charge-transfer peaks at ϵ_d and $\epsilon_d + U$ ("Hubbard satellites") and a characteristic narrow resonance of width proportional to $k_B T_K$ pinned near the Fermi level ("Kondo resonance"). The zero-energy spectral function is related to the impurity occupancy by the Friedel sum rule. Comparison of the conductance calculated for bands with different hybridization functions which have the same value at the Fermi level shows that differences are small; they are the most perceptible in the valence fluctuation regime where the relevant energy scale (T_K) becomes comparable to the band-width. In an applied magnetic (Zeeman) field, the Kondo resonance splits into two peaks that are centered at $\epsilon_d - g\mu_B|B|/2$ and $\epsilon_d + U + g\mu_B|B|/2$ for $\mu_B g B \gtrsim \epsilon_d, U$.

While it might appear that everything is already known about single-impurity models, I would like to point out that, for example, models where an impurity is coupled to bosonic bath (or even both fermionic and bosonic bath at the same time) only recently came under

scrutiny by bosonic generalization of NRG.

Two-impurity models

Systems of two impurities such as double quantum dots (DQD) are the simplest systems where the competition between magnetic ordering and Kondo screening can be studied.

Parallel double quantum dots (and N-dot generalizations) can be described by the multi-impurity Anderson model. At low temperature, this model maps to a multi-impurity Kondo model. It is found that the conduction-band-mediated RKKY exchange interaction is ferromagnetic, $J_{\mathrm{RKKY}} \sim U(\rho J_K)^2 = (64/\pi^2)(\Gamma^2/U)$, therefore the impurity spins order and the system effectively behaves as a single-impurity $S = N/2$ Kondo model which undergoes $S = N/2$ Kondo effect. The Kondo temperature is the same irrespective of the number of the impurities N. The residual spin at zero-temperature is $N/2 - 1/2$ if there is no coupling to additional screening channels. The ferromagnetically ordered regime and the ensuing $S = N/2$ Kondo effect are fairly robust against various perturbations. Very strong perturbations lead, however, to quantum phase transitions (QPT) of different kinds, which have been meticulously studied for the $N = 2$ case.

If the parallel DQD system is moved from the particle-hole symmetric point by equally increasing both on-site energies, a QPT of the first kind between $S = 1/2$ and $S = 0$ ground states occurs. This transition is triggered by charge fluctuations which compete with RKKY ferromagnetic ordering; the ferromagnetic ordering temperature drops to zero as an exponential function of the on-site energies.

If symmetric splitting between the two on-site energy levels is induced, a singlet-triplet QPT of the Kosterlitz-Thouless kind occurs. This is a transition between an inter-impurity triplet and a local spin-singlet on one of the impurities. The cross-over temperature is an exponential function $T^* \propto \exp[-T_K/J_{12}]$ where J_{12} is an exchange-interaction between two fictitious spins which itself is an exponential function of the energy splitting.

The ferromagnetic ordering can be compensated by direct antiferromagnetic inter-impurity exchange interaction. The value of the RKKY interaction can be extracted in this manner and it is found to agree with the analytical estimates derived by fourth-order perturbation theory in hybridization parameters. Hopping between the impurities has similar effect via the superexchange mechanism. The critical hopping parameter $t_{12,c}$ is of the order of the hybridization Γ and does not depend on the value of U. It is interesting that the effect of the level splitting $\propto t$ is less pronounced than the effect of the induced exchange interaction $\propto t^2$.

If the inter-impurity electron repulsion U_{12} is increased to U, the decoupled impurities have SU(4) symmetry, since an additional $\mathrm{SU}(2)_{\mathrm{orb}}$ orbital pseudo-spin symmetry is established. The SU(4) symmetry is broken by the coupling to the conduction channel, therefore there is no SU(4) Kondo effect. Instead, the effective level degeneracy decreases from 6 (SU(4)

sextuplet) to 4 (product of two spin-doublets) on the symmetry-breaking scale, then from 4 to 2 in a $S = 1/2$ SU(2) Kondo effect; there is a double degeneracy of the ground state due to an effectively decoupled electron in the ungerade molecular orbital.

In the case of unequal coupling of the two impurities to the conduction channel, the high energy singlet state admixes with the ground triplet states; second order scaling calculation gives a good estimate of the Kondo temperature in this case. For very strong asymmetry, the ferromagnetic locking-in is destroyed and the single-impurity $S = 1/2$ Kondo effect occurs with the more strongly coupled impurity while the other spin remains uncompensated.

The behavior of the double quantum dot system in the side-coupled configuration strongly depends on the value of the inter-impurity hopping. For strong hopping, the system maps to an effective single-impurity Anderson model where the role of the impurity orbital is played by the bonding or anti-bonding molecular orbital. The use of eigenvalue diagrams for studying the low-temperature behavior was demonstrated: the Kondo temperatures can be accurately estimated from the energies of the lowest excited states of the double dot. Two wide Kondo plateaus are expected in the conductance as a function of the on-site energies in this regime. The spectral functions must be computed using the density-matrix NRG in this model; the conventional approach leads to spurious discontinuities and to the violation of the spectral sum rule. Density-matrix NRG in the basis with well defined charge Q and total spin S quantum numbers has been implemented for this purpose.

For weak coupling, the two-stage Kondo effect occurs: the spin on the directly coupled impurity is screened at a higher Kondo temperature $T_K^{(1)}$, while the spin on the side-coupled impurity is screened at an exponentially reduced lower Kondo temperature $T_K^{(2)}$. The conductance can be high at finite temperatures even in the vicinity of the particle-hole symmetric point if $T_K^{(1)} < T < T_K^{(2)}$. In addition, at finite temperatures a Fano resonance appears in the conductance; its origin lies in the sudden filling of the side-coupled dot when its on-site energy crosses the Fermi level.

It can be claimed on quite general grounds that there are three different types of the Kondo effect in the two-impurity Anderson models that are especially important for double quantum dot systems: double Kondo effect (realized in serial DQD), $S = 1$ Kondo effect (parallel DQD), and two-stage Kondo effect (side-coupled DQD). It would be interesting to study the cross-overs (and, very likely, quantum phase transitions) between the different strong-coupling fixed points of these systems; this is experimentally relevant, since the parameters of DQD systems can be finely tuned using gate electrodes and various realizations of DQD topology can be achieved in the same physical system.

Three-impurity models

Systems with even and odd number of impurities have markedly different behavior. The simplest three-impurity system consists of three quantum dots coupled in series between

two conduction channels. The behavior of the system depends strongly on the values of the on-site energies and on the inter-impurity hopping. Based on extensive calculations using several complementary methods, a phase diagram was established. It indicates the parameter ranges where the zero-temperature conductance is high.

For strong inter-impurity coupling, the system can be mapped to an effective single-impurity Anderson model where the role of the impurity orbital is played by the bonding, non-bonding, or anti-bonding molecular orbital. In this regime, the conductance is high when the occupancy is odd, and it is nearly zero when the occupancy is even.

For smaller inter-impurity coupling, the molecular orbital description becomes inappropriate as the local behavior of the spins becomes important. Near the particle-hole symmetric point (three electrons in the dots), the system crosses over from the molecular orbital regime ($t \gtrsim U$) to the antiferromagnetic spin-chain regime ($J \sim t$), and finally to the two-stage Kondo regime ($J < T_K^{(1)}$). In the antiferromagnetic spin-chain (AFM) regime, the three spins lock at $T \sim J$ into a rigid spin-doublet state; at lower temperature, this collective spin is screened by the conventional $S = 1/2$ Kondo effect. In the two-stage Kondo (TSK) regime, the spins on the first and third sites are screened at higher Kondo temperature $T_K^{(1)}$, then the spin on the central site is screened at an exponentially reduced second Kondo temperature $T_K^{(2)} \propto T_K^{(1)} \exp(-cT_K^{(1)}/J)$, where $J = 4t^2/U$. AFM and TSK regimes are separated by a cross-over region in which the system approaches the two-channel Kondo model NFL fixed point at finite temperatures. The NFL regime is robust with respect to various perturbations, such as particle-hole symmetry breaking, parity breaking and unequal electron-electron repulsions; the only "dangerous" perturbations are those that increase the channel asymmetry.

At the particle-hole symmetric point, the conductance increases to the unitary limit at $T = 0$ for any non-zero value of the inter-dot hopping parameter t. Furthermore, the stable low-temperature fixed point is found to be the same for all values of t: the odd channel gathers a $\pi/2$ phase shift, while there is no phase shift in the even channel.

The NFL physics can be detected by measuring and comparing the conductance through one of the side dots and through the system. It is found that the conductance though the side dots increases to $G_0/2$ while the conductance through the system is still low when the NFL region is entered by decreasing the temperature. When the system crosses over from NFL to FL fixed point, the conductance through the system increases to G_0. This agrees with the observation that the charge transfer from one channel to the other is a relevant perturbation which destabilizes NFL fixed point. The evolution of the spectral functions as a function of the hopping parameter demonstrates how the molecular-orbital peak evolves into a peak at J (AFM regime) and then into the first Kondo peak (TSK regime).

The two-stage Kondo regime is found to extend from the region of triple occupancy to the region of double occupancy. Near double occupancy, the electron on the central site undergoes Kondo screening by coupling to the quasiparticles from the valence fluctuating states on each side dot.

Accurate studies of the properties of more general three-impurity models are just commencing and there is a vast parameter space to explore. A very interesting system appears to be the triangular triple quantum dot coupled to two conduction channels. Depending on the parameters, this system can behave, for example, as a two-channel single-impurity Kondo model, two-impurity Kondo model, or as a frustrated antiferromagnet.

Low-temperature scanning tunneling microscopy

Scanning tunneling microscope (STM) is a versatile tool in the field of nanotechnology. It can be used to both assemble and characterize a nanostructure; tunneling spectroscopy provides insight into electronic and vibrational properties of the adsorbates.

Liquid-helium-cooled low-temperature STM operating at 5.9 K was constructed. It achieves atomic resolution on low corrugation metal surfaces such as Cu(111). The STM head is adapted to accommodate Omicron sample plates in order to retain compatibility with the existing equipment. The assembly of the instrument was described with many details and two methods to test and characterize the vibrational and electronic behavior of the scanner were given: measurement of the double piezo response and spectral analysis of the tunneling current. The lowest mechanical resonance is found at 900 Hz, which is comparable to the values for similar scanners used by other groups.

The tips are prepared by electrochemically etching W wire in KOH solution using a home-made rapid-shutdown electronic circuit. The tips are cleaned in hydrofluoric acid to remove tungsten oxides and then further improved in-situ by intentionally crashing them into a soft surface while increased voltage is applied.

A sample transfer mechanism was designed and constructed; its purpose is to carry the sample from the sample storage chamber to the STM head. In order to avoid cold welding, the mechanism uses UHV-compatible ball bearings and hard coatings on surfaces where friction occurs.

To ensure that the surfaces remain clean, the STM is housed in an ultra-high vacuum (UHV) system. The UHV is established by vacuum pumping in several stages and baking the system to 105 °C. In order to reduce the ultimate pressure, it is essential that the outgassing is kept to a minimum by using suitable materials and by keeping the surface area small. The volume of the system mainly affects the pump-down time.

The preparation of clean and ordered sample surfaces consists of alternating cycles of ion sputtering and sample annealing. The process has been automatized by using computer control. The surface condition is monitored by low-energy electron diffraction and by Auger electron spectroscopy. With high quality samples, the surface of suitable quality for STM work can be prepared in less than ten cleaning cycles. To evaporate materials on the surface, a Knudsen evaporator is used.

Imaging of Cu(111) and Cu(211) surfaces was performed with atomic resolution. We have

observed surface-electron standing waves (energy-resolved Friedel oscillations) and diffusion of CO molecules on Cu(111). Dynamic changes of the condition of the tip can be inferred from the changes in the image quality during a single scan.

A new bath cryostat with improved characteristics was recently designed and built. It is expected to have longer holding time and the base temperature of the STM should be further decreased due to better thermal insulation and better heat sinking of wires. The cryostat also has better adjustment capabilities and it is easier to maintain.

Clusters of magnetic adatoms and surface Kondo effect

Magnetic properties of clusters of magnetic adatoms can be studied by tunneling spectroscopy even without spin-polarized tips. One possible approach involves probing the signature of the Kondo effect which takes the form of an asymmetric narrow anti-resonance near the Fermi level in the $\mathrm{d}I/\mathrm{d}V$ tunneling spectrum.

The surface Kondo effect occurs in single magnetic adatoms, dimers and trimers, in adsorbed molecules with embedded magnetic ion, and in metal clusters on carbon nanotubes. To compare experimental measurements to theoretical calculations, it is important to find a relation between the width of the anti-resonance to the true Kondo temperature of the system. The inter-impurity interactions can be studied by following the evolution of the anti-resonance as the impurities are brought together to form a cluster.

The anti-resonance in the tunneling spectrum can be explained by taking into account that the d-level wave-function is strongly localized, so that the tunneling current flows mostly into the sp-like states of the adsorbate that are strongly hybridized with the substrate conduction bands. The tunneling spectrum is thus proportional, in a first approximation, to the spectral function of the conduction band electrons at the position of the impurity. An improved approximation is to describe the impurity using a two-level model featuring a localized interacting d-level and a non-interacting s-level; the s-level strongly hybridizes with the continuum, while the d level couples to the s-level predominantly via exchange interaction.

There is currently a lack of experimental data at variable temperatures, especially in the mK range, and in variable magnetic field. Such data would help resolve a number of open questions. On the theoretical front, the relevant multi-level quantum impurity models should be studied, especially their two-impurity generalizations; this is clearly a formidable two-channel four-level impurity problem, but it appears within reach of the present-day computers and NRG implementations.

Poglavje 12

Povzetek disertacije v slovenskem jeziku

V tem poglavju je povzeta vsebina disertacije v slovenskem jeziku. Navedene so tudi nekatere možnosti za nadaljnje raziskovanje.

Modeli kvantnih nečistoč

Modeli kvantnih nečistoč opisujejo raznovrstne fizikalne sisteme, pri katerih je nečistoča z notranjimi prostostnimi stopnjami sklopljena s kontinuom stanj v njeni okolici. Tipičen primer so magnetne nečistoče v notranjosti ali na površini kovin in nanostrukture, kot so, denimo, sistemi sklopljenih kvantnih pik. Njihovo nenavadno vedenje je posledica notranjih prostostnih stopenj, ki vodijo k močnemu sipanju pri nizkih temperaturah – to je Kondov pojav. Pri visokih temperaturah imajo ti modeli lastnost asimptotske svobode in jih lahko proučujemo z uporabo teorije motenj, medtem ko so režimi močne sklopitve pri nizkih temperaturah neperturbativni. V primeru magnetnih nečistoč vodi Kondov pojav k senčenju lokalne vrtilne količine in nečistoča se obnaša, kot da bi bila nemagnetna. Poleg tega se pojavi značilna ozka Kondova resonanca v bližini Fermijevega nivoja. Ta močno vpliva na transportne lastnosti sistema pri nizkih temperaturah.

Modeli, obravnavani v disertaciji, vključujejo največ dva kontinua (rečemo tudi dva kanala). Dvokanalni pasovi prostih elektronov imajo notranjo simetrijo SO(8); sklopitev nečistoče s pasom podre simetrijo na neko podgrupo grupe SO(8). Lastnosti modelov kvantnih nečistoč so izrazito odvisne od simetrije in izkaže se, da pride do najbolj nenavadnih pojavov, ko je simetrija visoka. Posebno pomembne so simetrijske grupe $\mathrm{SU}(2)_{\mathrm{spin}}$, ki je posledica izotropije v spinskem prostoru, $\mathrm{SU}(2)_{\mathrm{iso}}$, ki je povezana z ohranitvijo naboja in s simetrijo med delci in vrzelmi, in $\mathrm{SU}(2)_{\mathrm{flavor}}$, ki opisuje simetrijo med obema kanaloma, ter različne podgrupe navedenih grup.

Ker smemo nečistoče obravnavati kot točkasta telesa, se te efektivno sklapljajo le z enodimenzionalnim kontinuom stanj (lahko pa tudi s končnim številom takšnih kontinuov).

Kadar gostota stanj v kontinuu nima posebnosti v bližini Fermijevega nivoja, lahko disperzijo pri nizkih energijah lineariziramo. Modeli kvantnih nečistoč se potem poenostavijo na enodimenzionalne efektivne teorije polja, ki imajo značilne lastnosti, kot je, denimo, ločitev spina in naboja. Njihove nizko-temperaturne fiksne točke imajo lahko značaj Fermijevih tekočin ali ne-Fermijevih tekočin. Pomembno orodje za proučevanje fiksnih točk in njihovih okolic je teorija konformnega polja z robom, ki nudi uporabno intuitivno sliko bistva Kondovega pojava: notranje prostostne stopnje nečistoče izginejo iz problema in njihov edini učinek je ta, da spremenijo robne pogoje za sipanje delcev kontinua.

Četudi vemo že veliko o simetrijskih lastnostih modelov kvantnih nečistoč ter o povezavi med simetrijami in stabilnostjo različnih fiksnih točk, bi bilo nadvse koristno natančno proučiti možne netrivialne fiksne točke z lastnostmi ne-Fermijevih tekočin v modelih, ki opisujejo transport skozi nanostrukture. Zato je vredno omeniti, da teorija konformnega polja z robom načeloma omogoča sistematično iskanje vseh fiksnih točk v modelih, kjer je interakcija povsem lokalna (torej samo na mestu nečistoče).

Renormalizacijska grupa

Ideja renormalizacijske grupe pomaga razumeti obnašanje nekega fizikalnega sistema na različnih energijskih skalah. Pojmi renormalizabilnosti, univerzalnosti in dimenzijske pretvorbe so med seboj tesno prepleteni; modeli kvantnih nečistoč se običajno obnašajo na univerzalen način, ki ga lahko opišemo s peščico parametrov. V perturbativnem režimu pri visokih temperaturah lahko te modele obravnavamo s preprosto renormalizacijo roba pasu (skaliranjem), ki pa odpovejo v bližini režima močne sklopitve.

Wilsonova numerična renormalizacijska grupa (NRG) je neperturbativen pristop k izvajanju renormalizacijskih transformacij. V Mathematici in C++ sem napisal novo implementacijo metode,"NRG Ljubljana", za računanje lastnosti problemov kvantnih nečistoč, ki nastopijo pri opisovanju kvantnega transporta skozi nanostrukture.

Metoda NRG temelji na logaritemski diskretizaciji pasov ter iterativni diagonalizaciji zaporedja Hamiltonovih operatorjev. Logaritemska diskretizacija (oziroma, bolj natančno, zanemaritev višjih Fourierovih načinov v vseh energijskih intervalih) je resda približek, vendar se izkaže a posteriori, da je tudi za visoke vrednosti diskretizacijskega parametra Λ to dober približek. Pri kompleksnih problemih z večjim številom nečistoč in kanalov je ključnega pomena, da upoštevamo vse simetrijske elemente in s tem poenostavimo računsko nalogo. V "NRG Ljubljana" sem uporabil avtomatsko generiranje programske kode z uporabo sistema za računalniško algebro Mathematica, kar znatno poenostavi pripravo različic programa za različne tipe simetrij. V primeru velikih simetrijskih grup, kot je, na primer, $\mathrm{SU}(2)_{\mathrm{spin}} \times \mathrm{SU}(2)_{\mathrm{iso}} \times \mathrm{Z}_2$, postane ročno izpeljevanje potrebnih koeficientov neizvedljivo.

Pri iterativni diagonalizaciji zaporedoma dodajamo mesta iz Wilsonove verige in opravljamo točne diagonalizacije. Rezultat diagonalizacije (lastne vrednosti in lastni vektorji)

v N-ti iteraciji predstavlja opis začetnega problema na energijski skali $\propto \Lambda^{-N/2}$. Ker število stanj v celotnem Fockovem prostoru narašča eksponentno s številom iteracij, moramo po vsaki diagonalizaciji omejiti število obdržanih stanj na neko izbrano vrednost. Tudi to je dober približek, saj se pri vsaki renormalizacijski transformaciji renormirajo le nizko ležeči nivoji.

Z NRG lahko izračunamo številne pomembne fizikalne količine. Že iz spektrov vzbujenih stanj samih lahko marsikaj razberemo. Določimo lahko, denimo, fiksne točke problema in proučujemo prehajanje med njimi. Izluščimo lahko celo efektivne Hamiltonove operatorje, ki opisujejo obnašanje sistema v bližini različnih fiksnih točk, in določimo, ali je neka motnja relevantna, marginalna ali irelevantna. Iz spektrov lahko izračunamo še statične termodinamske količine (različne susceptibilnosti, entropijo). Računati je možno tudi korelacijske funkcije (fluktuacije naboja, spinsko-spinske korelacije) in dinamične količine (spektralne funkcije, dinamične spinske susceptibilnosti). Pri posplošeni metodi density-matrix NRG spektralne funkcije računamo z uporabo reducirane gostotne matrike, s čimer upoštevamo dejansko osnovno stanje sistema tudi pri visokih vzbuditvenih energijah.

Zaradi ponovnega velikega zanimanja za modele nečistoč znatno napreduje tudi področje metod NRG. Izpostavim naj le izboljšave pri računanju spektralnih funkcij, s čimer je NRG postal odlikovano orodje za reševanje efektivnih modelov nečistoč pri teoriji dinamičnega povprečnega polja za razsežne sisteme koreliranih elektronov.

Ostale metode za modele nečistoč

Poleg NRG sta za obravnavo problemov nečistoč uporabni metodi tudi Gunnarsson-Schönhammerjeva variacijska metoda in metode kvantni Monte Carlo.

Temelj variacijske metode je preizkusna valovna funkcija, ki upošteva zmanjšane fluktuacije naboja v Andersonovem modelu, in ki jo uporabimo kot variacijski nastavek. Primerno obliko nastavka določimo tako, da projeciramo funkcijo, dobljeno v približku Hartree-Fock, na podprostore z različnimi zasedenostmi orbital nečistoče. Pristop postane še bolj natančen, če dopustimo, da so tudi parametri efektivnega kvazidelčnega Hamiltonovega operatorja prosti. Variacijsko energijo nato minimiziramo iterativno.

V metodi auxiliary-field Quantum Monte Carlo (QMC) problem fermionov na rešetki preslikamo na klasičen model podoben Isingovemu z uporabo Trotterjevega razcepa in Hubbard-Stratonovicheve transformacije, čemur sledi še integracija po vseh fermionskih prostostnih stopnjah. V metodi constrained path QMC težave s predznakom fermionskih determinant omilimo tako, da račun omejimo na eno izmed dveh degeneriranih polovic prostora Slaterjevih determinant.

Zanimivo bi bilo implementirati variacijsko metodo, pri kateri bi pas prevodniških elektronov diskretizirali logaritemsko. Tako bi nemara dobili boljši opis dogajanja pri nizkih energijskih skalah. Druga perspektivna smer bi bil razvoj variacijskih nastavkov, ki bi

upoštevali prostostne stopnje, ki se pri nizkih energijah razklopijo od prevodniških elektronov, ki tvorijo Fermijevo tekočino. Tako bi morda lahko variacijsko metodo uporabili za obravnavo singularnih Fermijevih tekočin. Tretja zanimiva možnost bi bila izvedba variacijske metode z uporabo Majoranovih fermionov, s čimer bi se lahko odprla možnost za opis sistemov, ki so ne-Fermijeve tekočine.

Teorija kvantnega transporta

Transport skozi sistem kvantnih pik in tunelska spektroskopija magnetnih adsorbatov na površini kovin sta sorodna problema in oba lahko opišemo z modeli kvantnih nečistoč.

Prevodnost skozi območje z interakcijami pri absolutni ničli lahko izračunamo iz kvazidelčnih sipalnih faznih premikov, kadar je osnovno stanje sistema Fermijeva tekočina. Ta pristop temelji na Landauer-Büttikerjevemu formalizmu. Sipalne fazne premike zlahka razberemo iz spektrov vzbujenih stanj, ki jih izračunamo z NRG.

Prevodnost pri absolutni ničli Fermijevih tekočin lahko določimo tudi z uporabo "sinusne formule", pri čemer moramo izračunati razliko energij dveh pomožnih sistemov s periodičnimi ali antiperiodičnimi robnimi pogoji, v katera je vstavljeno območje z interakcijami. Ta pristop je še posebno uporaben skupaj z variacijsko metodo, s katero lahko zelo natančno določimo energijo osnovnega stanja.

Prevodnost lahko dobimo tudi iz spektralnih funkcij z uporabo Meir-Wingreenove formule. Poglavitna prednost tega pristopa je, da lahko temperaturno odvisnost prevodnosti v prvem približku razberemo kar iz frekvenčne odvisnosti spektralnih funkcij.

Nadaljnje raziskave na področju teorije kvantnega transporta bi lahko usmerili k neravnovesnim in časovno odvisnim problemom, ter k transportu pri končnih temperaturah. Čeprav je osnovni formalizem transportne teorije že dobro razvit, je računanje neravnovesnih lastnosti koreliranih sistemov še vedno zelo težka naloga. Ustrezen pristop je morda pred kratkim razvita metoda časovno odvisne NRG.

Modeli ene nečistoče

Značilna lastnost prototipskega modela kvantne nečistoče (Kondovega modela) je senčenje magnetnega momenta pod Kondovo temperaturo T_K. Pri zelo nizkih temperaturah, $T \ll T_K$, se sistem obnaša kot Fermijeva tekočina, katere interagirajoč značaj je razviden iz netrivialnega Wilsonovega razmerja $R = 2$. Brez dodatnega potencialnega sipanja je obnašanje Kondovih sistemov univerzalno in opisljivo z univerzalno funkcijo brezdimenzijske količine T/T_K. V prisotnosti potencialnega sipanja dobimo črto fiksnih točk, ki je parametrizirana z dodatno količino, kvazidelčnim faznim premikom δ_{qp}.

V dvokanalnem Kondovem modelu vodi prekomerno senčenje spina nečistoče k vzpostavitvi stanja, ki je ne-Fermijeva tekočina (NFL). Nečistoča ima tedaj rezidualno entropijo $k_B \ln 2/2$, energije vzbujenih stanj pa tvorijo nenavaden spekter: $0, 1/8, 1/2, 5/8, 1, 1+1/8$, itd. NFL fiksno točko destabilizira asimetrija med kanaloma in sistem zato preide v fiksno točno Fermijeve tekočine pri neki nižji temperaturi.

Andersonov model ene nečistoče opisuje nastanek lokalnega magnetnega momenta v sistemih, kot so magnetne nečistoče (orbitala d) in kvantne pike. Sistem ob renormalizaciji teče iz visokotemperaturnega režima proste orbitale (kjer prihaja do spinskih in nabojskih fluktuacij) v režim valenčnih fluktuacij (fluktuacije naboja med dvema vrednostima) in nato v režim lokalnega momenta (samo fluktuacije spina), pri nizkih temperaturah pa konča v režimu močne sklopitve, v katerem je lokalni moment zasenčen. Obnašanje sistema v odvisnosti od temperature in energije orbitale lahko predstavimo v obliki "faznega diagrama". Pri zadosti nizkih temperaturah lahko Andersonov model preslikamo na Kondov model s Schrieffer-Wolffovo transformacijo, ki iz problema izprojecira fluktuacije naboja na nečistoči.

Fluktuacije naboja na nečistoči za majhen Γ/U so podane z univerzalno funkcijo $\langle q^2 \rangle = (4/\pi)(\Gamma/U)$. Odklon fluktuacij naboja na prvem mestu Wilsonove verige, $\langle q_f^2 \rangle$, od vrednosti $1/2$, ki velja v neinteragirajočih sistemih, dokazuje, da nečistoča zares povzroči korelirano vedenje elektronov v pasu. Nabojsko-nabojska korelacijska funkcija $\langle q q_f \rangle$ je negativna za velike Γ/U in pozitivna za $\Gamma/U \lesssim 1$. Spinsko-spinska korelacijska funkcija $\langle \mathbf{S} \cdot \mathbf{S}_f \rangle$ je negativna zaradi efektivne antiferomagnetne interakcije med magnetnim momentom nečistoče in prevodniškimi elektroni. Ko zmanjšujemo hibridizacijo Γ, gre spinsko-spinska korelacija proti nič, kar dokazuje, da je Kondov senčitveni oblak razsežen objekt.

Spektralna funkcija nečistoče v Kondovem režimu ima dva široka vrhova pri ϵ_d in $\epsilon_d + U$ (to sta "Hubbardova satelita") in značilno ozko resonanco, katere širina je sorazmerna s $k_B T_K$, in ki se drži Fermijevega nivoja (to je "Kondova resonanca"). Vrednost spektralne funkcije pri energiji nič je povezana z zasedenostjo nečistoče preko Friedelovega vsotnega pravila. Prevodnosti, izračunane za pasove z različnimi hibridizacijskimi funkcijami, ki pa imajo enako vrednost pri Fermijevem nivoju, se ne razlikujejo veliko; razlike so še najbolj opazne v režimu valenčnih fluktuacij, ko postane ključna energijska skala ($k_B T_K$) primerljiva s širino pasu. Če vzpostavimo Zeemanovo magnetno polje, se Kondova resonanca razcepi na dva vrha, ki ležita za $g\mu_B B \gtrsim \epsilon_d, U$ pri $\epsilon_d - g\mu_B |B|/2$ in $\epsilon_d + U + g\mu_B |B|/2$.

Čeprav bi nemara lahko pričakovali, da o modelih ene nečistoče vemo domala vse, to ne drži. Izpostavil bi rad, da se je, denimo, šele nedavno pričelo temeljito proučevanje modelov, pri katerih je nečistoča sklopljena z bozonsko kopeljo (ali celo sočasno s fermionsko in bozonsko kopeljo), z uporabo bozonske posplošitve NRG

Modeli dveh nečistoč

Sistemi dveh nečistoč, kot je dvojna kvantna pika (DQD), so najpreprostejši sistemi, kjer lahko proučujemo tekmovanje med magnetnim urejanjem in Kondovim senčenjem.

Vzporedno dvojno kvantno piko (in posplošitve na N vzporednih pik) lahko opišemo z Andersonovim modelom več nečistoč. Pri nizkih temperaturah se ta model preslika na Kondov model več nečistoč. Izkaže se, da je efektivna izmenjalna interakcija med nečistočami, ki se prenaša prek prevodniškega pasu (RKKY), feromagnetna, $J_{\mathrm{RKKY}} \sim U(\rho J_K)^2 = (64/\pi^2)(\Gamma^2/U)$. Spini nečistoč se zato uredijo in sistem se efektivno obnaša kot Kondov model ene same nečistoče z velikim spinom, $S = N/2$, pri katerem pride do $S = N/2$ Kondovega pojava. Kondova temperatura je vselej enaka, ne glede na število nečistoč. Rezidualni spin je $N/2 - 1/2$, če le ni sklopitve na dodatne senčitvene kanale. Režim feromagnetne urejenosti in posledični $S = N/2$ Kondov pojav sta dokaj robustna napram različnim motnjam. Zelo močne motnje vseeno vodijo h kvantnim faznim prehodom različnih vrst, ki smo jih bolj natančno proučili v primeru $N = 2$.

Če v vzporedni dvojni kvantni piki odpravimo simetrijo med delci in vrzelmi tako, da obema nečistočama povišamo energijo v enaki meri, pride do kvantnega faznega prehoda prve vrste med osnovnima stanjema s spinom $S = 1/2$ oziroma $S = 0$. Ta prehod povzročijo fluktuacije naboja, ki tekmujejo s feromagnetnim urejanjem preko mehanizma RKKY; temperatura feromagnetne ureditve pada proti nič kot eksponentna funkcija energij nečistoč.

Če vzpostavimo simetričen razcep energij na obeh nečistočah, pride do Kosterlitz-Thoulessovega kvantnega faznega prehoda med singletom in tripletom. To je prehod med kolektivnim tripletnim stanjem elektronov na obeh nečistočah in lokalnim singletnim stanjem na nečistoči z nižjo energijo. Temperatura prehoda je eksponentna funkcija $T^* \propto \exp[-T_K/J_{12}]$, kjer je J_{12} izmenjalna interakcija med namišljenima spinoma, ki je eksponentno odvisna od energijskega razcepa.

Če odboj med elektroni na obeh nečistočah (kapacitivna sklopitev) povečamo do $U_{12} = U$, imata izolirani nečistoči simetrijo SU(4), saj se vzpostavi dodatna orbitalna psevdospinska simetrija $\mathrm{SU}(2)_{\mathrm{orb}}$. Simetrijo SU(4) zlomi sklopitev nečistoč na prevodniški pas, zato ne pride do Kondovega pojava vrste SU(4). Namesto tega pade efektivna degeneracija s 6 (sekstuplet SU(4)) na 4 (produkt dveh spinskih dubletov) na skali zloma simetrije, nato pa s 4 na 2 ob Kondovem pojavu tipa SU(2) s spinom $S = 1/2$. Osnovno stanje ostane dvakrat degenerirano, saj v lihi molekularni orbitali ostane nezasenčen elektron, ki je povsem razklopljen od preostalega sistema.

V primeru neenakega sklapljanja obeh nečistoč na prevodniški pas, se višje-energijsko singletno stanje primeša k osnovnemu tripletnemu stanju. V tem primeru dobimo dober približek za Kondovo temperaturo z uporabo skaliranja drugega reda. Pri zelo močni asimetriji se feromagnetna ureditev poruši in pride do Kondovega pojava z $S = 1/2$ na nečistoči, ki je močneje sklopljena, medtem ko ostane drugi spin nezasenčen.

Lastnosti stransko sklopljene dvojne kvantne pike so močno odvisne od sklopitve med nečistočama, torej od vrednosti parametra skakanja. Pri močni sklopitvi se sistem preslika na efektiven Andersonov model za eno nečistočo, pri čemer igra vlogo orbitale vezavna ali anti-vezavna molekularna orbitala. Predstavljena je bila uporaba diagramov lastnih stanj za napovedovanje obnašanja pri nizkih temperaturah: Kondovo temperaturo lahko dokaj natančno določimo iz energij najnižjih vzbujenih stanj dvojne kvantne pike. V tem režimu pričakujemo dve široki Kondovi planoti v prevodnosti kot funkciji energije nečistoč. Spektralne funkcije moramo v tem modelu računati z metodo density-matrix (DM) NRG, saj običajni pristop vodi k nefizikalnim nezveznostim in h kršitvi vsotnega pravila. V ta namen sem izpeljal DM NRG v bazi dobro določenega naboja Q in celotnega spina S.

V primeru šibke sklopitve med pikama pride do dvostopenjskega Kondovega pojava: spin na neposredno sklopljeni nečistoči je zasenčen pri višji Kondovi temperaturi $T_K^{(1)}$, medtem ko je spin na stransko sklopljeni nečistoči zasenčen pri eksponentno nižji Kondovi temperaturi $T_K^{(2)}$. Prevodnost je lahko pri končnih temperaturah visoka tudi v bližini točke, kjer obstaja simetrija med delci in vrzelmi, če je le izpolnjen pogoj $T_K^{(2)} \ll T \ll T_K^{(1)}$. Poleg tega se pri končnih temperaturah pojavi Fanova resonanca v prevodnosti, katere izvor je nenadna sprememba zasedenosti stransko sklopljene pike, ko njena energija prečka Fermijev nivo.

V Andersonovih modelih za dve kvantni piki imamo lahko v splošnem tri različne vrste Kondovega pojava, ki so pomembni za sisteme dvojne kvantne pike: dvojni Kondov pojav (do katerega pride v zaporedno sklopljeni DQD), $S = 1$ Kondov pojav (vzporedna DQD), ter dvostopenjski Kondov pojav (stransko-sklopljena DQD). Zanimivo bi bilo proučiti prehajanje (ali, predvidoma, celo prave kvantne fazne prehode) med različnimi fiksnimi točkami močne sklopitve v teh sistemih. To je relevantno za eksperimente, saj lahko parametre dvojne pike natančno nadziramo s spreminjanjem napetosti na elektrodah in tako dosežemo različne efektivne topologije dvojne kvantne pike v istem fizikalnem sistemu.

Modeli treh nečistoč

Sistemi z lihim številom nečistoč imajo opazno drugačne lastnosti kot sistemi s sodim številom. Najbolj preprost sistem treh nečistoč sestoji iz treh kvantnih pik, zaporedno vezanih med dva prevodna kanala. Obnašanje sistema je močno odvisno od vrednosti orbitalnih energij in sklopitve med nečistočami. Na podlagi obširne numerične raziskave z različnimi komplementarnimi metodami nam je uspelo določiti fazni diagram, ki določa območja parametrov, kjer je prevodnost pri absolutni ničli visoka.

V primeru močne sklopitve med nečistočami lahko sistem preslikamo na efektiven Andersonov model ene same nečistoče, v katerem igra vlogo orbitale vezavna, nevezavna ali antivezavna molekularna orbitala. V tem režimu je prevodnost visoka, ko je zasedenost pik liha, in zelo nizka, ko je zasedenost soda.

Pri šibki sklopitvi med nečistočami opis z molekularnimi orbitalami ni primeren, saj postane pomembno obnašanje posameznih spinov. V bližini točke, kjer imamo simetrijo med

delci in vrzelmi (torej ko so v sistemu trije elektroni), sistem preide iz režima molekularne orbitale ($t \gtrsim U$) v režim antiferomagnetne spinske verige ($J \sim t$), in nato v režim dvostopenjskega Kondovega pojava ($J < T_K^{(1)}$). V režimu antiferomagnetne spinske verige (AFM) se trije spini uredijo pri $T \sim J$ v togo dubletno stanje, pri nižjih temperaturah pa je ta kolektivni spin senčen v običajnem $S = 1/2$ Kondovem pojavu. V režimu dvostopenjskega Kondovega pojava (TSK) se spina na prvem in tretjem mestu zasenčita pri višji Kondovi temperaturi $T_K^{(1)}$, spin na sredinskem mestu pa pri eksponentno nižji drugi Kondovi temperaturi $T_K^{(2)} \propto T_K^{(1)} \exp(-cT_K^{(1)}/J)$, kjer je $J = 4t^2/U$. Režima AFM in TSK sta ločena s prehodnim območjem, v katerem se sistem pri končnih temperaturah približa fiksni točki dvokanalnega Kondovega modela, ki ima lastnosti ne-Fermijeve tekočine (NFL). Režim NFL je robusten napram različnim motnjam, kot so, denimo, zlom simetrije med delci in vrzelmi, zlom parnosti in neenak odboj med elektroni na različnih mestih. Edine "nevarne" motnje so tiste, ki dodatno povečajo asimetrijo med kanaloma.

V točki, kjer obstaja simetrija med delci in vrzelmi, prevodnost naraste na unitarno mejo pri $T = 0$ za poljubno od nič različno vrednost parametra skakanja med pikami t. Poleg tega se izkaže, da je stabilna nizkotemperaturna fiksna točka enaka za vse t: v lihem kanalu je fazni premik $\pi/2$, v sodem kanalu pa faznega premika ni.

Fiziko ne-Fermijeve tekočine lahko zaznamo s primerjanjem prevodnosti skozi eno izmed stranskih pik in skozi celoten sistem. Prevodnost skozi stranski piki naraste na $G_0/2$, medtem ko je prevodnost skozi sistem še vedno nizka, ko temperatura pade pod Kondovo temperaturo. Ko preidemo iz fiksne točko NFL v fiksno točko Fermijeve tekočine, naraste prevodnost skozi sistem na G_0. To je v skladu z opažanjem, da je prenos naboja iz enega kanala v drugega natanko tista motnja, ki destabilizira fiksno točko ne-Fermijeve tekočine. Spreminjanje spektralnih funkcij v odvisnosti od parametra skakanja t prikazuje, kako se spektralni vrh molekularne orbitale razvije v vrh pri $\omega = J$ (režim AFM), ta pa nato v prvi Kondov vrh (režim TSK).

Režim dvostopenjskega Kondovega pojava se razteza od območja trojne zasedenosti do območja dvojne zasedenosti. V bližini dvojne zasedenosti je spin elektrona na sredinskem mestu senčen preko sklopitve na kvazidelce, ki izvirajo iz stanj valenčne fluktuacije na obeh stranskih mestih.

Natančno proučevanje lastnosti bolj splošnih modelov treh nečistoč je šele v povojih in prostor modelskih parametrov, ki ga moramo raziskati, je ogromen. Zelo zanimiv sistem je gotovo trikotnik iz treh kvantnih pik, sklopljen na dva prevodniška kanala. V odvisnosti od parametrov se lahko ta sistem obnaša, denimo, kot dvokanalni Kondov model ene nečistoče, kot Kondov model dveh nečistoč, ali pa kot frustriran antiferomagnet.

Nizkotemperaturni vrstični tunelski mikroskop

Vrstični tunelski mikroskop (STM) je vsestransko orodje na področju nanotehnologije. Lahko ga uporabimo za sestavljanje in karakterizacijo nanostruktur: tunelska spektroskopija nudi vpogled tako v elektronske kot v vibracijske lastnosti adsorbatov.

Sestavili smo s tekočim helijem hlajeni nizkotemperaturni STM, ki deluje pri 5.9 K. Instrument doseže atomsko ločljivost na površinah kovin z zelo nizko korugacijo, kot je Cu(111). Glavo mikroskopa smo priredili tako, da lahko vanjo vstavimo vzorce, pritrjene na Omicronove nosilce. Tako smo ohranili združljivost z že obstoječo opremo. Sestavljanje instrumenta sem opisal s številnimi podrobnostmi in podal sem dve metodi za preizkušanje in karakterizacijo vibracijskega in električnega obnašanja skenerja: meritev dvojnega piezo odziva in spektralno analizo tunelskega toka. Najnižjo mehansko resonanco najdemo pri 900 Hz, kar je primerljivo z vrednostmi podobnih skenerjev, ki jih uporabljajo drugod.

Konice pripravljamo z elektrokemijskim jedkanjem volframove žice v raztopini KOH s pomočjo doma narejenega elektronskega vezja, ki hitro prekine tok, ko je jedkanje končano. Konice nato očistimo v fluorovodikovi kislini, da odstranimo volframove okside, in jo dodatno izboljšamo in-situ z nadzorovanim zaletavanjem konice v mehko površino.

Sestavili smo mehanizem za prenos vzorca iz komore za shranjevanje vzorcev v glavo mikroskopa. Da se prepreči hladno privarjenje, mehanizem uporablja vakuumsko združljive krogline ležaje in trde prevleke na površinah, kjer prihaja do trenja.

Da opazovana površina ostane čista, je mikroskop vgrajen v ultravisoko vakuumski sistem. Ultravisoki vakuum (UHV) dobimo z večstopenjskim črpanjem in s pregrevanjem sistema na 105 °C. Da bi bil končni pritisk čim nižji, je ključnega pomena kar se da zmanjšati degasiranje z uporabo primernih materialov in čimbolj omejiti notranjo površino sistema. Prostornina sistema vpliva predvsem na čas črpanja, da dosežemo UHV.

Čisto in urejeno površino vzorca dobimo z izmeničnim ionskim sputtranjem in popuščanjem vzorca. Ta postopek smo računalniško avtomatizirali, stanje površine pa nadzorujemo z uklonom nizkoenergijskih elektronov in spektrostopijo Augerjevih elektronov. Pri zelo kvalitetnih vzorcih dobimo površino, ki je zadosti dobra za tunelsko mikroskopijo, v manj kot desetih ciklih čiščenja. Različne adsorbate nato naprašimo na površino z uporabo Knudsenove celice.

Površine Cu(111) in Cu(211) smo slikali z atomsko ločljivostjo. Opazovali smo stoječa valovanja površinskih elektronov (energijsko razločene Friedelove oscilacije) in difuzijo molekul CO na Cu(111). Dinamične spremembe stanja konice so razvidne iz sprememb kvalitete slik med skeniranjem.

Pred kratkim smo konstruirali nov kriostat na helijevo kopel, ki bo imel daljši čas pred potrebnim dotakanjem kriogenih tekočin. Poleg tega bo mikroskopska glava dosegla nižje temperature, saj bo sistem bolje izoliran, žice pa bodo bolje toplotno sidrane. Kristat bo imel boljše možnosti za nastavljanje in ga bo lažje vzdrževati.

Skupki magnetnih nečistoč in Kondov pojav na površinah

Magnetne lastnosti skupkov adsorbatov lahko proučujemo s tunelskim mikroskopom tudi brez spinsko polarizirane konice. Možen pristop je, denimo, zaznavanje značilne posledice Kondovega pojava, ki se pojavi v obliki ozke antiresonance v bližini Fermijevega nivoja v diferencialnem tunelskem spektru $\mathrm{d}I/\mathrm{d}V$.

Do Kondovega pojava na površinah lahko pride v posameznih magnetnih adatomih, dimerih in trimerih, v adsorbiranih molekulah, ki vključujejo magnetni ion, ter v skupkih kovinskih atomov na ogljikovih nanocevkah. Interakcije med nečistočami lahko proučujemo tako, da dva adatoma postopno približujemo, dokler se ne povežeta v skupek, ob tem pa spremljamo, kako se spreminja oblika antiresonance v spektrih. Pri primerjavah meritev s teoretičnimi izračuni je potrebno najti povezavo med širino antiresonance ter pravo Kondovo temperaturo sistema.

Antiresonanco v tunelskem spektru najlaže razumemo, če upoštevamo, da so valovne funckije orbital d močno lokalizirane, zato večina tunelskega toka teče v orbitale sp adsorbata, ki so močno hibridizirane s pasom prevodniških elektronov v podlagi. Tunelski spekter je zato v prvem približku sorazmeren kar s spektralno funkcijo prevodniškega pasu na mestu nečistoče. Še boljši približek je, če nečistočo opišemo z dvonivojskim modelom, ker upoštevamo tako orbitalo d kot orbitalo s; orbitala s je močno hibridizirana s kontinuom, medtem ko se orbitala d sklaplja z orbitalo s predvsem preko izmenjalne interakcije.

Še vedno primanjkujejo eksperimentalni podatki pri spremenljivih temperaturah, predvsem v območju milikelvinov, ter v spremenljivih magnetnih poljih. Ti podatki bi lahko nudili odgovore na številna odprta vprašanja. Na področju teorije bi bilo vredno temeljito proučiti ustrezne večnivojske modele kvantnih nečistoč, predvsem njihove razširitve na dve nečistoči. To je težaven dvokanalni štirinivojski problem, ki pa je verjetno v dosegu zmogljivosti današnjih računalnikov in implementacij metode NRG.

Part V

Appendices

Appendix A

Tensor operators and Wigner-Eckart theorem

We consider a spherical tensor operator $\hat{O}$ of rank M with $2M+1$ components indexed by $\mu = -M, \ldots, +M$. By definition, it satisfies the following relations

$$\begin{aligned} \left[J_z, O^M_\mu\right] &= \mu O^M_\mu \\ \left[J_+, O^M_\mu\right] &= A(M,\mu) O^M_{\mu+1} \\ \left[J_-, O^M_\mu\right] &= A(M,-\mu) O^M_{\mu-1} \end{aligned} \tag{A.1}$$

where J are the generators of an SU(2) symmetry group and $A(M,\mu) = \sqrt{(M-\mu)(M+\mu+1)}$. The eigenstates of a system with SU(2) symmetry then satisfy the Wigner-Eckart theorem:

$$\langle \alpha, j, j_z | O^M_\mu | \alpha', j', j'_z \rangle = \left\langle j' j'_z ; M\mu \middle| j j_z \right\rangle \langle \alpha, j \| O^M \| \alpha', j' \rangle, \tag{A.2}$$

where j, j' are spin quantum numbers, j_z, j'_z are projection (magnetic) quantum numbers and α, α' are additional non-angular quantum numbers. $\left\langle j_1 j_{z1} ; j_2 j_{z2} \middle| J J_z \right\rangle$ are SU(2) Clebsch-Gordan coefficients. The theorem is proved by inserting the defining commutators (A.1) between bras and kets and operating with the generators J to the left on bras and to the right on kets. The system of equations thus obtained is identical to the generating equations for the Clebsch-Gordan coefficients.

Appendix B

Green's functions

This appendix recapitulates essential formulas from many-particle physics and sets notation for the main text.

An operator in the Heisenberg representation is defined by

$$O(t) = e^{iHt} O(0) e^{-iHt} \tag{B.1}$$

or by the equation of motion

$$i\frac{\partial}{\partial t} O(t) = [O(t), H]. \tag{B.2}$$

In general (and in particular for non-equilibrium problems) we need to define several Green's functions:[280,550]

$$\begin{aligned}
G^{>}(x_1, x_2) &= -i\langle \psi(x_1)\psi^{\dagger}(x_2)\rangle \\
G^{<}(x_1, x_2) &= i\langle \psi^{\dagger}(x_2)\psi(x_1)\rangle \\
G^{t}(x_1, x_2) &= \theta(t_1 - t_2)G^{>}(x_1, x_2) + \theta(t_2 - t_1)G^{<}(x_1, x_2) \\
G^{\bar{t}}(x_1, x_2) &= \theta(t_2 - t_1)G^{>}(x_1, x_2) + \theta(t_1 - t_2)G^{<}(x_1, x_2) \\
G^{r}(x_1, x_2) &= G_t - G^{<} = G^{>} - G^{\bar{t}} \\
&= \theta(t_1 - t_2)\left(G^{>}(x_1, x_2) - G^{<}(x_1, x_2)\right) \\
&= -i\theta(t_1 - t_2)\langle \psi(x_1)\psi^{\dagger}(x_2) + \psi^{\dagger}(x_2)\psi(x_1)\rangle \\
G^{a}(x_1, x_2) &= G^{t} - G^{>} = G^{<} - G^{\bar{t}}.
\end{aligned} \tag{B.3}$$

$G^{>}$ is greater Green's function (GF), $G^{<}$ is lesser GF, G^{t} is time-ordered GF, $G^{\bar{t}}$ is anti-time-ordered GF, G^{r} is retarded GF and G^{a} is advanced GF. Here x_1 stands for time t_1, position $\mathbf{r}_1$ and any other quantum numbers such as spin. Note that the Green's functions are defined in the Heisenberg representation.

At nonzero temperatures, the retarded Green's function for systems in steady state can be expressed as:

$$G^{r}_{i,j}(t - t') = -i\theta(t - t')\mathrm{Tr}\left(e^{-\beta(K-\Omega)}[c_i(t)c_j^{\dagger}(t') + c_j^{\dagger}(t')c_i(t)]\right) \tag{B.4}$$

Here and in the following i, j stand for any quantum numbers, in particular for the site number and the spin of electron. $K = H - \mu N$, $c_i(t) = e^{iKt}c_i(0)e^{-iKt}$ and Ω is the grand-canonical partition function. We set $t' = 0$, so that G^r depends only on t and we perform a Fourier transform to the energy (frequency) space:

$$G^r_{i,j}(\omega) = \int_{-\infty}^{\infty} \mathrm{d}t e^{i\omega t} G^r_{i,j}(t). \tag{B.5}$$

The spectral representation in terms of the eigenstates defined by $K|m\rangle = E_m|m\rangle$ can be derived as follows:

$$\begin{aligned} G^r_{i,j}(t) &= -i\theta(t)e^{\beta\Omega}\sum_{n,m}\langle n|e^{-\beta K}c_i(t)|m\rangle\langle m|c_j^\dagger(0)|n\rangle + \langle n|e^{-\beta K}c_j^\dagger(0)|m\rangle\langle m|c_i(t)|n\rangle \\ &= -i\theta(t)e^{\beta\Omega}\sum_{n,m}e^{-\beta E_n}\left(e^{it(E_n-E_m)}\langle n|c_i|m\rangle\langle m|c_j^\dagger|n\rangle + e^{it(E_m-E_n)}\langle n|c_j^\dagger|m\rangle\langle m|c_i|n\rangle\right) \\ &= -i\theta(t)e^{\beta\Omega}\sum_{n,m}e^{it(E_n-E_m)}\langle n|c_i|m\rangle\langle m|c_j^\dagger|n\rangle\left(e^{-\beta E_n} + e^{-\beta E_m}\right) \end{aligned} \tag{B.6}$$

and after Fourier transforming we obtain

$$G^r_{i,j}(\omega) = e^{\beta\Omega}\sum_{n,m}\left(\langle m|c_i^\dagger|n\rangle\right)^*\langle m|c_j^\dagger|n\rangle\frac{e^{-\beta E_n} + e^{-\beta E_m}}{\omega + E_n - E_m + i\delta}. \tag{B.7}$$

For $i = j$, we have $\left(\langle m|c_i^\dagger|n\rangle\right)^*\langle m|c_j^\dagger|n\rangle = |\langle m|c_i^\dagger|n\rangle|^2$. Plemelj formula $\frac{1}{x+i\delta} = P\frac{1}{x} - i\pi\delta(x)$ can then be used to obtain the imaginary part:

$$\mathrm{Im}\, G^r_{i,j}(\omega) = -\pi e^{\beta\Omega}\sum_{n,m}|\langle m|c_i^\dagger|n\rangle|^2\left(e^{-\beta E_n} + e^{-\beta E_m}\right)\delta\left(\omega + E_n - E_m\right). \tag{B.8}$$

We define the spectral function as

$$A_i(\omega) = -\frac{1}{\pi}\mathrm{Im}\, G^r_{i,i}. \tag{B.9}$$

It should be noted that some people define the spectral function without the π factor! Our definition is such that $\int A_i \mathrm{d}\omega = 1$, while others prefer $\int A_i \frac{\mathrm{d}\omega}{2\pi} = 1$. Note also that in the case of $S = \frac{1}{2}$ fermions, our spectral function A_i refers to a particular spin orientation, since index i includes σ, i.e. $A_i(\omega) = A_{n,\sigma}(\omega)$.

In the zero-temperature case we obtain:

$$\begin{aligned} A_i(\omega > 0) &= \frac{1}{Z}\sum_{m,n_0}|\langle m|c_i^\dagger|n_0\rangle|^2\delta\left(\omega - E_m\right) \\ A_i(\omega < 0) &= \frac{1}{Z}\sum_{m_0,n}|\langle m_0|c_i^\dagger|n\rangle|^2\delta\left(\omega + E_n\right) \\ Z &= \sum_{n_0}1 \end{aligned} \tag{B.10}$$

where indexes m_0, n_0 indicate summation over the eventually degenerate ground states, while indexes m and n correspond to sums over all states. Z is the partition function.

For $i \neq j$, we consider the symmetrized function $G^r_{i,j} + G^r_{j,i}$. Denoting the braket product $\left(\langle m|c_i^\dagger|n\rangle\right)^* \langle m|c_j^\dagger|n\rangle$ by a, we see that the replacement $i \leftrightarrow j$ yields a^*. The symmetric sum of Green's functions then features a real factor $a + a^* = 2\mathrm{Re}\, a$ and we can again use the Plemelj formula to obtain

$$\begin{aligned} &\mathrm{Im}\, \left(G^r_{i,j}(\omega) + G^r_{j,i}(\omega)\right) = \\ &e^{\beta\Omega} \sum_{n,m} 2\mathrm{Re}\, \left[\left(\langle m|c_i^\dagger|n\rangle\right)^* \langle m|c_j^\dagger|n\rangle\right] \left(e^{-\beta E_n} + e^{-\beta E_m}\right) \delta\left(\omega + E_n - E_m\right). \end{aligned} \tag{B.11}$$

We define mixed spectral function

$$A_{i,j}(\omega) = -\frac{1}{2\pi} \mathrm{Im}\, \left(G^r_{i,j} + G^r_{j,i}\right). \tag{B.12}$$

Specializing to $T = 0$ we obtain:

$$\begin{aligned} A_{i,j}(\omega > 0) &= \frac{1}{Z} \sum_{m,n_0} \mathrm{Re}\, \left[\left(\langle m|c_i^\dagger|n_0\rangle\right)^* \langle m|c_j^\dagger|n_0\rangle\right] \delta\left(\omega - E_m\right) \\ A_{i,j}(\omega < 0) &= \frac{1}{Z} \sum_{m_0,n} \mathrm{Re}\, \left[\left(\langle m_0|c_i^\dagger|n\rangle\right)^* \langle m_0|c_j^\dagger|n\rangle\right] \delta\left(\omega + E_n\right) \end{aligned} \tag{B.13}$$

Note that there is a sum rule

$$\int \mathrm{d}\omega A_{i,j}(\omega) = \delta_{i,j}, \tag{B.14}$$

which is a consequence of the anticommutation relation for fermionic operators $c_i c_j^\dagger + c_j^\dagger c_i = \delta_{i,j}$.

Appendix C

Generalized Schrieffer-Wolff transformation

In this section I derive the Schrieffer-Wolff transformation to the Kondo model applicable to the systems of multiple impurities. The derivation is based on the approach of Ref. 551. We separate the Hamiltonian into a Hamiltonian of the isolated dots and conduction band H_0 and a coupling Hamiltonian H_1:

$$H_0 = \sum_{k,\sigma} \epsilon_k c^\dagger_{k,\sigma} c_{k,\sigma} + \sum_\alpha E_\alpha |\alpha\rangle\langle\alpha| \tag{C.1}$$

$$H_1 = \sum_{k,\sigma,\alpha,\beta} t_{k\sigma|\beta\to\alpha}\ |\alpha\rangle\langle\beta|\ c_{k,\sigma} + t^*_{k\sigma|\beta\to\alpha} c^\dagger_{k\sigma}\ |\beta\rangle\langle\alpha|. \tag{C.2}$$

where multi-indexes α and β stand for the quantum numbers, for example the set (Q, S, S_z, ω). Coefficient $t_{k\sigma|\beta\to\alpha}$ correspond to electron excitations on the dots, while $t^*_{k\sigma|\beta\to\alpha}$ correspond to hole excitations on the dots.

We perform a unitary transformation so that the transformed Hamiltonian will contain no operators linear in coupling coefficients t.

$$\tilde{H} = e^P H e^{-P} = H + [P, H] + \frac{1}{2!}[P, [P, H]] + \cdots \tag{C.3}$$

$$\tilde{H} = H_0 + H_1 + [P, H_0] + [P, H_1] + O(V^3). \tag{C.4}$$

We require $[P, H_0] = -H_1$, so that we will obtain

$$\tilde{H} = H_0 + [P, H_1]\,. \tag{C.5}$$

Let $|a\rangle$ and $|b\rangle$ be two eigenstates of H_0. We get

$$\langle a|H_0 P - P H_0|b\rangle = \langle a|H_1|b\rangle, \tag{C.6}$$

hence

$$\langle a|P|b\rangle = \frac{(H_1)_{ab}}{E_a - E_b}, \tag{C.7}$$

where E_a and E_b are eigenenergies. By premultiplying by $|a\rangle$ and postmultiplying by $\langle b|$ and summing, we obtain

$$P = \sum_{a,b} \frac{(H_1)_{ab}}{E_a - E_b} |a\rangle\langle b|. \tag{C.8}$$

Hamiltonian H_1 connects states that differ by one electron in the dot region, $\Delta Q = \pm 1$ and $\Delta S = \pm\frac{1}{2}$. For transitions where an electron is added to the dots, we write $a = (\alpha, 0)$ and $b = (\beta, k\sigma)$, where multi-indexes $\beta = (Q, S, S_z, \omega)$ and $\alpha = (Q+1, S+\tau, S_z+\sigma, \omega')$ correspond to eigenstates of isolated dots, $\tau = \pm 1/2$, and the energy difference is $E_\alpha - E_\beta - \epsilon_k$. For transitions where an electron is removed from the dots, we write $a = (\alpha, k\sigma)$ and $b = (\beta, 0)$ with $\alpha = (Q-1, S-\tau, S_z-\sigma, \omega')$ and the energy difference is $E_\alpha + \epsilon_k - E_\beta$. Taking into account the definition of H_1, we then obtain

$$P = \sum_{\alpha,\beta,k\sigma} t_{k\sigma|\beta\to\alpha} \frac{|\alpha\rangle\langle\beta|}{E_\alpha - E_\beta - \epsilon_k} c_{k,\sigma} + t^*_{k\sigma|\alpha\to\beta} \frac{|\alpha\rangle\langle\beta|}{E_\alpha - E_\beta + \epsilon_k} c^\dagger_{k,\sigma}. \tag{C.9}$$

Note that some $|\alpha\rangle\langle\beta|$ projectors contain all-in-all an odd number of fermionic operators, because the electron number changes by ± 1. Then $c_{k\sigma}|\alpha\rangle\langle\beta| = -|\alpha\rangle\langle\beta|c_{k\sigma}$.

Now we need to compute the commutator $[P, H_1]$. Outside charge fluctuation regions, we may disregard two-electron hopping terms such as

$$t_{k\sigma|\beta\to\alpha} t_{k'\sigma'|\alpha\to\alpha'} \frac{|\alpha'\rangle\langle\beta|}{E_\alpha - E_\beta - \epsilon_k} c_{k'\sigma'} c_{k\sigma}, \tag{C.10}$$

because they only contribute as high-order corrections. The only relevant terms are those that correspond to electron/hole hopping on and off the dots which are initially in the ground state. These terms are

$$\begin{aligned} \sum_{\alpha,\alpha',\beta,k\sigma,k'\sigma'} & t_{k\sigma|\alpha\to\beta} t^*_{k'\sigma'|\alpha'\to\beta} |\alpha'\rangle\langle\alpha| \left(\frac{1}{E_\beta - E_\alpha - \epsilon_k} + \frac{1}{E_\beta - E_\alpha - \epsilon_{k'}} \right) c^\dagger_{k'\sigma'} c_{k\sigma} \\ & - t_{k\sigma|\beta\to\alpha} t^*_{k'\sigma'|\beta\to\alpha'} |\alpha\rangle\langle\alpha'| \left(\frac{1}{E_\beta - E_\alpha + \epsilon_k} + \frac{1}{E_\beta - E_\alpha + \epsilon'_k} \right) c_{k'\sigma'} c^\dagger_{k\sigma} \end{aligned} \tag{C.11}$$

The states $|\alpha\rangle$ and $|\alpha'\rangle$ correspond to degenerate ground states, which may in some cases correspond to different (Q, S, ω) multiplets. These clearly cannot be mapped to a simple Kondo-like problem, so from here on we assume that there is a single ground multiplet.

We're especially interested in terms with $\sigma = -\sigma'$. Then $S_z(\alpha') = S_z(\alpha) + 2\sigma$ and $|\alpha'\rangle\langle\alpha|$ raises or lowers spin by 1. This corresponds to $S^+\sigma^- + S^-\sigma^+$ term in the Kondo Hamiltonian. Due to spin isotropy, there must also exist corresponding $S^z\sigma^z$ terms for $\sigma = \sigma'$ which lead to $\mathbf{S}\cdot\boldsymbol{\sigma}$ expression.

There are also terms with $\sigma = \sigma'$, which correspond to mere energy renormalization of the ground and excited states, and, in the absence of the particle-hole symmetry, potential scattering terms, that we disregard.

Finally, the effective Hamiltonian is

$$H_{\text{eff}} = H_0 + \sum_{kk'\mu\mu'} J_{kk'} \mathbf{S} \cdot \left(c^\dagger_{k'\mu'} \tfrac{1}{2} \boldsymbol{\sigma}_{\mu' mu} c_{k\mu} \right). \tag{C.12}$$

At low temperatures, only scattering near the Fermi energy is important, and we may use $J_{kk'} \sim J \equiv J_{k_F,k_F}$, where

$$J = \frac{8|t_{k_F\sigma|\alpha\to\beta}|^2}{E_\beta - E_\alpha}. \tag{C.13}$$

The final expression is then

$$H_{\text{eff}} = H_0 + J\mathbf{S} \cdot \mathbf{s}. \tag{C.14}$$

Appendix D

Scaling equations to second order in J

In this section Hubbard's X-operator notation is used. This notation is defined by $X_{p;q} = |p\rangle\langle q|$, where $|p\rangle$ and $|q\rangle$ are states in a complete set of many particle states. The diagonal elements $X_{p;p}$ are projection operators for the state $|p\rangle$. Products of operators can be contracted:

$$X_{p;q}X_{p';q'} = \delta_{p',q}X_{p;q'}. \tag{D.1}$$

We consider an effective Hamiltonian of the form

$$H = \sum_{k\sigma} \epsilon_k c^\dagger_{k\sigma} c_{k\sigma} + \sum_m E_m X_{mm} + \sum_{mm',kk',\sigma\sigma'} J^{\sigma\sigma'}_{mm'} X_{mm'} c^\dagger_{k\sigma} c_{k'\sigma'}, \tag{D.2}$$

where $J^{\sigma\sigma'}_{mm'}$ are generalized exchange constants. We write[2]

$$\Big[H_{11} + H_{12}\left(E - H_{22}\right)^{-1} H_{21} + H_{10}\left(E - H_{00}\right)^{-1} H_{01}\Big]\psi_1 = E\psi_1, \tag{D.3}$$

where subspaces 2 corresponds to states with one electron in the upper $|\delta D|$ edge of the conduction band, 0 corresponds to states with one hole in the lower $|\delta D|$ edge of the band, and 1 corresponds to states with no excitations in the edges that are being traced-over. Furthermore, $H_{ij} = P_i H P_j$, where P_i are projectors to the corresponding subspaces i. After some tedious algebra, we find that to second order the coupling constant are changed by

$$\delta J^{\sigma\sigma'}_{mm'} = \rho|\delta D| \sum_{n\tau} \frac{1}{E - D + \epsilon_k - E_n - H_0} J^{\tau\sigma}_{nm} J^{\tau\sigma'}_{nm'} - \rho|\delta D| \sum_{n\tau} \frac{1}{E - D - \epsilon_{k'} - E_n - H_0} J^{\sigma'\tau}_{nm} J^{\sigma\tau}_{nm'}. \tag{D.4}$$

Appendix E

Transformations of band and coupling Hamiltonians

In this appendix I map the conduction-band and coupling Hamiltonians in discrete form (sum over wave-numbers k) to a continuous Hamiltonian in the energy space that is used in NRG. The derivation roughly follows that of Ref. 30. The main difference is that I specialize from the outset to a one-dimensional conduction channel such as a tight-binding chain. Furthermore, the wave-number k ranges from 0 to π, whereas in bulk each component of the wave vector ranges from $-\pi$ to π. The Hamiltonian of a one-dimensional single-mode conduction lead with a coupling term is

$$H' = H_{\mathrm{band}} + H_{\mathrm{c}} = \sum_k \epsilon_k c^\dagger_{k\mu} c_{k\mu} + \sum_k V_k (c^\dagger_{k\mu} d_\mu + \mathrm{H.c.}). \tag{E.1}$$

Operators c_k are normalized so that $\{c^\dagger_k, c_{k'}\} = \delta_{k,k'}$. We first go from discrete k to a continuum k in the standard way. Let a_k be the continuum operators normalized so that $\{a^\dagger_k, a_{k'}\} = \delta(k-k')$. The replacement rule for sums over k is

$$\sum_k \to \frac{N_c}{\pi} \int_0^\pi \mathrm{d}k, \tag{E.2}$$

where N_c is the number of sites in the chain. The operators c_k transform as

$$c_k \to \sqrt{\frac{\pi}{N_c}} a_k. \tag{E.3}$$

This follows from the requirement that $\sum_{k,k'} \{c^\dagger_k, c_k\} = N_c$ corresponds to $\int \mathrm{d}k \mathrm{d}k' \{a^\dagger_k, a_k\} = \pi$. We obtain

$$\sum_k \epsilon_k c^\dagger_k c_k \to \int \mathrm{d}k \; \epsilon_k \; a^\dagger_k a_k; \tag{E.4}$$

$$\sum_k V_k c_k \to \left(\frac{N_c}{\pi}\right)^{1/2} \int \mathrm{d}k V_k a_k. \tag{E.5}$$

Next we introduce energy representation by defining $a_E = (\mathrm{d}E(k)/\mathrm{d}k)^{-1/2} a_k$, where $E(k) = \epsilon_k$, which makes

$$\{a_E^\dagger, a_{E'}\} = \left(\frac{\mathrm{d}E(k)}{\mathrm{d}k}\right)^{-1} \delta(k-k') = \delta(E-E'). \tag{E.6}$$

This gives

$$\int \mathrm{d}k \epsilon_k a_k^\dagger a_k = \int \mathrm{d}k \epsilon_k \left(\frac{\mathrm{d}E(k)}{\mathrm{d}k}\right) a_E^\dagger a_E = \int_{-D}^{D} \mathrm{d}E \; E \; a_E^\dagger a_E, \tag{E.7}$$

and

$$\left(\frac{N_c}{\pi}\right)^{1/2} \int \mathrm{d}k V_k a_k \tag{E.8}$$

$$= \left(\frac{N_c}{\pi}\right)^{1/2} \int \mathrm{d}k \left(\frac{\mathrm{d}E(k)}{\mathrm{d}k}\right)^{1/2} V_k a_E \tag{E.9}$$

$$= \left(\frac{N_c}{\pi}\right)^{1/2} \int_{-D}^{D} \mathrm{d}E \left(\frac{\mathrm{d}E(k)}{\mathrm{d}k}\right)^{-1/2} V(E) \; a_E. \tag{E.10}$$

Here D is the band edge (or half-bandwidth). As the density of states per spin is

$$\rho(E) = \sum_k \delta(E - E(k)) = \frac{N_c}{\pi} \int \mathrm{d}k \; \delta(E - E(k)) = \frac{N_c}{\pi} \int \mathrm{d}k \; \frac{\delta(k-k_E)}{\frac{\mathrm{d}E(k)}{\mathrm{d}k}} = \frac{N_c}{\pi} \left(\frac{\mathrm{d}E(k)}{\mathrm{d}k}\right)^{-1}, \tag{E.11}$$

we finally obtain

$$H_\mathrm{c} \to \int_{-D}^{D} \mathrm{d}E [\rho(E)]^{1/2} V(E) a_E. \tag{E.12}$$

The energy-representation version of H' is therefore

$$H' = \int_{-D}^{D} \mathrm{d}E \; E \; a_{E\mu}^\dagger a_{E\mu} + \int_{-D}^{D} \mathrm{d}E [\rho(E)]^{1/2} V(E) (a_{E\mu}^\dagger d_\mu + \mathrm{H.c.}). \tag{E.13}$$

In NRG calculations it is customary to measure all energies relative to the band edge D by working in terms of the dimensionless variable $\epsilon = E/D$ and operators $a_{\epsilon\mu} = \sqrt{D} a_{E\mu}$. We also define the hybridization function as $\Gamma(\epsilon) = \pi \rho(\epsilon) V(\epsilon)^2$. It should be noted that all information about the energy dependence of the density of states and of the coupling V is contained in the function Γ alone.[165] The final expression is thus

$$\frac{H'}{D} = \int_{-1}^{1} \mathrm{d}\epsilon \; \epsilon \; a_{\epsilon\mu}^\dagger a_{\epsilon\mu} + \int_{-1}^{1} \mathrm{d}\epsilon \; \left(\frac{\Gamma(\epsilon)}{\pi D}\right)^{1/2} \left(a_{\epsilon\mu}^\dagger d_\mu + \mathrm{H.c.}\right). \tag{E.14}$$

Let us consider the example of a one-dimensional tight-binding chain with hopping parameter t and dispersion $E_k = -2t\cos(k)$. The bandwidth is $D = 2t$ and the density of states is

$$\rho(E) = \frac{N_c}{\pi} \frac{1}{\sqrt{D^2 - E^2}}, \tag{E.15}$$

Furthermore, we take $H_c = -t' \sum_\mu (d_\mu^\dagger c_1 \mu + \text{H.c.})$, i.e the coupling consists of simple hopping from the first site of the chain to the impurity site. The hybridization matrix elements are

$$V_k = -t' \sqrt{\frac{2}{N_c + 1}} \sin k. \tag{E.16}$$

The hybridization function is thus

$$\Gamma(E) = \pi \left(\frac{N_c}{\pi} \frac{1}{\sqrt{D^2 - E^2}} \right) \left(t'^2 \frac{2}{N_c + 1} \sin^2 k \right), \tag{E.17}$$

which for large N_c becomes

$$\Gamma(\epsilon) = \Gamma_0 \sqrt{1 - \epsilon^2} \tag{E.18}$$

where $\Gamma_0 = 2t'^2/D = \frac{1}{2}(t'/t)^2 D$. If a single quantum dot is coupled to two such tight-binding chains, Γ is twice as large, i.e. $\Gamma_0/D = (t'/t)^2$.

Appendix F

Majorana fermions

Let us consider a single fermion mode described by creation-annihilation operator pair $c^\dagger, c$ with $\{c^\dagger, c\} = 1$ and $\{c, c\} = 0$ and $\{c^\dagger, c^\dagger\} = 0$. These operators span a two-level Fock space so that $c^\dagger|0\rangle = |1\rangle$ and $c|1\rangle = |0\rangle$. We decompose the annihilation operator c in real and imaginary parts by defining

$$c \equiv \mathrm{Re}\, c + i\mathrm{Im}\, c \equiv \chi + i\xi, \tag{F.1}$$

where χ and ξ are real, in the sense that $\chi^\dagger = \chi$ and $\xi^\dagger = \xi$. From this it follows

$$c^\dagger = \chi - i\xi. \tag{F.2}$$

The anti-commutation relations then lead to $\xi^2 = 1/4$, $\chi^2 = 1/4$ and $\{\chi, \xi\} = 0$.

Two operators (c, $c^\dagger$) are needed to span a two-level Fock space in the case of complex fermions. Likewise, both χ and ξ need to be present to generate a two-level space; a single real Majorana fermion by itself can only be associated with a trivial single-level space. The degeneracy of a system with N Majorana modes is thus $2^{[N/2]}$, where $[x]$ denotes the integer part of x.

Spin operators for $S = 1/2$ can also be expressed in terms of two Majorana fermions a and b:

$$\sigma^x = \frac{b}{\sqrt{2}},\ \sigma^y = \frac{a}{\sqrt{2}},\ \sigma^z = -iab. \tag{F.3}$$

Bibliography

[1] W. G. van der Wiel, S. De Franceschi, J. M. Elzerman, T. Fujisawa, S. Tarucha, and L. P. Kouwenhoven. Electron transport through double quantum dots. *Rev. Mod. Phys.*, **75** 1, 2003.

[2] A. C. Hewson. The Kondo Problem to Heavy-Fermions. Cambridge University Press, Cambridge, 1993.

[3] K. Vladár and A. Zawadowski. Theory of the interaction between electrons and the two-level system in amorphous metals. I. Noncommutative model Hamiltonian and scaling of first order. *Phys. Rev. B*, **28** 1564, 1983.

[4] V. Madhavan, W. Chen, T. Jamneala, M. Crommie, and N. S. Wingreen. Tunneling into a single magnetic atom: Spectroscopic evidence of the Kondo resonance. *Science*, **280** 567, 1998.

[5] J. Li, W.-D. Schneider, R. Berndt, and B. Delley. Kondo Scattering Observed at a Single Magnetic Impurity. *Phys. Rev. Lett.*, **80** 2893, 1998.

[6] S. M. Cronenwett, T. H. Oosterkamp, and L. P. Kouwenhoven. A Tunable Kondo Effect in Quantum Dots. *Science*, **281** 540, 1998.

[7] D. Goldhaber-Gordon, H. Shtrikman, D. Mahalu, D. Abusch-Magder, U. Meirav, and M. A. Kastner. Kondo effect in a single-ellectron transistor. *Nature*, **391** 156, 1998.

[8] J. Park, A. N. Pasupathy, J. I. Goldsmith, C. Chang, Y. Yaish, J. R. Petta, M. Rinkoski, J. P. Sethna, H. D. Abruna, P. L. McEuen, and D. C. Ralph. Coulomb blockade and the Kondo effect in single-atom transistors. *Nature*, **417** 722, 2002.

[9] Wenjie Liang, Matthew P. Shores, Marc Bockrath, Jeffrey R. Long, and Kongkun Park. Kondo resonance in a single-molecule transistor. *Nature*, **417** 725, 2002.

[10] Lam H. Yu and Douglas Natelson. The Kondo effect in C_{60} single-molecule transistors. *Nanoletters*, **4** 79, 2004.

[11] M. Pustilnik and L. Glazman. Kondo effect in quantum dots. *J. Phys.: Condens. Matter*, **16** R513, 2004.

[12] J. Schmid, J. Weis, K. Eberl, and K. v. Klitzing. Absence of Odd-Even Parity Behavior for Kondo Resonance in Quantum Dots. *Phys. Rev. Lett.*, **84** 5824, 2000.

[13] V. Madhavan, T. Jamneala, K. Nagaoka, W. Chen, Je-Luen Li, S. G. Louie, and M. F. Crommie. Observation of spectral evolution during the formation of Ni_2 Kondo molecule. *Phys. Rev. B*, **66** 212411, 2002.

[14] T. Jamneala, V. Madhavan, and M. F. Crommie. Kondo response of a single antiferromagnetic Chromium trimer. *Phys. Rev. Lett.*, **87** 256804, 2001.

[15] P. Wahl, L. Diekhoner, G. Wittich, L. Vitali, M. A. Schneider, and K. Kern. Kondo effect of molecular complexes at surfaces: ligand control of the local spin coupling. *Phys. Rev. Lett.*, **95** 166601, 2005.

[16] H. Jeong, A. M. Chang, and M. R. Melloch. The Kondo Effect in an Artificial Quantum Dot Molecules. *Science*, **293** 2221, 2001.

[17] A. W. Holleitner, R. H. Blick, A. K. Hüttel, K. Eberl, and J. P. Kotthaus. Probing and Controlling the Bonds of an Artificial Molecule. *Science*, **297** 70, 2002.

[18] N. J. Craig, J. M. Taylor, E. A. Lester, C. M. Marcus, M. P. Hanson, and A. C. Gossard. Tunable Nonlocal Spin Control in a Coupled-Quantum Dot System. *Science*, **304** 565, 2004.

[19] J. C. Chen, A. M. Chang, and M. R. Melloch. Transition between Quantum States in a Parallel-Coupled Double Quantum Dot. *Phys. Rev. Lett.*, **92** 176801, 2004.

[20] B. A. Jones, C. M. Varma, and J. W. Wilkins. Low-temperature properties of the two-impurity Kondo Hamiltonian. *Phys. Rev. Lett.*, **61** 125, 1988.

[21] I. Affleck, A. W. W. Ludwig, and B. A. Jones. Conformal-field-theory approach to the two-impurity Kondo problem: Comparison with numerical renormalization-group results. *Phys. Rev. B*, **52** 9528, 1995.

[22] G. R. Stewart. Heavy-fermion systems. *Rev. Mod. Phys.*, **56** 755, 1984.

[23] Y. Oreg and D. Goldhaber-Gordon. Two-Channel Kondo Effect in a Modified Single Electron Transistor. *Phys. Rev. Lett.*, **90** 136602, 2003.

[24] T. Kuzmenko, K. Kikoin, and Y. Avishai. Towards two-channel Kondo effect in triple quantum dots. *Europhys. Lett.*, **64** 218, 2003.

[25] F. B. Anders, E. Lebanon, and A. Schiller. Coulomb blockade and non-Fermi-liquid behavior in quantum dots. *Phys. Rev. B*, **70** 201306(R), 2004.

[26] M. Pustilnik, L. Borda, L. I. Glazman, and J. von Delft. Quantum phase transition in a two-channel-Kondo quantum dot device. *Phys. Rev. B*, **69** 115316, 2004.

[27] C. J. Bolech and N. Shah. Prediction of the Capacitance Line Shape in Two-Channel Quantum Dots. *Phys. Rev. Lett.*, **95** 036801, 2005.

[28] D. L. Cox and A. Zawadowski. Exotic Kondo effects in metals: magnetic ions in a crystalline electric field and tunneling centres. *Adv. Phys.*, **47** 599, 1998.

[29] K. G. Wilson. The renormalization group: Critical phenomena and the Kondo problem. *Rev. Mod. Phys.*, **47** 773, 1975.

[30] H. R. Krishna-murthy, J. W. Wilkins, and K. G. Wilson. Renormalization-group approach to the Anderson model of dilute magnetic alloys. I. Static properties for the symmetric case. *Phys. Rev. B*, **21** 1003, 1980.

[31] H. R. Krishna-murthy, J. W. Wilkins, and K. G. Wilson. Renormalization-group approach to the Anderson model of dilute magnetic alloys. II. Static properties for the asymmetric case. *Phys. Rev. B*, **21** 1044, 1980.

[32] G. Grüner and A. Zawadowski. Magnetic impurities in non-magnetic metals. *Rep. Prog. Phys.*, **37** 1497, 1974.

[33] B. Coqblin and J. R. Schrieffer. Exchange interaction in alloys with cerium impurities. *Phys. Rev.*, **185** 847, 1969.

[34] Teemu Pohjola, Herbert Schoeller, and Gerd Schon. Orbital and spin Kondo effects in a double quantum dot. *Europhys. Lett.*, **54** 241, 2001.

[35] A. W. Holleitner, A. Chudnovskiy, D. Pfannkuche, K. Eberl, and R. H. Blick. Pseudospin Kondo correlations versus hybridized molecular states in double quantum dots. *Phys. Rev. B*, **70** 075204, 2004.

[36] R. López, D. Sánchez, M. Lee, M.-S. Choi, P. Simon, and K. Le Hur. Probing spin and orbital Kondo effects with a mesoscopic interferometer. *Phys. Rev. B*, **71** 115312, 2005.

[37] B. Lazarovits, P. Simon, G. Zaránd, and L. Szunyogh. Exotic Kondo Effect from Magnetic Trimers. *Phys. Rev. Lett.*, **95** 077202, 2005.

[38] Kevin Ingersent, Andreas W. Ludwig, and Ian Affleck. Kondo Screening in a magnetically frustrated nanostructure: Exact results on a stable non-Fermi-liquid phase. *Phys. Rev. Lett.*, **95** 257204, 2005.

[39] A. C. Hewson and D. Meyer. Numerical renormalization group study of the Anderson-Holstein model. *J. Phys. - Condens. Mat.*, **14** 427, 2002.

[40] P. S. Cornaglia, H. Ness, and D. R. Grempel. Many-Body Effects on the Transport Properties of Single-Molecule Devices. *Phys. Rev. Lett.*, **93** 147201, 2004.

[41] J. Mravlje, A. Ramšak, and T. Rejec. Conductance of deformable molecules with interaction. *Phys. Rev. B*, **72** 121403(R), 2005.

[42] A. Taraphder and P. Coleman. Heavy-Fermion Behavior in a Negative-U Anderson Model. *Phys. Rev. Lett.*, **66** 2814, 1991.

[43] Rok Žitko and Janez Bonča. Spin-charge separation and simultaneous spin and charge Kondo effect. *Phys. Rev. B*, **74** 224411, 2006.

[44] Qimiao Si, Silvio Rabello, Kevin Ingersent, and J. Lleweilun Smith. Locally critical quantum phase transitions in strongly correlated metals. *Nature*, **413** 804, 2001.

[45] A. J. Leggett, S. Chakravarty, A. T. Dorsey, Matthew P. A. Fisher, Anupam Garg, and W. Zwerger. Dynamics of the dissipative two-state systems. *Rev. Mod. Phys.*, **59** 1, 1987.

[46] L. I. Glazman and M. E. Raikh. Resonant Kondo transparency of a barrier with quasilocal impurity states. *JETP Lett.*, **47** 452, 1988.

[47] T. K. Ng and P. A. Lee. On-Site Coulomb Repulsion and Resonant Tunneling. *Phys. Rev. Lett.*, **61** 1768, 1988.

[48] T. Kasuya. A Theory of Metallic Ferro- and Antiferromagnetism on Zener's Model. *Prog. Theor. Phys.*, **16** 45, 1956.

[49] J. Kondo. Resistance Minimum in Dilute Magnetic Alloys. *Prog. Theor. Phys.*, **32** 37, 1964.

[50] N. Andrei, K. Furuya, and J. H. Lowenstein. Solution of the Kondo problem. *Rev. Mod. Phys.*, **55** 331, 1983.

[51] Rok Žitko and Janez Bonča. Multi-impurity Anderson model for quantum dots coupled in parallel. *Phys. Rev. B*, **74** 045312, 2006.

[52] P. D. Sacramento and P. Schlottmann. Low-temperature properties of a two-level system interacting with conduction electrons: An application of the overcompensated multichannel Kondo model. *Phys. Rev. B*, **43** 13294, 1991.

[53] P. Nozières and C. T. de Dominicis. Singularities in the X-Ray Absorption and Emission of Metals III: One-body theory exact solution. *Phys. Rev.*, **178** 1097, 1969.

[54] Luiz N. Oliveira and John W. Wilkins. New approach to the x-ray-absorption problem. *Phys. Rev. B*, **24** 4863, 1981.

[55] I. Affleck. A current algebra approach to the Kondo effect. *Nucl. Phys. B*, **336** 517, 1990.

[56] Ian Affleck. Conformal field theory approach to the Kondo effect. cond-mat/9512099, 1995.

[57] Leo Kouwenhoven and Leonid Glazman. Revival of the Kondo effect. *Physics World*, **Jan** 33, 2001.

[58] D. C. Mattis. Symmetry of Ground State in a Dilute Magnetic Metal Alloy. *Phys. Rev. Lett.*, **19** 1478, 1968.

[59] V. T. Rajan, J. H. Lowenstein, and N. Andrei. Thermodynamics of the Kondo model. *Phys. Rev. Lett.*, **49** 497, 1982.

[60] Kei Yosida. Bound State Due to the s-d Exchange Interaction. *Phys. Rev.*, **147** 223, 1966.

[61] C. M. Varma and Y. Yafet. Magnetic susceptibility of mixed-valence rare-earth compounds. *Phys. Rev. B*, **13** 2950, 1976.

[62] S. Sasaki and S. Tarucha. The Kondo Effect Enhanced by State Degeneracy. *J. Phys. Soc. Japan*, **74** 88, 2005.

[63] S. Sasaki, S. de Franceschi, J. M. Elzerman, W. G. van der Wiel, M. Eto, S. Tarucha, and L. P. Kouwenhoven. Kondo effect in an integer-spin quantum dot. *Nature*, **405** 764, 2000.

[64] W. Izumida, O. Sakai, and S. Tarucha. Tunneling through a Quantum Dot in Local Spin Singlet-Triplet Crossover Region with Kondo Effect. *Phys. Rev. Lett.*, **87** 216803, 2001.

[65] J. Nygard, D. H. Cobden, and P. E. Lindelof. Kondo physics in carbon nanotubes. *Nature*, **408** 342, 2000.

[66] Mikio Eto and Yuli V. Nazarov. Enhancelment of Kondo Effect in Quantum Dots with an Even Number of Electrons. *Phys. Rev. Lett.*, **85** 1306, 2000.

[67] Michael Pustilnik, Yshai Avishai, and Konstantin Konik. Quantum dots with even number of electrons: Kondo effect in a finite magnetic field. *Phys. Rev. Lett.*, **84** 1756, 2000.

[68] O. Entin-Wohlman, A. Aharony, and Y. Levinson. Double quantum dot with two electrons: Singlet-triplet transitions. *Phys. Rev. B*, **64** 085332, 2001.

[69] M. Pustilnik and L. I. Glazman. Kondo Effect in Real Quantum Dots. *Phys. Rev. Lett.*, **87** 216601, 2001.

[70] W. G. van der Wiel, S. De Franceschi, J. M. Elzerman, S. Tarucha, L. P. Kouwenhoven, J. Motohisa, F. Nakajima, and T. Fukui. Two-Stage Kondo Effect in a Quantum Dot at a High Magnetic Field. *Phys. Rev. Lett.*, **88** 126803, 2002.

[71] W. Hofstetter and H. Schoeller. Quantum phase transition in a multilevel dot. *Phys. Rev. Lett.*, **88** 016803, 2002.

[72] A. Kogan, G. Granger, M. A. Kastner, D. Goldhaber-Gordon, and H. Shtrikman. Singlet-triplet transition in a single-electron transistor at zero magnetic field. *Phys. Rev. B*, **67** 113309, 2003.

[73] M. Pustilnik, L. I. Glazman, and W. Hofstetter. Singlet-triplet transition in a lateral quantum dot. *Phys. Rev. B*, **68** 161303(R), 2003.

[74] A. Fuhrer, T. Ihn, K. Ensslin, W. Wegscheider, and M. Bichler. Singlet-triplet transition tuned by asymmetric gate voltages in a quantum ring. *Phys. Rev. Let.*, **91** 206802, 2004.

[75] W. Hofstetter and G. Zarand. Singlet-triplet transition in lateral quantum dots: A renormalization group study. *Phys. Rev. B*, **69** 235301, 2004.

[76] Juan M. Maldacena and Andreas W. W. Ludwig. Majorana Fermions, Exact Mapping between Quantum Impurity Fixed Points with four bulk Fermion species, and solution of the Unitarity Puzzle. *Nucl. Phys. B*, **506** 565, 1997.

[77] I. Affleck and Andreas W. W. Ludwig. The Kondo effect, conformal field theory and fusion rules. *Nucl. Phys. B*, **352** 849, 1991.

[78] Andreas W. W. Ludwig and Ian Affleck. Exact, Asymptotic, Three-Dimensional, Spece- and Time-Dependent, Green's Functions in the Multichannel Kondo Effect. *Phys. Rev. Lett.*, **67** 3160, 1991.

[79] I. Affleck and A. W. W. Ludwig. Exact Critical Theory of the Two-Impurity Kondo Model. *Phys. Rev. Lett.*, **68** 1046, 1992.

[80] I. Affleck, A. W. W. Ludwig, H.-B. Pang, and D. L. Cox. Relevance of anisotropy in the multichannel Kondo effect: Comparison of conformal field theory and numerical renormalization-group results. *Phys. Rev. B*, **45** 7918, 1992.

[81] Ian Affleck and Andreas W. W. Ludwig. Exact conformal-field-theory results on the multichannel Kondo effect: Single-fermion Green's function, self-energy, and resistivity. *Phys. Rev. B*, **48** 7297, 1993.

[82] D. Sénéchal. An introduction to bosonization. cond-mat/9908262, 1999.

[83] Philippe Di Francesco, Pierre Mathieu, and David Sénéchal. Conformal field theory. Springer-Verlag, New York, 1995.

[84] Robert M. Konik, Hubert Saleur, and Andreas W. W. Ludwig. Interplay of the scaling limit and the renormalization group: Implications for symmetry restoration. *Phys. Rev. B*, **66** 075105, 2002.

[85] M. Guerrero and Clare C. Yu. Kondo insulators modeled by the one-dimensional Anderson lattice: A numerical-renormalization-group study. *Phys. Rev. B*, **51** 10301, 1995.

[86] T. Nishino and Kazuo Ueda. Spin- and charge-excitation gaps in the one-dimensional periodic Anderson model. *Phys. Rev. B*, **47** 12451, 1993.

[87] Rajiv R. P. Singh and Richard T. Scalettar. Exact demonstration of η Pairing in the Ground state of an attractive-U Hubbard model. *Phys. Rev. Lett.*, **66** 3203, 1991.

[88] Shoucheng Zhang. Pseudospin Symmetry and New Collective Modes of the Hubbard Model. *Phys. Rev. Lett.*, **65** 120, 1990.

[89] Yoichiro Nambu. Quasi-particles and gauge invariance in the theory of superconductivity. *Phys. Rev.*, **117** 648, 1960.

[90] P. W. Anderson. Random-phase approximation in the theory of superconductivity. *Phys. Rev.*, **112** 1900, 1958.

[91] H. B. Pang and D. L. Cox. Stability of the fixed point of the two-channel Kondo Hamiltonian. *Phys. Rev. Lett.*, **44** 9454, 1991.

[92] Jinwu Ye. Solution of the two-channel spin-flavor Kondo model. *Phys. Rev. B*, **56** R489, 1997.

[93] Gergely Zaránd, Chung-Hou Chung, Pascal Simon, and Matthias Vojta. Quantum criticality in a double quantum-dot system. *Phys. Rev. Lett.*, **97** 166802, 2006.

[94] P. Nozières. Fermi-liquid description of Kondo problem at low temperatures. *J. Low. Temp. Phys.*, **17** 31, 1974.

[95] C. M. Varma, Z. Nussinov, and Wim van Saarloos. Singular and non-Fermi liquids. *Phys. Rep.*, **361** 267, 2002.

[96] I. Affleck. Non-Fermi liquid behavior in Kondo models. *J. Phys. Soc. Japan*, **74** 59, 2005.

[97] D. C. Mattis. Symmetry of ground state in a dilute magnetic metal alloy. *Phys. Rev. Lett.*, **19** 1478, 1967.

[98] P. Mehta, N. Andrei, P. Coleman, L. Borda, and G. Zaránd. Regular and singular Fermi-liquid fixed points in quantum impurity models. *Phys. Rev. B*, **72** 014430, 2005.

[99] W. Koller, A. C. Hewson, and D. Meyer. Singular dynamics of underscreened magnetic impurity models. *Phys. Rev. B*, **72** 045117, 2005.

[100] P. Nozières and A. Blandin. Kondo effect in real metals. *J. Physique*, **41** 193, 1980.

[101] Hanbin Pang. Non-Fermi-Liquid States in a Generalized Two-Channel Kondo Model. *Phys. Rev. Lett.*, **73** 2736, 1994.

[102] Anirvan M. Sengupta and Yong Baek Kim. Overscreened single-channel Kondo problem. *Phys. Rev. B*, **54** 14918, 1996.

[103] P. Coleman, L. B. Ioffe, and A. M. Tsvelik. Simple formulation of the two-channel Kondo model. *Phys. Rev. B*, **52** 6611, 1995.

[104] P. Coleman and A. J. Schofield. Simple description of the anisotropic two-channel Kondo problem. *Phys. Rev. Lett.*, **75** 2184, 1995.

[105] R. Bulla, A. C. Hewson, and G.-M. Zhang. Low-energy fixed points of the σ-τ and the O(3) symmetric Anderson models. *Phys. Rev. B*, **56** 11721, 1997.

[106] Jinwu Ye. On two channel flavor anisotropic and one channel compactified Kondo models. *Nucl. Phys. B*, **512** 543, 1998.

[107] S. C. Bradley, R. Bulla, A. C. Hewson, and G-M. Zhang. Spectral densities of response functions for the $O(3)$ symmetric Anderson and two channel Kondo models. *Eur. Phys. J. B*, **11** 535, 1999.

[108] Gergely Zaránd and Jan von Delft. Analytical calculation of the finite-size crossover spectrum of the anisotropic two-channel Kondo model. *Phys. Rev. B*, **61** 6918, 2000.

[109] V. J. Emery and S. Kivelson. Mapping of the two-channel Kondo problem to a resonant-level model. *Phys. Rev. B*, **46** 10812, 1992.

[110] Jinwu Ye. Emery-Kivelson line and universality of Wilson ratio of spin anisotropic Kondo model. *Phys. Rev. Lett.*, **77** 3224, 1996.

[111] Jinwu Ye. Abelian bosonization approach to quantum impurity problems. *Phys. Rev. Lett.*, **79** 1385, 1997.

[112] Jinwu Ye. Solution of the effective Hamiltonian of impurity hopping between two sites in a metal. *Phys. Rev. B*, **56** 1316, 1997.

[113] P. Coleman. Mixed valence as an almost broken symmetry. *Phys. Rev. B*, **35** 5072, 1987.

[114] J. Voit. One-dimensional Fermi liquids. *Rep. Prog. Phys.*, **57** 977, 1995.

[115] B. J. Kim, H. Koh, E. Rotenberg, S.-J. Oh, H. Eisaki, N. Motoyama, S. Uchida, T. Tohyama, S. Maekawa, Z.-X. Shen, and C. Kim. Distinct spinon and holon dispersions in photoemission spectral functions from one-dimensional $SrCuO_2$. *Nature Phys.*, **2** 397, 2006.

[116] O. M. Auslaender, H. Steinberg, A. Yacoby, Y. Tserkovnyak, B. I. Halperin, K. W. Baldwin, L. N. Pfeiffer, and K. W. West. Spin-Charge separation and localization in one dimension. *Science*, **308** 88, 2005.

[117] F. D. M. Haldane. Luttinger liquid theory of one-dimensional quantum fluids. I. Properties of the Luttinger model and their extension to the general 1D interacting spinless Fermi gas. *J. Phys. C: Solid State Phys.*, **14** 2585, 1981.

[118] Jan von Delft, Gergely Zaránd, and Michele Fabrizio. Finite-Size Bosonization of 2-Channel Kondo model: A bridge between numerical renormalization group and conformal field theory. *Phys. Rev. Lett.*, **81** 196, 1998.

[119] M. Blume, V. J. Emery, and A. Luther. Spin-boson systems: One-dimensional equivalents and the Kondo problem. *Phys. Rev. Lett.*, **25** 450, 1970.

[120] Sumathi Rao and Diptiman Sen. An introduction to bosonization and some of its applications, 2000.

[121] I. Affleck and Andreas W. W. Ludwig. Critical theory of overscreened Kondo fixed points. *Nucl. Phys. B*, **360** 641, 1991.

[122] Ian Affleck and Andreas W. W. Ludwig. Universal Noninteger Ground-State Degeneracy in Critical Quantum Systems. *Phys. Rev. Lett.*, **67** 161, 1991.

[123] P. W. Anderson. Basic notions of condensed matter physics. The Benjamin-Cummings Publishing Company, 1984.

[124] Kenneth G. Wilson and Michael E. Fisher. Critical exponents in 3.99 dimensions. *Phys. Rev. Lett.*, **28** 240, 1972.

[125] Kenneth G. Wilson. Feynman-Graph Expansion for Critical Exponents. *Phys. Rev. Lett.*, **28** 548, 1972.

[126] Michael E. Fisher. Renormalization group theory: Its basis and formulation in statistical physics. *Rev. Mod. Phys.*, **70** 653, 1998.

[127] R. Shankar. Renormalization group approach to interacting fermions. *Rev. Mod. Phys.*, **66** 129, 1994.

[128] R. Shankar. Effective field theory in condensed matter physics. cond-mat/9703210, 1997.

[129] Ralf Bulla, Theo Costi, and Thomas Pruschke. The numerical renormalization group method for quantum impurity systems. cond-mat/0701106, 2007.

[130] A. A. Abrikosov and A. A. Migdal. On the theory of the Kondo effect. *J. Low Temp. Phys.*, **3** 519, 1970.

[131] M. Fowler. Renormalization-Group Techniques in the Kondo effect. *Phys. Rev. B*, **6** 3422, 1972.

[132] D. M. Cragg and P. Lloyd. Universality and the renormalisability of rotationally invariant Kondo Hamiltonians. *J. Phys. C: Solid State Phys.*, **12** 3301, 1979.

[133] Frank Wilczek. Quantum field theory. *Rev. Mod. Phys.*, **71** S85, 1998.

[134] Michael C. Ogilvie. The Gross-Neveu model: dynamical symmetry breaking at a Kosterlitz-Thouless phase transition. *J. Phys. A: Math. Gen.*, **14** L519, 1981.

[135] David J. Gross. The discovery of asymptotic freedom and the emergence of QCD. Nobel Lecture, 2004.

[136] D. J. Gross and A. Neveu. Dynamical symmetry breaking in an asymptotically free theory. *Phys. Rev. D*, **10** 3235, 1974.

[137] P. W. Anderson and G. Yuval. Exact results in the Kondo problem: Equivalence to a classical one-dimensional Coulomb gas. *Phys. Rev. Lett.*, stran 89, 1969.

[138] P. W. Anderson, G. Yuval, and D. R. Hamann. Exact resultsin the Kondo problem II: Scaling Theory, Qualitatively correct solution and some new results on one-dimensional classical statistical models. *Phys. Rev. B*, **1** 4464, 1970.

[139] G. Yuval and P. W. Anderson. Exact results for the Kondo Problem: One-Body Theory and Extension to Finite Temperature. *Phys. Rev. B*, **1** 1522, 1970.

[140] P. W. Anderson. A poor man's derivation of scaling laws for the Kondo problem. *J. Phys. C: Solid St. Phys.*, **3** 2436, 1970.

[141] D. M. Cragg and P. Lloyd. Potential scattering and the Kondo problem. *J. Phys. C: Solid State Phys.*, **11** L597, 1978.

[142] D. M. Cragg and P. Lloyd. Kondo Hamiltonians with a non-zero ground-state spins. *J. Phys. C: Solid State Phys.*, **12** L215, 1979.

[143] W. Koller, A. C. Hewson, and D. Meyer. Singular dynamics of underscreened magnetic impurity models. *Phys. Rev. B*, **72** 045117, 2005.

[144] D. M. Cragg, P. Lloyd, and P. Nozières. On the ground states of some s-d exchange Kondo Hamiltonians. *J. Phys. C: Solid St. Phys.*, **13** 803, 1980.

[145] H. Kusunose, K. Miyake, Y. Shimizu, and O. Sakai. Numerical renormalization-group study of particle-hole symmetry breaking in two-channel Kondo problem: Effect of repulsion among conduction electrons and potential scattering. *Phys. Rev. Lett.*, **76** 271, 1996.

[146] H. R. Krishna-murthy, J. W. Wilkins, and K. G. Wilson. Temperature-Dependent Susceptibility of the Symmetric Anderson Model: Connection to the Kondo Model. *Phys. Rev. Lett.*, **35** 1101, 1975.

[147] O. Sakai, Y. Shimizu, and T. Kasuya. Single-particle and magnetic excitation spectra of degenerate Anderson model with finite f-f Coulomb interaction. *J. Phys. Soc. Japan*, **58** 3666, 1989.

[148] Michele Fabrizio, Andrew F. Ho, Lorenzo De Leo, and Giuseppe E. Santoro. Nontrivial fixed point in a twofold orbitally degenerate Anderson impurity model. *Phys. Rev. Lett.*, **91** 246402, 2003.

[149] Lorenzo De Leo and Michele Fabrizio. Spectral properties of a two-orbital Anderson impurity model across a non-Fermi-liquid fixed point. *Phys. Rev. B*, **69**(24) 245114, 2004.

[150] A. K. Zhuravlev, V. Yu. Irkhin, M. I. Katsnelson, and A. I. Lichtenstein. Kondo Resonance for Orbitally Degenerate Systems. *Phys. Rev. Lett.*, **93**(23) 236403, 2004.

[151] R. Allub, H. Ceva, and B. R. Alascio. Magnetic susceptibility of a model for valence fluctuations between two magnetic configurations: Renormalization-group approach. *Phys. Rev. B*, **29** 3098, 1984.

[152] C. Jayaprakash, H. R. Krishna-murthy, and J. W. Wilkins. Two-impurity Kondo problem. *Phys. Rev. Lett.*, **47** 737, 1981.

[153] B. A. Jones and C. M. Varma. Study of Two Magnetic Impurities in a Fermi Gas. *Phys. Rev. Lett.*, **58** 843, 1987.

[154] J. B. Silva, W. L. C. Lima, W. C. Oliveira, J. L. N. Mello, L. N. Oliveira, and J. W. Wilkins. Particle-Hole assymetry in the Two-Impurity Kondo model. *Phys. Rev. Lett.*, **76** 275, 1996.

[155] O. Sakai and Y. Shimizu. Excitation spectra of two impurity Anderson model. I. Critical Transition in the Two Magnetic Impurity Problem and the Roles of the Parity Splitting. *J. Phys. Soc. Japan*, **61** 2333, 1992.

[156] C. A. Paula, M. F. Silva, and L. N. Oliveira. Low-energy spectral density for the Alexander-Anderson model. *Phys. Rev. B*, **59** 85, 1999.

[157] R. Žitko, J. Bonča, A. Ramšak, and T. Rejec. Kondo effect in triple quantum dots. *Phys. Rev. B*, **73** 153307, 2006.

[158] Rok Žitko and Janez Bonča. Fermi-liquid versus non-Fermi-liquid behavior in triple quantum dots. *Phys. Rev. Lett.*, **98** 047203, 2007.

[159] D. Meyer, A. C. Hewson, and R. Bulla. Gap formation and soft phonon mode in the Holstein model. *Phys. Rev. Lett.*, **89** 196401, 2002.

[160] Gun Sang Jeon, Tae-Ho Park, and Han-Yong Choi. Numerical renormalization-group study of the symmetric Anderson-Holstein model: Phonon and electron spectral functions. *Phys. Rev. B*, **68** 045106, 2003.

[161] P. S. Cornaglia and D. R. Grempel. Magnetoconductance through a vibrating molecule in the Kondo regime. *Phys. Rev. B*, **71** 245326, 2005.

[162] R. Bulla, Hyun-Jung Lee, Ning-Hua Tong, and Matthias Vojta. Numerical renormalization group for quantum impurities in a bosonic bath. *Phys. Rev. B*, **71** 045122, 2005.

[163] K. Chen and C. Jayaprakash. X-ray-edge singularities with nonconstant density of states: A renormalization-group approach. *Phys. Rev. B*, **52** 14436, 1995.

[164] Kevin Ingersent. Behavior of magnetic impurities in gapless Fermi systems. *Phys. Rev. B*, **54** 11936, 1996.

[165] R. Bulla, Th. Pruschke, and A. C. Hewson. Anderson impurity in pseudo-gap Fermi systems. *J. Phys.: Codens. Matter.*, **9** 10463, 1997.

[166] Kan Chen and C. Jayaprakash. Kondo effect in Fermi systems with a gap: A renormalization-group study. *Phys. Rev. B*, **57** 5225, 1998.

[167] Carlos Gonzalez-Buxton and Kevin Ingersent. Renormalization-group study of Anderson and Kondo impurities in gapless Fermi systems. *Phys. Rev. B*, **57** 14254, 1998.

[168] Ralf Bulla, Matthew T Glossop, David E Logan, and Thomas Pruschke. The soft-gap Anderson model: comparison of renormalization group and local moment approaches. *J. Phys.: Condens. Matter*, **12** 4899, 2000.

[169] Tae-Suk Kim, L. N. Oliveira, and D. L. Cox. Non-Fermi-liquid fixed point. *Phys. Rev. B*, **55** 12460, 1997.

[170] M. Koga, G. Zaránd, and D. L. Cox. Crystal Field Triplets: A new route to non-fermi-liquid physics. *Phys. Rev. Lett.*, **83** 2421, 1999.

[171] M. Koga. Hidden non-Fermi-liquid behavior due to a crystal-field quartet. *Phys. Rev. B*, **61** 395, 2000.

[172] Matthias Vojta and Ralf Bulla. Kondo effect of impurity moments in d-wave superconductors: Quantum phase transitions and spectral properties. *Phys. Rev. B*, **65** 014511, 2002.

[173] Mikito Koga and Masashige Matsumoto. Nonvanishing Local Moment in Triplet Superconductors. *J. Phys. Soc. Japan*, **71** 943, 2002.

[174] M. Vojta, R. Bulla, and W. Hofstetter. Quantum phase transitions in models of coupled magnetic impurities. *Phys. Rev. B*, **65** 140405(R), 2002.

[175] Matthias Vojta. Quantum phase transitions. *Rep. Prog. Phys.*, **66** 2069, 2003.

[176] W. Izumida, O. Sakai, and Y. Shimizu. Kondo effect in single quantum dot systems – Sutdy with Numerical Renormalization Group Method. *J. Phys. Soc. Japan*, **67** 2444, 1998.

[177] W. Hofstetter and J. Konig adn H. Schoeller. Kondo Correlations and the Fano Effect in Closed Aharonov-Bohm Interferometers. *Phys. Rev. Lett.*, **87** 156803, 2001.

[178] D. Boese, W. Hofstetter, and H. Schoeller. Interference and interaction effects in multilevel quantum dots. *Phys. Rev. B*, **64** 125309, 2001.

[179] W. Izumida and O. Sakai. Kondo Effect in Quantum Dot Systems – Numerical Renormalization Group Study. *J. Phys. Soc. Japan*, **74** 103, 2005.

[180] Wataru Izumida, Osamu Sakai, and Yukihiro Shimizu. Many body effects on electron tunneling through quantum dots in an Aharonov-Bohm circuit. *J. Phys. Soc. Japan*, **66** 717, 1997.

[181] W. Izumida and O. Sakai. Two-impurity Kondo effect in double-quantum-dot systems: Effect of interdot kinetic exchange coupling. *Phys. Rev. B*, **62** 10260, 2000.

[182] D. Boese, W. Hofstetter, and H. Schoeller. Interference in interacting quantum dots with spin. *Phys. Rev. B*, **66** 125315, 2002.

[183] P. S. Cornaglia and D. R. Grempel. Strongly correlated regimes in a double quantum dot device. *Phys. Rev. B*, **71** 075305, 2005.

[184] M. R. Galpin, D. E. Logan, and H. R. Krishnamurthy. Quantum phase transition in capacitively coupled double quantum dot. *Phys. Rev. Lett.*, **94** 186406, 2005.

[185] M. Sindel, A. Silva, Y. Oreg, and J. von Delft. Charge oscillations in quantum dots: Renormalization group and Hartree method calculations. *Phys. Rev. B*, **72** 125316, 2005.

[186] Martin R. Galpin, David E. Logan, and H R Krishnamurthy. Renormalization group study of capacitively coupled double quantum dots. *J. Phys.: Condens. Matter*, **18** 6545, 2006.

[187] Martin R. Galpin, David E. Logan, and H R Krishnamurthy. Dynamics of capacitively coupled double quantum dots. *J. Phys.: Condens. Matter*, **18** 6571, 2006.

[188] R. Žitko and J. Bonča. Enhanced conductance through side-coupled double quantum dots. *Phys. Rev. B*, **73** 035332, 2006.

[189] Akira Oguri, Yunori Nisikawa, and A. C. Hewson. Determination of the Phase Shifts for Interacting Electrons Connected to Reservoirs. *J. Phys. Soc. Japan*, **74** 2554, 2005.

[190] A. Oguri and A. C. Hewson. NRG approach to the transport through a finite Hubbard chain connected to reservoirs. *J. Phys. Soc. Japan*, **74** 988, 2005.

[191] J. Martinek, M. Sindel, J. Barnas, J. Konig, G. Schon, and J. von Delft. Kondo Effect in the Presence of Itinerant-Electron Ferromagnetism Studied with the Numerical Renormalization Group Method. *Phys. Rev. Lett.*, **91** 247202, 2003.

[192] Mahn-Soo Choi, David Sanchez, and Rosa Lopez. Kondo Effect in a Quantum Dot Coupled to Ferromagnetic Leads: A Numerical Renormalization Group Analysis. *Phys. Rev. Lett.*, **92** 056601, 2004.

[193] W. Hofstetter and H. Schoeller. Quantum Phase Transition in a Multilevel Dot. *Phys. Rev. Lett.*, **88** 016803, 2002.

[194] L. Borda, G. Zaránd, W. Hofstetter, B. I. Halperin, and J. von Delft. SU(4) Fermi liquid state and spin filtering in a double quantum dot system. *Phys. Rev. Lett.*, **90** 026602, 2003.

[195] Gabriel Kotliar. Quantum impurity models as reference systems for strongly correlated materials: the road from the Kondo impurity model to first principles electronic structure calculations with dynamical mean-field theory. *J. Phys. Soc. Japan*, **74** 147, 2005.

[196] Antoine Georges, Gabriel Kotliar, Werner Krauth, and Marcelo J. Rozenberg. Dynamical mean-field theory of strongly correlated fermion systems and the limit of infinite dimensions. *Rev. Mod. Phys.*, **68** 13, 1996.

[197] R. Bulla. Zero Temperature Metal-Insulator Transition in the Infinite-Dimensional Hubbard Model. *Phys. Rev. Lett.*, **83** 136, 1999.

[198] Th. Pruschke, R. Bulla, and M. Jarrell. Low-energy scale of the periodic Anderson model. *Phys. Rev. B*, **61** 12799, 2000.

[199] W. Koller, D. Meyer, Y. Ono, and A. C. Hewson. First- and second-order phase transitions in the Holstein-Hubbard model. *Europhys. Lett.*, **66** 559, 2004.

[200] Gun Sang Jeon, Tae-Ho Park, Jung Hoon Han, Hyun C. Lee, and Han-Yong Choi. Dynamical mean-field theory of the Hubbard-Holstein model at half filling: Zero temperature metal-insulator and insulator-insulator transitions. *Phys. Rev. B*, **70** 125114, 2004.

[201] Th. Pruschke and R. Bulla. Hund's coupling and the metal-insulator transition in the two-band Hubbard model. *Eur. Phys. J. B*, **44** 217, 2005.

[202] Rok Zitko. NRG Ljubljana. `http://nrgljubljana.ijs.si/`, 2006.

[203] E. Anderson, Z. Bai, C. Bischof, S. Blackford, J. Demmel, J. Dongarra, J. Du Croz, A. Greenbaum, S. Hammarling, A. McKenney, and D. Sorensen. LAPACK Users' Guide. Society for Industrial and Applied Mathematics, Philadelphia, PA, third izdaja, 1999.

[204] Free Software Foundations. GNU General Public License. `http://www.gnu.org/copyleft/gpl.html`, 1991.

[205] W. C. Oliveira and L. N. Oliveira. Generalized numerical renormalization-group method to calculate the thermodynamical properties of impurities in metals. *Phys. Rev. B*, **49** 11986, 1994.

[206] W. Hofstetter. Renormalization group methods for quantum impurity systems. Disertacija, Uni. Augsburg, Germany, 2000.

[207] F. D. M. Haldane. Theory of the atomic limit of the Anderson model: I. Perturbation expansions re-examined. *J. Phys. C: Solid State Phys.*, **11** 5015, 1978.

[208] M. Yoshida, M. A. Whitaker, and L. N. Oliveira. Renormalization-group calculation of excitation properties for impurity models. *Phys. Rev. B*, **41** 9403, 1990.

[209] Vivaldo L. Campo and Luiz N. Oliveira. Thermodynamics of the two-impurity Kondo model. *Phys. Rev. B*, **70** 153401, 2004.

[210] V. L. Campo and L. N. Oliveira. Alternative discretization in the numerical renormalization group. *Phys. Rev. B*, **72** 104432, 2005.

[211] F. D. M. Haldane. Scaling theory of the Asymmetric Anderson Model. *Phys. Rev. Lett.*, **40** 416, 1978.

[212] M. Sindel. Numerical Renormalization Group studies of Quantum Impurity Models in the Strong Coupling Limit. Disertacija, Fak. für Physik, Ludwig-Maximilians-Universität München, 2004.

[213] Jr. V. L. Campo and L. N. Oliveira. Renormalization-group approach to the problem of conduction through a nanostructure. *Phys. Rev. B*, **68** 035337, 2003.

[214] R. Bulla, A. C. Hewson, and Th. Pruschke. Numerical renormalization group calculation for the self-energy of the impurity Anderson model. *J. Phys.: Condens. Matter*, **10** 8365, 1998.

[215] L. N. Oliveira and J. W. Wilkins. Specific heat of the Kondo model. *Phys. Rev. Lett.*, **47** 1553, 1981.

[216] S. C. Costa, C. A. Paula, V. L. Libero, and L. N. Oliveira. Numerical renormalization-group calculation of specific heats. *Phys. Rev. B*, **55** 30, 1997.

[217] H. O. Frota. Charge susceptiblity of the spin-degenerate Anderson model. *Phys. Rev. B*, **44** 8433, 1991.

[218] J. W. M. Pinto and H. O. Frota. Electron spin resonance of a magnetic impurity in the resonant level model. *Phys. Rev. B*, **64** 092404, 2001.

[219] Kan Chen, C. Jayaprakash, and H. R. Krishnamurthy. Spatially dependent zero-frequency response functions and correlation functions in the Kondo model. *Phys. Rev. B*, **45** 5368, 1992.

[220] Franz J. Wegner. Correction to scaling laws. *Phys. Rev. B*, **5** 4529, 1972.

[221] A. Ramšak, J. Mravlje, R. Žitko, and J. Bonča. Spin qubits in double quantum dots: Entanglement versus the Kondo effect. *Phys. Rev. B*, **74** 241305(R), 2006.

[222] H. O. Frota and L. N. Oliveira. Photoemission spectroscopy for the spin-degenerate Anderson model. *Phys. Rev. B*, **33** 7871, 1986.

[223] J. J. S. Brito and H. O. Frota. Core-level photoemission spectrum for the spin-degenerate Anderson model. *Phys. Rev. B*, **42** 6378, 1990.

[224] V. L. Libero and L. N. Oliveira. Spectral density for fermion tunneling between two centers in a metallic environment. *Phys. Rev. Lett.*, **65** 2042, 1990.

[225] T. A. Costi and A. C. Hewson. Resistivity cross-over for the non-degenerate Anderson model. *Phil. Mag. B*, **65** 1165, 1992.

[226] H. O. Frota and G. D. Mahan. Tunneling in fermion systems. *Phys. Rev. B*, **49** 2152, 1994.

[227] T. A. Costi and A. C. Hewson. Transport-coefficients of the Anderson model. *J. Phys. - Cond. Mat.*, **5** L361, 1993.

[228] T. A. Costi, A. C. Hewson, and V. Zlatic. Transport coefficients of the Anderson model via the numerical renormalization group. *J. Phys.: Condens. Matter*, **6** 2519, 1994.

[229] T. A. Costi. Magnetotransport through a strongly interacting quantum dot. *Phys. Rev. B*, **64** 241310(R), 2001.

[230] M. Sindel, W. Hofstetter, J. von Delft, and M. Kindermann. Frequency-dependent transport through a quantum dot in the Kondo regime. *Phys. Rev. Lett.*, **94** 196602, 2005.

[231] G. Zaránd, L. Borda, J. von Delft, and N. Andrei. Theory of Inelastic Scattering from Magnetic Impurities. *Phys. Rev. Lett.*, **93** 107204, 2004.

[232] R. Bulla, T. A. Costi, and D. Vollhardt. Finite-temperature numerical renormalization group study of the Mott transition. *Phys. Rev. B*, **64** 045103, 2001.

[233] Walter Hofstetter. Generalized Numerical Renormalization Group for Dynamical Quantities. *Phys. Rev. Lett.*, **85** 1508, 2000.

[234] F. B. Anders and A. Schiller. Real-time dynamics in Quantum Impurity Systems: A time-dependent Numerical Renormalization Group Approach. *Phys. Rev. B*, **74** 245113, 2006.

[235] Andreas Weichselbaum and Jan von Delft. Sum-rule conserving spectral functions from the Numerical Renormalization Group. cond-mat/0607497, 2006.

[236] Robert Peters, Thomas Pruschke, and Frithjof B. Anders. A numerical renormalization group approach to Green's functions for quantum impurity models. *Phys. Rev. B*, **74** 245113, 2006.

[237] Rok Zitko. NRG Ljubljana - User's manual. `http://nrgljubljana.ijs.si/`, 2007.

[238] A. M. Tsvelick and P. B. Wiegmann. Exact results in the theory of magnetic alloys. *Adv. Phys.*, **32** 453, 1983.

[239] P. D. Sacramento and P. Schlottmann. Thermodynamics of the single-channel Kondo impurity of spin $S(\leq 7/2)$ in a magnetic field. *Phys. Rev. B*, **40** 431, 1989.

[240] A. M. Tsvelick and P. B. Wiegmann. Exact solution of the Anderson model: II. Thermodynamic properties at finite temperatures. *J. Phys. C: Solid State Phys.*, **16** 2321, 1983.

[241] K. Schönhammer. Variational Ansatz for the Anderson model of chemisorption. *Phys. Rev. B*, **13** 4336, 1976.

[242] O. Gunnarson and K. Schönhammer. Double occupancy of the f orbital in the Anderson model for Ce compounds. *Phys. Rev. B*, **31** 4815, 1985.

[243] O. Gunnarsson and K. Schonhammer. Photoemission from Ce Compounds: Exact Model Calculation in the Limit of Large Degeneracy. *Phys. Rev. Lett.*, **50** 604, 1983.

[244] O. Gunnarsson and K. Schonhammer. Electron spectroscopies for Ce compounds in the impurity model. *Phys. Rev. B*, **28** 4315, 1983.

[245] T. Rejec and A. Ramšak. Formulas for zero-temperature conductance through a region with interaction. *Phys. Rev. B*, **68** 035342, 2003.

[246] J. Bonča, A. Ramšak, and T. Rejec. Comment on "Kondo resonances and Fano antiresonances in transport through quantum dots". cond-mat/0407590, 2004.

[247] T. Rejec and A. Ramšak. Conductance of interacting Aharonov-Bohm systems. *Phys. Rev. B*, **68** 033306, 2003.

[248] J. Mravlje, A. Ramšak, and T. Rejec. Kondo effect in double quantum dots with interdot repulsion. *Phys. Rev. B*, **73** 241305(R), 2006.

[249] J. Mravlje, A. Ramšak, and T. Rejec. Conductance of a molecule with a center of mass motion. *Phys. Rev. B*, **74** 205320, 2006.

[250] F. F. Assaad. Quantum Monte Carlo Methods on Lattices: the Determinantal Approach. In J. Grotendorst, D. Marx, and A. Muramatsu, editors, *Quantum Simulations of Complex Many-Body Systems: From Theory to Algorithms*, volume 10, strani 447–457. John von Neumann Institute for Computing, 2002.

[251] C. Cohen-Tannoudji, B. Diu, and F. Laloe. Quantum Mechanics. Wiley-Interscience, 1977.

[252] H. F. Trotter. On the product of semigroups of operators. *Proc. Am. Math. Soc.*, **10** 545, 1959.

[253] J. Hubbard. Calculation of partition functions. *Phys. Rev. Lett.*, **3** 77, 1959.

[254] J. E. Hirsch. Discrete Hubbard-Stratonovich transformation for fermion lattice models. *Phys. Rev. B*, **28** 4059, 1983.

[255] N. Metropolis, A. W. Rosenbluth, M. N. Rosenbluth, A. H. Teller, and E. Teller. Equations of State Calculated by Fast Computing Machines. *J. Chem. Phys*, **21** 1087, 1953.

[256] Matthias Troyer and Uwe-Jens Wiese. Computational complexity and fundamental limitations to fermionic Quantum Monte Carlo simulations. *Phys. Rev. Lett.*, **94** 170201, 2005.

[257] E. Y. Loh, J. E. Gubernatis, R. T. Scalettar, S. R. White, D. J. Scalapino, and R. L. Sugar. Sign problem in the numerical simulation of many-electron systems. *Phys. Rev. B*, **41** 9301, 1990.

[258] E. Y. Loh and J. E. Gubernatis. Stable Simulations of Models of Interacting Electrons. In W. Hanke and Yu. V. Kopaev, editors, *Electronic Phase Transitions*. Elsevier-Science, Amsterdam, 1991.

[259] S. Fahy and D. R. Hamann. Diffusive behavior of states in the Hubbard-Stratonovich transformation. *Phys. Rev. B*, **53** 765, 1991.

[260] S. Zhang, J. Carlson, and J. E. Gubernatis. Constrained Path Quantum Monte Carlo Method for Fermion Ground State. *Phys. Rev. Lett.*, **74** 3652, 1995.

[261] S. Zhang, J. Carlson, and J. E. Gubernatis. Constrained path Monte Carlo method for fermion ground state. *Phys. Rev. B*, **55** 7464, 1997.

[262] J. Carlson, J. E. Gubernatis, G. Ortiz, and S. Zhang. Issues and observations on applications of the constrained-path Monte Carlo method to many-fermion systems. *Phys. Rev. B*, **59** 12788, 1999.

[263] M. Guerrero, G. Ortiz, and J. E. Gubernatis. Correlated wave functions and the absence of long-range order in numerical studies of the Hubbard model. *Phys. Rev. B*, **59** 1706, 1999.

[264] M. Guerrero, G. Ortiz, and J. E. Gubernatis. Pairing correlations in the attractive Hubbard model on chains, ladders, and squares. *Phys. Rev. B*, **62** 600, 2000.

[265] J. Bonča and J. E. Gubernatis. Effects of doping on spin correlations in the periodic Anderson model. *Phys. Rev. B*, **58** 6992, 1998.

[266] Yoseph Imry. Introduction to mesoscopic physics. Oxford University Press, second izdaja, 2002.

[267] Nicolás Agraït, Alfredo Levy Yeyati, and Jan M. van Ruitenbeek. Quantum properties of atomic-sized conductors. *Phys. Rep.*, **377** 81, 2003.

[268] L. Limot, J. Kröger, R. Berndt, A. Garcia-Lekue, and W. A. Hofer. Atom transfer and Single-Adatom Contacts. *Phys. Rev. Lett.*, **94** 126102, 2005.

[269] N. Néel, J. Kröger, L. Limot, K. Palotas, W. A. Hofer, and R. Berndt. Conductance and Kondo Effect in a Controlled Single-Atom Contact. *Phys. Rev. Lett.*, **98** 016801, 2007.

[270] K. Schwab, E. A. Henriksen, J. M. Worlock, and M. L. Roukes. Measurement of the quantum of thermal conductance. *Nature*, **404** 974, 2000.

[271] Matthias Meschke, Wiebke Guichard, and Jukka P. Pekloa. Single-mode heat conduction by photons. *Nature*, **444** 187, 2006.

[272] R. M. Potok, I. G. Rau, Hadas Shtrikman, Yuval Oreg, and D. Goldhaber-Gordon. Observation of the two-channel Kondo effect. cond-mat/0610721, 2006.

[273] Yunori Nisikawa and Akira Oguri. Numerical renormalization group approach to a quartet quantum-dot array connected to reservoirs: Gate-voltage dependence of the conductance. *Phys. Rev. B*, **73** 125108, 2006.

[274] Lijun Zhu and C. M. Varma. Coherence in the Two Kondo Impurity Problem. cond-mat/0607426, 2006.

[275] Yoseph Imry and Rolf Landauer. Conductance viewed as transmission. *Rev. Mod. Phys.*, **71** S306, 1999.

[276] Daniel S. Fisher and Patrick A. Lee. Relation between conductivity and transmission matrix. *Phys. Rev. B*, **23** 6851, 1981.

[277] Henk van Houten and Carlo Beenakker. Quantum point contacts. *Physics Today*, stran 22, July 1996.

[278] Rafael A. Molina, Dietmar Weinmann, Rodolfo A. Jalabert, Gert-Ludwig Ingold, and Jean-Louis Pichard. Conductance through a one-dimensional correlated system: Relation to persistent currents and the role of the contacts. *Phys. Rev. B*, **67** 235306, 2003.

[279] T. Rejec and A. Ramšak. Private communication.

[280] Y. Meir and N. S. Wingreen. Landauer formula for the current through an interacting electron region. *Phys. Rev. Lett.*, **68** 2512, 1992.

[281] Alex Kamenev. Les Houches Summer School on Nanoscopic Quantum Transport, chapter Many-body theory of non-equilibrium systems. 2004.

[282] J. Tersoff and D. R. Hamann. Theory of the scanning tunneling microscope. *Phys. Rev. B*, **31** 805, 1985.

[283] N. Andrei and C. Destri. Solution of the Multichannel Kondo Problem. *Phys. Rev. Lett.*, **52** 364, 1984.

[284] A. M. Tsvelick. The thermodynamics of the multichannel Kondo problem. *J. Phys. C: Solid State Phys.*, **18** 159, 1985.

[285] A. M. Tsvelick. The transport properties of magneitc alloys with multi-channel Kondo impurities. *J. Phys.: Cond. Mat.*, **2** 2833, 1990.

[286] D. L. Cox. Quandrupolar Kondo Effect in Uranium Heavy-Electron Materials? *Phys. Rev. Lett.*, **59** 1240, 1987.

[287] A. Muramatsu and F. Guinea. Low-Temperature Behavior of a Tunneling Atom Interacting with a Degenerate Electron Gas. *Phys. Rev. Lett.*, **57** 2337, 1986.

[288] D. C. Ralph and R. A. Buhrman. Observation of Kondo Scattering without Magnetic Impurities: A Point Contact Study of Two-Level Tunneling Systems in Metals. *Phys. Rev. Lett.*, **69** 2118, 1992.

[289] D. C. Ralph, A. W. W. Ludwig, J. von Delft, and R. A. Buhrman. 2-Channel Kondo Scaling in Conductance Signals from 2-Level Tunneling Systems. *Phys. Rev. Lett.*, **72** 1064, 1994.

[290] I. L. Aleiner, B. L. Altshuler, Y. M. Galperin, and T. A. Shutenko. Kondo Temperature for the Two-Channel Kondo Models of Tunneling Centers. *Phys. Rev. Lett.*, **86** 2629, 2001.

[291] G. Zaránd. Existence of a two-channel Kondo regime for tunneling impurities with resonant scattering. *Phys. Rev. B*, **72** 245103, 2005.

[292] H-U Desgranges. Thermodynamics of the n-channel Kondo problem (numerical solution). *J. Phys. C: Solid State Phys.*, **18** 5481, 1985.

[293] Christian Kolf and Johann Kroha. Strong versus weak coupling duality and coupling dependence of the Kondo temperature in the two-channel Kondo model. *Phys. Rev. B*, **75** 045129, 2007.

[294] P. W. Anderson. Localized Magnetic States in Metals. *Phys. Rev.*, **124** 41, 1961.

[295] A. C. Hewson. Renormalized perturbation expansion and Fermi liquid theory. *Phys. Rev. Lett.*, **70** 4007, 1993.

[296] M. Fabrizio. Clusters of Anderson impurities and beyond: How Kondo effect dies and what can we learn about the Mott transition. Lecture notes, XI Training Course in the Physics of Strongly Correlated Systems, 2006.

[297] B. Horvatic and V. Zlatic. Equivalence of the perturbative and Bethe-Ansatz solution of the symmetric Anderson Hamiltonian. *J. Physique*, **46** 1459, 1985.

[298] J. R. Schrieffer and P. A. Wolff. Relation between the Anderson and Kondo Hamiltonians. *Phys. Rev.*, **149** 491, 1966.

[299] B. Caroli. On the determination of the exchange integral for magnetic impurities in metals. *J. Phys. F: Metal Phys.*, **5** 1399, 1975.

[300] J. R. Schrieffer. The Kondo effect - the link between magnetic and nonmagnetic impurities in metals? *J. Appl. Phys.*, **38** 1143, 1967.

[301] P. W. Anderson. Antiferromagnetism. Theory of superexchange interaction. *Phys. Rev.*, **79** 350, 1950.

[302] Martin R. Galpin and David E. Logan. Single-particle dynamics of the Anderson model: a two-self-energy description within the numerical renormalization group approach. *J. Phys.: Condens. Matter*, **17** 6959, 2005.

[303] László Borda. Kondo screening cloud in a one-dimensional wire: Numerical renormalization group study. *Phys. Rev. B*, **75** 041307(R), 2007.

[304] D. C. Langreth. Friedel Sum Rule for Anderson's Model of Localized Impurity States. *Phys. Rev.*, **150** 516, 1966.

[305] Nigel L. Dickens and David E. Logan. On the scaling spectrum of the Anderson impurity model. *J. Phys.: Condens. Matter*, **13** 4505, 2001.

[306] B. A. Jones, B. G. Kotliar, and A. J. Millis. Mean-field analysis of two antiferromagnetically coupled Anderson impurities. *Phys. Rev. B*, **39** 3415, 1989.

[307] O. Sakai and Y. Shimizu. Excitation spectra of the two impurity Anderson model. II. Interplay between Kondo effect and the inter site interactions. *J. Phys. Soc. Japan*, **61** 2348, 1992.

[308] C. Sire, C. M. Varma, and H. R. Krishnamurthy. Theory of the non-Fermi-liquid transition point in the two-impurity Kondo model. *Phys. Rev. B*, **48** 13833, 1993.

[309] Junwu Gan. Solution of the two-impurity Kondo model: Critical point, Fermi-liquid phase, and crossover. *Phys. Rev. B*, **51** 8287, 1995.

[310] Tzanko Ivanov. ac response of a double quantum dot. *Phys. Rev. B*, **56** 12339, 1997.

[311] T. Pohjola, J. Konig, M. M. Salomaa, J. Schmid, H. Schoeller, and G. Schon. Resonant tunneling through a two-level dot and double quantum dots. *Europhys. Lett.*, **40** 189, 1997.

[312] T. Aono, M. Eto, and K. Kawamura. Conductance through Quantum Dot Dimer Below the Kondo Temperature. *J. Phys. Soc. Japan*, **67** 1860, 1998.

[313] R. H. Blick, D. Pfannkuche, R. J. Haug, K. v. Klitzing, and K. Eberl. Formation of a coherent mode in a double quantum dot. *Phys. Rev. Lett.*, **80** 4032, 1998.

[314] W. Izumida, O. Sakai, and Y. Shimizu. Kondo effects in quantum dot systems. *Physica B*, **259-261** 215, 1999.

[315] A. Georges and Y. Meir. Electronic correlations in transport through coupled quantum dots. *Phys. Rev. Lett.*, **82** 3508, 1999.

[316] N. Andrei, G. T. Zimanyi, and G. Schon. Quantum phase transition in coupled quantum dots. *Phys. Rev. B*, **60** R5125, 1999.

[317] Ramon Aguado and Davic C. Langreth. Out-of-equilibrium Kondo effect in double quantum dots. *Phys. Rev. Lett.*, **85** 1946, 2000.

[318] T. Aono and M. Eto. Kondo effect in coupled quantum dots under magnetic fields. *Phys. Rev. B*, **64** 073307, 2001.

[319] R. Lopez, R. Aguado, and G. Platero. Nonequilibrium Transport through Double Quantum Dots: Kondo effect versus Antiferromagnetic coupling. *Phys. Rev. Lett.*, **89** 136802, 2002.

[320] M. A. Ruderman and C. Kittel. Indirect Exchange Coupling of Nuclear Magnetic Moments by Conduction Electrons. *Phys. Rev.*, **96** 99, 1954.

[321] K. Yosida. Magnetic Properties of Cu-Mn Alloys. *Phys. Rev.*, **106** 893, 1957.

[322] Hirokazu Tsunetsugu, Mandred Sigrist, and Kazuo Ueda. The ground-state phase diagram of the one-dimensional Kondo lattice model. *Rev. Mod. Phys.*, **69** 809, 1997.

[323] P. Simon, R. Lopez, and Y. Oreg. Ruderman-Kittel-Kasuya-Yosida and Magnetic-field Interactions in coupled Kondo Quantum Dots. *Phys. Rev. Lett.*, **94** 086602, 2005.

[324] M. G. Vavilov and L. I. Glazman. Transport Spectroscopy of Kondo Quantum Dots Coupled by RKKY Interaction. *Phys. Rev. Lett.*, **94** 086805, 2005.

[325] Hiroyuki Tamura and Leonid Glazman. Tunable Kondo screening in a quantum dot device. *Phys. Rev. B*, **72**(12) 121308(R), 2005.

[326] P. S. Cornaglia, D. R. Grempel, and H. Ness. Quantum transport through a deformable molecular transistor. *Phys. Rev. B*, **71** 075320, 2005.

[327] A. M. Lobos and A. A. Aligia. Conductance through an array of quantum dots. *Phys. Rev. B*, **74** 165417, 2006.

[328] A. A. Aligia. Effective Kondo model for a trimer on a metallic surface. *Phys. Rev. Lett.*, **96** 096804, 2006.

[329] P. Wahl, P. Simon, L. Diekhöner, V. S. Stepanyuk, P. Bruno, M. A. Schneider, and K. Kern. Exchange interaction between single magnetic adatoms. *Phys. Rev. Lett.*, **98** 056601, 2007.

[330] S. Alexander and P. W. Anderson. Interaction between localized states in metals. *Phys. Rev.*, **133** A1594, 1964.

[331] T. Hatano, M. Stopa, and S. Tarucha. Single-Electro Delocalization in Hybrid Vertical-Lateral Double Quantum Dots. *Science*, **309** 268, 2005.

[332] A. K. Hüttel, S. Ludwig, H. Lorenz, K. Eberl, and J. P. Kotthaus. Direct control of the tunnel splitting in a one-electron double quantum dot. *Phys. Rev. B*, **72** 081310, 2005.

[333] U. Fano. Effects of configuration interaction on intensities and phase shifts. *Phys. Rev.*, **124** 1866, 1961.

[334] J. Göres, D. Goldhaber-Gordon, S. Heemeyer, M. A. Kastner, Hadas Shtrikman, D. Mahalu, and U. Meirav. Fano resonances in electronic transport through a single-electron transistor. *Phys. Rev. B*, **62** 2188, 2000.

[335] A. C. Johnson, C. M. Marcus, M. P. Hanson, and A. C. Gossard. Coulomb-Modified Fano Resonance in a One-Lead Quantum Dot. *Phys. Rev. Lett.*, **93** 106803, 2004.

[336] Kensuke Kobayashi, Hisashi Aikawa, Shingo Katsumoto, and Yasujiro Iye. Tuning of the Fano Effect through a Quantum Dot in an Aharonov-Bohm Interferometer. *Phys. Rev. Lett.*, **88** 256806, 2002.

[337] Masahiro Sato, Hisashi Aikawa, Kensuke Kobayashi, Shingo Katsumoto, and Yasuhiro Iye. Observation of the Fano-Kondo Antiresonance in a Quantum Wire with a Side-Coupled Quantum Dot. *Phys. Rev. Lett.*, **95** 066801, 2005.

[338] J. R. Schrieffer and D. C. Mattis. Localized magnetic moments in dilute metallic alloys: correlation effects. *Phys. Rev.*, **140** 1412, 1965.

[339] L. Gaudreau, S. A. Studenikin, A. S. Sachrajda, P. Zawadzki, A. Kam, J. Lapointe, M. Korkusinski, and P. Hawrylak. Stability diagram of a few-electron triple dot. *Phys. Rev. Lett.*, **97** 036807, 2006.

[340] Marek Korkusinski, Irene Puerto Gimenez, Pawel Hawrylak, Louis Gaudreau, Sergei A. Studenkikin, and Andrew S. Sachrajda. Topological Hund's rules and the electronic properties of a triple lateral quantum dot molecule. cond-mat/0610175, 2006.

[341] C. A. Stafford and S. Das Sarma. Collective Coulomb blockade in an array of quantum dots: A Mott-Hubbard approach. *Phys. Rev. Lett.*, **72** 3590, 1994.

[342] Guanlong Chen, Gerhard Klimeck, Supriyo Datta, Gyanhua Chen, and William A. Goddard III. Resonant tunneling through quantum-dot arrays. *Phys. Rev. B*, **50** 8035, 1994.

[343] Akira Oguri. Quasiparticle description for transport through a small interacting system. *Phys. Rev. B*, **63** 11535, 2001.

[344] T. Kuzmenko, K. Kikoin, and Y. Avishai. Dynamical symmetries in Kondo tunneling through Complex Quantum Dots. *Phys. Rev. Lett.*, **89** 156602, 2002.

[345] T. Kuzmenko. Kondo effect in artificial and real molecules. Disertacija, Ben-Gurion University, Beer-Sheva, 2005.

[346] Zhao tan Jiang, Qing feng Sun, and Yupeng Wang. Kondo transport through serially coupled triple quantum dots. *Phys. Rev. B*, **72** 045332, 2005.

[347] C. A. Büsser, A. Moreo, and E. Dagotto. Conductance Dip in the Kondo Regime of Linear Arrays of Quantum Dots. *Phys. Rev. B*, **70** 035402, 2004.

[348] A. Oguri. Transmission probability for interacting electrons connected to reservoirs. *J. Phys. Soc. Japan*, **70** 2666, 2001.

[349] D. Goldhaber-Gordon, J. Göres, M. A. Kastner, H. Shtrikman, D. Mahalu, and U. Meirav. From the Kondo regime to the mixed-valence regime in a single-electron transistor. *Phys. Rev. Lett.*, **81** 5225, 1998.

[350] C. Caroli, R. Combescot, P. Nozieres, and D. Saint-James. Calculation of the tunneling current. *J. Phys. C*, **4** 916, 1971.

[351] Y. Meir, N. S. Wingreen, and P. A. Lee. Low-temperature transport through a quantum dot: The Anderson model out of equilibrium. *Phys. Rev. Lett.*, **70** 2601, 1993.

[352] G. Binnig, H. Rohrer, C. Gerber, and E. Weibel. Surface studies by scanning tunneling microscopy. *Phys. Rev. Lett.*, **49** 57, 1982.

[353] C. Julian Chen. Introduction to scanning tunneling microscopy. Oxford University Press, 1993.

[354] Roland Wiesendanger. Scanning probe microscopy and spectroscopy. Cambridge University Press, 1994.

[355] R. Wiesendanger. Nano-scale studies of quantum phenomena by scanning probe microscopy. *Ann. Phys.*, **9** 895, 2002.

[356] H. J. Güntherodt and R. Wiesendanger, editors. Scanning tunneling microscopy I: General Principles and Applications to Clean and Adsorbate-Covered Surfaces. Springer Verlag Berlin, 1992.

[357] H. J. Güntherodt and R. Wiesendanger, editors. Scanning tunneling microscopy II: Further Applications and Related Scanning Techniques. Springer Verlag Berlin, 1992.

[358] Dawn A. Bonnell, editor. Scanning tunneling microscopy and spectroscopy. VCH Publishers, 1993.

[359] L. E. C. van de Leemput and H. van Kempen. Scanning tunnelling microscopy. *Rep. Prog. Phys.*, **55** 1165, 1992.

[360] G. Binnig and H. Rohrer. In touch with atoms. *Rev. Mod. Phys.*, **71** S324, 1999.

[361] F. Besenbacher. Scanning tunneling microscopy studies of metal surfaces. *Rep. Prog. Phys.*, **59** 1737, 1996.

[362] D. Drakova. Theoretical modelling of scanning tunneling microscopy, scanning tunneling spectroscopy and atomic force microscopy. *Rep. Prog. Phys.*, **64** 205, 2001.

[363] M. F. Crommie. Observing electronic scattering in atomic-scale structures on metals. *J. Elec. Spectr. and Rel. Phen.*, **109** 1, 2000.

[364] W. A. Hofer. Challanges and erros: interpreting high resolution images in scanning tunneling microscopy. *Prog. Surf. Sci.*, **71** 147, 2003.

[365] G. A. D. Briggs and A. J. Fisher. STm experiment and atomistic modelling hand in hand: individual molecules on semiconductor surfaces. *Surf. Sci. Reports*, **33** 1, 1999.

[366] Gerhard Meyer, Jascha Repp, Sven Zöphel, Kai-Felix Braun, Saw Wai Hla, Stefan Fölsch, Ludwig Bartels, Francesca Moresco, and Karl Heinz Rieder. Controlled manipulation of atoms and small molecules with a low temperatgure scanning tunneling microscope. *Single molecules*, **1** 79, 2000.

[367] T. Komeda. Chemical identification and manipulation of molecules by vibrational excitation via inelastic tunneling process with scanning tunneling microscopy. *Prog. Surf. Sci.*, **78** 41, 2005.

[368] Saw-Wai Hla. Scanning tunneling microscopy single atom/molecule manipulation and its applications to nanoscience and technology. *J. Vac. Sci. Technol. B*, **23** 1351, 2005.

[369] F. Moresco. Manipulation of large molecules by low-temperature STM: model systems for molecular electronics. *Phys. Rep.*, **399** 175, 2004.

[370] W. Ho. Single-molecule chemistry. *J. Chem. Phys.*, **117** 11033, 2002.

[371] F. Rosei, M. Schunack, P. Jiang, A. Gourdon, E. Laegsgaard, I. Stensgaard, C. Joachim, and F. Besenbacher. Organic molecules acting as templates on metal surfaces. *Science*, **296** 328, 2002.

[372] Abraham Nitzan and Mark A. Ratner. Electron transport in molecular wire junction. *Science*, **300** 1384, 2003.

[373] P. H. Lippel, R. J. Wilson, M. D. Miller, Ch. Wöll, and S. Chaing. High-resolution imaging of Copper-phthalocyanine by Scanning-Tunneling Microscopy. *Phys. Rev. Lett.*, **62** 171, 1989.

[374] V. J. Langlais, R. R. Schlitter, H. Tang, A. Gourdon, C. Joachim, and J. K. Gimzewski. Spatially Resolved Tunneling along a Molecular Wire. *Phys. Rev. Lett.*, **83** 2809, 1999.

[375] M. Schunack, E. Lægsgaard, I. Stensgaard, and F. Besenbacher. Bonding and ordering of decacyclene molecules on Cu(110) studied by scanning tunneling microscopy. *J. Chem. Phys.*, **117** 8493, 2002.

[376] J. Kuntze, R. Berndt, P. Jiang, H. Tang, A. Gourdon, and C. Joachin. Conformations of a molecular wire adsorbed on a metal surface. *Phys. Rev. B*, **65** 233405, 2002.

[377] Federico Rosei, Michael Schunack, Yoshitaka Naitoh, Ping Jiang, André Gourdon, Erik Laegsgaard, Ivan Stensgaard, Christian Joachim, and Flemming Besenbacher. Properties of large organic molecules on metal surfaces. *Prog. Surf. Sci.*, **71** 95, 2003.

[378] P. S. Weiss and D. M. Eigler. Site dependence of the apparent shape of a molecule in scanning tunneling microscope images - benzene on Pt(111). *Phys. Rev. Lett.*, **71** 3139, 1993.

[379] V. M. Hallmark, S. Chiang, J. K. Brown, and Ch. Woll. Real-space imaging of the molecular organization of napththalene on Pt(111). *Phys. Rev. Lett.*, **66** 48, 1991.

[380] B. S. Swartzentruber. Direct Measurement of Surface Diffusion Using Atom-Tracking Scanning Tunneling Microscopy. *Phys. Rev. Lett.*, **76** 459, 1996.

[381] B. G. Briner, M. Doering, H.-P. Rust, and A. M. Bradshaw. Microscopic molecular diffusion enhanced by adsorbate interactions. *Science*, **278** 257, 1997.

[382] Jens Weckesser, Johannes V. Barth, and Klaus Kern. Direct observation of surface diffusion of large organic molecules at metal surfaces: PVBA on Pd(110). *J. Chem. Phys.*, **110** 5351, 1999.

[383] Federico Rosei and Renzo Rosei. Atomic description of elementary surface processes : diffusion and dynamics. *Surf. Sci.*, **500** 395–413, 2002.

[384] L. J. Lauhon and W. Ho. Direct observation of the quantum tunneling of single hydrogen atoms with a scanning tunneling microscope. *Phys. Rev. Lett.*, **85** 4566, 2000.

[385] A. G. Naumovets and Zhenyu Zhang. Fidgety particles on surfaces: how do they jump, walk, group, and settle in virgin areas? *Surf. Sci.*, **500** 414, 2002.

[386] M. Schunack, T. R. Linderoth, F. Rosei, E. Laegsgaard, I. Stensgaard, and F. Besenbacher. Long jumps in the surface diffusion of large molecules. *Phys. Rev. Lett.*, **88** 156102, 2002.

[387] F. Moresco, G. Meyer, K. H. Rieder, H. Tand, A. Gourdon, and C. Joachim. Conformational changes of single molecules induced by scanning tunneling microscopy manipulations: A route to molecular switching. *Phys. Rev. Lett.*, **86** 672, 2001.

[388] V. M. Hallmark, S. Chiang, K.-P. Meinhardt, and K. Hafner. Observation and calculation of internal structure in scanning tunneling microscopy images of related molecules. *Phys. Rev. Lett.*, **70** 3740, 1993.

[389] L. A. Bumm, J. J. Arnold, M. T. Cygan, T. D. Dunbar, T. P. Burgin, L. Jones II, D. L. Allara, J. M. Tour, and P. S. Weiss. Are Single Molecular Wires Conducting ? *Science*, **271** 1705, 1996.

[390] Z. J. Donhauser, B. A. Mantooth, K. F. Kelly, L. A. Bumm, J. D. Monnell, J. J. Stapleton, D. W. Price Jr., A. M. Rawlett, D. L. Allara, J. M. Tour, and P. S. Weiss. Conductance Switching in Single Molecule Through Conformational Changes. *Science*, **292** 2303, 2001.

[391] P. G. Piva, G. A. DiLabio, J. L. Pitters, J. Zikovsky, M. Rezeq, S. Dogel, W. A. Hofer, and R. A. Wolkow. Field regulation of single-molecule conductivity by a charged surface atom. *Nature*, **435** 658, 2005.

[392] J. F. Weaver, A. F. Carlsson, and R. J. Madix. The adsorption and reaction of low molecular weight alkanes on metallic single crystal surfaces. *Surf. Sci. Rep.*, **50** 107, 2003.

[393] G. Meyer, S. Zöpfel, and K. H. Rieder. Controlled manipulation of ethen molecules and lead atoms on Cu(211) with a low temperature scanning tunneling microscope. *Appl. Phys. Lett.*, **69** 3185, 1996.

[394] L. J. Lauhon and W. Ho. Control and characterization of a multistep unimolecular reaction. *Phys. Rev. Lett.*, **84** 1527, 2000.

[395] B. C. Stipe, H. A. Rezaei, and W. Ho. Localization of inelastic tunneling and the determination of atomic-scale structure with chemical specificity. *Phys. Rev. Lett.*, **82** 1724, 1999.

[396] Yousoo Kim, Tadahiro Komeda, and Maki Kawai. Single-Molecule Reaction and Characterization by Vibrational Excitation. *Phys. Rev. Lett.*, **89** 126104, 2002.

[397] L. Bartels, G. Meyer, and K.-H. Rieder. Basic steps of lateral manipulation of single atoms and diatomic clusters with a scanning tunneling microscope tip. *Phys. Rev. Lett.*, **79** 697, 1997.

[398] L. bartels, G. Meyer, and K.-H. Rieder. Controlled vertical manipulation of single CO molecules with the scanning tunneling microscope: A route to chemical contrast. *Appl, Phys. Lett.*, **71** 213, 1997.

[399] L. Bartels, G. Meyer, K. H. Rieder, D. Velic, E. Knoesel, A. Hotzel, M. Wolf, and G. Ertl. Dynamics of electron-induced manipulation of individual CO molecules on Cu (111). *Phys. Rev. Lett.*, **80** 2004, 1998.

[400] H. Ohtani, R. J. Wilson, S. Chiang, and C. M. Mate. Scanning tunneling microscopy observations of benzene molecules on the Rh(111)-(3x3)(C_6H_6+2CO) surface. *Phys. Rev. Lett.*, **60** 2398, 1988.

[401] J. I. Pascual, J. J. Jackiw, Z. Song, P. S. Weiss, H. Conrad, and H.-P. Rust. Adsorbate-Substrate Vibrational Modes of Benzene on Ag(110) Resolved with Scanning Tunneling Spectroscopy. *Phys. Rev. Lett.*, **86** 1050, 2001.

[402] D. N. Fatuba, J. P. Landry, A. Loui, and S. Chiang. Experimental and theoretical STM imaging of xylene isomers on Pd(111). *Phys. Rev. B*, **65** 045106, 2002.

[403] M. Bohringer, W.-D. Schneider, and R. Berndt. Scanning tunneling microscope-induced molecular motion and its effect on the image formation. *Surf. Sci.*, **408** 72, 1998.

[404] Jerome Lagoute, Kiyoshi Kanisawa, and Stefan Fölsch. Manipulation and adsorption-site mapping of single pentacene molecules on Cu(111). *Phys. Rev. B*, **70** 245415, 2004.

[405] S.-W. Hla, K.-F. Braun, B. Wassermnann, and K.-H. Rieder. Controlled Low-Temperature Molecular Manipulation of Sexiphenyl Molecules on Ag(111) Using Scanning Tunneling Microscopy. *Phys. Rev. Lett.*, **93** 208302, 2004.

[406] D. J. Frankel, Q. Chen, and N. V. Richardson. Adsorption of α-pyridone on Cu(110). *J. Chem. Phys.*, **116** 8988, 2002.

[407] J. Gaudioso, L. J. Lauhon, and W. Ho. Vibrationally mediated negative differential resistance in a single molecule. *Phys. Rev. Lett.*, **85** 1918, 2000.

[408] S. W. Wu, G. V. Nazin, X. Chen, X. H. Qiu, and W. Ho. Control of relative tunneling rates in single molecule bipolar electron transport. *Phys. Rev. Lett.*, **93** 236802, 2004.

[409] A. M. Baró, Saw-Wai Hla, and K. H. Rieder. LT-STM study of self-organization of β-carotene molecular layers on Cu(111). *Chem. Phys. Lett.*, **369** 240, 2003.

[410] M. Schunack, L. Petersen, A. Kühnle, E. Lægsgaard, I. Stensgaard, I. Johannsen, and F. Besenbacher. Anchoring of organic molecules to a metal surface: HtBDC on Cu (111). *Phys. Rev. Lett.*, **86** 456–459, 2001.

[411] M. Lackinger, S. Grissl, W. M. Heckl, and M. Hietschold. Coronene on Ag(111) investigated by LEED and STM in UHV. *J. Phys. Chem. B*, **106** 4482, 2002.

[412] Takashi Yokoyama, Shiyoshi Yokoyama, Toshiya Kamikado, and Shinro Mashiko. Nonplanar adsorption and orientation ordering of porphyrin molecules on Au(111). *J. Chem. Phys.*, **115** 3814, 2001.

[413] M. Bohringer, W.-D. Schneider, K. Glockler, E. Umbach, and R. Berndt. Adsorption site determination of PTCDA on Ag(110) by manupulation of adatoms. *Surf. Sci.*, **419** 95, 1998.

[414] L. Gross, F. Moresco, L. Savio, A. Gourdon, C. Joachim, and K.-H. Rieder. Scattering of Surface State Electrons at Large Organic Molecules. *Phys. Rev. Lett.*, **93** 056103, 2004.

[415] R. J. Wilson, G. Meijer, D. S. Bethune, R. D. Johnson, D. D. Chambliss, M. S. de Vries, H. E. Hunziker, and H. R. Wendt. Imaging C_{60} clusters on a surface using a scanning tunneling microscope. *Nature*, **348** 621, 1990.

[416] J. K. Gimzewski, S. Modesti, and R. R. Schlittler. Cooperative self-assembly of Au atoms and C_{60} on Au(110) surfaces. *Phys. Rev. Lett.*, **72** 1036, 1994.

[417] Woei Wu Pai and Ching-Ling Hsu. Ordering of an incommensurate molecular layer with adsorbate-induced reconstruction: C_{60}/Ag(100). *Phys. Rev. B*, **68** 121403(R), 2003.

[418] X. Lu, M. Grobis, K. H. Khoo, S. G. Louie, and M. F. Crommie. Spatially Mapping the Spectral Density of a Single C_{60} Molecule. *Phys. Rev. Lett.*, **90** 096802, 2003.

[419] S. Heinze, M. Bode, O. Pietzsch, A. Kubetzka, X. Nie, S. Blügel, and R. Wiesendanger. Real-space imaging of two-dimensional antiferromagnetism on the atomic scale. *Science*, **288** 1805, 2000.

[420] A. Kubetzka, M. Bode, O. Pietzsch, and R. Wiesendanger. Spin-polarized scanning tunneling microscopy with antiferromagnetic probe tips. *Phys. Rev. Lett.*, **88** 057201, 2002.

[421] A. Wachowiak, J. Wiebe, M. Bode, O. Pietzsch, M. Morgenstern, and R. Wiesendanger. Direct observation of internal spin structure of magnetic vortex cores. *Science*, **298** 577, 2002.

[422] O. Pietzsch, A. Kubetzka, M. Bode, and R. Wiesendanger. Observation of magnetic hysteresis at the nanometer scale by spin-polarized scanning tunneling spectroscopy. *Science*, **292** 2053, 2001.

[423] Y. Manassen, R. J. Hamers, J. E. Demuth, and Jr. A. J. Castellano. Direct observation of the precession of individual paramagnetic spins on oxidized silicon surfaces. *Phys. Rev. Lett.*, **62** 2531, 1989.

[424] C. Durkan and M. E. Welland. Electronic spin detection in molecules using scanning-tunneling-microscopy-assites electron-spin resonance. *Appl. Phys. Lett.*, **80** 458, 2002.

[425] N. D. Lang. Spectroscopy of single atoms in the scanning tunneling microscope. *Phys. Rev. B*, **34** 5947, 1986.

[426] H. C. Manoharan, C. P. Lutz, and D. M. Eigler. Quantum mirages formed by coherent projection of electronic structure. *Nature*, **403** 512, 2000.

[427] V. Madhavan, W. Chen, T. Jamneala, M. F. Crommie, and N. S. Wingreen. Local spectroscopy of a Kondo impurity: Co on Au(111). *Phys. Rev. B*, **64** 165412, 2001.

[428] T. Hanke, M. Bode, S. Krause, L. Berbil-Bautista, and R. Wiesendanger. Temperature-dependent scanning tunneling spectroscopy of Cr(001): Orbital Kondo resonance versus surface state. *Phys. Rev. B*, **72** 085453, 2005.

[429] A. Zhao and others. Controlling the Kondo effect of an adsorbed magnetic ion through its chemical bonding. *Science*, **309** 1542, 2005.

[430] A. Yazdani, B. A. Jones, C. P. Lutz, M. F. Crommie, and D. M. Eigler. Probing the local effects of magnetic impurities on superconductivity. *Science*, **275** 1767, 1997.

[431] A. Yazdani, C. M. Howald, C. P. Lutz, A. Kapitulnik, and D. M. Eigler. Impurity-induced bound excitations on the surface of $Bi_2Sr_2CaCu_2O_8$. *Phys. Rev. Lett.*, **83** 176, 1999.

[432] S. H. Pan, E. W. Hudson, K. M. Lang, H. Eisaki, S. Uchida, and J. C. Davis. Imaging the effects of individual zinc impurity atoms on superconductivity in $Bi_2Sr_2CaCu_2O_{8+\delta}$. *Nature*, **403**, 1993.

[433] K. McElroy, R. W. Simmonds, J. E. Hoffman, D.-H. Lee, J. Orenstein, H. Eisaki, S. Uchida, and J. C. Davis. Relating atomic-scale electronic phenomena to wave-like quasiparticle states in superconducting $Bi_2Sr_2CaCu_2O_{8+\delta}$. *Nature*, **422** 592, 2001.

[434] D. J. Derro, E. W. Hudson, K. M. Lang, S. H. Pan, J. C. Davis, J. T. Markert, and A. L. de Lozanne. Nanoscale one-dimensional scattering resonances in the CuO chains of $YBa_2Cu_3O_{6+x}$. *Phys. Rev. Lett.*, **88** 097002, 2002.

[435] Oystein Fischer, Martin Kugler, Ivan Maggio-Aprile, Christophe Berthod, and Christoph Renner. Scanning tunneling spectroscopy of high-temperature superconductors. *Rev. Mod. Phys.*, **79** 353, 2007.

[436] N. Nilius, T. M. Wallis, and W. Ho. Development of One-Dimensional Band Structure in Artificial Gold Chains. *Science*, **297** 1853, 2002.

[437] B. C. Stipe, M. A. Rezaei, and W. Ho. Single-Molecule Vibrational Spectroscopy and Microscopy. *Science*, **280** 1732, 1998.

[438] J. R. Hahn and W. Ho. Single molecule imaging and vibrational spectroscopy with a chemically modified tip of a scanning tunneling microscope. *Phys. Rev. Lett.*, **87** 196102, 2001.

[439] A. J. Heinrich, J. A. Gupta, C. P. Lutz, and D. M. Eigler. Single-Atom Spin-Flip Spectroscopy. *Science*, **306** 466, 2004.

[440] Cyrus F. Hirjibehedin, Christopher P. Lutz, and Anreas J. Heinrich. Spin coupling in engineered atomic structures. *Science*, **312** 1021, 2006.

[441] Harald Brune. Assembly and probing of spin chains of finite size. *Science*, **312** 1005, 2006.

[442] O. Pietzsch, S. Okatov, A. Kubetzka, M. Bode, S. Heinze, A. Lichtenstein, and R. Wiesendanger. Spin-resolved electronic structure of nanoscale cobalt islands on Cu(111). *Phys. Rev. Lett.*, **96** 237203, 2006.

[443] X. H. Qui, G. V. Nazin, and W. Ho. Vibronic states in single molecule electron transport. *Phys. Rev. Lett.*, **92** 206102, 2004.

[444] D. M. Eigler and E. K. Schweizer. Positioning single atoms with a scanning tunneling microscope. *Nature*, **344** 524, 1990.

[445] J. A. Stroscio and D. M. Eigler. Atomic and molecular manipulation with the scanning tunneling microscope. *Science*, **254** 1319, 1991.

[446] D. M. Eigler, C. P. Lutz, and W. E. Rudge. An atomic switch realized with the scanning tunneling microscope. *Nature*, **352** 600, 1991.

[447] G. Meyer, S. Zöpfel, and K. H. Rieder. Scanning tunneling microscopy manipulation of native substrate atoms: A new way to obtain registry information on foreign adsorbates. *Phys. Rev. Lett.*, **77** 2113, 1996.

[448] G. Meyer, L. Bartels, S. Zöphel, E. Henze, and K. H. Rieder. Controlled atom by atom restructuring of a metal surface with the scanning tunneling microscope. *Phys. Rev. Lett.*, **78** 1512, 1997.

[449] J. A. Stroscio and R. J. Celotta. Controlling the dynamics of a single atom in lateral atom manipulation. *Science*, **306** 242, 2004.

[450] S. W. Hla, A. Hühnle, L. Bartels, G. Meyer, and K. H. Rieder. Controlled lateral manipulation of single diiodobenzene molecules on the Cu(111) surface with the tip of a scanning tunneling microscope. *Surf. Sci.*, **454** 1079, 2000.

[451] F. Moresco, G. Meyer, K.-H. Rieder, H. Tang, A. Gourdon, and C. Joachim. Recording Intramolecular Mechanics during the Manipulation of a Large Molecule. *Phys. Rev. Lett.*, **87** 088302, 2001.

[452] A. J. Heinrich, C. P. Lutz, J. A. Gupta, and D. M. Eigler. Molecular cascades. *Sciencexpress*, stran 1076768, oct 2002.

[453] F. Moresco, G. Meyer, K. H. Rieder, H. Tang, A. Gourdon, and C. Joachim. Low temperature manipulation of big molecules in constant height mode. *Appl. Phys. Lett.*, **78** 306, 2001.

[454] Saw-Wai Hla, Kai-Felix Braun, Violeta Iancu, and Aparna Deshpande. Single-atom extraction by scanning tunneling microscope tip crash and nanoscale surface engineering. *Nanoletters*, **4** 1997, 2004.

[455] Saw-Wai Hla, Ludwig Bartels, Gerhard Meyer, and Karl-Heinz Rieder. Inducing All Steps of a Chemical Reaction with the Scanning Tunneling Microscope Tip: Towards Single Molecule Engineering. *Phys. Rev. Lett.*, **85** 2777, 2000.

[456] B. C. Stipe, M. A. Rezaei, W. Ho, S. Gao, M. Persson, and B. I. Lundqvist. Single-molecule dissociation by tunneling electrons. *Phys. Rev. Lett.*, **78** 4410, 1997.

[457] H. J. Lee and W. Ho. Single-bond formation and characterization with a scanning tunneling microscope. *Science*, **286** 1719, 2003.

[458] Franz J. Giessibl and Calvin F. Quate. Exploring the nanoworld with atomic force microscopy. *Physics Today*, **59**(10), Dec 2006.

[459] Franz J. Giessibl. Advances in atomic force microscopy. *Rev. Mod. Phys.*, **75** 949, 2003.

[460] S. Hembacher, F. J. Giessibl, and J. Mannhart. Force Microscopy with Light-Atom Probes. *Science*, **305** 380, 2004.

[461] G. Binnig, C. F. Quate, and C. Gerber. Atomic Force Microscope. *Phys. Rev. Lett.*, **56** 930, 1986.

[462] M. A. Lantz, H. J. Hug, R. Hoffmann, P. J. A. van Schendel, P. Kappenberger, S. Martin, A. Baratoff, and H.-J. Güntherodt. Quantitative Measurement of Short-Range Chemical Bonding Forces. *Science*, **291** 2580, 2001.

[463] G. Meyer. A simple low-temperature ultrahigh-vacuum scanning tunneling microscope capable of atomic manipulation. *Rev. Sci. Instrum.*, **67** 2960, 1996.

[464] S. Behler, M. K. Rose, J. C. Dunphy, D. F. Ogletree, M. Salmeron, and C. Chapelier. Scanning tunneling microscope with continuous flow cryostat sample cooling. *Rev. Sci. Instrum.*, **68** 2479, 1997.

[465] B. C. Stipe, M. A. Rezaei, and W. Ho. A variable-temperature scanning tunneling microscope capable of single-molecule vibrational spectroscopy. *Rev. Sci. Instrum.*, **70** 137, 1999.

[466] H. P. Rust, M. Doering, J. I. Pascual, T. P. Pearl, and P. S. Weiss. Temperature control of a liquid helium cooled Eigler-style scanning tunneling microscope. *Rev. Sci. Instrum.*, **72** 4393, 2001.

[467] E. T. Foley, N. L. Yoder, N. P. Guisinger, and M. C. Hersam. Cryogenic variable temperature ultrahigh vacuum scanning tunneling microscope for single molecule studies on silicon surfaces. *Rev. Sci. Instrum.*, **75** 5280, 2004.

[468] Guy K. White and Philip J. Meeson. Experimental techniques in low-temperature physics. Oxford Science Publications, fourth izdaja, 2002.

[469] R. Berman and C. F. Mate. Thermal contact at low temperatures. *Nature*, **182** 1661, 1958.

[470] R. Berman. Some experiments on thermal contact at low temperature. *J. Appl. Phys.*, **27** 318, 1956.

[471] K. Besocke. An easily operable scanning tunneling microscope. *Surf. Sci.*, **181** 145, 1987.

[472] J. Frohn, J. F. Wolf, K. Besocke, and M. Teske. Coarse tip distance adjustment and positioner for a scanning tunneling microscope. *Rev. Sci. Instrum.*, **60** 1200, 1989.

[473] N. Pertaya, K.-F. Braun, and K.-H. Rieder. On the stability of Besocke-type scanners. *Rev. Sci. Instrum.*, **75** 2608, 2004.

[474] G. Binnig and D. P. E. Smith. Single-tube three-dimensional scanner for scanning tunneling microscopy. *Rev. Sci. Instrum.*, **57** 1688, 1986.

[475] C. Julian Chen. Electrochemical deflection of piezoelectric tubes with quartered electrodes. *Appl. Phys. Lett.*, **60** 132, 1991.

[476] K-F. Braun. Oberflächenuntersuchungen und atomare Manipulation mit einem Rastertunnelmikroskop bei tiefen Temperaturen. Disertacija, Freie Universität Berlin, 2000.

[477] W. F. Smith, M. C. Abraham, J. M. Sloan, and M. Switkes. Simple retrofittable long-range x-y translation system for scanned probe microscopes. *Rev. Sci. Intrum.*, **67** 3599, 1996.

[478] T. Tiedje and A. Brown. Performance limits for the scanning tunneling microscopes. *J. Appl. Phys.*, **68** 649, 1990.

[479] Stefan Behler, Mark K. Rose, D. Frank Ogletree, and Miquel Salmeron. Method to characterize the vibrational response of a beetle type scanning tunneling microscope. *Rev. Sci. Instrum.*, **68** 124, 1997.

[480] W. F. Smith and B. W. Axelrod. Measurements of the double piezoelectric effect. *Rev. Sci. Instrum.*, **71** 1772, 2000.

[481] Henry W. Ott. Noise reduction techniques in electronic systems. Wiley-Interscience, second izdaja, 1988.

[482] David Nečas and Petr Klapetek. Gwyddion SPM data analysis software. `http://gwyddion.net/`.

[483] D. K. Biegelsen, F. A. Ponce, J. C. Tramontana, and S. M. Koch. Ion milled tips for scanning tunneling microscopy. *Appl. Phys. Lett.*, **50** 696, 1987.

[484] A. Cricenti, E. Paparazzo, M. A. Scarselli, L. Moretto, and S. Selci. Preparation and characterization of tungsten tips for scanning tunneling microscopy. *Rev. sci. Instrum.*, **65** 1558, 1994.

[485] L. Ottaviano, L. Lozzi, and S. Santucci. Scanning Auger microscopy study of W tips for scanning tunneling microscopy. *Rev. Sci. Instrum.*, **74** 3368, 2003.

[486] L. A. Hockett and S. E. Creager. A convenient method for removing surface oxides from tungstem STM tips. *Rev. Sci. Instrum.*, **64** 263, 1993.

[487] M. Cavallini and F. Biscarini. Electrochemically etched nickel tips for spin polarized scanning tunneling microscopy. *Rev. Sci. Instrum.*, **71** 4457, 2000.

[488] C. Albonetti and others. Electrochemical preparation of cobalt tips for scanning tunneling microscopy. *Rev. Sci. Instrum.*, **73** 4254, 2002.

[489] Y. Nakamura, Y. Mera, and K. Maeda. A reproducible method to fabricate atomically sharp tips for scanning tunneling microscopy. *Rev. Sci. Instrum.*, **70** 3373, 1999.

[490] J. P. Ibe and others. On the electochemical etching of tips for scanning tunneling microscopy. *J. Vac. Sci. Tech. A*, **8** 3570, 1990.

[491] I. Ekvall, E. Wahlstrom, D. Claesson, H. Olin, and E. Olsson. Preparation and characterization of electrochemically etched W tips for STM. *Meas. Sci. Technol.*, **10** 11, 1999.

[492] A.-D. Muller, F. Muller, M. Hietschold, F. Demming, J. Jersch, and K. Dickmann. Characterization of electrochemically etched tungsten tips for scanning tunneling microscopy. *Rev. Sci. Instrum.*, **70** 3970, 1999.

[493] Maarten Bischoff. Chemical identification in scanning tunneling microscopy by detection of element-specific localized surface states. Disertacija, Nijmegen, 2002.

[494] Paul A. Redhead. Foundations of vacuum science and technology, chapter Ultrahigh and Extreme High Vacuum. In Lafferty,[496] 1999.

[495] C. Benvenuti. Extreme high vacuum technology for particle accelerators. Proceedings of the 2001 Particle Accelerator Conference, Chicago, 2001.

[496] J. M. Lafferty, editor. Foundations of vacuum science and technology. Whiley-Interscience, 1999.

[497] Chin Shuang Lee, Tzu Ming Yen, and Jing Hui Lin. Light emission from an oxygen covered copper surfaces by ion bombardment. *Surf. Sci.*, **488** 379, 2001.

[498] M. H. Mintz, U. Atzmony, and N. Shamir. Interrelations between planes affecting adsorption kinetics on polycrystalline surfaces: oxygen adsorption on copper. *Phys. Rev. Lett.*, **59** 90, 1987.

[499] John B. Hudson. Foundations of vacuum science and technology, chapter Gas-Surface Interactions and Diffusion. In Lafferty,[496] 1999.

[500] R. Gordon Livesey. Foundations of vacuum science and technology, chapter Flow of gases through tubes and orifices. In Lafferty,[496] 1999.

[501] Ron Reid. Gas load origins in synchrotron light sources. Vacuum design note, VDN/10/96, Vacuum Support Group, Synchrotron Radiation Department, CLRC Daresbury Laboratory, 1996.

[502] R. G. Musket. Preparation of atomically clean surfaces of selected elements: a review. *Appl. Surf. Sci.*, **10** 143, 1982.

[503] Vincent S. Smentkowski. Trends in sputtering. *Prog. Surf. Sci.*, **64** 1, 2000.

[504] H. W. Edwards. Evaporation of metals in vacuum. *Rev. Sci. Instrum.*, **4** 449, 1933.

[505] K. J. Ross and B. Sonntag. High temperature metal atom beam sources. *Rev. Sci. Instrum.*, **66** 4409, 1995.

[506] J. Kirschner, H. Engelhard, and D. Hartung. An evaporation source for ion beam assisted deposition in ultrahigh vacuum. *Rev. Sci. Instrum.*, **73** 3853, 2002.

[507] L. Bartels, G. Meyer, and K.-H. Rieder. Lateral manipulation of single Cu atoms on flat and stepped surfaces. *J. Vac. Sci. Technol. A*, **16** 1047, 1998.

[508] Andreas Eichler Marek Gajdoš, Jürgen Hafner, Gerhard Meyer, and Karl-Heinz Rieder. CO adsorption on a Cu(211) surface: First-principle calculation and STM study. *Phys. Rev. B*, **71** 035402, 2005.

[509] M. F. Crommie, C. P. Lutz, and D. M. Eigler. Imaging standing waves in a 2-dimensional electron-gas. *Nature*, **363** 524, 1993.

[510] E. J. Heller, M. F. Crommie, C. P. Lutz, and D. M. Eigler. Scattering and absorption of surface electron waves in quantum corrals. *Nature*, **369** 464, 1994.

[511] Y. Hasegawa and Ph. Avouris. Direct observation of Standing Wave Formation at Surface Steps Using Scanning Tunneling Spectroscopy. *Phys. Rev. Lett.*, **71** 1071, 1993.

[512] J. Friedel. *Nuovo Cimento (Suppl)*, **7** 287, 1958.

[513] K. Hojrup Hansen, J. Gottschalck, L. Petersen, B. Hammer, F. Besenbacher, and I. Stensgaard. Surface waves on NiAl(110). *Phys. Rev. B*, **63** 115421, 2001.

[514] M. A. Schneider, L. Vitali, N. Knorr, and K. Kern. Observing the scattering phase shift of isolated Kondo impurities at surfaces. *Phys. Rev. B*, **65** 121406, 2002.

[515] M. Neef and K. Doll. CO adsorption on the Cu(111) surface: A density functional study. *Surf. Sci.*, **600** 1085, 2006.

[516] Isabelle M. L. Billas, A. Chatelain, and Walt A. de Heer. Magnetism from the atom to the bulk in iron, cobalt, and nickel clusters. *Science*, **265** 1682, 1994.

[517] P. Gambardella, S. Rusponi, M. Veronese, S. S. Dhesi, C. Grazioli, A. Dallmeyer, I. Cabria, R. Zeller, P. H. Dederichs, K. Kern, C. Carbone, and H. Brune. Giant magnetic anisotropy of single cobalt atoms and nanoparticles. *Science*, **300** 1130, 2003.

[518] Walt A. de Heer. The physics of simple metal clusters: experimental aspects and simple models. *Rev. Mod. Phys.*, **65** 611, 1993.

[519] Matthias Brack. The physics of simple metal clusters: self-consistent jellium model and semiclassical approaches. *Rev. Mod. Phys.*, **65** 677, 1993.

[520] H. J. Lee, W. Ho, and M. Persson. Spin splitting of s and p states in single atoms and magnetic coupling in dimers on a surface. *Phys. Rev. Lett.*, **92** 186802, 2004.

[521] F. Patthey, J.-M. Imer, W.-D. Schneider, H. Beck, and Y. Baer. High-resolution photoemission study of the low-energy excitations in $4f$-electron systems. *Phys. Rev. B*, **42** 8864, 1990.

[522] O. Ujsaghy, J. Kroha, L. Szunyogh, and A. Zawadowski. Theory of the Fano resonance in the STM tunneling density of states due to a single Kondo impurity. *Phys. Rev. Lett.*, **85** 2557, 2000.

[523] W. Chen, T. Jamneala, V. Madhavan, and M. F. Crommie. Disappearance of the Kondo resonance for atomically fabricated cobalt dimers. *Phys. Rev. B*, **60** R8529, 1999.

[524] M. A. Schneider, L. Vitali, P. Wahl, N. Knorr, L. Diekhöner, G. Wittich, M. Vogelgesang, and K. Kern. Kondo state of Co impurities at noble metal surfaces. *Appl. Phys. A*, **80** 937, 2005.

[525] N. Knorr, M. Alexander Schneider, L. Diekh:oner, P. Wahl, and K. Kern. Kondo Effect of Single Co Adatoms on Cu Surfaces. *Phys. Rev. Lett.*, **88** 096804, 2002.

[526] N. Quaas, M. Wenderoth, A. Weismann, R. G. Ulbrich, and K. Schönhammer. Kondo resonance of single Co atoms embedded in Cu(111). *Phys. Rev. B*, **69** 201103, 2004.

[527] T. Jamneala, V. Madhavan, W. Chen, and M. F. Crommie. Scanning tunneling spectroscopy of transition-metal impurities at the surface of gold. *Phys. Rev. B*, **61** 9990, 2000.

[528] K. Nagaoka, T. Jamneala, M. Grobis, and M. F. Crommie. Temperature dependence of a single Kondo impurity. *Phys. Rev. Lett.*, **88** 077205, 2002.

[529] P. S. Cornaglia and C. A. Balseiro. Scanning tunneling microscopy conductance of Kondo impurities on open and structured surfaces. *Phys. Rev. B*, **67** 205420, 2003.

[530] A. Schiller and S. Herschfield. Theory of scanning tunneling spectroscopy of a magnetic adatom on a metallic surface. *Phys. Rev. B*, **61** 9036, 2000.

[531] P. Wahl, L. Diekhöner, M. A. Schneider, L. Vitali, G. Wittich, and K. Kern. Kondo temperature of magnetic impurities at Surfaces. *Phys. Rev. Lett.*, **93** 176603, 2004.

[532] D. M. Eigler, C. P. Lutz, M. F. Crommie, H. C. Manoharan, A. J. Heinrich, and J. A. Gupta. Information transport and computation in nanometre-scale structures. *Philos. transact. A, Math. phys. eng. sci.*, **362** 1137, 2004.

[533] G. A. Fiete, J. S. Hersch, E. J. Heller, H. C. Manoharan, C. P. Lutz, and D. M. Eigler. Scattering theory of Kondo mirages and observation of signle Kondo atom phase shift. *Phys. Rev. Lett.*, **86** 2392, 2001.

[534] G. A. Fiete and E. J. Heller. Theory of Quantum corrals and Quantum Mirages. *Rev. Mod. Phys.*, **75** 933, 2003.

[535] G. Chiappe and A. A. Aligia. Interaction between Kondo impurities in a quantum corral. *Phys. Rev. B*, **66** 075421, 2002.

[536] G. Chiappe and A. A. Aligia. Erratum: Interaction between Kondo impurities in a quantum corral. *Phys. Rev. B*, **70** 129903(E), 2004.

[537] M. C. Michelini, R. Pis Diez, and A. H. Jubert. Density function study of small Ni_n clusters, with $n = 2 - 6, 8$ using the generalized gradient approximation. *Int. J. Quant. Chem.*, **85** 22, 2001.

[538] V. V. Savkin, A. N. Rubtsov, M. I. Katsnelson, and A. I. Lichtenstein. Correlated adatom trimer on a metal surface: A continuous-tiem quantum Monte Carlo study. *Phys. Rev. Lett.*, **94** 026402, 2005.

[539] T. W. Odom, J.-L. Huang, C. L. Cheung, and C. M. Lieber. Magnetic clusters on Single-Walled Carbon Nanotubes: The Kondo effect in a one-dimensional host. *Science*, **290** 1549, 2000.

[540] N. D. Lang. Apparent Size of an Atom in the Scanning Tunneling Microscope as a Function of Bias. *Phys. Rev. Lett.*, **58** 45, 1987.

[541] J. Merino and O. Gunnarsson. Role of surface states in scanning tunneling spectroscopy of (111) metal surfaces with Kondo adsorbates. *Phys. Rev. Lett.*, **93** 156601, 2004.

[542] Gediminas Gaigalas and C. Froese Fischer. A general Hartree-Fock program. *Comp. Phys. Comm.*, **98** 244, 1996.

[543] K. Yamada. Perturbation Expansion for the Anderson Hamiltonian. II. *Prog. Theor. Phys.*, **53** 970, 1975.

[544] C.-Y. Lin, A. H. Casto Neto, and B. A. Jones. Microscopic theory of the single impurity surface Kondo resonance. *Phys. Rev. B*, **71** 035417, 2005.

[545] Chiung-Yuan Lin, A. H. Castro Neto, and B. A. Jones. First-principles calculation of the single impurity surface Kondo resonance. *Phys. Rev. Lett.*, **97** 156102, 2006.

[546] M. Plihal and J. W. Gadzuk. Nonequilibrium theory of scanning tunneling spectroscopy via adsorbate resonances: Nonmagnetic and Kondo impurities. *Phys. Rev. B*, **63** 085404, 2001.

[547] L. Limot and R. Berndt. Kondo effect and surface-state electrons. *Appl. Surf. Sci.*, **237** 576, 2004.

[548] A. A. Aligia and A. M. Lobos. Mirages and many-body effects in quantum corrals. *J. Phys.: Condens. Matter*, **17** S1095, 2005.

[549] Luis G. G. V. Dias da Silva, Nancy P. Sandler, Kevin Ingersent, and Sergio E. Ulloa. Zero-field splitting and quantum-critical transition in double quantum dots. *Phys. Rev. Lett.*, **97** 096603, 2006.

[550] G. D. Mahan. Many-particle physics. Kluwer Academic, New York, 2000.

[551] J. V. B. Ferreira. Modelo de Anderson de dois canais. Disertacija, Universidade de Sao Paulo, 2000.

Index

Izjava

Izjavljam, da sem v disertaciji predstavil rezultate lastnega znanstvenoraziskovalnega dela.

Ljubljana, 28.3.2007 Rok Žitko